Triannual Report 2005 – 2007
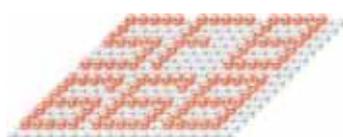
Research Group "Scanning Probe Methods"

University of Hamburg
Institute of Applied Physics

Microstructure Advanced
Research Center Hamburg (MARCH)

Interdisciplinary Nanoscience Center
Hamburg (INCH)

Sonderforschungsbereich 668
(Collaborative Research Center)

Contact:
Prof. Dr. Roland Wiesendanger
Tel.   (++49) 40-42838-5244 (direct)
          (++49) 40-42838-3203/-7045 (secretary)
FAX   (++49) 40-42838-6188
e-mail   `wiesendanger@physnet.uni-hamburg.de`
WWW   www.nanoscience.de

Contents

Chapter 1

Preface

This is the fifth triannual report of the research group "Scanning Probe Methods" at the Institute of Applied Physics and "Microstructure Advanced Research Center Hamburg (MARCH)" of the University of Hamburg. MARCH was officially opened in February 1996 and was established as a joint effort of the Federal Government (the "Bund") and the State of Hamburg. Six experimental research groups are involved in MARCH covering the following topics: nanostructure physics, semiconductor physics, scanning probe methods, surface and interface physics, magnetism and low temperature physics, and growth of semiconductor heterostructures and nanostructures. About 180 scientists are working at MARCH.

In 1997, one year after the opening of MARCH, a Collaborative Research Center funded by the German Research Foundation (DFG-Sonderforschungsbereich SFB 508) on "Quantum materials" was established (chairperson: Prof. Dr. Detlef Heitmann, MARCH) which involves research groups from MARCH, from the I. Institute of Theoretical Physics, from HASYLAB/DESY, and from the Institute of Physical Chemistry. The SFB 508 deals with quantum phenomena in nanostructured III-V-semiconductors including energy-quantization, electron tunneling, as well as Coulomb, exchange, and correlation effects. The three primary research areas are "lateral nanostructures", "hybrid structures", and "clusters". Currently, the fourth funding period of the very successful SFB 508 is running and we are involved with two projects on semiconductor quantum dots, semiconductor heterostructures, and diluted magnetic semiconductors.

Since the beginning of 2006, we have established a second DFG-Sonderforschungsbereich (SFB 668) at our Institute of Applied Physics entitled "Magnetism from the single atom to the nanostructure" (chairperson: Prof. Dr. Roland Wiesendanger). The SFB 668 is focussed on fundamental studies of magnetic properties of nanostructures in contact with a substrate, including spin structures in thermal equilibrium as well as transport and dynamic properties. It involves research groups from MARCH, from the I. Institute of Theoretical Physics, from the Institute of Experimental Physics, from the Institute of Inorganic and Applied Chemistry (all from Hamburg University), and from the Institute of Experimental Physics of the University of Kiel. In total more than 100 researchers are working within the SFB 668 being the largest Collaborative Research Center at our University. Right from

the beginning of this new initiative outstanding scientific achievements have been made and reported in several articles in "Nature", "Science", and "Physical Review Letters".

The research group "Scanning Probe Methods" continues to be engaged in the interdisciplinary Research Training Network on "Design and characterization of functional materials" which is funded by the DFG since 2001 and coordinated by the Institute of Inorganic and Applied Chemistry. In 2006 another Research Training Network on "Tailored metal-semiconductor hybrid systems" (chairperson: Prof. Dr. Ulrich Merkt) could be established with participation of groups from the departments of physics and informatics. Within the framework of such Research Training Groups about 20 to 25 Ph.D. students obtain an excellent education and training in an inter-disciplinary scientific environment.

Since 1998 MARCH has been hosting a coordination site of the German "Center of Competence in Nano-scale Analysis" (CCN) funded by the Federal Ministry for Education and Research (BMBF). This Center of Competence has been organized as a transregional network of research groups at universities, at research centers, and in industry and has promoted technology transfer, activities leading to new start-up companies, and public information services in the area of nanoscience and nanotechnology. Since 2003, the CCN coordination site at Hamburg has been refocussed towards a more regional perspective and has been named "HanseNanoTec". It has provided a valuable support of the infrastructure at MARCH, e.g. for secretary services, public relation services, technology transfer, and preparation of research proposals. Unfortunately, the funding from the BMBF for this initiative has ceased in 2006.

An important event in 2005 was the decision of the Free and Hanseatic City of Hamburg to establish a new Interdisciplinary Nanoscience Center Hamburg (INCH, chairperson: Prof. Dr. Roland Wiesendanger). The declared long-term goal of the new center is to gain fundamental insight into nanoscience-related problems through more intense research in areas bordering the traditional disciplines. In particular, INCH allows bridging the gap between the activities in physical-based ("dry") nanotechnology and biochemical-based ("wet") nanotechnology. After a one-year construction period in 2006, an "International Nanoscience Symposium" has been held in May/June 2007 at the University of Hamburg on the occasion of the inauguration of INCH. Several new junior research groups are currently being established within this new university center. Since the beginning of 2007, INCH is a member of the Association of Competence Centers in Nanotechnology in Germany (AGeNT-D).

Following the strategic development of nanoscience-related infrastructure at the University of Hamburg over a time period of 15 years, the scientific excellence of the nanoscience activities in Hamburg has been recognized worldwide: In Europe we have become partners within numerous research networks funded by the European Community. Together with colleagues from the US and Argentina, we have been successful in the prestigious program "Partnerships for International Research and Education (PIRE)" funded by the NSF (only 17 out of 517 initiatives were successful

in 2007). Moreover, we recently obtained funding by the DFG and JST for establishing a scientific cooperation between Hamburg University and the National Institute for Materials Science (NIMS) at Tsukuba (Japan) in the field of spin-dependent transport in nanostructures. Unfortunately, the decision-making committees of the "Excellence Initiative" to support university-based research in Germany were recently not in favour for supporting our nanoscience activities in Hamburg. As a result, we have lost many young bright researchers in the past few months.

In the present triannual report 2005-2007 the scientific achievements of the research group "Scanning Probe Methods" are summarized covering the following topics: magnetic nanostructures, semiconductor quantum structures and hybrid systems, insulators, molecular systems, and instrumental developments. The research activities of our group in the time period 2005-2007 resulted in 70 scientific publications (among them 4 in Science / Nature / Nature Materials and 5 in "Physical Review Letters") and 265 presentations at conferences, colloquia or seminars (including 80 plenary and invited talks at international meetings). Several prizes and awards were given to members of our group in the past three years, including the Hertha Sponer Prize 2005 of the German Physical Society (Dr. Elena Vedmedenko), the Gaede Prize 2006 of the German Vacuum Society (Jun.-Prof. Dr. Stefan Heinze), and the IEEE Distinguished Lecturer Award 2007 (Dr. Matthias Bode). Furthermore, Prof. Dr. Roland Wiesendanger became Founding Member of the recently established Academy of Sciences in Hamburg (2005).

This research report provides a good opportunity to thank all funding agencies including the DFG, the BMBF, the EU, the Stifterverband für die Deutsche Wissenschaft, as well as several industrial companies (in particular Beiersdorf and Wella) for their financial support of our research activities. In particular we would like to thank the Ministry of Science and Research (BWF) of the Free and Hanseatic City of Hamburg and the University of Hamburg for their continuous strong support of our activities in nanoscience and nanotechnology. I would also like to take the opportunity to thank all the past and present members of the research group "Scanning Probe Methods" for their strong devotion to establish MARCH, INCH, and SFB 668 as internationally recognized Centers of Excellence. Finally, we gratefully acknowledge the excellent support by our central mechanical and electronic workshops, as well as by our secretaries and administration staff.

Hamburg, December 2007

Prof. Dr. Roland Wiesendanger

(Managing Director of the Institute of Applied Physics, Chairman of the DFG Collaborative Research Center SFB 668, and Scientific Coordinator of the Interdisciplinary Nanoscience Center Hamburg)

Chapter 2

Staff Members

Head

Prof. Dr. Roland Wiesendanger

Secretary

Andrea Beese
Ute Brenger
Sigrid Schmidtke

Public Relations Office

Dipl.-Chem. Heiko Fuchs

Technical Support

PTA Norbert Dix
Dipl.-Ing. Michael Langer

Senior Scientists

Dr. Makoto Ashino
Dr. Kirsten von Bergmann
Dr. habil. Matthias Bode (until March 2007)
Dr. Kai-Felix Braun (until June 2007)
Dr. Shih-Hsin Chang
Dr. Katsushi Hashimoto (until October 2006)
Dr. Daniel Haude
Dr. Germar Hoffmann
Dr. Uwe Kaiser
Dr. André Kubetzka

Dr. Giuseppe Maruccio (until December 2005)
Dr. Tomohiro Matsui (until September 2006)
Dr. Focko Meier
Dr. Christian Meyer (until March 2006)
Dr. Nikolai Mikuszeit
Dr. Ung-Hwan Pi (until April 2007)
Dr. Oswald Pietzsch
Dr. Robert Ravlić
Dr. Tobias Richter (until February 2006)
Dr. Alexander Schwarz
Dr. David Serrate
Dr. Elena Vedmedenko
Dr. Francois Vonau (until December 2006)
Dr. Jens Wiebe
Dr. André Wachowiak (until December 2005)
Dr. Robert Wieser

Ph. D. Students

Luis Berbil-Bautista (until October 2006)
Jens Brede
Mike Gyamfi
Torben Hänke (until June 2005)
Gabriela Herzog
Stefan Krause
Stefan Kuck
Knud Lämmle
Felix Marczinowski
Stefan Meckler
Matthias Menzel
Lilli Sacharow (until March 2006)
René Schmidt
Jörg Schwöbel
Martin von Sprekelsen
Lihui Zhou

Diploma Students

Henning von Allwörden
Thomas Eelbo
Anika Emmenegger
Oliver Ferdinand
Henning Gutzmann

Thimo Göllnitz
Matthias Nohme
Anett Preßler
Matthias Prostak
Paul Stanoszek
Thim Stapelfeldt
Niklas Stein (until January 2006)
Jan Wienhausen (until December 2006)
Rolf Würdemann

Guest Researchers

Dr. Alexander V. Balatsky, Los Alamos National Lab, USA (June/July 2006)
Dr. Julian Chen, IBM Yorktown Heights, USA (until September 2006)
Prof. Dr. Silvio Modesti, University of Trieste, Italy
Dipl.-Phys. Alessandro Scarfato, University of Salerno, Italy

Chapter 3

Research Activities 2005-2007

3.1 Overview

R. Wiesendanger

Our research activities are concentrated on nanometer-scale probe methods. In particular, emphasis is put on the investigation of the fundamental relationship between nanostructure and nanophysical properties. Scanning probe methods are ideally suited for such investigations because they provide atomic-scale spatial resolution combined with spectroscopical capabilities at low energy scales. By choosing an appropriate type of interaction between probe tip and sample, almost any kind of nanophysical property can be studied by scanning probe methods. We apply scanning probe methods (SPM) to various classes of materials, including metals, semiconductors, insulators, superconductors, magnetic materials, as well as organic thin films and molecular materials.

To be able to make significant contributions to this rapidly developing field, a major part of our activities is devoted to new developments or further improvements on SPM instrumentation, including the development of new positioning devices with nanometer-scale accuracy, the development of new types of sensors, or the development of dedicated SPM instruments which can operate under extreme conditions (e.g. UHV, low temperatures and high magnetic fields). Special emphasis is also put on the development of new experimental methods based on the local probe geometry, which usually requires adjustments of the hardware and software for SPM data acquisition. These developments are often made in close collaboration with European companies specialized in SPM instrumentation.

In the following, a brief summary of the highlights of our research activities in the time period of 2005 - 2007 is provided. For further information, please do not hesitate to contact us. We will be glad to provide reprints of publications on specific topics.

3.2   Magnetic nanostructures

3.2.1   Spin-polarized scanning tunneling microscopy (SP-STM) and spectroscopy (SP-STS) studies

In recent years great progress has been achieved in the preparation of self-organized and lithographically manufactured magnetic nanostructures. The structural properties of these nanostructures could routinely be investigated by high-resolution real-space imaging techniques like scanning electron microscopy (SEM) and scanning tunneling microscopy (STM) down to the atomic scale. In contrast, a detailed understanding of nanomagnetic properties has been hindered by the fact that experimental data have been obtained by methods which average over a fraction of the sample surface being much larger than the atomic length scale. So far, the limit of spatial resolution of the most advanced magnetic imaging techniques like magnetic force microscopy (MFM) and SEM with polarization analysis (SEMPA) has been on the order of ten nanometers (nm). Therefore, it has been proposed very early to make the tip of the STM sensitive to the spin of the tunneling electrons by illuminating GaAs tips with circularly polarized light or by using magnetic probe tips. Although spin-polarized electron tunneling in planar junctions is an established experimental technique it turned out that the realization of this idea is difficult. Spin-polarized tunneling using an STM has first been observed by Wiesendanger and co-workers in the early 1990s [1,2]. In this experiment, CrO_2 thin film tips with a high degree of spin polarization were successfully used to detect periodic alternations of the measured monatomic step heights in constant-current images. The deviations of the measured step height values from the topographic monatomic step height could directly be related with the effective spin polarization of the tunnel junction. A drawback of this experimental approach was the superposition of topographic and magnetic structure information. As we have shown in the previous triannual reports of our research group we could overcome this problem by combining SP-STM with spectroscopic techniques [3,4]. This allowed the successful separation of topographic, electronic and magnetic information thereby achieving magnetic domain and domain wall images of even micromagnetically complicated magnetic surfaces with subnanometer spatial resolution. On the other hand, spin-polarized scanning tunneling microscopy (SP-STM) performed in the constant-current mode is still the method of choice to resolve complex surface spin-structures, as, e.g., collinear or non-collinear antiferromagnetic structures, on the atomic scale [5–8].

References

[1] R. Wiesendanger, H.-J. Güntherodt, G. Güntherodt, R. J. Gambino, and R. Ruf, Phys. Rev. Lett. **65**, 247 (1990).

[2] R. Wiesendanger, D. Bürgler, G. Tarrach, A. Wadas, D. Brodbeck, H.-J. Güntherodt, G. Güntherodt, R. J. Gambino, and R. Ruf, J. Vac. Sci. Technol. **B9**, 519 (1991).

[3] M. Bode, M. Getzlaff, and R. Wiesendanger, Phys. Rev. Lett. **81**, 4256 (1998).

[4] M. Kleiber, M. Bode, R. Ravlić, and R. Wiesendanger, Phys. Rev. Lett. **85**, 4606 (2000).

[5] S. Heinze, M. Bode, O. Pietzsch, A. Kubetzka, X. Nie, S. Blügel, and R. Wiesendanger, Science **288**, 1805 (2000).

[6] A. Kubetzka, P. Ferriani, M. Bode, S. Heinze, G. Bihlmayer, K. von Bergmann, O. Pietzsch, S. Blügel, and R. Wiesendanger, Phys. Rev. Lett. **94**, 087204 (2005).

[7] M. Bode, E. Y. Vedmedenko, K. von Bergmann, A. Kubetzka, P. Ferriani, S. Heinze, and R. Wiesendanger, Nature Materials **5**, 477 (2006).

[8] M. Bode, M. Heide, K. von Bergmann, P. Ferriani, S. Heinze, G. Bihlmayer, A. Kubetzka, O. Pietzsch, S. Blügel, and R. Wiesendanger, Nature **447**, 190 (2007)

3.2.2 Magnetic domain structure of ferromagnetic Dy/W(110) films

S. Krause, L. Berbil-Bautista, M. Bode, and R. Wiesendanger,

The interaction of ordered spin structures with lattice defects significantly influences material parameters like the coercive and the nucleation field [1,2]. Three different types of lattice defects can be distinguished [1]: (a) planar, (b) line, and (c) point defects. While planar defects like stacking faults [3], antiphase [4] and grain boundaries [5], and complex defect structures [6] were frequently studied, the experimental investigation of individual line and point defects was hindered by spatial resolution limitations. This is the more deplorable as the ever decreasing size of magnetic grains and nanoparticles requires high-anisotropy materials with the magnetic exchange length L approaching the length scale of typical crystal lattice constants [7]. Consequently, pinning by atomic-scale defects becomes more and more important [1] as it may lead to an undesirable enhancement of the switching field in magneto-electronic applications.

Our experiments show that the two fundamental defects of crystal lattices, screw dislocations and edge dislocations, effectively pin the domain walls in ferromagnetic Dy films on W(110). This finding is accomplished by spin-polarized scanning tunneling microscopy (SP-STM), a high-resolution imaging technique which allows the direct correlation of structural and magnetic properties on the atomic scale [8–10]. Dy is a rare-earth metal (REM) and exhibits a helical antiferromagnetic (AFM) and a ferromagnetic (FM) phase with bulk transition temperatures $T_\mathrm{N} = 178\,\mathrm{K}$ and $T_\mathrm{C} = 85\,\mathrm{K}$, respectively. It is a particularly suited material for pinning studies on the atomic scale since the domain walls in FM Dy are very narrow, $w = (2 \pm 1)\,\mathrm{nm}$, such that atomic-scale defects should be relevant. Indeed, SP-STM images of Dy films reveal pronounced domain wall pinning.

The topography and magnetic $\mathrm{d}I/\mathrm{d}U$ map of 90 AL Dy/W(110) in the ferromagnetic regime is shown in Fig. 3.1. In agreement with the six equivalent in-plane magnetization directions at the Dy(0001) surface the histogram of the spin-resolved $\mathrm{d}I/\mathrm{d}U$ signal exhibits six contrast levels [Fig. 3.1(c)]. Higher magnification images show numerous defects at step edges (arrows) and on terraces (circles) [Fig. 3.1(e)]. Correlation with the magnetic $\mathrm{d}I/\mathrm{d}U$ map indicates that these defect sites act as pinning centers for domain walls. By making use of the high spatial resolution of SP-STM we revealed that the two fundamental defects of crystal lattices, perfect screw dislocations and edge dislocations, effectively pin the domain structure. A simple model explains the formation of perfect screw dislocations by nucleation of differently stacked patches in early stages of REM film growth. For films thicker than 60 AL the defect density continuously decreases. Thereby, pinning becomes less and less important.

Fig. 3.2(a) shows the topography and the magnetic structure of a $4 \times 4\ \mu\mathrm{m}^2$ area of a 450 AL Dy/W(110) film. The topography of the film is dominated by areas which had different stacking in early stages of the growth but which eventually relaxed by
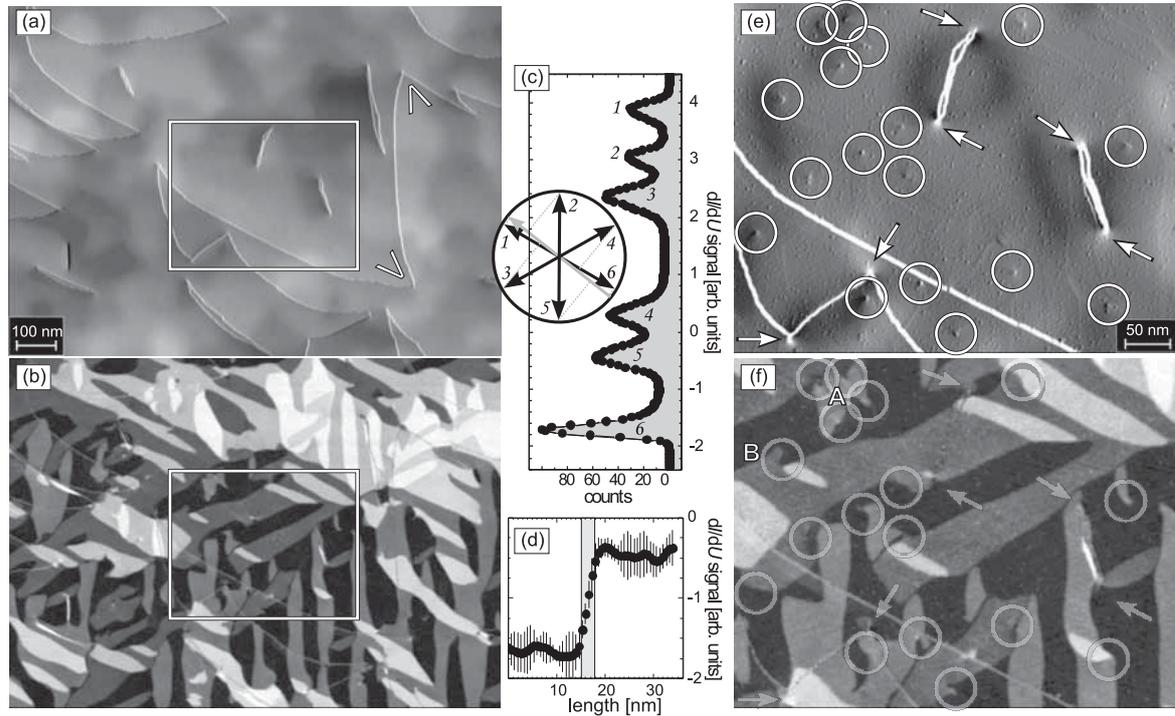
Figure 3.1: (a) Topography and (b) magnetic dI/dU map of $90\,\text{AL}$ Dy/W(110) (tunneling parameters: $U = -1\,\text{V}$, $I = 30\,\text{nA}$, $U_{\text{mod}} = 30\,\text{mV}$). (c) In agreement with the six equivalent in-plane magnetization directions at the Dy(0001) surface the histogram of the spin-resolved dI/dU signal from (b) exhibits six contrast levels (*1–6*). (d) Line section of the magnetic dI/dU signal across a 60° domain wall. Higher magnification images of the differentiated topography and the magnetic dI/dU signal within the marked boxes are shown in (e) and (f), respectively.

gliding planes with $\vec{b} = \pm\frac{1}{2}[0001]$ [11]. As can be seen in the simultaneously measured magnetic dI/dU map of Fig. 3.2(b) the magnetic structure is characterized by a stripe domain pattern with two types of domains for which the magnetization directions alternate by 60°. These structures are as long as $800\,\text{nm}$. The width of these stripe domains amounts to about $40\,\text{nm}$ and is very regular. Probably, the large magneto-elastic coupling in Dy results in a limited and regular domain size. However, not only 60° domain walls were observed, but also 120° and 180° walls. Comparison of the experimental domain profiles with calculated domain profiles reveals that the domain walls at the Dy/W(110) surface are Néel walls. This result is in contrast to the behavior of ferromagnetic bulk materials which prefer Bloch domain walls because this avoids internal magnetic charges [12]. Furthermore, the large uniaxial anisotropy along the *c*-axis in Dy [13–15] should also result in the formation of Bloch domain walls. We have to consider, however, that the magnetization of a Bloch wall also produces a magnetic stray field at the surface. Therefore, the Bloch walls of a ferromagnetic sample are usually capped with a Néel-type structure [16,17]. The origin of this ordered
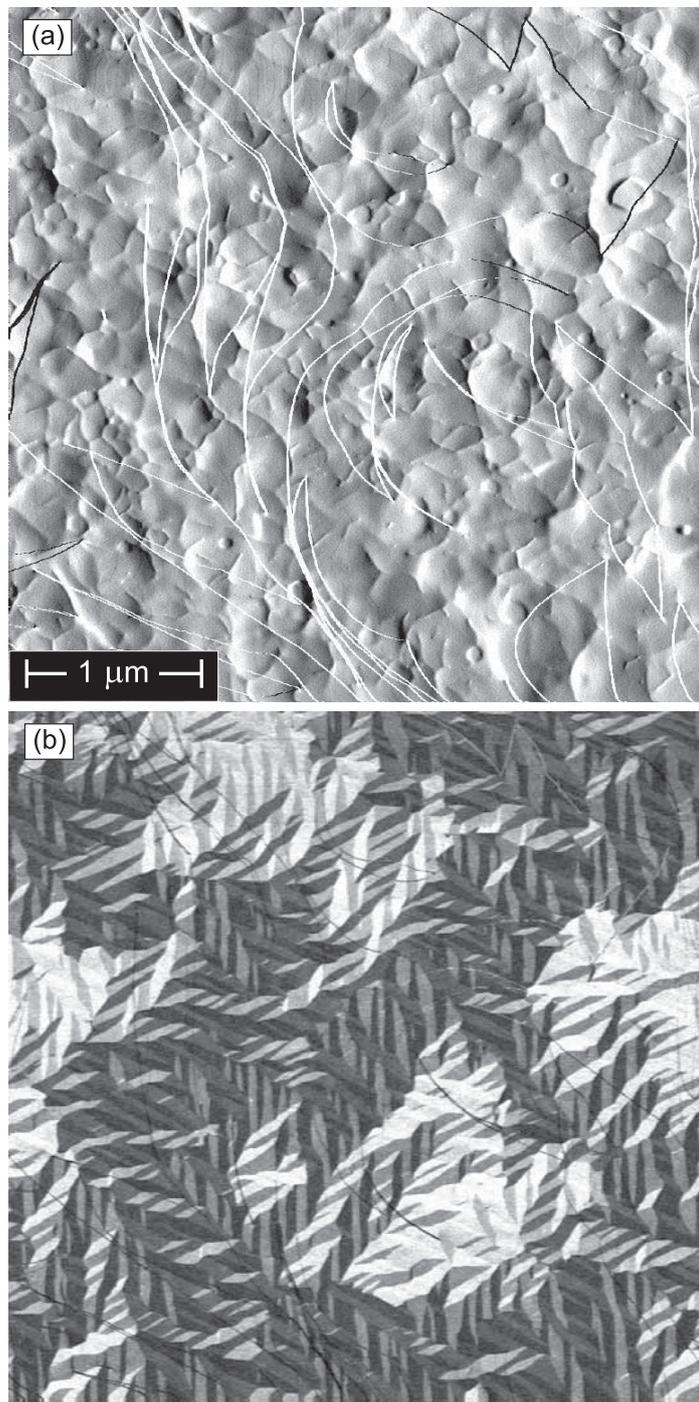
Figure 3.2: (a) Differentiated STM topograph and (b) magnetic dI/dU map of a 4×4 μm^2 area of 450 AL Dy/W(110) film ($T = 60$ K, $U = -0.6$ V, $I = 30$ nA).

domain pattern is unclear but probably the competition between magnetostriction energy favoring lateral confined domains and magnetocrystalline energy favoring 60° magnetic domain walls is the driving force for the complex magnetic structure.

References

[1] H. Kronmüller, AIP Conf. Proc. **10**, 1006 (1973).

[2] H. R. Hilzinger, Appl. Phys. A **12**, 253 (1977).

[3] H. Zijlstra and H. B. Haanstra, J. Appl. Phys. **37**, 2853 (1966).

[4] A. J. Lapworth and J. P. Jakubovics, Philos. Mag. **29**, 253 (1973).

[5] J. P. Attané *et al.*, Appl. Phys. Lett. **79**, 794 (2001).

[6] A. J. Kurtzig and J. P. Patel, Phys. Lett. A **33**, 123 (1970).

[7] D. Weller and A. Moser, IEEE Trans. Magn. **35**, 4423 (1999).

[8] S. Heinze *et al.*, Science **288**, 1805 (2000).

[9] M. Bode, Rep. Prog. Phys. **66**, 523 (2003).

[10] A. Kubetzka *et al.*, Phys. Rev. Lett. **94**, 087204 (2005).

[11] S. Krause *et al.*, Europhys. Lett. **76**, 637 (2006).

[12] A. Hubert and R. Schäfer, *Magnetic Domains*, Springer (1998).

[13] E. Callen and H. B. Callen, J. Phys. Chem. Solids **27**, 1271 (1966).

[14] J. J. Rhyne and A. E. Clark, J. Appl. Phys. **38**, 1379 (1967).

[15] J. L. Feron, Ph.D. thesis, University of Grenoble (1969).

[16] H. P. Oepen and J. Kirschner, Phys. Rev. Lett. **62**, 819 (1989).

[17] M. R. Scheinfein, J. Unguris, R. J. Celotta, and D. T. Pierce, Phys. Rev. Lett. **63**, 668 (1989).

3.2.3 SP-STS studies of the Cr(001) surface

Absence of a spin-flip transition at the Cr(001) surface

T. Hänke, S. Krause, L. Berbil-Bautista, M. Bode, R. Wiesendanger, V. Wagner,
D. Lott, and A. Schreyer,

Since the discovery of an incommensurate spin density wave (I-SDW) in 1959, [1] the complex magnetic structure of Cr has been of continuing interest. As the SDW in bulk chromium has been intensively studied it is generally accepted as a typical example of how the electronic structure and the topology of the Fermi surface may influence magnetism in itinerant systems. Cr is a $3d$ transition metal and has to be considered as an itinerant antiferromagnet with a Néel transition temperature $T_N = 311\,\mathrm{K}$ in the bulk. Pure Cr exhibits an incommensurate spin density wave which originates from the nesting of the Fermi surface. It consists of a static sinusoidal modulation of the magnetic moments with a period L between $27a_{Cr}$ ($\approx 7.8\,\mathrm{nm}$) at room temperature and $21a_{Cr}$ ($\approx 6.1\,\mathrm{nm}$) at $10\,\mathrm{K}$ [2]. Two different modifications exist, i.e., the transverse (T) and the longitudinal (L) SDW below the Néel temperature $T_N = 311$ K and the spin-flip temperature $T_{SF} = 123$ K, respectively. While in case of the T-SDW the magnetic moment $\vec{\mu}$ is perpendicular to the propagation direction $\vec{Q}$ of the SDW ($\vec{\mu} \perp \vec{Q}$), the longitudinal SDW exhibits a parallel configuration ($\vec{\mu} \parallel \vec{Q}$). For both SDW types the propagation vector $\vec{Q}$ points along one of the three possible $\langle 100 \rangle$ directions.

This situation may change completely if the symmetry is reduced by introducing a surface or an interface. Investigations by means of spin-polarized scanning tunneling microscopy (SP-STM) and spectroscopy (SP-STS) delivered a detailed picture of the Cr(001) surface magnetic structure for $T > T_{SF}$: A direct comparison of magnetically in-plane sensitive differential conductance dI/dU maps with simultaneously measured topographic STM images revealed that the dI/dU signal abruptly changes between two discrete levels whenever a monatomic step edge is crossed. This variation is caused by the fact that adjacent terraces have opposite in-plane magnetization directions. Moreover, it was found that the magnetization direction of adjacent Cr(001) terraces persistently alternates even over a large number of terraces without any change in the dI/dU contrast [3]. The magnetic structure of the perfect Cr(001) surface is thereby adequately described by the model of the "topological antiferromagnetism" [4], where the magnetic moments of any atomically flat terrace couple parallel, but adjacent terraces are magnetized antiparallel.

From the in-plane orientation of the magnetization as well as from the absence of any phase slip or long wavelength modulation of the surface magnetic moment it is deduced that the propagation vector of the transverse SDW is always oriented perpendicular to the surface at room temperature.
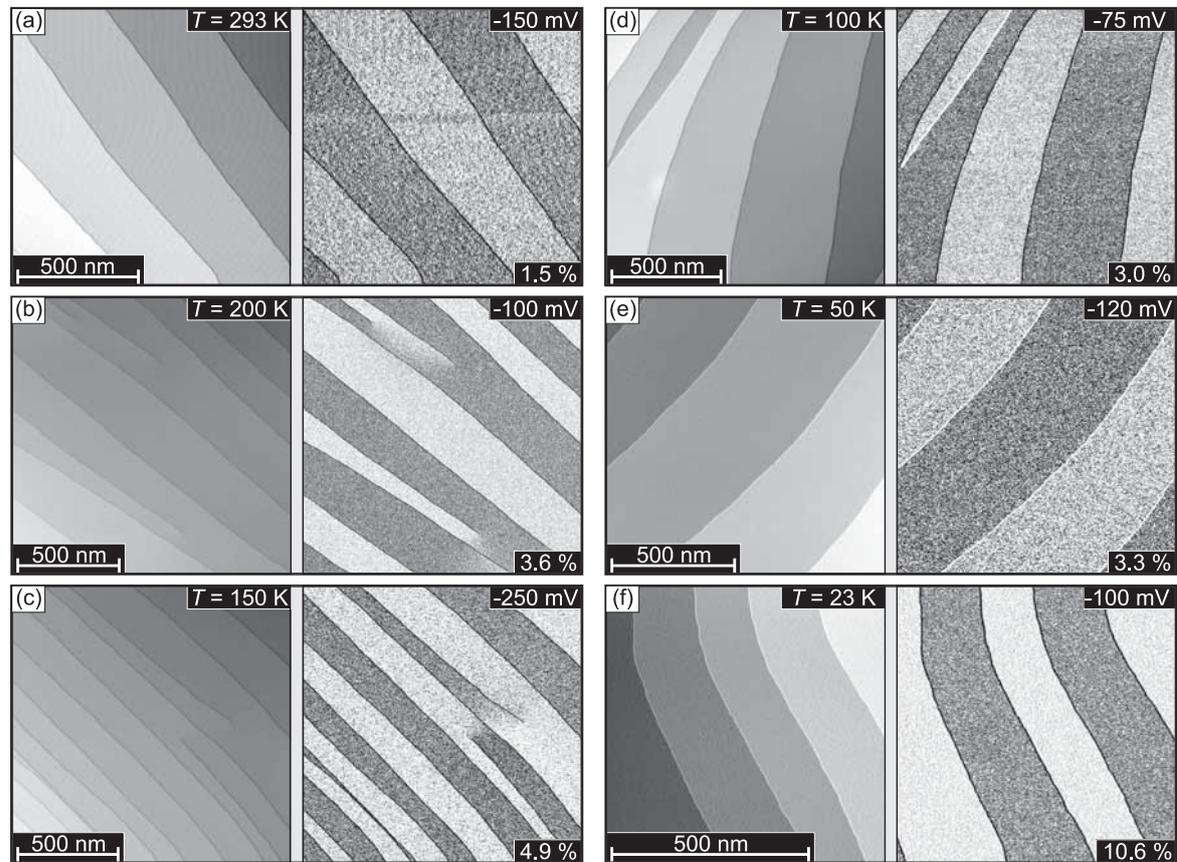
Figure 3.3: Temperature-dependent SP-STM series of Cr(001) measured with an Fe-coated W tip for $23 \leq T \leq 293$ K. The topography (left) and the dI/dU map (right) are shown for any temperature. The bias voltage U and the asymmetry P_{asym} are indicated in the upper right and lower right corner of the dI/dU map, respectively.

The question arises how the bulk spin-flip reorientation influences the magnetic structure of the Cr(001) surface below T_{SF} when the SDW becomes longitudinally polarized. There are two simple scenarios: Either the direction of the magnetic moment $\vec{\mu}$ or the propagation vector $\vec{Q}$ must be modified. In the former case $\vec{Q}$ remains perpendicular to the (001) surface. This would lead to surface magnetic order exhibiting topological antiferromagnetism, but with an out-of-plane magnetization of the surface. In the second scenario $\vec{Q}$ may be oriented parallel to the (001) surface. In this case the surface magnetization remains in-plane but topological antiferromagnetism is not expected to be observable. Instead, a modulation of the magnetic moment with the period L of the SDW should be visible on atomically flat terraces .

A combined temperature-dependent investigation of the Cr bulk SDW by neutron scattering and of the Cr(001) surface by SP-STS was performed on the same Cr single crystal. The neutron scattering experiments were carried out at POLDI, a neutron

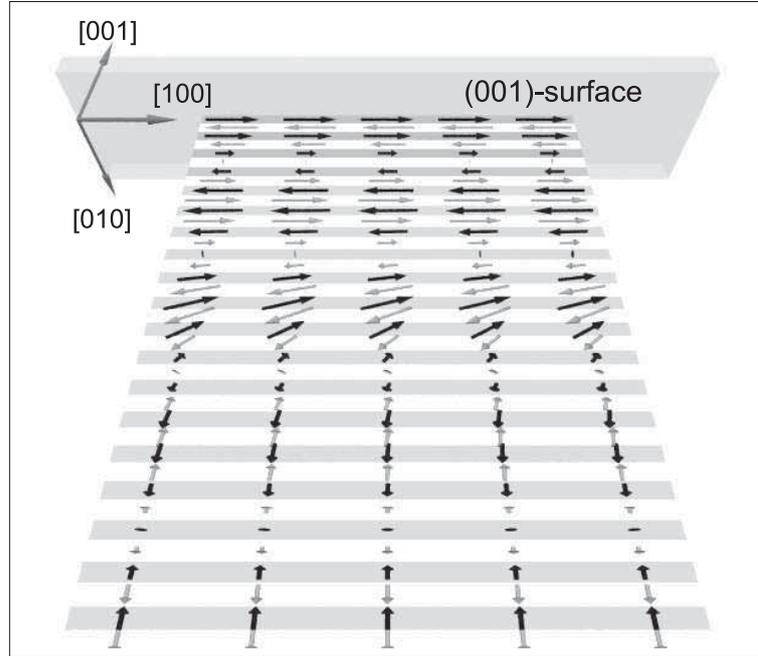Figure 3.4: Model of the low-temperature spin configuration of Cr(001). At $T < T_{SF}$ the bulk exhibits a L-SDW. A single $\vec{Q}$ state with $\vec{Q}$ perpendicular to the surface dominates in the near-surface region. The surface layer, in contrast, still exhibits a T-SDW with the magnetization lying within the surface plane. A 90° domain wall interconnects the L-SDW to the surface spins.

diffractometer, situated on a thermal neutron guide at the Geesthacht Neutron Scattering Facility (GENF). These experiments confirm that the incommensurable SDW dominates the bulk magnetic structure and that the spin-flip transition occurs at the expected temperature. The results of our SP-STS experiments on the Cr(001) surface are shown in Fig. 3.3. A series of six SP-STS measurements were taken at temperatures between room temperature ($T = 293$ K) and 23 K, thereby crossing the spin-flip temperature $T_{SF} = 123$ K. The simultaneously measured topography and spin-resolved dI/dU map are presented for the different temperatures. In contrast to the neutron scattering experiments, no transition is observed on the surface but topological antiferromagnetic order with the magnetization lying in the surface plane is found by SP-STS within the entire studied temperature range. Obviously, the surface magnetic structure cannot be described appropriately by a simple continuation of the bulk SDW.

A possible magnetic configuration at the surface is schematically shown in Fig. 3.4. Here, the Cr surface layer exhibits the same magnetic structure as for $T > T_{SF}$, i.e., a T-SDW ($\vec{Q} \perp \vec{\mu}$) with $\vec{Q}$ perpendicular to the surface plane. This T-SDW with the spins in-plane forms a quasi closure domain. A continuous connection of the surface T-SDW to the L-SDW in the near-surface region is accomplished by the formation

of a 90° domain wall. Hereby, our experimental result is interpreted in terms of a high surface anisotropy large enough to overcompensate the energy required for the formation of a 90° domain wall which interconnects the in-plane magnetized near-surface region with the L-SDW in the bulk.

The Cr(001) surface: Orbital Kondo resonance versus surface state

T. Hänke, M. Bode, S. Krause, L. Berbil-Bautista, and R. Wiesendanger,
[Phys. Rev. B **72**, 085453 (2005)]

The electronic structure of the Cr(001) surface has recently been intensively investigated, mainly due to peculiar magnetic properties of elemental Cr exhibiting antiferromagnetism and a long-period spin density wave. Though the experimental and theoretical data remained contradictory. In a combined experimental and theoretical work, Klebanoff et al [5]. found occupied and empty surface states of $d_{xz,yz}$-orbital symmetry, which are energetically located about 1 eV below and above the Fermi level E_{F}, respectively. Furthermore, a peak close to E_{F} was observed and explained in terms of a d_{z^2}-like surface state [6]. Later on, Stroscio et al. [7] supported this interpretation using scanning tunneling spectroscopy (STS). Kolesnychenko et al. [8] proposed a different interpretation of the density of states peak close to E_{F} in terms of a Kondo resonance. Owing to a sophisticated preparation procedure that is based on the cleavage of bulk crystals at low temperature [9], they were able to produce the Cr(001) surface with an unprecedented cleanliness only limited by the concentration of bulk impurities. STM experiments performed on these surfaces revealed interference patterns which are inconsistent with a d_{z^2}-like surface state but rather supports a $d_{xz,yz}$-orbital symmetry.

In contrast to earlier interpretations, the narrow resonance is explained by an orbital Kondo resonance formed by the above mentioned two degenerated spin-split d_{xz}, d_{yz} surface states located about 1 eV below and above E_{F}. Similar to the conventional "magnetic" Kondo effect, where the local magnetic moment is screened by a spin-flip mechanism, the orbital Kondo resonance results from the flip of the orbital moment of the d_{xz}, d_{yz} surface state, thereby forming a many-body "orbital singlet".

To get a better data basis for the decision as to which one of the two inconsistent physical interpretations mentioned above is correct, the Shockley-like surface state model within single-particle band theory or the many-body Kondo resonance model, we have performed a temperature dependent STS study of the spectral shape of the relevant peak. These experiments cover a wide temperature range between 22 K and 350 K, thereby crossing both the magnetic phase transition temperatures of bulk Cr, i.e., the Néel temperature $T_{\mathrm{N}} = 311$ K and the spin-flip temperature $T_{\mathrm{SF}} = 123$ K, and the Kondo temperature T_{K}. While the peak position remains essentially unchanged, our experiments reveal a significant broadening of the peak with increasing temper-
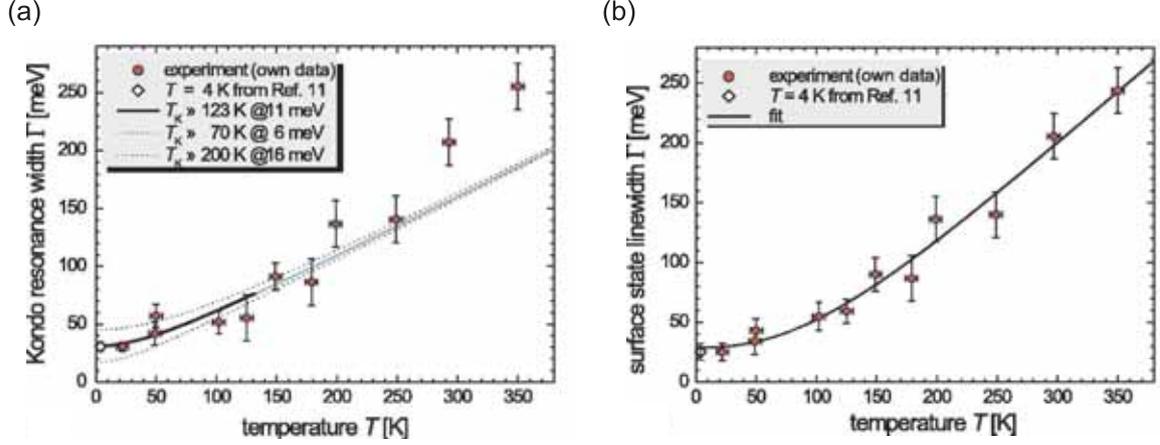
(a)

(b)

Figure 3.5: Fitted line shapes of STS spectra on Cr(001) measured at eight different temperatures between 22 K and 350 K. **(a)** Width Γ_K of the Fano peak used to fit the data. The solid and the dotted curves show the theoretical temperature dependence for different Kondo temperatures T_K. The best fit is obatined for $T_K = 123$ K. **(b)** Width Γ_{e-ph} of the Lorentzian used to fit the data. The solid curve shows the theoretical temperature dependence for $\hbar\omega_D = 52.2$ meV and $\lambda = 1.5$.

ature. The temperature-dependent surface state linewidth Γ was fitted within the framework of the two models. For a Kondo resonance, Γ is given by

$$\Gamma_K = 2\sqrt{(\pi k_B T)^2 + 2(k_B T_K)^2}\,, \tag{3.1}$$

whereas the single-particle band theory gives

$$\Gamma_{e-ph} = \lambda \frac{2\pi}{(\hbar\omega_D)^2} \int_0^{\hbar\omega_D} dE' E'^2 \times [1 - f(E - E') + 2n(E') + f(E + E')]\,, \tag{3.2}$$

where ω_D is the Debye frequency, λ the electron-phonon mass-enhancement factor, $f(E)$ the Fermi distribution, and $n(E)$ the Bose-Einstein distribution.

Our experimental data of the temperature-dependent peak shape of Cr(001) can nicely be fitted within the respective limits of validity of both physical models, i.e., a many-body Kondo effect and single particle band theory, as shown in Fig. 3.5. This is not unexpected as the peak width in both cases rises linear at high temperature. One possibility to estimate which of the two models describes the physical basis of the observations is an evaluation whether the procedures lead to reasonable fitting parameters. In each model there is just one fitting parameter, i.e., the Kondo temperature T_K or the mass-enhancement factor λ.

Using the Kondo model, a Kondo temperature T_K of 123 K is obtained. If interpreted in terms of a single-particle band theory, the fit results in an electron-phonon mass-enhancement factor $\lambda = 1.5$ which is 5 to 10 times larger than the Cr bulk value

of 0.13 [10]. In this case the experimental data in the entire temperature range can be nicely reproduced by the theory.

We may conclude that our temperature-dependent STS data of Cr(001) are not sufficient for a definite decision between the two available models. For the Kondo resonance we found a quite good agreement between our experiment and the theoretical prediction, although the theory was formally developed for spin-flip scattering at single magnetic impurity atoms on open surfaces. On the other hand, the analysis in terms of thermally broadened electron bands leads to a rather large mass-enhancement factor λ which is much larger than the bulk value - a scenario which cannot be excluded at present.

References

[1] L. M. Corliss, J. M. Hastings, and R. J. Weiss, Phys. Rev. Lett. **3**, 211 (1959).

[2] H. Zabel, J. Phys.: Condens. Matter **11**, 9303 (1999).

[3] M. Kleiber, M. Bode, R. Ravlic, N. Tezuka, and R. Wiesendanger, J. Magn. Magn. Mater. **240**, 64 (2002).

[4] S. Blügel, D. Pescia, and P. H. Dederichs, Phys. Rev. B **39**, R1392 (1989).

[5] L. E. Klebanoff, S. W. Robey, G. Liu, and D. A. Shirley, Phys. Rev. B **30**, 1048 (1984).

[6] L. E. Klebanoff, R. H. Victora, L. M. Falicov, and D. A. Shirley, Phys. Rev. B **32**, 1997 (1985).

[7] J. A. Stroscio, D. T. Pierce, A. Davies, R. J. Celotta, and M. Weinert, Phys. Rev. Lett. **75**, 2960 (1995).

[8] Y. Kolesnychenko, R. de Kort, M. I. Katsnelson, A. I. Lichtenstein, and H. van Kempen, Nature (London) **415**, 507 (2002).

[9] Y. Kolesnychenko, R. de Kort, and H. van Kempen, Surf. Sci. **490**, 537 (2001).

[10] S. D. Brorson, A. Kazeroonian, J. S. Moodera, D. W. Face, T. K. Cheng, E. P. Ippen, M. S. Dresselhaus, and G. Dresselhaus, Phys. Rev. Lett. **64**, 2172 (1990).

3.2.4   Complex magnetic order on the atomic scale revealed by SP-STM

Introduction

The investigation of magnetism in thin films and nanostructures on surfaces by spin-polarized scanning tunneling microscopy (SP-STM) has demonstrated the capability of this method to study ferromagnetic, ferrimagnetic or even antiferromagnetic structures down to the atomic scale [1–3]. Already the investigation of homoatomic monolayers of $3d$ transition metals on $5d$ substrates has revealed fascinating physics [3, 4] and allows an interpretation of the experimental results based on the atomic scale magnetic structure [5]. While the formation of a ferromagnetic or antiferromagnetic state can be the result of a dominating nearest neighbor exchange interaction, complex magnetic structures often reflect a situation of competing magnetic interactions. Exchange interactions in a homoatomic monolayer on a substrate can be described by mapping the results of ab-initio electronic structure calculations on a two-dimensional classical Heisenberg model. This makes it possible to search for the origin of a specific magnetic ground state, i.e. to find out which interactions dominate or compete. This of course facilitates a general understanding of magnetism and might allow the tailoring of magnetic properties in the future.

Complex magnetism of the Fe monolayer on Ir(111)

K. von Bergmann, S. Heinze, M. Bode, G. Bihlmayer, S. Blügel, and R. Wiesendanger, [Phys. Rev. Lett. **96**, 167203 (2006) and New J. of Physics **9**, 396 (2007)].

The system of Fe on Ir(111) is an interesting candidate for complex atomic scale structures: if pseudomorphic growth is achieved the Fe layer is ordered hexagonally, in contrast to the body-centered cubic structure of bulk Fe. Small precipitates of hexagonal Fe have been stabilized in a Cu matrix and were found to exhibit spin spiral structures [6, 7]. A preparation of a hexagonal symmetry in a monolayer film allows access to the magnetic structure in real space with spin-polarized scanning tunneling microscopy.

Figure 3.6(a) shows a monolayer area of Fe on the Ir(111) substrate, connected to a substrate step edge at the right side. No superstructure is observed which indicates pseudomorphic growth. Since the measurement is done with an Fe-coated W tip which is sensitive to the in-plane component of magnetization (see inset) another conclusion can be drawn from the lack of any contrast changes on the monolayer: it is either in a single ferromagnetic domain state or it has no magnetic in-plane component.

To study the out-of plane component of the sample magnetization the measurement of Fig. 3.6(b) was performed: a magnetic field is applied along the tip axis to change its
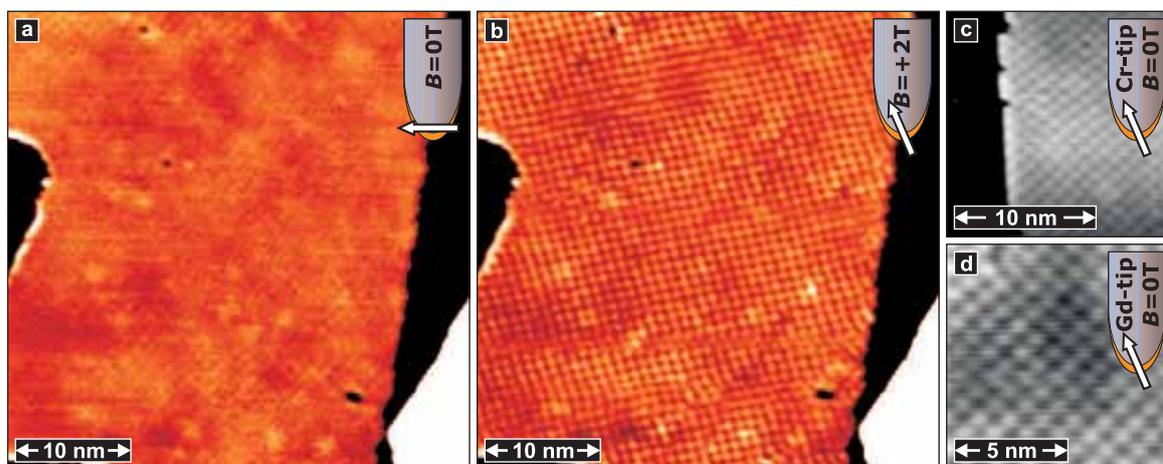
Figure 3.6: Fe monolayer on Ir(111) measured with an Fe-coated W-tip (a) without external magnetic field and (b) at the same sample area but with external field as indicated; (c), (d) measurements without applied field with out-of-plane sensitive tips (all: $U = +50\,\text{mV}$).

magnetization direction (see inset). Now a superstructure becomes visible at the same sample area studied before which can directly be related to the sample magnetization: parallel to the tip magnetization at maximal intensity and antiparallel at the minima (or vice versa depending on the polarization). The observed magnetic structure has a square unit cell of about $1\,\text{nm} \times 1\,\text{nm}$ with one diagonal along a closed packed row. Further experiments indicate that the total magnetic moment of the structure is compensated, i.e. the amount of moments pointing up and down with respect to the sample surface is balanced. This is the reason that the application of the external magnetic field changes the magnetization of the ferromagnetic tip but is expected to leave the sample magnetization unaffected. To prove that the magnetic structure is not a result of the presence of an external magnetic field the measurements shown in (c) and (d) are performed with tips that are sensitive to the out-of-plane component of sample magnetization without external magnetic field. Again the same magnetic structure is observed.

From these experimental results a magnetic structure is proposed: when assumed to be commensurable the determined unit cell holds 15 atoms as sketched in Fig. 3.7. We call this magnetic state *mosaic structure* and three rotational domains are possible. Considering the odd number of atoms in the unit cell, a balanced collinear structure is not possible when the size of the moments is constant. One possibility to construct a completely balanced structure in accordance with the experimental results could be a canting of some of the moments as indicated by the white ellipse in Fig. 3.7. Even though now there is a small in-plane component to this structure we doubt that we could routinely resolve this in the spin-resolved measurements. Ab-initio density functional theory calculations of the mosaic structure with this magnetic unit cell of 15 atoms show that it is lower in energy than the ferromagnetic state.
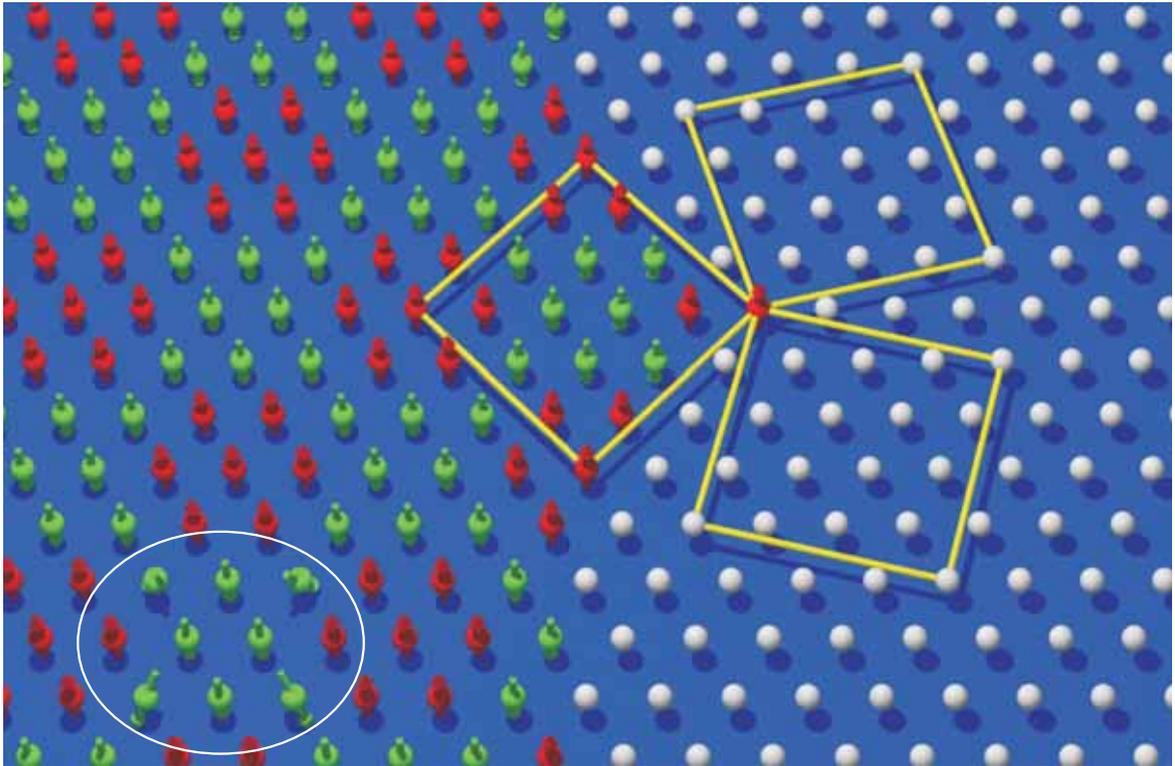
Figure 3.7: Mosaic structure: magnetic structure of the Fe monolayer on Ir(111) proposed on the basis of the experimental results. The unit cell consists of 15 atoms, with seven spins in one direction (red) and eight spins in the opposite direction (green). Three rotational domains are possible. To construct a truly balanced structure a canting of some moments is suggested as sketched exemplary for one cell indicated by the white ellipse.
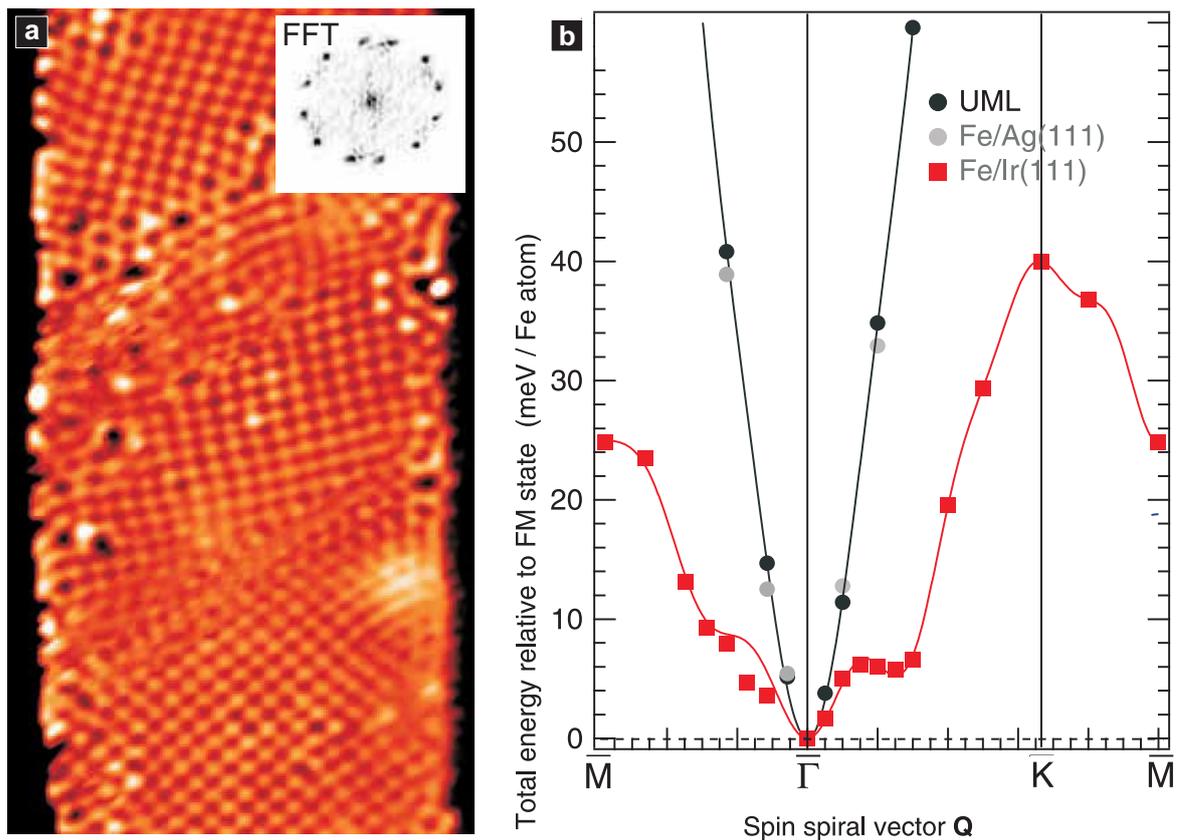
Figure 3.8: Magnetism of the Fe monolayer on Ir(111). (a) SP-STM image measured with an out-of-plane sensitive magnetic tip displaying all possible rotational domains ($U = 50\,\mathrm{mV}$, $I = 0.25\,\mathrm{nA}$), inset: FFT of the image. (b) Energy $E(Q)$ of flat spin spirals along high symmetry directions for an hexagonal Fe monolayer in different environments: for an unsupported Fe monolayer (UML) with the Ir lattice constant, an Fe monolayer on the Ag(111) surface and on the Ir(111) surface. Symbols mark values from first-principles calculations while the lines are a fit to the Heisenberg model including interactions up to eight nearest in-plane neighbors.

All three rotational domains are observed experimentally as shown in the image of Fig. 3.8(a). The fast Fourier transform of this image (inset) clearly shows the three sets of four spots located on a circle around the center. Spin spiral calculations as shown in (b) for the unsupported Fe monolayer and an Fe monolayer on Ag(111) show a typical dispersion for ferromagnetic ground states: the energy minimum is at $\overline{\Gamma}$ with a large energy difference to other magnetic states located at the high symmetry points of the Brillouin zone. In contrast to this, when Fe is on the Ir(111) surface, the dispersion shows an additional minimum at about $Q = 0.25 \times 2\pi/a$ and the difference to other states is strongly reduced. Even though the ferromagnetic state is still the ground state within the classical Heisenberg model, the appearance of another local minimum in the dispersion is very peculiar. Interestingly, the periodicity corresponding to the local minimum is in very nice agreement with the experimentally observed magnetic unit cell, indicating that a superposition of degenerate spin spirals –a so called multi-Q state– could be the origin of the magnetic structure.

References

[1] R. Wiesendanger, I. V. Shvets, D. Bürgler, D. Tarrach, H.-J. Güntherodt, J. M. D. Coey, and S. Gräser, Science **255**, 583 (1992).

[2] S. Heinze, M. Bode, A. Kubetzka, O. Pietzsch, X. Nie, S. Blügel, and R. Wiesendanger, Science **288**, 1805 (2000).

[3] A. Kubetzka, P. Ferriani, M. Bode, S. Heinze, G. Bihlmayer, K. von Bergmann, O. Pietzsch, S. Blügel, and R. Wiesendanger, Phys. Rev. Lett. **94**, 087204 (2005).

[4] M. Pratzer, H. J. Elmers, M. Bode, O. Pietzsch, A. Kubetzka, and R. Wiesendanger, Phys. Rev. Lett. **87**, 127201 (2001).

[5] S. Heinze, Appl. Phys. A **85**, 407 (2006).

[6] Y. Tsunoda, J. Phys.: Condens. Matter **1**, 10427 (1998).

[7] K. Knöpfle, L. M. Sandratskii and J. Kübler, J Phys. Rev. B **62**, 5564 (2000).

Atomic spin structure of antiferromagnetic domain walls in the Fe monolayer on W(001)

M. Bode, E. Y. Vedmedenko, K. von Bergmann, A. Kubetzka, P. Ferriani, S. Heinze, and R. Wiesendanger,
[Nature Materials **5**, 477 (2006)].

The ability of imaging antiferromagnets on the atomic scale has been demonstrated on different systems [1, 2]. Anyhow, those structures are periodic and the question was posed, whether also non-periodic structures can be investigated with SP-STM. One possibility to induce non-periodic antiferromagnetic structures is to induce domain walls in antiferromagnets. While in bulk materials orientational domain walls have been observed with photoelectron emission microscopy with linearly polarized X-rays [3], in monolayer films with out-of-plane anisotropy no orientational domains are expected. Instead phase domain boundaries should occur, but their observation has not been reported so far, neither in thin films nor bulk materials (see Fig. 3.9(a)).

The system of the Fe monolayer on W(001) exhibits an out-of-plane antiferromagnetic state [2] and is thus expected to be a suitable system to induce phase domain walls. Anyhow, clean monolayer samples as the one displayed in Fig. 3.9(b) show very large domains, and no wall could be found: one can clearly see the square lattice on the whole sample, the inset shows a closer view and a sketch of the antiferromagnetic atom arrangement. Not all atoms appear the same in the magnetic image, instead one sublattice of the antiferromagnetic structure, e.g. 'spin-up', is imaged as maximum and the other sublattice is imaged as depression. To deliberately induce walls samples which exhibit more islands of the second monolayer (ferromagnetic) are prepared to act as pinning centers for phase domain walls in the antiferromagnetic monolayer. Figure 3.9(c) shows a small region of such a sample with two second monolayer islands appearing white in this representation. In the top and the bottom part of the image the square magnetic superstructure can be recognized, while the central region appears somewhat blurred. Close analysis of the position of the maxima and minima reveals that there is a phase shift between the upper and lower superstructure (see dashed white lines), i.e. that a phase domain wall is located between the second monolayer islands. Since the magnetization axis of the monolayer is out-of-plane in both domains, the magnetic moments of the wall are expected to rotate through the in-plane direction. While the image of Fig. 3.9(c) is imaged with a magnetic tip sensitive to the out-of-plane component of the sample magnetization, one can use a tip which is magnetized parallel to the sample surface to investigate the in-plane component of the phase domain wall. This is done in the measurement of Fig. 3.9(d): here one is not sensitive to the magnetic superstructure of the domains, but instead the region of the domain wall is now resolved. One can see, that the overall appearance resembles the antiferromagnetic superstructure which over the distance of only a few atomic rows rotates from one domain to the other. A combined ab-initio/Monte-Carlo

study shows good agreement with the measured width of the domain wall. In addition it reveals, that the direction of the wall is decisive for it exhibiting a stray field or not. This could be important in conjunction with exchange bias systems, where the magnetization direction of a ferromagnetic layer is pinned to an antiferromagnet.
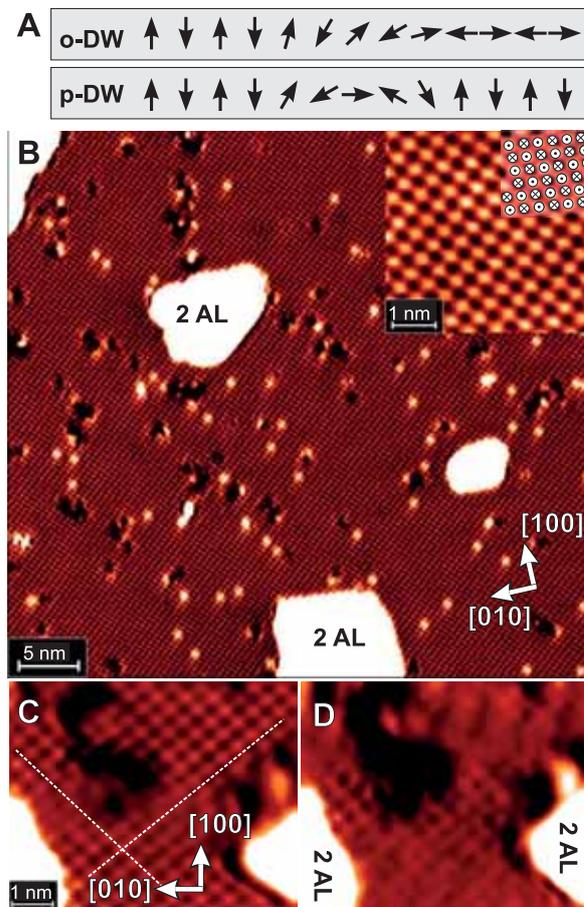
Figure 3.9: Schematic representation and experimental observation of domain walls (DW) at antiferromagnetic surfaces. (a) Scheme of an orientational domain wall (o-DW) and a phase domain wall (p-DW). (b) SP-STM image of 1.1 AL Fe/W(001) measured with an Fe-coated probe tip at $B = 2\,\mathrm{T}$. The antiferromagnetic structure, which is shown at higher resolution in the inset, exhibits long-range periodicity without any DW visible in the field of view. p-DWs only appear at higher defect density, which can be imaged with (c) out-of-plane ($B = 2\,\mathrm{T}$) and (d) in-plane sensitive tips (no field). In the constriction between the two double-layer islands, a p-DW, which runs along the [010] direction, can be seen. At the position of the p-DW, the magnetic structure shifts by one atomic site, that is, half the magnetic periodicity (see dashed lines in (c)).

References

[1] S. Heinze, M. Bode, A. Kubetzka, O. Pietzsch, X. Nie, S. Blügel, and R. Wiesendanger, Science **288**, 1805 (2000).

[2] A. Kubetzka, P. Ferriani, M. Bode, S. Heinze, G. Bihlmayer, K. von Bergmann, O. Pietzsch, S. Blügel, and R. Wiesendanger, Phys. Rev. Lett. **94**, 087204 (2005).

[3] N. B. Weber, H. Ohldag, H. Gomonaj and F. U. Hillebrecht, Phys. Rev. Lett. **91**, 237205 (2003).

Theoretical description of antiferromagnetic domain walls in the Fe monolayer on W(001)

M. Bode, E. Y. Vedmedenko, K. von Bergmann, A. Kubetzka, P. Ferriani, S. Heinze, and R. Wiesendanger
[Nature Materials **5**, 477 (2006)].

Magnetic systems on a square lattice with two nearest neighboring exchange constants J_1 and J_2, both antiferromagnetic, possess a checkerboard antiferromagnetic ground state. One of the lowest exited states of this configuration is a domain structure with so-called phase domains and phase domain walls (p-DW). Schematic representation of the orientational and p-DW is given in Fig. 3.9. In the phase domains the checkerboard spin structure shifts laterally by one structural lattice constant. Experimentally it can only be detected indirectly by the presence of domain walls. As shown above such domain walls have been found by means of the Spin Polarized Scanning Tunneling Microscopy (SP-STM). An exciting question is whether the phase domain walls can lead to uncompensated magnetic moments or not. This question is important as it has been postulated , that a small amount of uncompensated magnetic moments at the antiferromagnet/ferromagnet interface is responsible for the exchange bias effect which is widely used in state-of-the-art magnetic storage devices. The exchange bias is based on the direct exchange interaction between an antiferromagnet and a ferromagnet and leads to a sign-dependent magnetic coercivity of the latter. As it will be shown in the following experimental data together with Monte-Carlo simulations can infer the existence of uncompensated spins in p-DWs which are oriented along a main crystallographic direction. The uncompensated magnetization appears due to the spiral-like rotation of antiferromagnetic moments in a wall. Depending on the surface density of these p-DWs the resulting moment may lead to a significant contribution to the exchange bias.

It has been recently shown that one atomic layer of Fe on W(001) is an antiferromagnet with the nearest and the next-nearest neighbor exchange parameters $J_1 = 20.3 \cdot 10^{-3}$ and $J_2 = 2.4 \cdot 10^{-3}$ meV/atom, respectively. STM with non-magnetic tips is sensitive only to the spin-averaged local density of states (DOS) $n(\mathbf{r}, E_F)$ at

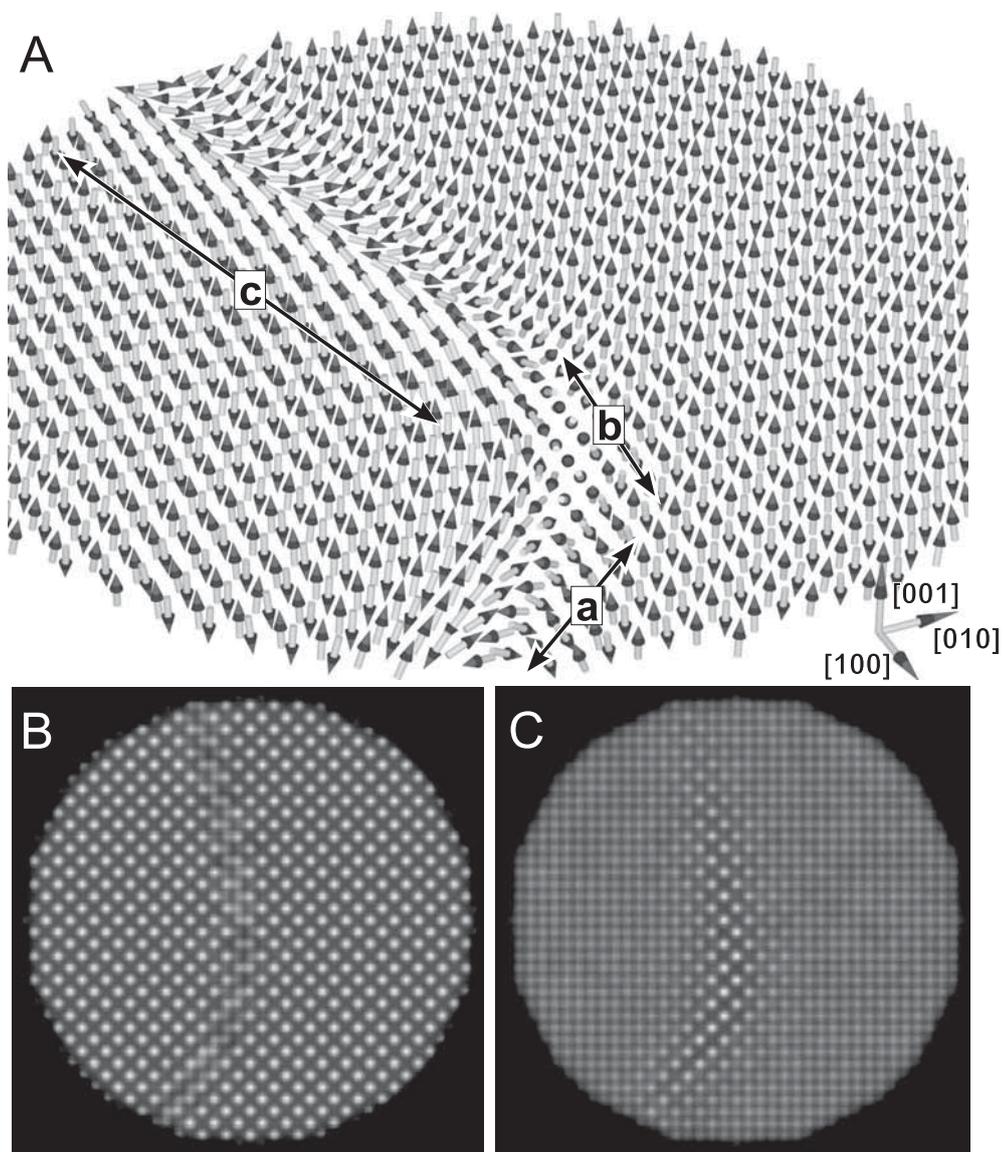Figure 3.10: Monte-Carlo (MC) simulation of antiferromagnetic domain walls. (A) Rendered perspective image of the quenched spin structure of an antiferromagnetic material as obtained by MC simulation. A domain wall can be recognized which exhibits three different orientations: (a) along the [110], (b) [100], and (c) an intermediate direction. Calculated SP-STM images for (B) out-of-plane and (C) in-plane sensitive magnetic tips.

the Fermi level (low-voltage approximation) and tip position $\mathbf{r}$. The intrinsic spin-polarization of magnetic tips, $P_T \equiv (n^\uparrow - n^\downarrow)(n^\uparrow + n^\downarrow)$, where $n^\uparrow$ and $n^\downarrow$ are the majority and minority density of states, introduces a spin-polarized contribution to the tunneling current I($\mathbf{r}$) which scales with the projection of the unit vector of tip magnetization $\mathbf{u}_T$ onto the local magnetization DOS at $\mathbf{m}(\mathbf{r}, E_F)$:

$$\mathbf{I}(\mathbf{r}) \propto n(\mathbf{r}, E_F) + P_T \mathbf{u}_T \cdot \mathbf{m}(\mathbf{r}, E_F). \tag{3.3}$$

This gives a magnetic contribution to constant-current mode images of periodic magnetic structures which is superimposed on the conventional topographic image. Eq. 3.3 can be used for calculations of a theoretical "SP-STM contrast" from the spin stucture revealed by, e.g., Monte-Carlo simulations. The internal spin structure of antiferromagnetic phase domain walls was investigated theoretically by the MC method, which is capable of simulating complex spin structures of antiferromagnets. The exchange constants J_1 and J_2 given above have been used in the calculations. Apart from the exchange interaction a perpendicular anisotropy and a dipolar interaction have been included into the simulations. The anisotropy energy density has been set to be $K_1 = 2.4$ meV/atom, while the strength of the magnetic dipole-dipole coupling is calculated by $D = (\mu_0 g^2 \mu_{Fe}^2)/(4\pi d^3)$ with μ_0 the permeability of the vacuum, μ_{Fe} the magnetic moment of antiferromagnetic iron and $d = 0.3165$ nm the interatomic Fe-Fe distance. In order to avoid that the sample eventually relaxes into a single domain state it had to be quenched rapidly from a random start configuration to the measurement temperature, i.e. , $T \approx 13$ K. A characteristic result is shown in Fig. 3.10. The magnetic structure inside of the wall is spiral-like. No preferred orientation of the domain wall has been found. The three wall segments are oriented approximately along (a) the [110], (b) the [100], and (c) an intermediate direction. In order to compare the theoretical spin structures with experimental STM data, SP-STM images of Monte-Carlo non-collinear magnetic structures have been modeled. The details of calculations can be found in [1]. The calculated STM images shown in Fig. 3.10B and C are in good qualitative agreement with the experiment: the c(2 x 2) superstructure is clearly observed in the domains (domain walls) with an out-of-plane (in-plane) sensitive tip. As also found experimentally the apparent domain wall width is slightly larger for in-plane than for out-of-plane sensitive tips. This can be explained on the basis of Eq. 3.3: the magnetic corrugation at the domain wall scales cosine-like for an out-of-plane sensitive tip but sine-like for an in-plane sensitive tip, with the former having a rather steep zero-crossing at the domain wall position. The very weak topographical (non-magnetic) atomic contrast observed wherever $\mathbf{u}_T \perp \mathbf{m}_r$ (see, e.g. the domains in Fig. 3.10C) is below the experimental resolution limit.

To discuss the question whether the non-collinear p-DWs can cause uncompensated magnetic moments four principal types of p-DWs are schematically illustrated in Fig. 3.11: The p-DWs may be centered between (top row of Fig. 3.11) or on top of atomic rows (middle row) and either oriented along the [010] (left column of Fig. 3.11) or along the [110] direction (right column), respectively. The sketch reveals that
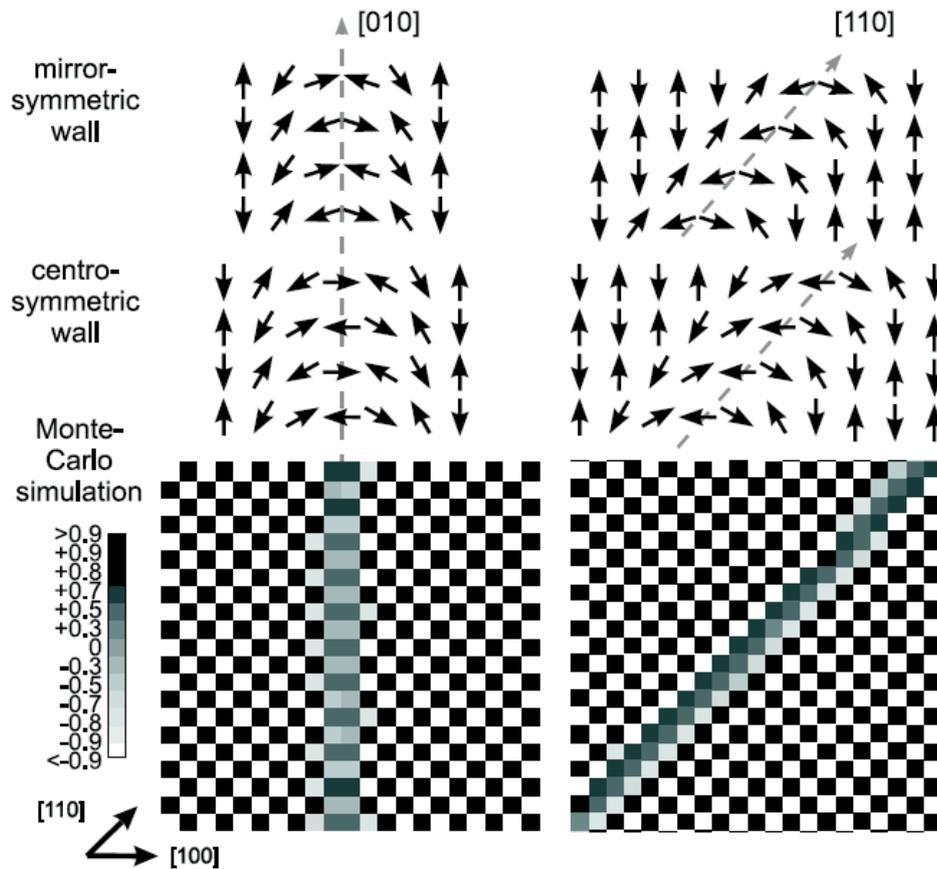
Figure 3.11: Spin configuration of [010]- and [110]-oriented domain walls. Schematic representation of p-DWs which are centered between (top row) and on top of atomic rows (middle row). (bottom row) Part of a p-DW oriented along the [010] (left) and the [110] direction (right) from Monte-Carlo simulations. The gray scale gives the calculated out-of-plane component of the magnetization.
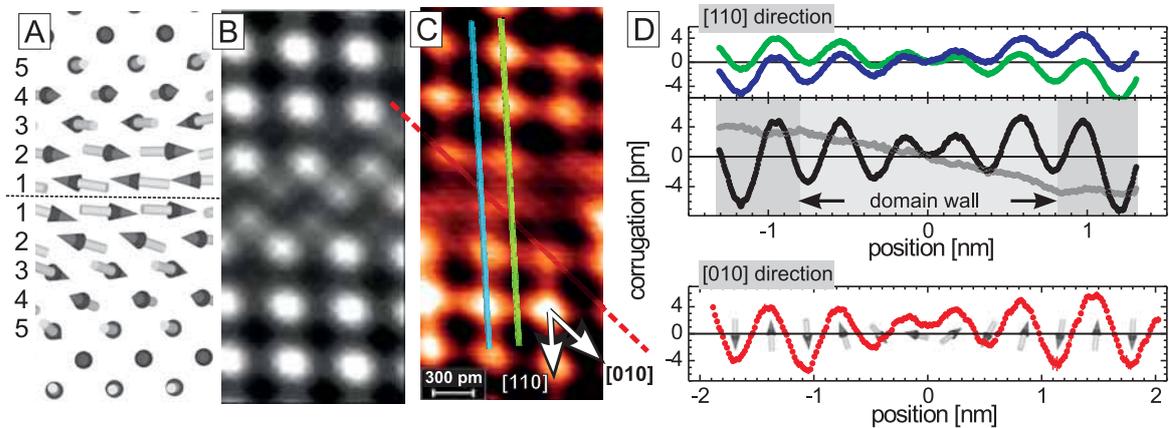
Figure 3.12: Detailed view of a [110]-oriented spiral p-DW. (A) Theoretical spin structure, (B) simulated, and (C) experimental SP-STM image of a p-DW in the out-of-plane anti-ferromagnetic Fe monolayer on W(001). (D) Height profiles drawn at the positions of the correspondingly colored lines in (C) along the [110] (upper panel) and the [010] direction (lower panel). Middle panel: Sum (black) and difference (gray) of the line profiles shown in the upper panel. The wall is about 1.6 nm wide and its out-of-plane component exhibits mirror symmetry.

irrespective of their symmetry [010]-oriented DWs are always compensated because adjacent spins within any row parallel to the wall point into opposite directions. The situation is different for p-DWs along [110] directions as their magnetic moments do not cancel. The direction of the uncompensated moment depends on the position of the p-DW center: if the p-DW center is on top of an atomic row it points along the spins that form the domain wall center, in the case of a wall which is centered between two atomic rows it is along the quantization axis within the domains. The bottom row of Fig. 3.11 shows the perpendicular component of the magnetization as obtained from MC simulations for p-DWs which almost perfectly run along the [010] (left column) and the [110] direction (right column). In agreement with the arguments mentioned above the [010]-oriented wall is compensated. Although not perfectly mirror symmetric, the domain wall center of [110]-oriented p-DWs is always found between two atomic rows and in agreement with the uncompensated moment in the simple sketch a finite perpendicular moment of about 0.6 μ_{Fe} per nm domain wall length remains. The azimuthal orientation of spins within the (110) wall of Fig. 3.10A [middle of segment (a)] is shown at a closer view in Fig. 3.12A. As mentioned above the MC simulations find the DW center between two atomic rows. For clarity the atomic rows are numbered successively (1)-(5) with respect to their distance from the DW center in Fig. 3.11A. The wall center is formed by two rows (1) with a predominant in-plane orientation (65°). With increasing distance from the DW center the moments tilt more and more into the out-of-plane direction; the in-plane component of rows (4) and (5) is already very small. Apparently, the wall is 6 to 8 atomic rows wide and

Bloch-like. Comparing equidistant atomic rows located on opposite sides of the DW center it becomes clear that the in-plane component is reversed while the out-of-plane component is equal. Thereby, the integrated in-plane component of magnetization is perfectly canceled but, interestingly, a non-vanishing net magnetic moment remains for the out-of-plane component.

Due to the fact that domain walls in antiferromagnets cost exchange energy but cannot lower the dipolar energy they are very rare and short on clean surfaces. It is, however, likely that they may be much more frequent in a typical exchange-bias situation. Here, the antiferromagnet is covered with a ferromagnetic film which typically exhibits a higher magnetic ordering temperature than the antiferromagnet. Consequently, the antiferromagnet is in contact with a ferromagnet when it orders magnetically. It is expected that in this case the exchange coupling to the ferromagnet induces a relevant number of p-DWs.

References

[1] M. Bode, E. Y. Vedmedenko, K. von Bergmann, A. Kubetzka, P. Ferriani, S. Heinze, and R. Wiesendanger, Nature Materials **5**, 477 (2006).

Observation of a spin spiral state in the Mn monolayer on W(110)

M. Bode, M. Heide, K. von Bergmann, P. Ferriani, S. Heinze, G. Bihlmayer,
A. Kubetzka, O. Pietzsch, S. Blügel and R. Wiesendanger,
[Nature **447**, 190 (2007)].

This system of the Mn monolayer on W(110) has been investigated previously with SP-STM and ab-initio calculations and local antiferromagnetic order was found [1]. Recent measurements on a larger scale are shown in Fig. 3.13: while the vertical stripes in the spin-resolved images (left) are clear indications for the antiferromagnetic order, they nearly vanish periodically about every 5 nm. Again measurements with differntly magnetized tips at the same sample position reveal the origin of this effect: while the tip used in (a) –magnetized parallel to the sample surface– reveals the antiferromagnetic arrangement of in-plane moments, the tip in (c) is magnetized perpendicular to the surface and shows the stripe pattern whereever the magnetic moments of the sample are out-of-plane. Clearly a comparison between (a) and (c) shows that the area where the magnetic superstructure dominates the image shifts, and the measurement of (b) with intermediate tip magnetization angle shows that the maximum amplitude of the stripes propagates to the left in this measurement. These observations prove that the Mn monolayer on W(110) has locally an antiferromagnetic structure, which rotates to form a spin spiral state along the $[1\bar{1}0]$ direction. Two possible mechanisms
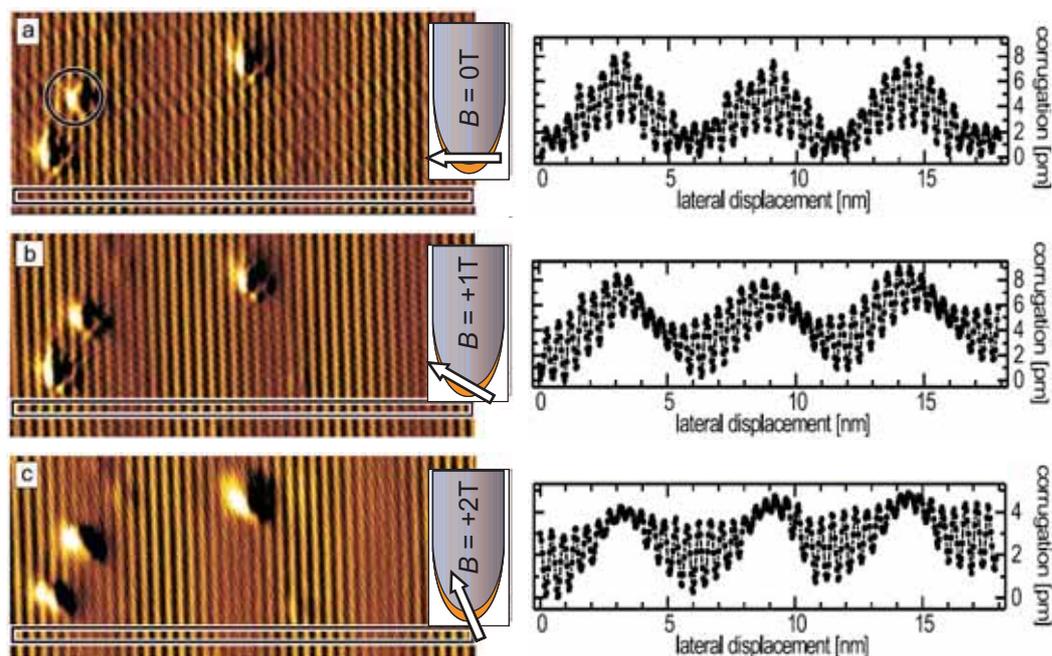
Figure 3.13: Field-dependent SP-STM measurements. Magnetically sensitive constant-current images of the Mn monolayer on W(110) (left panels) and corresponding line sections (right panels) taken with a ferromagnetic Fe-coated tip at external fields of $0\,T$ (a), $1\,T$ (b) and $2\,T$ (c). As sketched in the insets, the external field rotates the tip magnetization from in-plane (a) to out-of-plane (c), shifting the position of maximum spin contrast ($I = 2\,nA$, $U = 30\,mV$).

for the formation of a spin spiral come to mind: first, a competition of exchange interactions between atoms, e.g. antiferromagnetic nearest neighbor coupling and also antiferromagnetic next-nearest neighbor coupling, or a twist between adjacent magnetic moments due to Dzyaloshinskii-Moriya interaction, which is a result of spin-orbit interaction in an environment lacking inversion symmetry. While an exchange driven spin spiral can rotate either way and leads to both rotational senses, a spin spiral that is induced by Dzyaloshinskii-Moriya interaction favors one rotational sense and will never form a spiral with the opposite rotation.

To investigate the origin of the spin spiral in the Mn monolayer on W(110) the energy of spin spirals is calculated as a function of the periodicity, see Fig. 3.14 (left, with the two main crystallographic directions in upper and lower part, respectively). When spin orbit coupling is neglected the minimum in energy is at the high symmetry $\overline{N}$ point (crosses in Fig. 3.14 (left)), which corresponds to the collinear $c(2 \times 2)$ antiferromagnetic state, which was proposed before [1]. This finding indicates, that competing exchange interactions cannot be responsible for the spin spiral formation, since in that case two symmetric minima at $|\lambda| > 0$ would be expected. To find out whether Dzyaloshinskii-Moriya interaction is really responsible for the twist be-
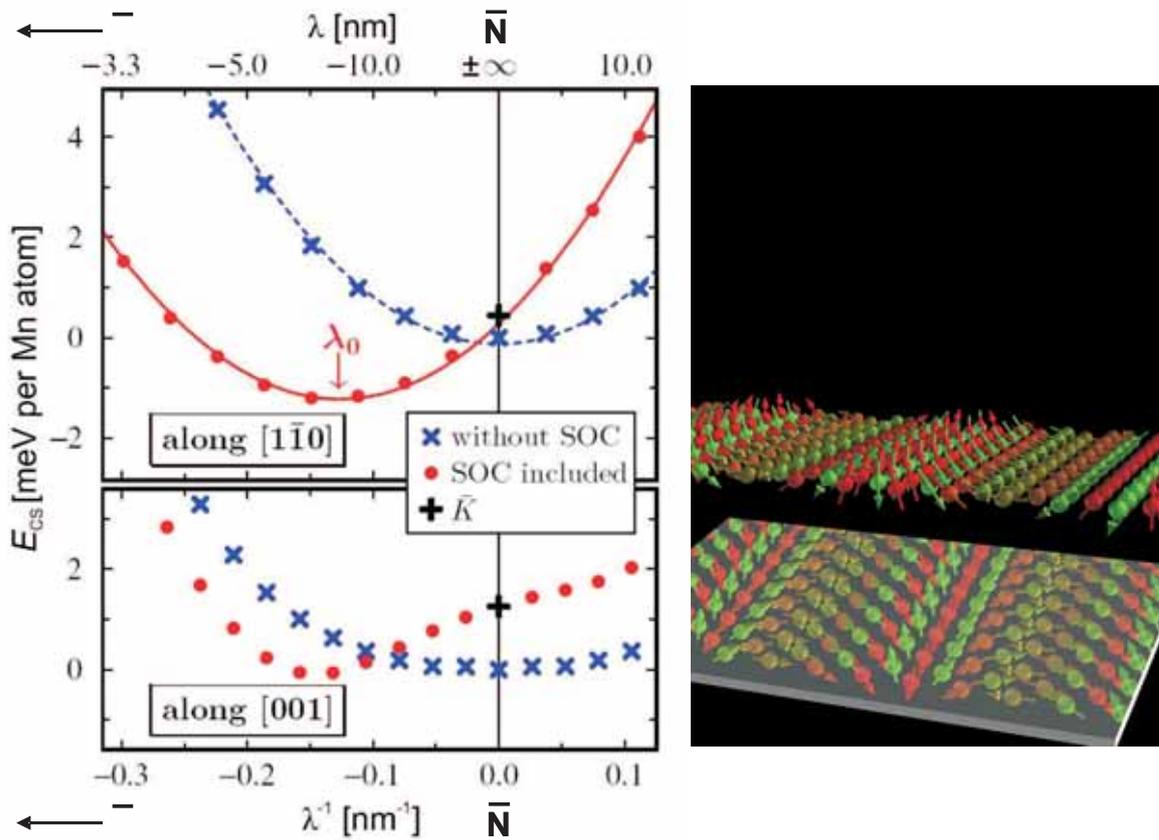
Figure 3.14: Left: Calculated energy of homogeneous cycloidal spin spirals propagating along the two high-symmetry directions [1$\bar{1}$0] (upper panel) and [001] (lower panel) as function of the period length, $|\lambda|$. Origin of energy is the c(2 × 2) antiferromagnetic state. The data points show the density functional theory results obtained without (blue crosses) and with (red dots) spin-orbit coupling (SOC) included. Broken ($D = \overline{K} = 0$) and solid lines are fits to the energy of a cycloidal spiral. Note that the possible energy gain is much larger for propagation along the [1$\bar{1}$0] direction than along the [001] direction. Right: shows a perspective view of an antiferromagnetic cycloidal spin spiral; in the mirror one can see the opposite rotational sense of such a spiral.

tween adjacent moments spin-orbit coupling was introduced into the calculation as a perturbation. Now the minimum shifts to lower energy and to only one side of the high symmetry point (dots in Fig. 3.14 (left)) which indeed shows that due to the Dzyaloshinskii-Moriya interaction the energy for a spin spiral with a specific rotational sense is lowered compared to the c(2×2) antiferromagnetic state. The right part of Fig. 3.14 shows a perspective view of such a cycloidal spin spiral, and the reflection in the mirror at the lower part of the image mimics the other rotational sense which is higher in energy.

References

[1] S. Heinze, M. Bode, A. Kubetzka, O. Pietzsch, X. Nie, S. Blügel, and R. Wiesendanger, Science **288**, 1805 (2000).

Chiral magnetic ordering in two-dimensional ferromagnets with competing Dzyaloshinskii-Moriya interactions

E. Y. Vedmedenko and R. Wiesendanger

Many magnetic systems possess certain periodicities. For single crystals the periodicities have at least two length scales – that of the atomic lattice, and that of the magnetic structure. Such systems, which consist of a perfectly periodic crystal and an additional periodic modulation of some order parameter, are denoted as modulated structures. In centrosymmetric, magnetically ordered crystals the handedness of modulated structures is energetically degenerate. However, if the inversion symmetry is broken for some reasons, this degeneracy may be lifted because the electronic spin-orbit scattering induces chiral asymmetry of exchange coupling. In such non-centrosymmetric systems an additional order parameter - chirality - might appear. The chiral ordering is very interesting from the theoretical point of view as well as for technical applications.

It has been shown recently that antisymmetric exchange interactions first predicted by Dzyaloshinskii [1] can be especially strong near magnetic surfaces and in nanostructures due to reduced symmetry and large strains [2]. The directions of Dzyaloshinskii-Moriya (DM) vectors have been investigated for several surfaces [2] and the existence of non-collinear magnetic structures in thin films has been postulated. Existing studies of chiral magnetic ordering have been limited up to now to one-dimensional chiral structures with a single DM vector or to frustrated bulk pyrochlores. The evolution of magnetic nano-ordering in mono/double layers as a function of length and orientation of several DM vectors has not been investigated so far.

The description of magnetic ordering in two-dimensional systems with several DM vectors is not trivial for several reasons. First, for many lattice symmetries the orientation and the strength of the DM interactions cannot be determined using the theoretical concepts of Ref. [1,2]. Second, different DM couplings may compete, and third, the influence of the magnetic anisotropy on the chiral ordering is not known. Magnetic order on the nanoscale, however, is very important for the description of hysteretic and dynamic properties of nano-objects. The aim of our investigation is to achieve a spatially resolved description of the magnetization patterning in two-dimensional lattices in the presence of competing DM interactions and a magnetocrystalline anisotropy.

Model Systems

In order to explore the intriguing question as to what extent the competition between several Dzyaloshinskii-Moriya vectors affects the magnetization patterning, we performed Monte-Carlo (MC) simulations for samples of up to 200×200 classical spins on two-dimensional lattices with open and periodic boundary conditions. Square, rectangular, 'losenge' and triangular symmetries have been chosen for the calculations as they correspond to different surfaces of sc, bcc, and fcc parent structures for which non-negligible DM interactions have been predicted [2]. Additionally we have performed calculations for three-dimensional Fe/W(110) nanowires. However, it has been assumed that the DM interactions have a non-vanishing amplitude only at the surface layer of a nanowire.

The interaction Hamiltonian reads

$$H = J(\vec{R}_{ij}) \sum_{i<j} \vec{S}_i \cdot \vec{S}_j +$$

$$+ \sum_{i,j} \vec{D}^{\vec{n}}_{\vec{R}_{ij}} \cdot (\vec{S}_i \times \vec{S}_j) + K(\vec{m}) \sum_i (\vec{S}_i \cdot \vec{m})^2 \qquad (3.4)$$

$$+ d \sum_{i<j} \left(\frac{\vec{S}_i \cdot \vec{S}_j}{R_{ij}^3} - 3\frac{\left(\vec{S}_i \cdot \vec{R}_{ij}\right)\left(\vec{S}_j \cdot \vec{R}_{ij}\right)}{R_{ij}^5} \right)$$

where $\vec{S}_i$ is a three-dimensional unit spin vector at a site i; $\vec{R}_{ij} = \vec{R}_i - \vec{R}_j$ the distance-vector between the ith and the jth site and the set $\{\vec{R}_i\}$ defines a three-dimensional lattice $L^{(3)}$. The vectorial DM interaction $\vec{D}^{\vec{n}}_{\vec{R}_{ij}}$ depends on both the distance vector $\vec{R}_{ij}$ and the orientation $\vec{n}$ of the DM vector in the three-dimensional space $O^{(3)}$. It has been found in our simulations that the periodicity of a spiral P is determined by the competition between the exchange and the DM interaction energy. Hence, P increases with a decreasing ratio $|\vec{D}^{\vec{n}}_{\vec{R}_{ij}}|/J$. The log-log plot reveals a power law $P \propto (|\vec{D}^{\vec{n}}_{\vec{R}_{ij}}|/J)^{-\beta(D/J)}$ for all types of studied lattices. In addition, for identical

$|\vec{D}^{\vec{n}}_{\vec{R}_{ij}}|/J$ ratio the periodicity of the DM spirals propagating along high symmetry directions of a lattice is somewhat larger than those along other directions because of the competition between the DM- and the strong exchange interaction.

In the next step the influence of the magnetic anisotropy $\vec{K}$ on a chiral ordering has been studied. The tendency is the following: when the anisotropy axis lies within the plane of magnetization rotation defined by the DM coupling the anisotropy favors the increase of the width of parts of the spiral parallel to $\vec{K}$. In other words a domain structure or an inhomogeneous spiral is formed. If $\vec{K}$ is perpendicular to the rotation plane it destroys the spiral already for very small $K/J \geq 0.1|\vec{D}^{\vec{n}}_{\vec{R}_{ij}}|$ ratios.

For several non-vanishing DM vectors we find that the magnetic ground state is a superposition of spirals. This superposition is non-trivial as quite a few configurations depending on the phase, strength and sign of the initial spirals are possible. In addition the lattice symmetry and the strength of the exchange interaction play a very important role. For example, for the calculations on a square lattice we considered two perpendicular DM vectors. One of them propagates along the [100] axis and is oriented parallel to [010] while another one runs along the [010] direction and is of [100] orientation.

If both DM vectors are of identical length the propagation direction $\vec{R}_p$ of the modulated structure forms an angle of 45 degrees with respect to each axis of high symmetry (see Fig. 3.15). There are two possibilities for such an orientation: [110] and [1$\bar{1}$0]. The two directions are energetically degenerate. Apparently the same should be true for the orientation of magnetization. For $|\vec{D}^{[010]}_{[100]}| = |\vec{D}^{[100]}_{[010]}|$ the magnetic moments are oriented with an angle of 45° with respect to the principal axes. However, for each direction of propagation characterized by a vector $\vec{R}_p$ two magnetization orientations
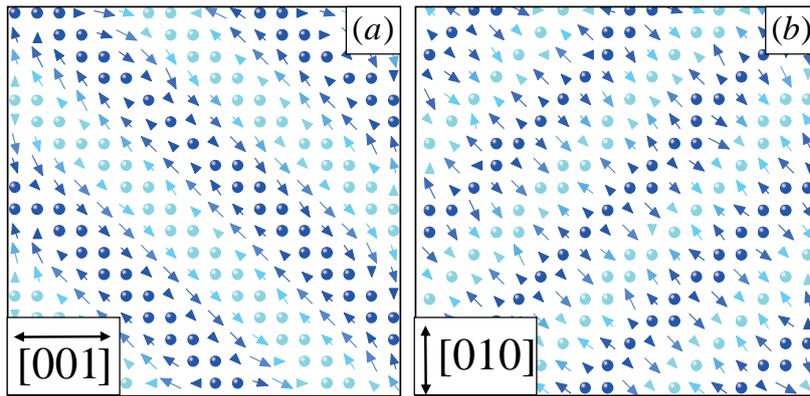
Figure 3.15: Top view of portions of stable MC configurations for a simple cubic lattice corresponding to a free standing bcc(001) monolayer with a ferromagnetic exchange interaction. (a) $|\vec{D}^{[010]}_{[100]}| = 0.8J = |\vec{D}^{[100]}_{[010]}|$; (b) $|\vec{D}^{[010]}_{[100]}| = 0.8J = -|\vec{D}^{[100]}_{[010]}|$; $kT/J = 0.05$. The insets at the bottom of (a) and (b) give averaged magnetization profiles along the [001] direction for the two cases. The grey scale denotes the vertical component of magnetization S_z.

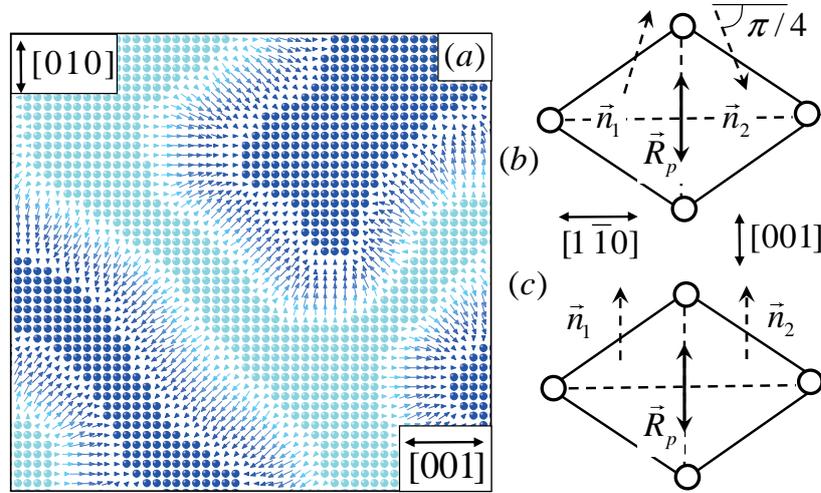Figure 3.16: a) Top view of a portion of a domain wall between energetically degenerate regions of a periodic DM modulation on a square lattice corresponding to a free standing bcc(001) monolayer with a ferromagnetic exchange interaction. The system is characterized by two DM vectors: $|\vec{D}_{[100]}^{[010]}| = -|\vec{D}_{[010]}^{[100]}| = 0.2J$; (b) and (c) Schematic representation of the orientation of DM vectors leading to the perfect chirality of $[1\bar{1}0]$ domain walls in Fe/W(110) with (b) a Néel and (c) a Bloch rotation of magnetization.

are possible: parallel or perpendicular to $\vec{R}_p$. Our calculations demonstrate that a sign of the DM interaction plays a crucial role for the orientation of magnetization. The sign of each DM vector determines the chirality of a spiral. For a single DM vector the spirals with opposite chirality have identical energy, but the energy of a superimposed state depends on the chirality of each constituent. While for $|\vec{D}_{[100]}^{[010]}| = |\vec{D}_{[010]}^{[100]}|$ and $\vec{D}_{[100]}^{[010]} \cdot [010] = \vec{D}_{[010]}^{[100]} \cdot [100]$ a Bloch like rotation is energetically favorable (see Fig. 3.15 (a)), for $|\vec{D}_{[100]}^{[010]}| = |\vec{D}_{[010]}^{[100]}|$ with $\vec{D}_{[100]}^{[010]} \cdot [010] = -\vec{D}_{[010]}^{[100]} \cdot [100]$ the Néel type of rotation applies (see Fig. 3.15 (a)). It is, however, worth mentioning that because of the symmetry considerations the Bloch type of the spiral ($\vec{D}_{[100]}^{[010]} \cdot [010] = \vec{D}_{[010]}^{[100]} \cdot [100]$) is not possible in solids consisting of one type of atoms only.

Because of the energetic degeneracy of the two propagation directions on (100) surfaces we find domain formation in samples with DM interactions. The energy cost for domain walls is small ($< 2\%$ of the total energy) for realistic values of $|\vec{D}_{\vec{R}_{ij}}^{\vec{n}}|$ as a very smooth transition from one spiral orientation to the other is possible. A typical domain wall generated by the Monte-Carlo procedure on a square lattice is shown in Fig. 3.16 (a).

Chirality of domain walls in Fe/W(110)

Double Fe layers on a stepped W(110) substrate have been extensively studied experimentally and theoretically. This very interesting system is characterized by alternating monolayer and double layer growth. Both regions show a periodic magnetic domain structure. The periodicity of the pattern as well as the width of mono/double layer regions depends on the Fe coverage. The typical distance between adjacent walls for the coverage of 1.7 monolayers is of the order of 20 nm. The domains are separated by 180° domain walls which always run along the $[1\bar{1}0]$ direction. While in monolayers domains with two opposite in-plane orientations have been observed, in double layers out-of-plane domains alternatingly magnetized up and down exist. Experimentally a perfect chirality of magnetic domain walls for the whole area of a large sample has been reported. This finding has never been supported by theoretical studies although all other parameters like the orientation of domain walls or the domain size have been described theoretically [3].

We have demonstrated that the DM interaction is responsible for the perfect chirality of magnetic domain walls in Fe/W(110). It follows from our calculations that there is a manifold of modulated magnetic structures depending on the relative orientation and the modulus of $\vec{n}_1$ and $\vec{n}_2$. However, only some solutions support the experimentally observed magnetic domain structure. Two possibilities are schematically shown in Fig. 3.16 (b), (c). The situation in Fig. 3.16 (b) corresponds to domain walls of Néel type, while that of Fig. 3.16 (c) to the Bloch type. In both cases the walls are running along $[1\bar{1}0]\perp\vec{R}_p$.

References

[1] I. Dzyaloshinskii, Sov. Phys. JETP **5**, 1259 (1957).

[2] A. Crépieux and C. Lacroix, J. Magn. Magn. Mater. **182**, 341 (1998).

[3] E. Y. Vedmedenko, A. Kubetzka, K. von Bergmann, O. Pietzsch, M. Bode, H. P. Oepen, J. Kirschner and R. Wiesendanger, Phys. Rev. Lett. **92**, 077207 (2004).

3.2.5 Spin-resolved electronic states of Co nanostructures on Pt(111)

F. Meier, K. von Bergmann, P. Ferriani, J. Wiebe, M. Bode, K. Hashimoto, S. Heinze, and R. Wiesendanger,
[Phys. Rev. B **74**, 195411 (2006) and J. Phys. D: Appl. Phys. **40**, 1306 (2007)].

Introduction

The magnetism of ultrathin films and nanostructures is a field of interest which is located at the border line between technology and basic research [1,2]. The magnetic properties of nanostructures cannot be rationalized without taking into account the dimensionality, size, and shape of the nanostructure as well as the structural and electronic properties of the substrate.

A highly interesting model system to study the impact of shape and reduced dimensions is Co/Pt(111). Thin Co films on Pt(111) [3,4], monolayer and double-layer high Co islands [5,6], Co wires [7,8] and single Co atoms on Pt(111) [9] have been investigated concerning their magnetic anisotropy by spatially averaging techniques.

In the following we report on a study of Co monolayer nanostructures by SP-STM [10]. Details of the measurement procedures can be found in Ref. [11].

Sample preparation

For the measurements presented here the Pt(111) surface was prepared by cycles of Ar^+-ion sputtering at room temperature and subsequent annealing at 1500 K for 4 min. Occasionally, an additional annealing at 1000 K in an oxygen atmosphere of $3 \cdot 10^{-7}$ mbar was carried out for 20 min. For monolayer high nanostructures Co was deposited on the clean Pt(111) surface from a rod in a water-cooled e-beam evaporator at room temperature. A typical deposition rate was 0.4 atomic layers (AL) per minute.

Structure and spin-resolved electronic properties of monolayer Co wires and islands

Spectroscopic results

All experiments were performed in a multi-chamber UHV system [12], which contains a home-built scanning tunneling microscope operating with tip and sample held at $T = 13 \pm 1$ K. Out-of-plane sensitive Fe- and Cr-coated tips were used. Figure 3.17(a) shows a topographic image of 0.3 AL Co deposited on Pt(111) at room temperature. On the terrace one atomic layer high Co islands are observed coexisting with one atomic layer high Co wires at the step edges.
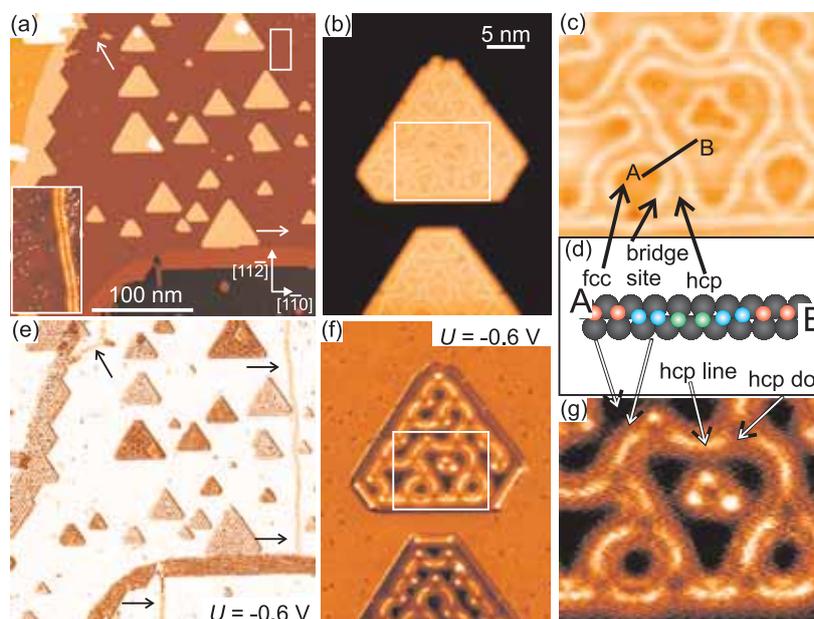
Figure 3.17: Co monolayer islands and wires prepared by Co deposition on the Pt(111) surface at room temperature. Upper panels (a)-(c): Topographic images. Inset in (a): Magnified view of the Co induced double row reconstruction lines. [14, 15] (d) Sketch of the different stacking along the line drawn in (c) (inspired by Ref. [13]). Lower panels (e)-(g): dI/dU maps measured simultaneously to the topographic images of the upper panel with an out-of-plane sensitive magnetic Fe-coated tip ($I = 1.0$ nA, $U_{\mathrm{mod}} = 20$ mV).

Figure 3.17(b) shows two slightly truncated triangular shaped Co islands. Both exhibit an almost voltage independent narrow dislocation network on top which is always found for Co monolayer islands as well as for Co wires [13]. Figure 3.17(c) displays a magnified view of the area marked by the box in (b) and reveals that the network is formed by brighter lines with a relative height of about 10 pm. The network is due to inhomogeneous stacking of the Co atoms caused by the strain of the overlayer, which is induced by the mismatch of -9.4% between the Co and the Pt lattice. According to Ref. [13] the Co atoms preferentially occupy the fcc sites of the Pt lattice. The dislocation lines appear slightly higher and are formed by Co atoms taking bridge-sites separating fcc and hcp stacked regions. Taking these results into account we can assign the more extended areas visible in Fig. 3.17(c) to fcc areas while the brighter lines are formed by Co atoms occupying bridge-sites. Furthermore, the narrow areas in between the lines consist of Co atoms in hcp positions of the Pt lattice. Figure 3.17(d) sketches the local stacking of the Co atoms below the line drawn in (c) which connects two fcc regions while passing two bridge-site lines and one narrow hcp area. The smallest distance between two bridge-site lines is about 8 ± 1 Å, which leads to very narrow hcp regions of only a couple of atoms.

Figure 3.17(e) shows an out-of-plane sensitive magnetic dI/dU map recorded si-

multaneously to Fig. 3.17(a). Above the Co wires and islands a dominating two color contrast in the dI/dU signal is found. Since all Co wires as well as all islands have an identical spin-averaged electronic structure we ascribe the origin of this contrast to oppositely magnetized domains of the Co monolayer which will be proven below. In addition to the magnetic contrast the appearance of the dI/dU signal above the nanostructures appears to be highly heterogeneous. A comparison of the dI/dU map of two oppositely magnetized single domain islands in (f) to the simultaneously recorded topographic image (b) reveals that these small scale variations of the dI/dU signal are directly correlated to the reconstruction due to the strain relief. Fig. 3.17(g) shows a magnified view of the regions marked in (f). By comparing this dI/dU map (g) to the corresponding topography in (c) each dI/dU level can directly be assigned to the local stacking of the atoms: While fcc and hcp areas show the same height in topography, both stackings show different dI/dU intensities and can easily be distinguished. At the applied bias voltage of $-0.6\,\mathrm{V}$ the highest dI/dU intensity is obtained for the hcp-lines. Interestingly, we can identify a fourth distinct area in dI/dU which has not been seen in the topography. This fourth distinct area is located at positions where three hcp lines come together and will be called hcp-dot in the following. By comparing the two oppositely magnetized islands in Fig. 3.17(f) it becomes obvious that the four stackings are also observed for the lower island. However, due to the different magnetic state they show different absolute dI/dU intensities compared to the stackings on the upper island.

In order to get access to the spin- and energy-resolved electronic structure of the different stackings we performed spatially and spin-resolved STS which is shown in Fig. 3.18. The very high lateral resolution of the spectroscopic field enables us to assign the spectra taken above the Co monolayer atoms to a certain stacking sequence. Figure 3.18(d) shows a dI/dU map of alternatingly out-of-plane magnetized Co wires. The area where the spin-resolved dI/dU spectra were taken, is indicated by the white rectangle. Although the absolute orientation of the magnetization is unknown, we arbitrarily mark the wires by arrows and refer to upwards and downwards magnetized wires in the following. Figure 3.18(a) shows the dI/dU spectra obtained above the four different Co stackings on each wire and the spectrum above the bare Pt substrate (all obtained by averaging approximately 30 spectra). The Pt spectrum shows no outstanding spectroscopic features apart from a gently increasing dI/dU signal in the negative voltage range. The onset of the surface state described in Ref. [16] is only faintly visible on this scale. All dI/dU spectra of the Co monolayer are also rather featureless in the positive voltage range. However, in contrast to the Pt spectrum they show a pronounced feature below E_F, with the peak energy depending on the specific stacking of the atoms. Independent of their magnetization direction, fcc-stacked Co atoms of monolayer wires reveal a dominant peak located around $0.28\,\mathrm{eV}$ below E_F. In the spectra of the hcp- and bridge-site lines the dominant peak is shifted to $-0.48\,\mathrm{eV}$ and $-0.42\,\mathrm{eV}$, respectively, while the peak of hcp-dot is located at $-0.40\,\mathrm{eV}$. In addition to variations originating from different stackings we observe spectroscopic
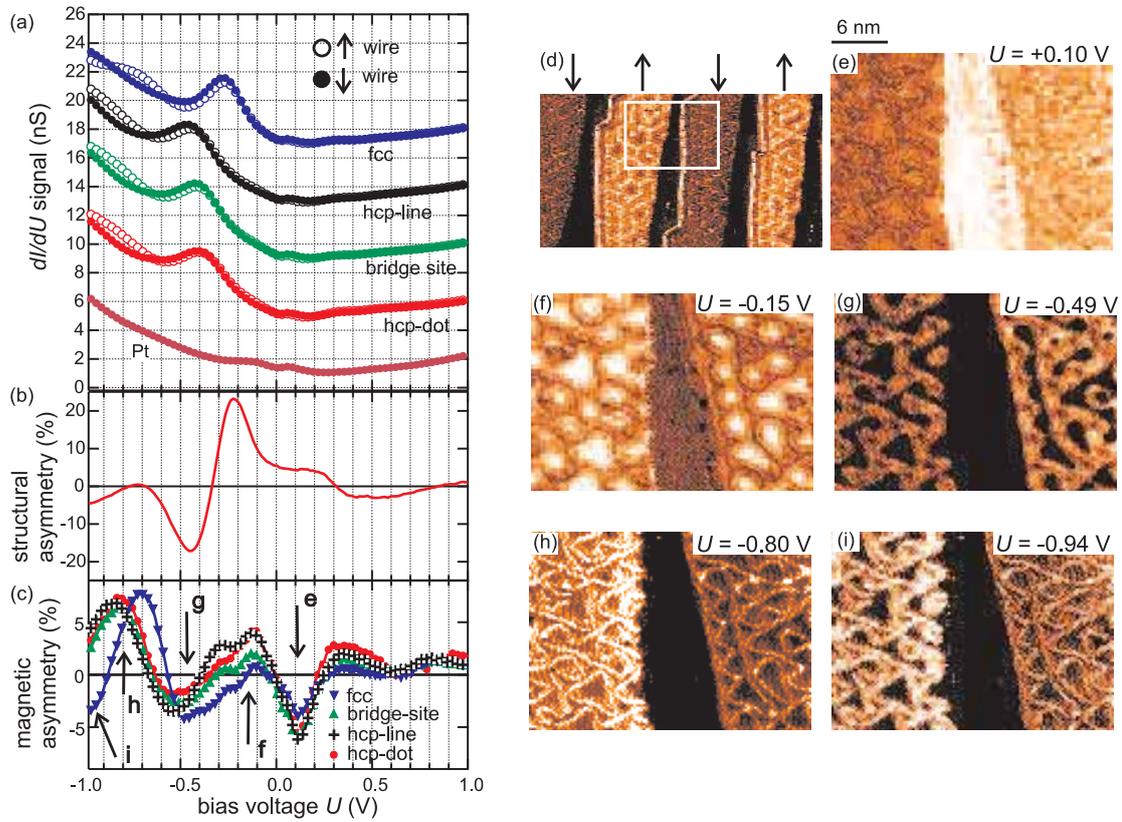
Figure 3.18: (a) Spin- and stacking-resolved dI/dU spectra on Co monolayer wires. Open and filled circles mark spectra taken on the upward and downward magnetized wire, respectively. The area of the spectroscopy measurement is indicated by the white rectangle in (d). For the stacking refer to Fig. 3.17(d). All Co spectra are offset by multiples of 4 nS. (b) Structural asymmetry between spin averaged fcc and hcp-dot spectra. (c) Magnetic asymmetry between upward and downward magnetized Co monolayer wires for different stacking. (d) dI/dU map of alternatingly out-of-plane magnetized Co wires. (e)–(i) Selected spin-resolved dI/dU slices of the STS field ($I_{stab} = 1.5$ nA, $U_{stab} = +1.0$ V, $U_{mod} = 20$ mV, Cr-coated tip).

differences due to the different magnetization directions, i.e. between the upward and downward magnetized wire. While these are generally small in the positive voltage range, we observe larger deviations close to the characteristic peak and in the energy range towards more negative bias voltages for all four different stackings.

In order to distinguish the spectroscopic differences due to a different stacking from those due to different magnetization, we calculate the structural asymmetry A_{struc} and the magnetic asymmetry A_{magn} of the spectra. The structural asymmetry is defined by

$$A_{struc} = \frac{dI/dU_{fcc} - dI/dU_{hcp}}{dI/dU_{fcc} + dI/dU_{hcp}} \, , \tag{3.5}$$

with dI/dU_{fcc} and dI/dU_{hcp} representing the calculated spin-averaged spectra of

fcc and hcp regions, respectively. The magnetic asymmetry is defined by

$$A_{\mathrm{magn}} \quad = \quad \frac{dI/dU_\uparrow - dI/dU_\downarrow}{dI/dU_\uparrow + dI/dU_\downarrow} \ , \tag{3.6}$$

with $dI/dU_\uparrow$ and $dI/dU_\downarrow$ representing the spin-resolved dI/dU spectra of the upward and downward magnetized wire for each stacking, respectively. Figure 3.18(b) shows exemplarily the structural asymmetry between the fcc and hcp-dot regions which confirms the impression that significant differences in dI/dU are located below E_{F} while the electronic structure in the positive voltage range is mostly stacking independent. The magnetic asymmetries for each stacking are shown in Fig. 3.18(c). In the negative voltage range the magnetic asymmetries for the Co monolayer are higher than in the positive voltage range. They show distinct minima at about $-0.50\,\mathrm{eV}$ and larger maxima around $-0.80\,\mathrm{eV}$. In order to visualize the interplay between structural and magnetic asymmetry we display dI/dU slices at selected energies in Figs. 3.18(e)-(i), the corresponding voltages are indicated in Fig. 3.18(c).

Up to this point we can conclude that the electronic structure of the Co monolayer on Pt(111) changes significantly between the areas of the four different atom positions on a length scale of only a few atoms. The main change in the electronic structure is a shift of the dominating peak in the negative voltage range, which appears at $-0.28\,\mathrm{eV}$ on the fcc areas and is shifted to lower energies for the other three stackings. Despite this strong heterogeneous electronic structure it is possible to deduce the magnetic orientation of the Co monolayer using the magnetic asymmetry of the spin-resolved dI/dU spectra.

Magnetism of Co monolayer nanostructures

In order to study the magnetic properties of the Co monolayer as well as to verify the magnetic origin of the observed contrasts in dI/dU maps we probed the Co structures in variable magnetic fields, which were applied along the surface normal.

Figures 3.19(a)–(d) show selected out-of-plane sensitive magnetic dI/dU maps with an applied external magnetic field B as indicated. While the Pt substrate has a uniform dI/dU signal with low intensity, a two stage magnetic contrast of the oppositely out-of-plane magnetized Co is clearly visible for the islands as well as for Co wires. Figure 3.19(a) displays the magnetic virgin state of the sample at $0\,\mathrm{T}$: the amount of Co structures with opposite magnetization directions is approximately equal. After increasing the magnetic field to $+0.3\,\mathrm{T}$ (b), some Co areas which are marked in the dI/dU map changed their magnetic orientation. From this contrast reversal we can directly conclude, that these bright areas are now aligned with the direction of the external field. For the left marked wire in (b), it can be observed that the field-induced reorientation process does not change the magnetization of the wire completely but a domain wall is trapped at a constriction. At a magnetic field of $+0.8\,\mathrm{T}$ all Co structures appear bright except one comparably large Co island marked in Fig. 3.19(c). Figure 3.19(d) displays the magnetic state at remanence. A direct comparison to the
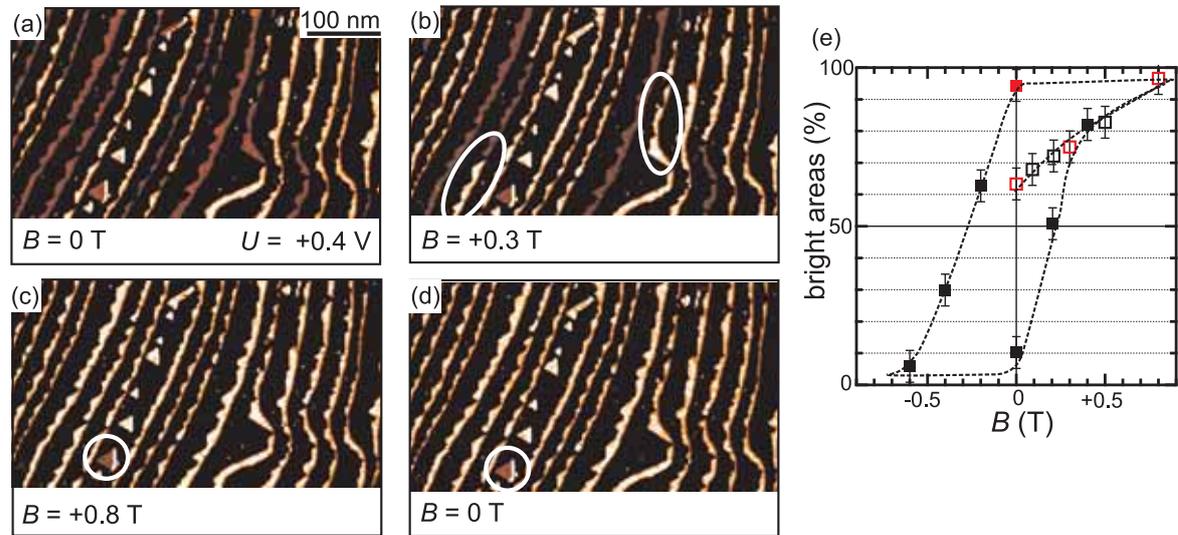
Figure 3.19: (a)–(d) Selection of dI/dU maps of Co monolayer wires and islands in the presence of an external magnetic field applied perpendicular to the surface plane measured with an out-of-plane sensitive magnetic Cr-coated tip. The bright or dark appearance of the Co corresponds to a parallel or antiparallel alignment of the tip and sample magnetization. (e) Hysteresis loop obtained by plotting the percentage of bright domains as a function of applied field. The dashed line is a guide to the eye. ($I = 0.7\,\text{nA}$, $U_{\text{mod}} = 20\,\text{mV}$)

previous dI/dU map in (c) shows that all wires and islands remain in their magnetic state.

Analyzing the magnetic state of the Co nanostructures and plotting the percentage of the bright Co areas at several applied magnetic fields leads to a hysteresis curve, which is displayed in Fig. 3.19(e). Since the external magnetic field is applied along the easy anisotropy axis, the hysteresis curve shows a typical ferromagnetic shape with a very high remaining magnetization after field removal. The extracted coercivity of this area of the monolayer Co sample is $\mu_0 H_c = 0.25 \pm 0.05\,\text{T}$. As visible in (e) the obtained hysteresis curve does not show a simple square loop shape but is slightly canted. This can be understood by taking into account that the magnetic reorientation process occurs not at the same magnetic field for each Co structure, but progresses successively [17]. In general we observe that larger islands as well as wider wires seem to switch abruptly from one saturated state to the opposite one at higher applied magnetic fields than smaller Co structures. Furthermore, the reorientation process itself is different for wires and islands. While the Co islands are always in a single domain state, wires with a sufficient width are reoriented by domain wall movement.

The existence of domain walls in wires allows the critical examination of recent results obtained on nanoscale Co monolayer islands. As shown in Fig. 3.19 domain walls are preferentially located at constrictions which are a few nanometers wide only, if the terraces are particularly narrow. We have studied Co nanowires which were
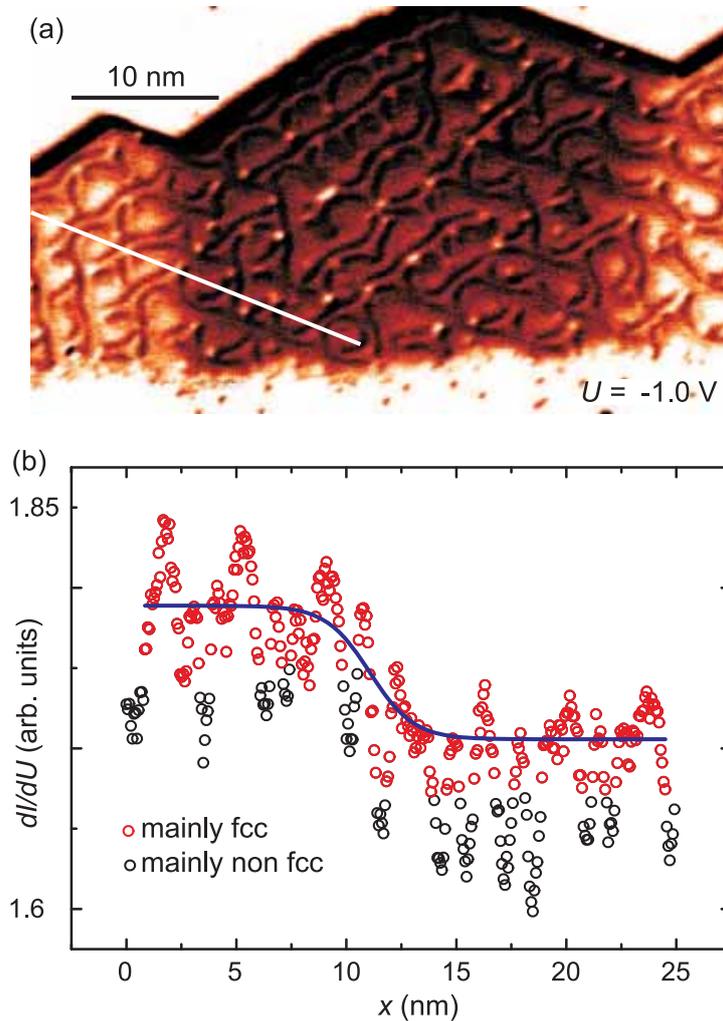
Figure 3.20: (a) dI/dU map of a Co monolayer wire with three domains measured with an out-of-plane sensitive magnetic Cr-coated tip. (b) Domain wall profile (open circles) along the line marked in (a). The solid line gives a fit to the red data points. ($I = 1.5\,\mathrm{nA}$, $U_{\mathrm{mod}} = 20\,\mathrm{mV}$)

grown on much wider Pt(111) terraces and exhibit a width of 15–25 nm as shown in the dI/dU map of Fig. 3.20(a). In the central part of the image a dark domain can be recognized which is surrounded by two bright domains. Both domain walls separating the three domains are located in constrictions and are about 20 nm long. Since these data were measured with an out-of-plane sensitive probe tip we can conclude that the Co nanowire is perpendicularly magnetized even 20 nm away from the Co step edge. But in which way is this distance related to the magnetic exchange length? This can be analyzed by a closer inspection of the domain wall profile. For this purpose we have taken a profile of the dI/dU signal along the white line in Fig. 3.20(a). The result

is plotted in Fig. 3.20(b). In order to minimize the influence of the inhomogeneous spin-averaged electronic structure due to different stacking (see Sec. 3.2.5) we have not taken the line section perpendicular to the domain wall but under an angle of 60°. Thereby, mostly fcc sites are crossed and hcp sites are avoided as far as possible. The line section shows two levels of dI/dU signal strength on the left and the right side which represent the oppositely magnetized domains and the transition area in between. While the data points on each domain still scatter due to the remaining stacking influence, the signal becomes much smoother when neglecting the data points originating from the hcp lines which are given in black color. The remaining red data points are fitted with a standard domain wall profile function [18]

$$y = y_0 + y_{\mathrm{sp}} \tanh\left(\frac{2(x - x_0)}{w} \right) \tag{3.7}$$

which is based on continuum micro-magnetic theory [19]. y_0 and y_{sp} are the spin-averaged and the spin-polarized part of the dI/dU signal, x_0 is the position of the domain wall center, and w represents the domain wall width, which is determined by the exchange stiffness A and the effective anisotropy constant K_{eff} by

$$w = 2\sqrt{\frac{A}{K_{\mathrm{eff}}}} \ . \tag{3.8}$$

As shown by a solid line in Fig. 3.20(b) the best fit is obtained for a domain wall width of approximately 4 nm, i.e., much narrower than the structural width of the Co nanowire. In order to obtain an appropriate value of the exchange stiffness of the ML, A_{ML} has been calculated in two ways. Together with the information that 0.8 ML Co/Pt(111) is still ferromagnetic above RT (Ref. [20]) and the assumption $T_{\mathrm{C}} \propto A$ we obtain $A_{\mathrm{ML}} = 7.0 \cdot 10^{-12}$ J/m with $T_{\mathrm{C,bulk}} \approx 1400$ K and $A_{\mathrm{bulk}} = 3.0 \cdot 10^{-11}$ J/m. A second way to obtain A_{ML} is using $n_c \propto A$ where n_c is the number of coordination of an atom. Since n_c is reduced from twelve for bulk atoms to six for a monolayer atom, A_{ML} is given by $1.5 \cdot 10^{-11}$ J/m. Since the correct value for A_{ML} is unknown, both roughly estimated values might be the lower and the upper limit for a reasonable value range. Using these reasonable values for A, the anisotropy constant results in $+0.08$ meV/atom $\leq K_{\mathrm{eff}} \leq +0.17$ meV/atom.

References

[1] F. J. Himpsel, J. E. Ortega, G. J. Mankey, R. F. Willis, Adv. Phys. **47**, 511 (1998).

[2] I. Zutic, J. Fabian, S. D. Sarma, Rev. Mod. Phys. **76**, 323 (2004).

[3] J. Thiele, C. Boeglin, K. Hricovini, F. Chevrier, Phys. Rev. B **53**, R11934 (1996).

[4] M. Wellhöfer, M. Weißenborn, R. Anton, S. Pütter, H. P. Oepen, J. Magn. Magn. Mater. **292**, 345 (2005).

[5] S. Rusponi, T. Cren, N. Weiss, M. Epple, P. Buluschek, L. Claude, H. Brune, Nature Materials **2**, 546 (2003).

[6] F. Meier, K. von. Bergmann, J. Wiebe, M. Bode, and R. Wiesendanger, J. Phys. D: Appl. Phys. **40**, 1306 (2007).

[7] P. Gambardella, A. Dallmeyer, K. Maiti, M. Malagoli, W. Eberhardt, K. Kern, C. Carbone, Nature **416**, 301 (2002).

[8] P. Gambardella, A. Dallmeyer, K. Maiti, M. Malagoli, S. Rusponi, P. Ohresser, W. Eberhardt, C. Carbone, K. Kern, Phys. Rev. Lett. **93**, 077203 (2004).

[9] P. Gambardella, S. Rusponi, M. Veronese, S. Dhesi, C. Grazioli, A. Dallmeyer, I. Cabria, R. Zeller, P. Dederichs, K. Kern, C. Carbone, H. Brune, Science **300**, 1130 (2003).

[10] F. Meier, K. von Bergmann, P. Ferriani, J. Wiebe, M. Bode, K. Hashimoto, S. Heinze, and R. Wiesendanger, Phys. Rev. B **74**, 195411 (2006).

[11] M. Bode, Rep. Prog. Phys. **66**, 523 (2003).

[12] O. Pietzsch, A. Kubetzka, D. Haude, M. Bode, R. Wiesendanger, Rev. Sci. Instrum. **71**, 424 (2000).

[13] E. Lundgren, B. Stanka, M. Schmid, P. Varga, Phys. Rev. B **62**, 2843 (2000).

[14] P. Grütter, U. Dürig, Phys. Rev. B **49**, 2021 (1994).

[15] E. Lundgren, B. Stanka, W. Koprolin, M. Schmid, P. Varga, Surf. Sci. **423**, 357 (1999).

[16] J. Wiebe, F. Meier, K. Hashimoto, G. Bihlmayer, S. Blügel, P. Ferriani, S. Heinze, R. Wiesendanger, Phys. Rev. B **72**, 193406 (2005).

[17] O. Pietzsch, A. Kubetzka, M. Bode, R. Wiesendanger, Science **292**, 2053 (2001).

[18] A. Kubetzka, M. Bode, O. Pietzsch, R. Wiesendanger, Phys. Rev. Lett. **88**, 057201 (2002).

[19] A. Hubert, R. Schäfer, Springer, Berlin, 1998.

[20] C. Shern, J. Tsay, H. Her, Y. Wu, R. Chen, Surf. Sci. **429**, L497 (1999).

3.2.6 Spin-polarized confinement states on magnetic nanoislands

Introduction

Standing wave patterns arising from scattering of surface state electrons off defects like terrace edges, impurities or adsorbates have raised great attention in scanning tunneling microscopy (STM) based research since their first observation more than ten years ago [1, 2]. These quantum interference phenomena can be observed by STM on densely packed noble metal surfaces as a lateral periodic modulation of the local density of states (LDOS). The LDOS is, according to STM theory [3], proportional to the energy dependent differential tunneling conductance, $dI/dU(eU_{bias}, x, y)$; this is the signal measured in scanning tunneling spectroscopy (STS), making the STM an ideal investigation tool. Here E is determined, with reference to the Fermi energy E_F, by the bias voltage between tip and sample, $eU_{bias} = E - E_F$. The STM has been used to study pertinent phenomena on noble metal surfaces also under the condition of lateral confinement, e.g., in quantum mechanical resonators (so-called quantum corrals) created by manipulation of individual adsorbate atoms [2, 4–6], on narrow terraces [7,8], in triangular structures created by controlled indentation of a Cu surface using a tunneling tip [9], or on nanometer-size Ag islands homoepitaxially grown on Ag(111) [10]. In more recent reports it was shown that standing wave patterns can also be observed on facets of sufficiently large noble metal clusters on graphite [11], and on transition metal islands heteroepitaxially grown on noble metal substrates [12–16]. Although in a number of cases the adsorbate atoms or the adlayer islands comprised of magnetic material, the STM data published so far are not spin resolved. The only exception, to our knowledge, is a study by von Bergmann *et al.* [17] reporting on a variation of standing wave patterns scattered from single oxygen atoms on oppositely magnetized domains of ultrathin Fe films on W(110).

Co islands on Cu(111)

O. Pietzsch, S. Okatov, A. Kubetzka, M. Bode, S. Heinze, A. Lichtenstein, and R. Wiesendanger

In a previous publication triangular Co islands with a typical base length of about 20 nm and a height of 2 atomic layers above the Cu surface were identified as ferromagnetic, exhibiting a perpendicular magnetization and strong coercivity and remanence [18]. Here we report on the spin-resolved electronic structure of the Co islands. Combining SP-STS experiments and *ab initio* spin-density functional theory calculations we find an interplay of contributions to the vacuum DOS from localized minority

d states and a dispersive majority $s-p$ – like band such that the sign of the spin polarization is changed repeatedly as a function of energy. The latter mentioned majority band is responsible for the observed standing wave patterns, confined to the islands' triangular geometry. Furthermore, the high lateral resolution achievable in STM experiments allows for a detection of another spin-polarized state occurring at zero bias which is localized in narrow regions bounding the Co islands. The spin character of this state is opposite to that of the corresponding island, emphasizing that the spin polarization, on a lateral scale of a few Ångstroms, may not only change its magnitude but also its sign, depending on the electronic states involved.

Sample and Tip Preparation

The Cu(111) single crystal was cleaned using standard procedures, i.e. repeated cycles of Ar^+ sputtering and anneal to $600°$ C. Co was evaporated at room temperature with no further anneal. It is well known that Co films on the Cu(111) surface are subject to severe intermixing even at room temperature [19]. Also, a Cu capping of Co islands on the time scale of hours has been reported [20]. In order to obtain Co islands of high purity, the sample was inserted into the cold microscope immediately after terminating the Co deposition (typical transfer time of $2.5-3$ minutes) and rapidly cooled down to 14 K to suppress as much as possible an intermixing or Cu capping of the islands [21].

We used a polycrystalline W tip coated with a Cr film of 75±50 ML thickness which was checked for sensitivity to the perpendicular magnetization component of the sample [22]. Acquisition of the data presented here was made in the following way. Simultaneously to taking a constant current image, spectroscopic data were obtained by stabilizing the tip at each pixel ($U_{\text{stab}} = +0.6$ V [voltage applied to the sample], $I_{\text{stab}} = 1$ nA), opening the feedback loop and then ramping the voltage from +0.5 V to -1 V. We recorded $I(U)$ curves and simultaneously $dI/dU(U)$ curves using a lock-in technique. The experimental curves shown in Fig. 3.21 were obtained by numerical differentiation of $I(U)$ curves, spectra shown in other Figures stem from the recorded lock-in data.

Spin-Dependent Electronic Structure

As was discussed in detail in Ref. [18], the Co islands grow in two orientations; one type is stacked following the substrate's fcc sequence while the other one contains a stacking fault at the interface, giving rise to a $180°$ rotation. The different stacking causes characteristic variations in the electronic structure, in particular at the large peak near 0.3 eV below the Fermi level. Here we restrict our considerations to a comparison of spectra from the two islands marked by boxes in Fig. 3.21(a); for the context of this report, stacking dependent variations play only a minor role.

As is usual, we define the spin polarization at an energy E (taken with reference to the Fermi level E_{F}) as the difference of spin-up and spin-down electronic state densities normalized to the total density, $P(E) = (n^{\uparrow}(E) - n^{\downarrow}(E))/(n^{\uparrow}(E) + n^{\downarrow}(E))$. In the
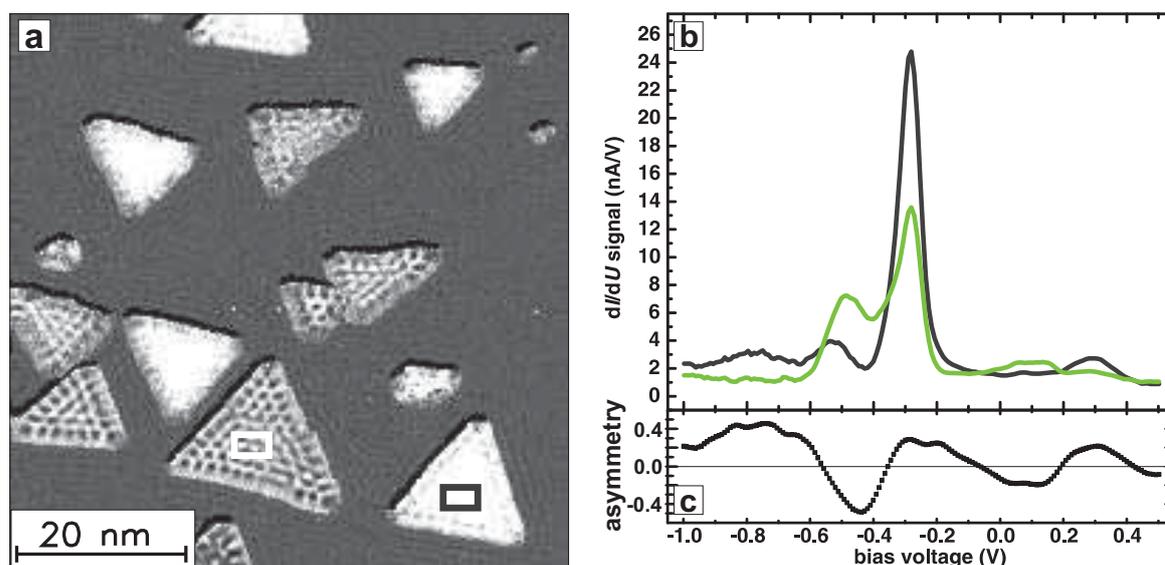
Figure 3.21: (a) Map of the differential tunneling conductance dI/dU of 0.6 ML Co on Cu(111) at $U = 0.291$ V. Contrast between islands is due to opposite perpendicular magnetization. Both the Cu substrate as well as the Co islands exhibit a standing wave pattern of scattered surface state electrons. (b) Tunneling spectra of oppositely magnetized islands. The curves were averaged over pixels inside the boxes in (a). (c) Magnetic asymmetry $A(U) = (dI/dU^{\downarrow\downarrow} - dI/dU^{\uparrow\downarrow})/(dI/dU^{\downarrow\downarrow} + dI/dU^{\uparrow\downarrow})$ of the tunneling spectra as a function of bias voltage; the sign changes several times as a function of U.

following we give a detailed overview of the evolution of the sign of the spin polarization as a function of energy, as determined from the tunneling spectra measured with a chromium coated tip (see Fig. 3.21). *Ab initio* spin density functional calculations provide further information, allowing to explain the experimental findings in terms of the spin-resolved Co band structure (see Fig. 3.22).

Fig. 3.21 shows (a) the map of the differential conductance dI/dU at $U_{\mathrm{bias}} = 0.291$ eV, (b) tunneling spectra with a color coding corresponding to the light gray and dark boxes in (a) which indicate the locations where the curves were averaged, and (c) the asymmetry $A(eU) = (dI/dU^{\downarrow\downarrow} - dI/dU^{\uparrow\downarrow})/(dI/dU^{\downarrow\downarrow} + dI/dU^{\uparrow\downarrow})$ of the curves as a function of bias voltage. The strong contrast observed among the islands in (a) is caused by their magnetization being opposite.

The most prominent feature in the spectra is a very intense and narrow peak at about 0.27 eV below E_{F} (occupied states). There is a large difference in intensity between the curves at the mentioned peak which is a result of the opposite magnetization of the islands. There is hardly any majority vacuum spin density at this energy, thus the sign of the sample spin polarization is negative at the peak position. Considering the fact that also the Cr material at the tip is dominated by minority states at the Fermi energy [23] and assuming spin conservation for tunneling through the vacuum gap [24], spin minority electrons from occupied states will find a high (low) density

of unoccupied spin minority states in the counter electrode if the magnetizations of island and tip are in a parallel (antiparallel) configuration [25], resulting in a high (low) differential tunneling conductance. We therefore conclude that the dark curve in Fig. 3.21 is indicative of a parallel (pp) alignment of island and tip magnetizations, while it is antiparallel (ap) for the curve. In the following, the right (left) island will be referred to as pp island (ap island). Likewise, the contrast between islands will be called *normal* (*inverted*) if in a dI/dU-map at a particular energy the pp island appears brighter (darker) than the ap island. It is clear that normal (inverted) contrast will be found in energy ranges where, in the asymmetry plot Fig. 3.21(c), $A > 0$ ($A < 0$).

The spin polarization of the Co islands is found to be strongly bias dependent, and in particular the sign is reversed several times in the observed energy interval. At the energetic position of the large peak both electrodes exhibit negative spin polarization, and the polarization sign of the tunneling junction, $P_{st} = P_s P_t$, is positive. Once the sign is determined here, it is clear that any crossover of the two spectral curves in Fig. 3.21(c) is associated with a sign inversion of P_{st}. In the dI/dU-maps at the respective energies this becomes visible by contrast reversals of the islands. In other words, also the island which has a magnetization antiparallel to that of the tip may appear brighter at certain energies. It thus remains to track the sign reversals of P_{st} to sign reversals of either sample or tip polarization. To the left of the sharp peak (larger negative bias values) the sign reversals are most likely not caused by the sample because on the sample side there is hardly any majority spin density available, see Fig. 3.22(a); considerable spin-up density becomes accessible only at energies below -1 eV. Also, it is well known that in STM experiments at negative sample bias the signal is increasingly dominated by empty tip states [26, 27]. We therefore attribute the sign reversals on the left-hand side of the large peak to variations of the tip's spin split electronic structure.
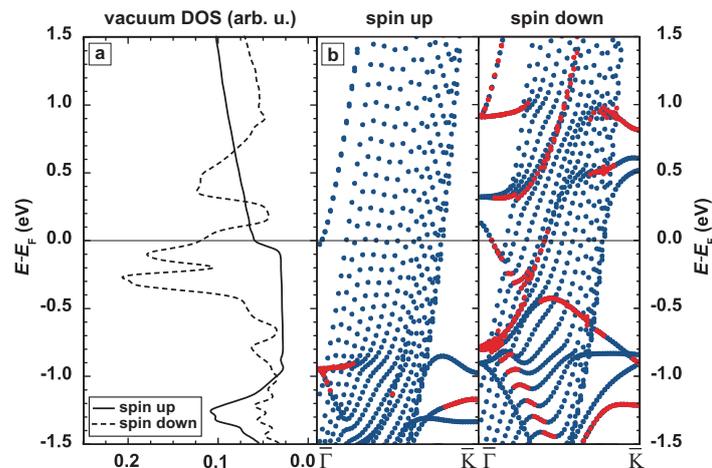

Figure 3.22: (a) Calculated vacuum spin density of a 2 ML thick hcp Co film on Cu(111), 3 Å above the surface. (b) Spin resolved band structure near the Fermi level.
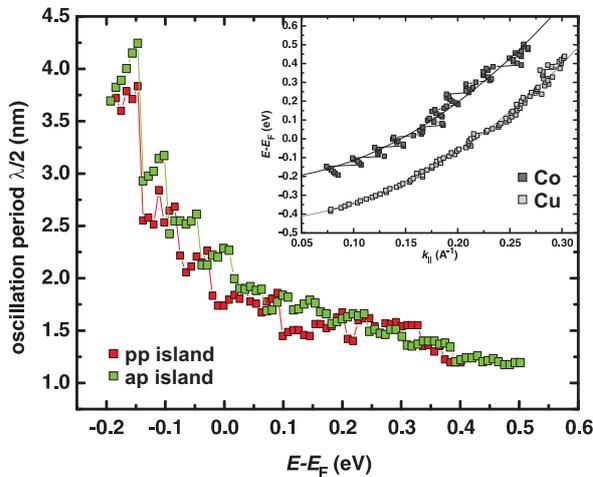
Figure 3.23: Evolution of the lateral standing wave periods with bias voltage. Inset: Dispersion relation of the Cu substrate and similar data from the Co islands. The step-like structure of the latter results from electron confinement to the triangular geometry.

To the right-hand side of the peak the calculated vacuum LDOS exhibits an onset of a surface state band at an energy just below the Fermi level with a nearly constant LDOS extending well into the unoccupied Co states, see the curve in Fig. 3.22(a). This $s - p$ – like band is of *majority* character, as was also found by Diekhöner *et al.* [16]. In the experimental spectra we do not see a noticeable onset of this surface state; a similar observation was explained in [16] by the onset being hidden in the tail of the huge d_{z^2} peak structure. As will be discussed in Section 3.2.6, our data suggest the band edge position to be at -0.22 eV. We believe that this enhanced majority spin density is responsible for the sign reversal observed experimentally starting at 0.07 eV below the Fermi level. The corresponding parabolic band is the predominant feature in a wide energy range, up to more than 1 eV above the Fermi energy. There is, however, a limited energy region (+0.2 eV – +0.43 eV in the experimental data) where both experimental and calculated spectra indicate a higher weight for minority states causing again the sign to be switched. The calculated band structure at this energy, Fig. 3.22(b), shows flat minority d-bands at the $\bar{\Gamma}$-point which outweigh the majority spin density in this energy region. In the following we will discuss how the interplay between the dispersive majority $s - p$ – like band and localized d states appears in our data.

Confinement States

As is visible in Fig. 3.21(a), not only the Cu surface displays its well known standing wave pattern [2, 8, 28], but also the Co islands exhibit their own pattern. This Co surface state has been investigated by STM and STS in some detail in Ref. [16]. The STM experiments reported, however, were not spin-sensitive. Here we report our spin-polarized STS data.

A first faint regular LDOS oscillation pattern can be discerned at 184 meV below the Fermi level. In islands having a shape sufficiently close to an ideal triangle, regular patterns of $n(n+1)/2, n = 1, 2, 3...$ dots emerge with increasing energy. We have
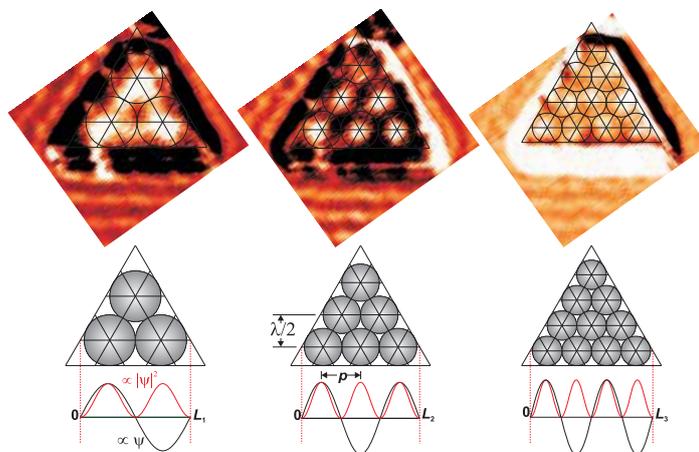
Figure 3.24: Standing wave patterns on a Co island and a schematic geometrical representation.

extracted the lateral oscillation periods as a function of energy by taking line sections along the outermost row of nodes through the corresponding sequence of dI/dU maps, that is in the energy range -0.184 eV $< eU < +0.5$ eV.

In Fig. 3.23 we have plotted the standing wave periods as a function of energy. In order to qualitatively understand the peculiar stepped evolution one may trace the transition between resonant states with well-ordered dot patterns in real space. In sufficiently small islands a first low-energy pattern is observed consisting of three dots, that is, along the triangle's baseline there are two dots in a row [29] fitting into the confinement length L_n, cf. Fig. 3.24. As the energy is increased from E_n towards E_{n+1} the dots are observed to slightly drift apart and the whole row of dots shifting towards the island edge thereby increasing also the effective confinement length L_n and, by the same token, the lateral period. Eventually, halfway between the two dots a new dot emerges; at this point, the period is discontinuously reduced, and with further energy increase the dot pattern relaxes into the $n+1$ state. This state has a dot at the row center which, upon further energy increase, attains a more and more elongated shape. Eventually this central dot splits up into two, and the pattern relaxes into the $n+2$ state. Thus, in the periods vs. energy diagram, Fig. 3.23, this behavior appears as a succession of sloped plateaus of increasing periods and sudden drops to the next state's period. As is expected, the islands' sizes affect the energy spacing between successive states E_n. We have evaluated three islands with base lengths of 10, 14 and 17 nm. In the energy interval considered here we observe 7, 10, and 12 resonant states, respectively.

From the oscillation periods one can obtain values for the wave number $k_{||}$, see the ap island example in the inset of Fig. 3.23. Assuming nearly free electron behavior in two dimensions, similar to that of the Cu surface state—albeit under the condition of lateral confinement—, a parabolic fit was applied to the Co values, resulting in a band edge at $E_0 = -0.22 \pm 0.01$ eV and an effective electron mass $m^* = 0.37 \pm 0.01 m_{\mathrm{e}}$.

In the inset of Fig. 3.23 we have also plotted corresponding data of the surface state of Cu, see the gray data points. One can immediately notice that there is a very distinct difference in the behavior of the LDOS oscillations on top of the Co islands as compared to that of the Cu surface. While the wavelengths and thus the $k_\parallel$ values evolve monotonically on the Cu substrate, it is step-like on the Co islands. This is a consequence of the lateral electron confinement inside the Co islands. Whereas on the open Cu surface the wavelength can vary continuously with energy this is not possible on the islands where the wave function must meet the boundary conditions imposed by the triangular geometry.

To account for the islands' patterns, we have used a multiple scattering approach as originally developed by Heller *et al.* [30] to describe the oscillation patterns in quantum corrals artificially created by manipulation of individual atoms [2]. In our simulation the island edges were modeled by point scatterers organized to form triangles with a spacing of twice the interatomic distance of the Cu(111) surface (which is sufficient as long as the wavelength of the surface state electrons is large compared to the spacing). Using Heller's recipe [30], an enhanced electron amplitude travels radially
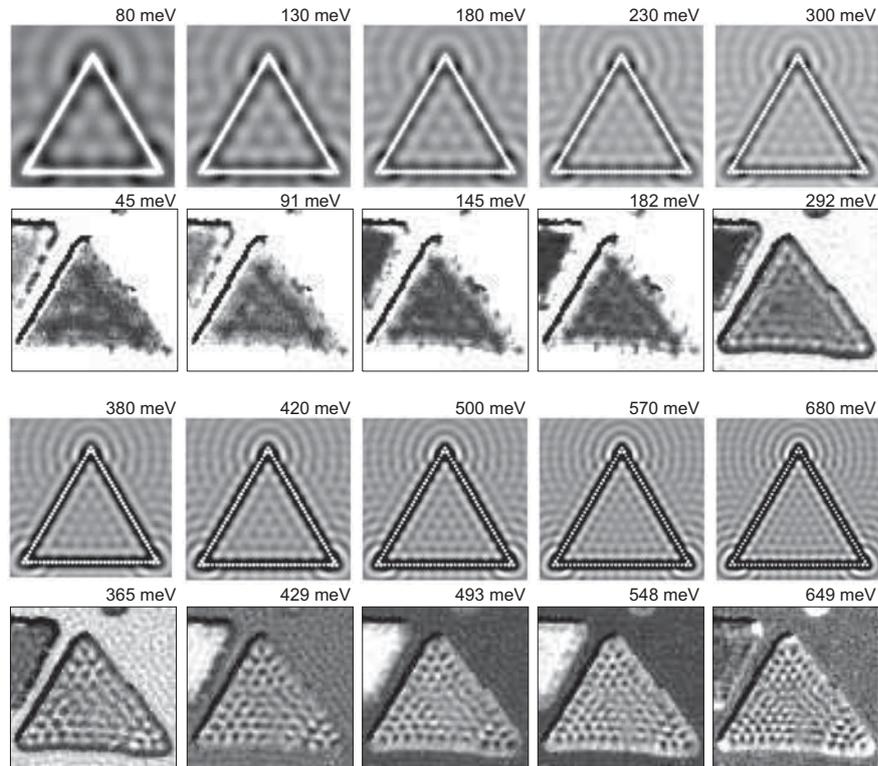

Figure 3.25: Multiple scattering approach as originally developed by Heller *et al.* [30] for quantum corrals artificially created by manipulation of individual atoms, in comparison to dI/dU maps of resonant states (energy values given with respect to the band edge at -0.22 eV as determined from fitting the data shown in the inset of Fig. 3.23).
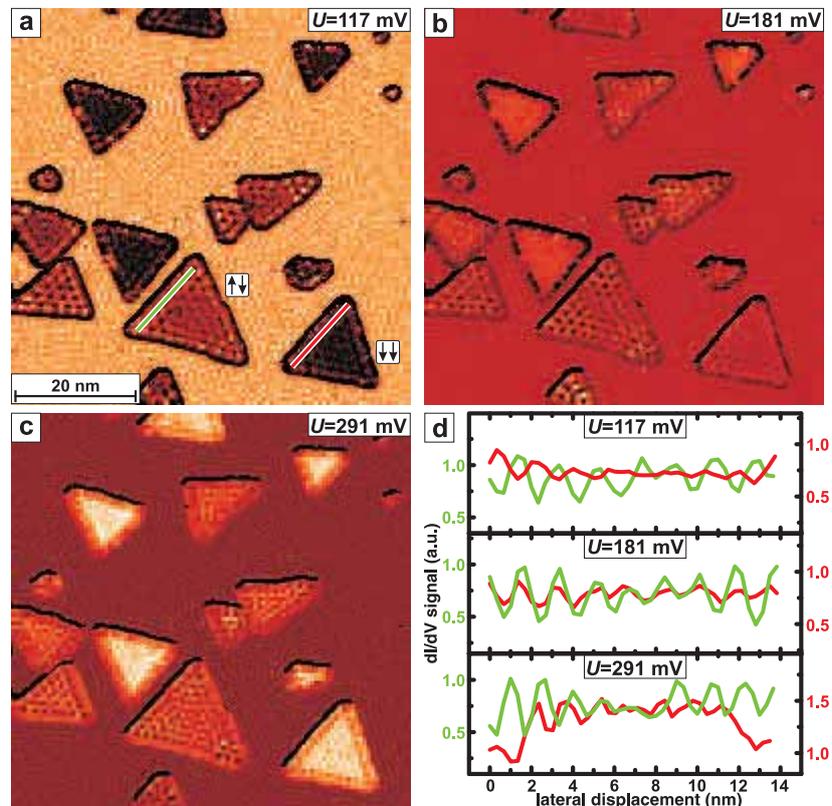
Figure 3.26: (a–c) Standing wave patterns at energies representing ranges of inverted, balanced, and normal island contrast. (d) Profiles taken along lines as indicated in (a). In each case the amplitude is larger on the ap island.

away from the tip, being scattered from one point scatterer, the scattered wave again being scattered by the next and all the other scattering centers, the multiply scattered wave eventually traveling back to the tip, interfering with the outgoing wave. An image is then calculated at a given energy by evaluating the square of the wave function $|\psi(r)|^2$ for each pixel. Incrementing the energy by 0.01 eV, in this way we obtained a series of images covering an energy interval 0.7 eV in width which can be compared to the experimental dI/dU maps, see Fig. 3.25. A scattering phase shift of -0.9π has been used in the simulations, giving a high degree of localization of amplitude *minima* rather than maxima, similar to the experimental observation.

Spin-Dependent Oscillation Amplitude

So far, the spin character of the electronic states responsible for the oscillation patterns has not been considered in detail. We have mentioned earlier that the oscillations on the Co islands are caused by a band of *majority* spin character. Because the tip has an effective *negative* spin polarization within the energy range in which the oscillations are observed, tunneling into the oscillatory state is not very efficient for the case of an island being magnetized parallel to the tip magnetization. On the other hand, in oppositely magnetized islands the role of minority and majority spins, as referenced from the tip's perspective, is exchanged. As a consequence, the oscillatory state in ap

islands has the matching spin character for a quite effective tunneling of the excess minority spin electrons from the tip. This leads to a significant enhancement of the oscillation amplitude in ap islands as compared to pp islands. In Fig. 3.26 maps of the two islands and corresponding line profiles are shown for three bias voltages which are representative for ranges of inverse, balanced, and normal spin contrast. Table 3.1 lists amplitude values for these energies, obtained by determining the difference between averages of 21 point spectra from local maxima and from 21 local minima. In each case the amplitude is found considerably larger for the ap island regardless of the sign of the bias dependent spin polarization, because only sample majority electrons take part in the LDOS oscillations while localized d-like electrons do not. Still, the net balance of contributions from majority and minority states to the sample LDOS determines the overall contrast between the islands which may be normal or inverted (or balanced at the point of sign inversion), depending on the energy range; the oscillations are then superimposed on this background signal.

Table 3.1: Oscillation amplitudes on the pp (ap) island in energy ranges of inverse, balanced, and normal SP.

bias (V)	SP	pp island (arb. u.)	ap island (arb. u.)	ratio
0.152	inverse	0.248	0.527	0.49
0.188	balanced	0.235	0.586	0.40
0.291	normal	0.250	0.784	0.32

Coupling between Co and Cu Surface States?

It has been shown with STS by several research groups [4,31–33] that a single magnetic impurity atom on a noble metal surface modifies the local electronic structure in a rather characteristic way which is known as the many-particle Kondo resonance [34,35]. The common perception is that the host electron system aligns the spins of nearby conduction electrons in such a way that the uncompensated spin of the magnetic adatom is surrounded by a screening cloud to avoid any net magnetic moment. Among the systems investigated, Co adsorbates on the Cu(111) surface played a prominent role [4,33]. So far, the STS experiments were carried out without direct spin sensitivity. It is therefore of considerable interest to study the case of a ferromagnetically stabilized spin system like the Co islands on the Cu(111) surface and to answer the question whether or not a spin-induced effect can be observed in the Cu surface in close vicinity to the islands due to the presence of the magnetic material. In particular, the existence of an oscillatory surface state in *both* Co and Cu, spin-polarized in one but not in the other material, may raise the question if there is any kind of interaction between the two which, in a spin-polarized experiment, may lead to measurable effects in the proximity of oppositely magnetized islands.
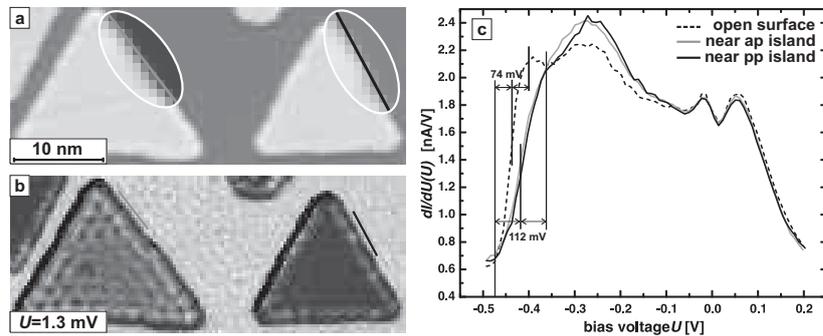
Figure 3.27: (a) Topography, (b) dI/dU map and (c) tunneling spectra of the Cu surface taken in close proximity to oppositely magnetized islands. No significant modification as an effect of the islands' magnetizations is observed. The Cu surface state onset is considerably broadened in comparison to spectra taken on the open surface, away from islands.

In Fig. 3.27 tunneling spectra of the Cu surface state in the immediate proximity to the oppositely magnetized Co islands are presented. The spectra were obtained by averaging over approximately 12 pixels along a line drawn as close as possible to the island edges. As a reference, a spectrum of the Cu surface state recorded on the open surface, away from islands, is also displayed. We observe a clear difference between the close-to-island spectra and the reference spectrum. The width of the surface state onset is larger near the islands (0.11 V) as compared to the open surface (0.075 V), indicative of considerable broadening due to scattering at the island edges. Within our lateral (pixel width $\approx$ 3 Å) and energy resolution (*ac*-modulation U_{mod} = 15 mV, energy increment 9 meV, thermal broadening of $\approx$ 3.6 meV) there is, however, no significant difference between spectra measured next to pp and ap islands. This is particularly true at the Fermi energy [36]. Further, we cannot detect any significant effect of the Co oscillations on those of the Cu surface in terms of amplitude or scattering phase alteration. Summarizing this point, at the lateral and energy resolution of the present experiment a definite statement about a *spin-dependent* modification of the Cu surface electronic structure cannot be made.

Spin-Polarized Rim State

While we do not see induced spin effects in the Cu surface, there is a remarkable feature found at the islands' rims. All islands are bounded by a rim with a typical apparent width of 1.7±0.2 nm, i.e. several atomic rows wide, as determined from both topographic and dI/dU images. In constant current (topographic) images this rim exhibits an increased apparent height; at small bias voltages ($\approx$ 10 mV) the effect is strongest and amounts to an enhancement of 55 pm. At the energy position of the large d – like peak the differential conductance of these rim areas is considerably lower than that of the inner part of the islands; accordingly, in dI/dU maps at this bias voltage these areas show up as a dark fringe around the islands. Right at the Fermi
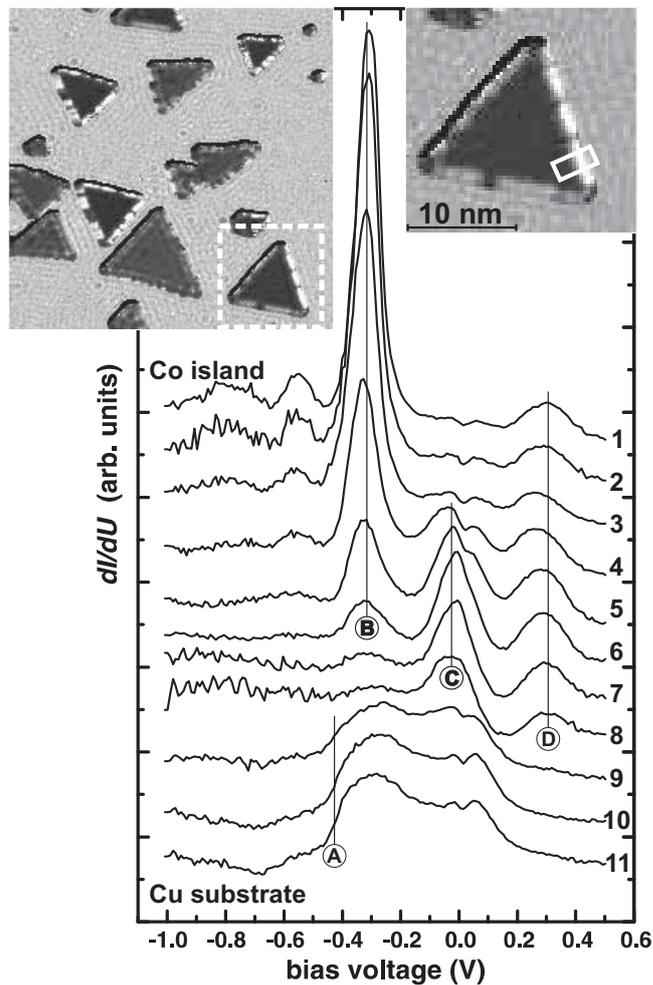
Figure 3.28: Enhanced zero bias conductance in the rim area of the pp island. The spectral curves were measured inside the box in the right inset, each curve displaying an average over pixels along a straight line running parallel to the short box side, the succession of lines starting on the inner Co island area, progressing through the rim, eventually ending up on the Cu surface. The curves are shifted vertically for clarity. Labels (A)–(D) mark characteristic features: (A) onset of the Cu surface state, (B) sharp d_{z^2} peak of the Co islands which is strongly attenuated in the rim area, (C) zero bias peak existing exclusively in the rim area, (D) another peak observed on the Co island as well as in the rim area but not on Cu.

energy, however, we observe a striking enhancement of the differential conductance. In fact, the strongest conductance at zero bias is found in rim areas. This observation is illustrated in the insets of Fig. 3.28 at a bias voltage $U = -1.3$ mV. In order to study this effect more closely we have taken spectra inside the white box shown in the right inset of Fig. 3.28, with the box covering parts of the island, the rim itself, and the Cu surface. Each spectral curve of the series numbered 1...11 in Fig. 3.28 (shifted vertically for clarity) samples 4–6 pixels along a line drawn parallel to the short box edge, with consecutive equidistant lines progressing from the Co island (curve 1) through the rim area to the Cu substrate (curve 11). In the Figure we have labeled by capital letters (A–D) some features which are particularly characteristic for the different materials. So (A) is the steep onset of the Cu surface state, and (B) is the large d_{z^2}-like peak of the Co islands. Progressing from the Co island surface into the rim region feature (B) is strongly attenuated and eventually fades out (curves 1 through 6). The rim area is represented by curves 4–8, showing that it has an electronic structure which is distinct from both the Co and the Cu surface. Starting at curve 4 a new peak (C) emerges which becomes maximal in curves 6 and 7 and vanishes beyond curve 8. This peak

Figure 3.29: (a) Rim state in pp and ap islands, measurements taken at locations indicated in the inset.
(b) Asymmetry of islands and rims. At the Fermi level, the sign of the rim state is opposite to that of the island state.
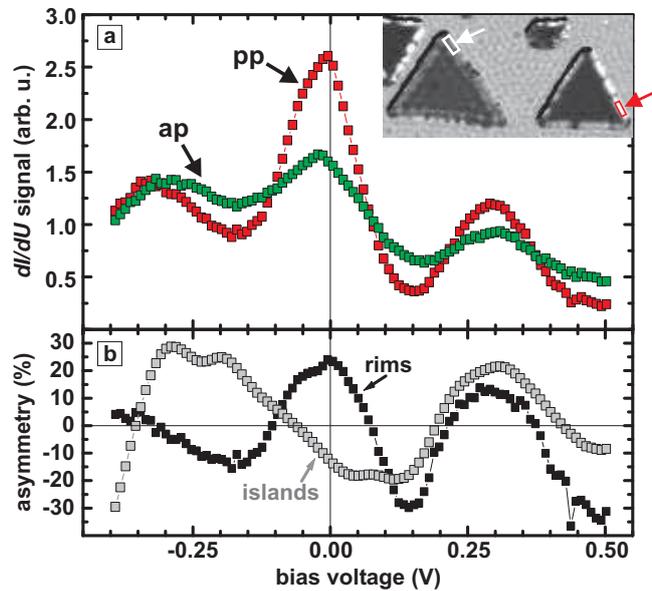
is energetically located right at the Fermi energy and is found neither in the inner Co island nor in Cu. It is the hallmark of the rim. Curves 9–11 clearly identify the Cu substrate surface. Peak (D) is observed on Co as well as in the rim area but is completely absent on Cu. This latter observation allows the conclusion to be drawn that the rim area mainly consists of Co and not of Cu. In this context it is noteworthy that the images also reveal some degree of inhomogeneity in the rim areas showing up as dark spots interrupting the bright lines, see e.g. the insets of Fig. 3.28. In the corresponding spectra we observe a strong intensity reduction or even a dip at the energetic position of the zero bias peak. A tentative explanation would be a locally varying degree of intermixing of Co and Cu atoms [37].

As is already obvious from inspecting the left inset of Fig. 3.28, not all islands show an equally bright rim at zero bias. In Fig. 3.29(a) we compare the rim spectrum of the pp island to a corresponding location of the ap island. The latter exhibits again a peak at the Fermi level but with considerably lower intensity. The asymmetry amounts to 24 percent, cf. Fig. 3.29(b). Thus, the rim state is clearly found to be spin-polarized. Remarkably, the spin contrast is *normal* for the rim while that of the islands is *inverted* at the same energy, the islands exhibiting an asymmetry of −13 percent. The left inset of Fig. 3.28 clearly shows that all dark islands (i.e. the pp ones) display the enhanced zero bias conductance in their rims, including islands of both stacking types. This observation suggests that the islands' electronic structure in this energy window is dominated by majority contributions whereas that of the rim, in contrast, is of minority character. The experimental observations are supported by *ab initio* electronic structure calculations of the Co island rim in comparison to an extended Co film [38]. The central result of the calculations is a LDOS peak structure found right at the Fermi energy for the rim atoms which is completely absent on the extended Co surface. The responsible state is of *d* character and has minority spin.

Orbitals with d_{z^2}, d_{xz}, d_{yz} symmetry provide almost equal weight; lower rim atoms exhibit a DOS roughly twice that of the top atoms. Contributions to the zero bias peak come exclusively from the rim atoms.

In conclusion, the spin polarization and also its sign in the Co islands may vary on a lateral scale of a few Ångstroms. Likewise, on the energy scale, a variation of a few meV may yield similar effects, highlighting the spatially- and spin-resolved electronic band structure as the source of the observed features.

References

[1] Y. Hasegawa and P. Avouris, Phys. Rev. Lett. **71**, 1071 (1993).

[2] M. F. Crommie, C. P. Lutz, and D. M. Eigler, Nature **363**, 524 (1993).

[3] J. Tersoff and D. R. Hamann, Phys. Rev. B **31**, 805 (1985).

[4] H. C. Manoharan, C. P. Lutz, and D. M. Eigler, Nature **403**, 512 (2000).

[5] J. Kliewer, R. Berndt, and S. Crampin, Phys. Rev. Lett. **85**, 4936 (2000).

[6] K. F. Braun and K.-H. Rieder, Phys. Rev. Lett. **88**, 096801 (2002).

[7] O. Sanchez, J. M. García, P. Segovia, J. Alvarez, A. L. V. de Parga, J. E. Ortega, M. Prietsch, and R. Miranda, Phys. Rev. B **52**, 7894 (1995).

[8] L. Bürgi, O. Jeandupeux, A. Hirstein, H. Brune, and K. Kern, Phys. Rev. Lett. **81**, 5370 (1998).

[9] J.-Y. Veullin, P. Mallet, L. Magaud, and S. Pons, J. Phys.: Condens. Matter **15**, S2547 (2003).

[10] J. Li, W. D. Schneider, R. Berndt, and S. Crampin, Phys. Rev. Lett. **80**, 3332 (1998).

[11] I. Barke and H. Hövel, Phys. Rev. Lett. **90**, 166801 (2003).

[12] J. Y. Park, U. D. Ham, S.-J. Kahng, Y. Kuk, K. Miyake, K. Hata, and H. Shigekawa, Phys. Rev. B **62**, 16341 (2000).

[13] T. Suzuki, Y. Hasegawa, Z.-Q. Li, K. Ohno, Y. Kawazoe, and T. Sakurai, Phys. Rev. B **64**, 081403 (2001).

[14] Y. Hasegawa, T. Suzuki, M. Ono, E. Ishikawa, A. Kamoshida, N. Matsuura, and T. Eguchi, Nanotechnology **12**, 710 (2002).

[15] S. Pons, P. Mallet, and J.-Y. Veuillen, Phys. Rev. B **64**, 193408 (2001).

[16] L. Diekhöner, M. Schneider, A. Baranov, V. Stepanyuk, P. Bruno, and K. Kern, Phys. Rev. Lett. **90**, 236801 (2003).

[17] K. von Bergmann, M. Bode, A. Kubetzka, M. Heide, S. Blügel, and R. Wiesendanger, Phys. Rev. Lett. **92**, 46801 (2004).

[18] O. Pietzsch, A. Kubetzka, M. Bode, and R. Wiesendanger, Phys. Rev. Lett. **92**, 057202 (2004).

[19] M. T. Kief and W. F. Egelhoff, Jr., Phys. Rev. B **47**, 10785 (1993).

[20] A. Rabe, N. Memmel, A. Steltenpohl, and T. Fauster, Phys. Rev. Lett. **73**, 2728 (1994).

[21] Even under these conditions we observe, especially at the substrate step edges, a certain degree of intermixing and an etching of vacancy islands as earlier described in Ref. [39]. These processes seem inevitably connected with room temperature growth. The coverage determination from STM images was made on atomically flat terraces neglecting the growth mode being different at step edges.

[22] Depending on the coating thickness, a Cr film at the tip may provide sensitivity to the out-of-plane or the in-plane component of the sample magnetization. For the purpose of tip characterization the well known stripe system of 1.5 ML Fe/W(110) was used as a reference [40]. It is then easy to distinguish between either domain or domain wall contrast, that is, perpendicular or in-plane sensitivity, respectively. This procedure was carried out immediately *before* and *after* the measurements presented in this paper, both times unambiguously revealing out-of-plane sensitivity.

[23] C. Rau and S. Eichner, Phys. Rev. Lett. **47**, 939 (1981).

[24] R. Wiesendanger, M. Bode, and M. Getzlaff, Appl. Phys. Lett. **75**, 124 (1999).

[25] While there is no net magnetization of the antiferromagnetic tip material, the spin of the outermost tip atom, carrying the tunneling current almost exclusively, will be uncompensated and therefore this atom will exhibit a distinct orientation of its magnetization vector.

[26] J. E. Griffith and G. P. Kochanski, Ann. Rev. Mater. Sci. **20**, 219 (1990).

[27] R. J. Hamers, Ann. Rev. Chem. **40**, 531 (1989).

[28] L. Petersen, P. Laitenberger, E. Lægsgaard, and F. Besenbacher, Phys. Rev. B **58**, 7361 (1998).

[29] In larger islands where the confinement length L_1 exceeds the ground state wave length the starting number of dots within a row may be 3 (see. e.g., Fig. 3.25) or more.

[30] E. J. Heller, M. F. Crommie, C. P. Lutz, and D. M. Eigler, Nature **369**, 464 (1994).

[31] J. Li, W.-D. Schneider, R. Berndt, and B. Delley, Phys. Rev. Lett. **80**, 2893 (1998).

[32] V. Madhavan, W. Chen, T. Jamneala, M. F. Crommie, and N. S. Wingren, Science **280**, 567 (1998).

[33] N. Knorr, M. A. Schneider, L. Diekhöner, P. Wahl, and K. Kern, Phys. Rev. Lett. **88**, 096804 (2002).

[34] J. Kondo, Prog. Theor. Phys. **32**, 37 (1964).

[35] U. Fano, Phys. Rev. **124**, 1866 (1961).

[36] Note that the two small peaks observed very close to the Fermi energy are caused by tip states; these features are present in any local spectrum on this sample, on Cu as well on Co, and must not be misinterpreted as arising from the particular location investigated here.

[37] The zero bias dI/dU-maps also show a variation in brightness of differently oriented island rims; these are most likely caused by an asymmetry of the tip geometry.

[38] O. Pietzsch, S. Okatov, A. Kubetzka, M. Bode, S. Heinze, A. Lichtenstein, and R. Wiesendanger, Phys. Rev. Lett. **96**, 237203 (2006).

[39] S. Speller, S. Degroote, J. Dekoster, G. Langouche, J. E. Ortega, and A. Närmann, Surf. Sci. **405**, L542 (1998).

[40] A. Kubetzka, M. Bode, O. Pietzsch, and R. Wiesendanger, Phys. Rev. Lett. **88**, 057201 (2002).

3.2.7 Spin-polarized STM in field emission mode

A. Kubetzka, M. Bode, and R. Wiesendanger

Introduction

Image-potential states, or more precisely image-potential-induced surface states, are two-dimensional model states for the understanding of electron interactions at metal surfaces. These states have a parabolic dispersion laterally, with effective masses close to the free electron mass. Vertically they are confined to a region above the surface by the reflective properties of the crystal and the collective response of the electron system resulting in an attractive image charge. Although studied for decades by theorists and with various experimental techniques, image-states have attracted renewed interest very recently, the two foci being dynamics and magnetism.

Whereas laterally averaging techniques like inverse photoemission (IPE) and two-photon photoemission (2PPE) have evolved into spin-polarized versions and therefore allow to access, e.g., spin-dependent binding energies and lifetimes on ferromagnetic surfaces [1, 2], scanning tunneling spectroscopy (STS) was only very recently used to access dynamic properties of these states on Cu(001) [3]. In particular, the energy- and k-dependent lifetime was extracted from the decay of electron wave patterns at step edges, and the influence of the tip-induced Stark-shift was determined. Spin-polarized (SP) STS applied to image states on ferromagnetic surfaces is an important experimental advancement allowing access to their spin-dependent local properties and to extend the technique of SP-STM to the high bias regime [4].

Experimental details and spin-averaged measurements

The experiments reported here have been performed with a home-built scanning tunneling microscope (STM) at $T = 13 \pm 1\,\mathrm{K}$, mounted in a multi-chamber system with a base pressure of $p < 1 \cdot 10^{-10}\,\mathrm{mbar}$. To achieve spin sensitivity tungsten tips were flashed *in situ* to $2300\,\mathrm{K}$, coated with Cr or Fe at room temperature, and subsequently annealed at $550\,\mathrm{K}$ for $4\,\mathrm{min}$. Tunneling spectra were taken at constant tunnel current with the feedback circuit switched on: while the bias voltage was ramped with a small modulation voltage added, the distance z was measured directly whereas the differential conductance dI/dU was obtained by a lock-in amplifier. The samples were prepared by evaporating Fe onto the clean W(110) crystal at room temperature, followed by moderate annealing which produces three-dimensional (3D) iron islands with (110) surfaces. Such Fe(110) islands are particularly suited as a sample since the magnetic domain structure has been characterized by SP-STM [5]. In addition, reference data of the magnetic splitting of the first image state of Fe(110) is available from IPE and 2PPE measurements, i.e. $57\pm5\,\mathrm{meV}$ [1] and $85\pm20\,\mathrm{meV}$ [6], respectively.
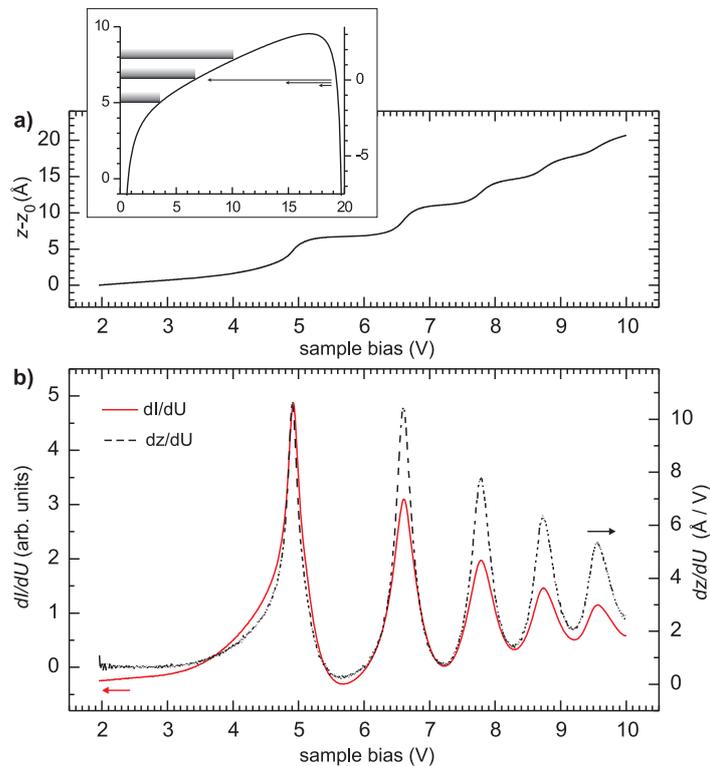
Figure 3.30: Spin-averaged data from an Fe island on W(110) (a) $z(U)$ characteristics at constant current ($I = 0.5\,\mathrm{nA}$), inset shows schematics of the tunnel barrier. (b) simultaneously acquired dI/dU spectroscopy ($U_{\mathrm{mod}} = 8\,\mathrm{mV}$) and derivative of data from (a) for comparison.

First we show spin-averaged data to introduce the measurement technique. In contrast to low bias spectroscopy where the current is recorded at constant tip-sample separation, the detection of image states is typically performed at constant current, in order to access a large energy range and to keep the electric field in the tunnel gap roughly constant. The image states then give rise to a series of steps in the $z(U)$ curve, as can be seen in the data in Fig. 3.30(a), taken above an Fe island on W(110). The inset in Fig. 3.30(a) schematically illustrates the onset of tunneling into the $n = 2$ state band and the fast decay of tunnel probability in a triangular shaped barrier, which restricts the contributing tunneling electrons to a narrow region below the Fermi level of the tip. Fig. 3.30(b) shows that the energetic positions of maximum slope in $z(U)$ coincide with maxima in dI/dU, within an error of $\pm 1\,\mathrm{meV}$, whereas the peak shapes and relative peak heights can be slightly different. This series of image states can be understood as hydrogen-like levels which exist in the sample's image potential being disturbed by the presence of the local tip potential. Energetic positions depend on the tip's work function and the chosen current set point: higher currents shift all levels to higher energies. Since these states would exist in the local tip potential even without the contribution from image charges, they are also called field emission resonances.

The observed line widths are always much broader than expected from the combined effects of electron life time, bias modulation amplitude, and measurement temperature (see e.g. Ref. [3]). Only very recently a first attempt has been undertaken to develop a qualitative understanding of the broadening mechanisms [7].

Spin-polarized measurements

To access the spin-dependent properties of image states and to elucidate whether they can be employed for magnetic domain imaging we have investigated Fe islands containing a magnetic vortex with in-plane magnetized tips. In the vortex core region areas of parallel and antiparallel orientation with respect to the tip magnetization can be compared. We have focused on the $n = 1$ state, preparing half a dozen tips and samples. Fig. 3.31 shows the (averaged) $z(U)$ data with the highest magnetic contrast we achieved in this series. The magnetic level splitting leads to distinct signals in the projected difference curves, about 20 pm in height and 25 meV in energy. The insets show the simultaneously acquired $dI/dU(U)$ spectra, and a map of the dI/dU signal at the vortex core region taken at $U = 4.96$ V from the full spectroscopic data set. Assuming a spin-polarization of the tip of roughly 40%, the value of 25 meV is in accordance with other experiments [1,6]. It is, however, not straightforward to deduce the precise intrinsic magnetic splitting from such data, even if the spin-polarization of the tip were known, because a quantitative theory of spectroscopic measurements in
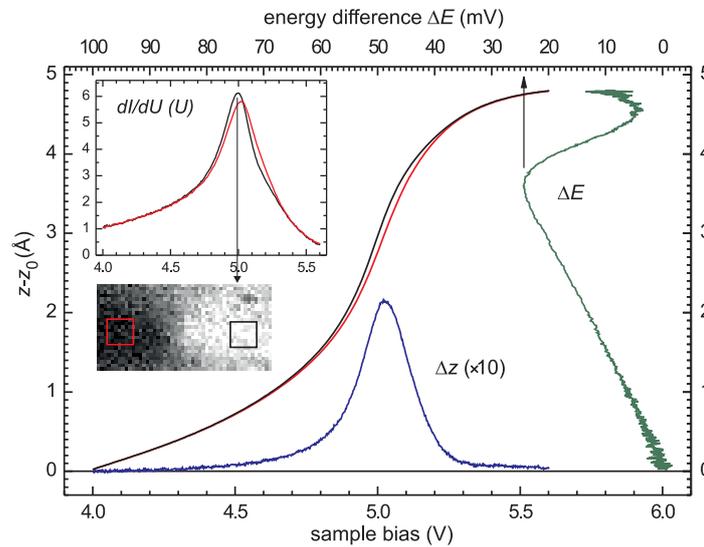
Figure 3.31: Averaged $z(U)$ curves of the $n = 1$ image-potential state on Fe/W(110), measured with a Cr coated W tip above antiparallel magnetized surface areas, as indicated in the inset. The spin-splitting of the state leads to distinct signals in the projected difference curves. Upper left inset: simultaneously recorded $dI/dU(U)$. Lower left inset: dI/dU at $U = 4.96$ V in a $20{\times}40$ nm^2 area around a magnetic vortex core. ($I = 4$ nA, $U_{\mathrm{mod}} = 3$ mV)

field emission mode is not available.
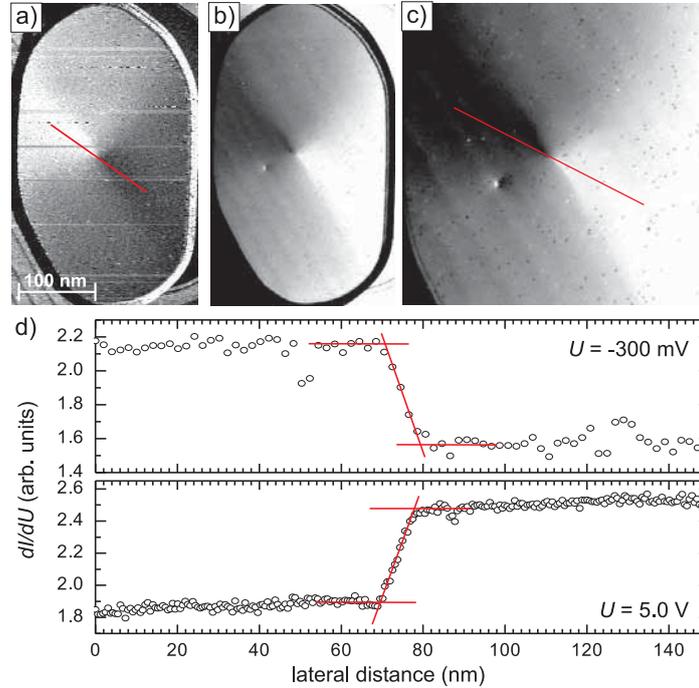
Figure 3.32: Under certain conditions the image quality can be improved by working at higher voltages and larger tip-sample distances. (a) dI/dU map at $U = -300$ mV. (b) and (c) dI/dU maps recorded subsequently at $U = 5.0$ V (falling edge of the $n = 1$ peak). (d) dI/dU line sections as indicated in (a) and (c). All images were recorded at $I = 1$ nA and with $U_{\mathrm{mod}} = 10$ mV.

The same value of $\Delta E = 25$ meV is observed in the $dI/dU(U)$ spectra. In this respect the dI/dU curves can be considered as redundant data; all information is in principle contained within $z(U)$. For magnetic domain imaging, however, a full spectroscopic curve is not needed. Instead, dI/dU maps at specific bias voltages allow fast and high resolution imaging and a partial separation of structural and magnetic information by leveling topographic features. The $dI/dU(U)$ spectra reveal that the highest magnetic contrast is not necessarily achieved at the peak positions. Significant contrast is found in a region of about 0.5 V in width and contrast inversion can be expected at 5.03 V for this tip and $I = 4$ nA. An example of this alternative magnetic imaging mode is given in Fig. 3.32 which compares low and high bias data. In Fig. 3.32(a), taken at $U = -300$ mV, an Fe island of size 400×230 nm^2 and an average height of 8 nm can be seen. The dI/dU map displays the typical Landau-type pattern with the vortex core in the middle of the island. The noise in this example is probably related to an electronically and magnetically unstable tip, since some scan lines display magnetic contrast inversion. Interestingly, the image quality could be improved by increasing the voltage to 5.0 V, leaving all other parameters unchanged

(Fig. 3.32(b)). For this tip $5.0\,\mathrm{V}$ is at the falling edge of the $n = 1$ peak in dI/dU and the tip is roughly $7\pm1\,\text{\AA}$ further away from the surface than at low bias. In the zoom-in in Fig. 3.32(c) a larger defect and a distribution of atomic scale point defects can be seen. A comparison of line sections across the vortex core in Fig. 3.32(d) reveals that the observed magnetic transition width is in both cases $8 \pm 1\,\mathrm{nm}$, which is also in agreement with previous results [5]. This example shows that the larger tip-sample distance does not lead to a significant loss of lateral magnetic resolution. It will be interesting to determine the resolution limit as a function of tip-sample distance and applied voltage for even sharper magnetic structures like, e.g., atomic scale domain walls.

This kind of spin-polarized field emission mode is not restricted to the first state. Fig. 3.33 shows data recorded in the same way as in Fig. 3.31. A small but distinct magnetic level splitting is observed in the spectroscopic data even for the higher states. The fast decay of spin-splitting with increasing state number n is absent. Theoretically, in the case of a pure image potential, ΔE_n is expected to scale with $1/n^3$ [8]. For this reason experiments have focused on the first state and only in rare cases ΔE_2 could be determined, e.g. by 2PPE on Fe/Cu(001) [2]. The $1/n^3$ decay is, however, related to the potential asymptotically developing zero slope and the accompanied clustering of states below the vacuum level. With the additional tip potential present the energy levels expand and so does the magnetic splitting [9]. We therefore expect that it can be tuned to higher values by using higher tunnel currents and that magnetic imaging can be performed at even larger tip-surface distances than shown here.

In conclusion we have shown that the spin-splitting of Stark-shifted image states can be accessed by spin-polarized scanning tunneling spectroscopy and that they offer the possibility of high resolution imaging of magnetic nanostructures at relatively large tip-sample distances. The technique might further lead to a better understanding of the spin dependence of these states, e.g. by accessing their spin-dependent life times
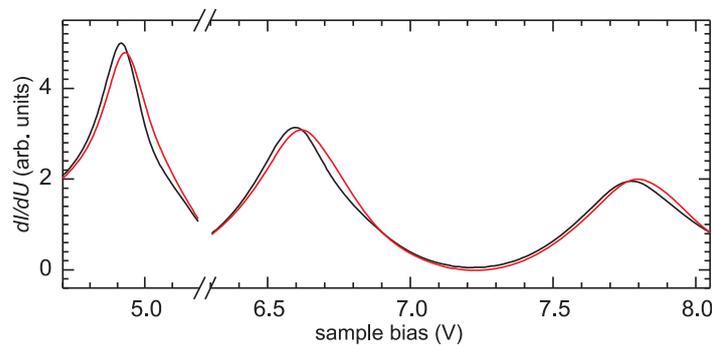
Figure 3.33: dI/dU spectra recorded with an Fe coated W tip above antiparallel magnetized areas like in Fig. 3.31 ($I = 0.5\,\mathrm{nA}$, $U_{\mathrm{mod}} = 8\,\mathrm{mV}$), exemplifying that also the higher states show a small but distinct magnetic splitting.

or by modifying their properties by tuning the confining potential.

References

[1] F. Passek, M. Donath, K. Ertl, and V. Dose, Phys. Rev. Lett. **75**, 2746 (1995).

[2] A. B. Schmidt, M. Pickel, M. Wiemhöfer, M. Donath, and M. Weinelt, Phys. Rev. Lett. **95**, 107402 (2005).

[3] P. Wahl, M. A. Schneider, L. Diekhöner, R. Vogelsang, and K. Kern, Phys. Rev. Lett. **91**, 106802 (2003).

[4] A. Kubetzka, M. Bode, R.Wiesendanger, Appl. Phys. Lett. **91**, 12508 (2007).

[5] A. Wachowiak, J. Wiebe, M. Bode, O. Pietzsch, M. Morgenstern, and R. Wiesendanger, Science **298**, 577 (2002).

[6] U. Thomann, C. Reuß, T. Fauster, F. Passek, and M. Donath, Phys. Rev. B **61**, 16163 (2000).

[7] J. I. Pascual, C. Corriol, G. Ceballos, I. Aldazabal, H.-P. Rust, K. Horn, J. M. Pitarke, P. M. Echenique, and A. Arnau, Phys. Rev. B **75**, 165326 (2007).

[8] M. Nekovee, S. Crampin, and J. E. Inglesfield, Phys. Rev. Lett. **70**, 3099 (1993).

[9] A. Hanuschkin, D. Wortmann, and S. Blügel, Phys. Rev. B **76**, 165417 (2007).

3.2.8 SP-STM through an adsorbate layer: Sulfur-covered Fe/W(110)

L. Berbil-Bautista, S. Krause, T. Hänke, M. Bode, and R. Wiesendanger,
[Surf. Sci. **600**, L20 (2006)]

Spin–polarized scanning tunneling microscopy and spectroscopy (SP-STM/STS) is an established and powerful technique for studying the magnetic properties of surfaces down to the atomic scale. So far, however, it was successfully used only under ultra-high vacuum (UHV) conditions because SP-STM requires clean and electronically homogeneous sample surfaces and well–defined magnetic thin film tips which are destroyed when exposed to ambient conditions, mainly due to oxidation. Extending this technique to operation under ambient condition would be of great relevance, allowing the study of industrial magnetic-nanostructure–based devices. One possibility to make surfaces inert against oxidation is passivation. There are several examples of metallic surfaces such as Mo(001) or Re(0001) which have been imaged with non–spin-resolved STM under ambient conditions upon passivation of the surface with a single layer of adsorbed sulfur. Beside the obvious advantages there is also a fundamental interest in spin-polarized STM experiments through adsorbate layers since they allow the investigation of spin transport properties under well–defined surface conditions.

Obviously, the ideal test sample for spin transport studies through adsorption layers should exhibit a magnetic domain structure that does not critically depend on the surface anisotropy but is instead determined by bulk properties. In the past we have studied the spin structures of numerous iron nanostructures grown on W(110) with SP-STM. Most of them, such as Fe double-layer nanowires or islands on W(110), are very sensitive to surface impurities [1]. One exception are three–dimensional Fe(110) islands on W(110). At suitable dimensions they exhibit a magnetic vortex structure which has recently been observed by SP-STM [2,3]. Micromagnetic calculations showed that even the surface spin structure of these islands is governed by bulk properties [2], making them preferable for spin-transport studies through a single molecular layer adsorbed on a magnetic surface.

Three–dimensional Fe islands were prepared by means of self-organized growth of 8–10 ML Fe on W(110) at RT and subsequent annealing at (800 ± 100) K for 10 min. This results in elongated Fe islands with lateral dimensions of about (350 ± 150) nm $\times (200 \pm 50)$ nm along the [001] and the [$1\bar{1}0$] direction, respectively, and an average height of 8–9 nm. H_2S (99.5% purity) was dosed by a leak valve at $p = 5.0 \times 10^{-8}$ mbar onto the sample held at RT.

Figure 3.34(a) shows the topography (top panel) and a line section (bottom) of a typical three-dimensional iron island. As can be seen in Fig. 3.34(b) the magnetic dI/dU map exhibits the characteristic pattern of a magnetic vortex [2].

Upon H_2S dosing (> 40 L) onto the Fe(110) surface, a characteristic c(3×1) reconstruction appears [4–7].

As mentioned above the vortex structure of Fe(110) islands is determined by bulk

properties. Therefore, the spin structure should not change upon sulfur adsorption. Indeed, the magnetic dI/dU map of the covered islands (Fig. 3.35) qualitatively shows the same vortex structure as the clean islands. Due to the different spin-averaged electronic properties, the structural domain walls appear as dark lines in the dI/dU map of Fig. 3.35(b). The adsorbed S certainly causes spin-flip scattering which leads to a decreasing contrast. However, there remains a finite spin polarization of the tunneling current which allows magnetic imaging through the S layer.

In order to study the reactivity of S–covered Fe(110), thick iron films were saturated with sulfur, and subsequently dosed with increasing amounts of O_2. We had to realize that the surface seriously degrades at O_2–dosings higher than 360 L. In this case, STM reveals an increased surface roughness (not shown). At high O_2 exposure the surface partially becomes non-conductive. As found by AES, exposition of the thick films to air completely removes the sulfur layer, and results in a high oxygen and carbon contamination.

In summary, we have shown that it is possible to observe magnetic domains by SP-STM through a S layer. Even though we found that sulfur does not passivate Fe(110), this may be a pathway to extend SP-STM to operation under ambient conditions.
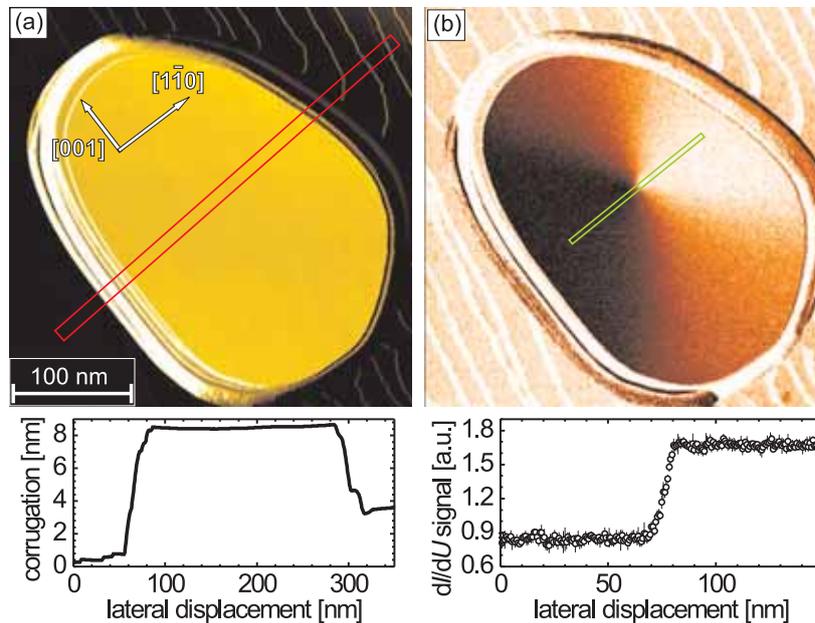
Figure 3.34: **(a)** Topography (top panel) and line scan (bottom) of a $\simeq 8$ nm high clean Fe(110) island at $T = 34$ K. **(b)** The magnetically sensitive dI/dU map (top) shows the characteristic pattern of a magnetic vortex. The line scan across the vortex core reveals that its diameter amounts to ≈ 10 nm. Measurement parameters: $I = 25$ nA, $U = -500$ mV.
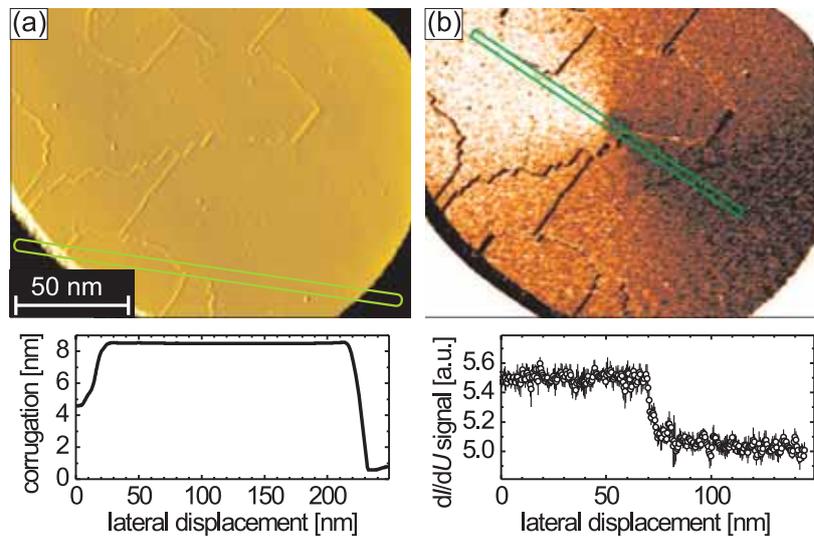
Figure 3.35: **(a)** Topography (top panel) and line section (bottom) of a Fe(110) island after 50 L H$_2$S dosing. Numerous structural domain boundaries with straight sections mainly along the [1$\bar{1}$0] direction appear. **(b)** Magnetic dI/dU map (top) of the island's vortex configuration imaged through the S layer. Due to their different spin-averaged electronic properties structural domain walls are visible as dark lines. The measured vortex core diameter [$d = (10 \pm 2)$ nm] is identical to clean islands. Measurement parameters: $I = 20$ nA , $U = -400$ mV.

References

[1] H. J. Elmers, J. Hauschild, and U. Gradmann, Phys. Rev. B **59**, 3688 (1999).

[2] A. Wachowiak, J. Wiebe, M. Bode, O. Pietzsch, M. Morgenstern, and R. Wiesendanger, Science **298**, 577 (2002).

[3] M. Bode, A. Wachowiak, J. Wiebe, A. Kubetzka, M. Morgenstern, and R.Wiesendanger, Appl. Phys. Lett. **84**, 948 (2004).

[4] S. R. Kelemen and A. Kaldor, J. Climate Meteor. **75**, 1530 (1981).

[5] A. J. Pignocco and G. E. Pellissier, Surf. Sci. **7**, 261 (1967).

[6] F. Portele, Z. Naturforschung **24a**, 1268 (1969).

[7] A. G. Naumovets and A. G. Fedorus, Sov. Phys. JETP **41**, 587 (1976).

3.2.9   Current-induced magnetization switching by SP-STM

S. Krause, L. Berbil-Bautista, G. Herzog, M. Bode, and R. Wiesendanger,
[Science **317**, 1430 (2007)]

The increase of hard disk and memory capacities is a result of continuously decreasing bit sizes. For example, the area of one bit in today's magnetic hard disks is on the order of $(60 \text{ nm})^2$. Two distinct effects are used to read and write information: The giant magnetoresistive effect is used for reading, whereas writing is done by a magnetic field. When exceeding a certain limit of bit density, however, switching the magnetization of one bit may also affect the magnetization of nearby bits because of the non-local character of magnetic fields, thereby accidentally destroying stored information. One solution may be the substitution of magnetic switching fields by a spin-polarized current locally exerting a magnetic torque that leads to the reversal of magnetization at sufficient current density, as has been proposed theoretically [1, 2] and demonstrated experimentally based on lithographically fabricated nanopillar devices [3–7]. This technique is expected to strongly reduce the circuit complexity and enable a further miniaturization of data storage devices, because the same electrical line to address a bit could be used to read information at low currents (by measuring the magnetoresistance) and write information at high currents (by the spin-torque effect).

Spin-polarized scanning tunneling micocopy (SP-STM) is a powerful tool used to determine the magnetization state of nanostructures with spatial resolution down to the atomic scale. In addition, the same SP-STM tip that reads out the magnetization information at low tunneling currents may also serve as a highly localized source or drain of spin-polarized electrons at high tunneling currents, thereby locally exerting a magnetic torque that can reverse the magnetization of an individual monodomain nanoparticle.

Figure 3.36(a) shows the topography of a 0.14 AL Fe/W(110) sample with monolayer islands of typical diameters between 2 and 6 nm. It is known that these islands are ferromagnetic with an in-plane easy axis along the $[1\bar{1}0]$ direction [8, 9]. Due to their small sizes they are monodomain particles. While the Curie temperature of the extended monolayer is about 220 K [10] we find that the blocking temperature of the nanoislands is below 40 K (not shown here). This is evidenced by the magnetic $\mathrm{d}I/\mathrm{d}U$ image of Fig. 3.36(b) which was taken at $T = 56.0$ K. A high (bright) or low (dark) $\mathrm{d}I/\mathrm{d}U$ signal represents islands with a magnetization oriented parallel or antiparallel with respect to the magnetization of the atom at the tip apex. Obviously, the magnetization of the islands is unstable. For instance, the spin-resolved $\mathrm{d}I/\mathrm{d}U$ signal of the island shown in the inset of Fig. 3.36(b) frequently switches between subsequent scan lines. As we know from earlier investigations on similar sample systems [11, 12] such observations are characteristic for superparamagnetic switching where the magnetization spontaneously reverses due to thermal activation.

We have recorded the magnetic $\mathrm{d}I/\mathrm{d}U$ signal as a function of time with the tip
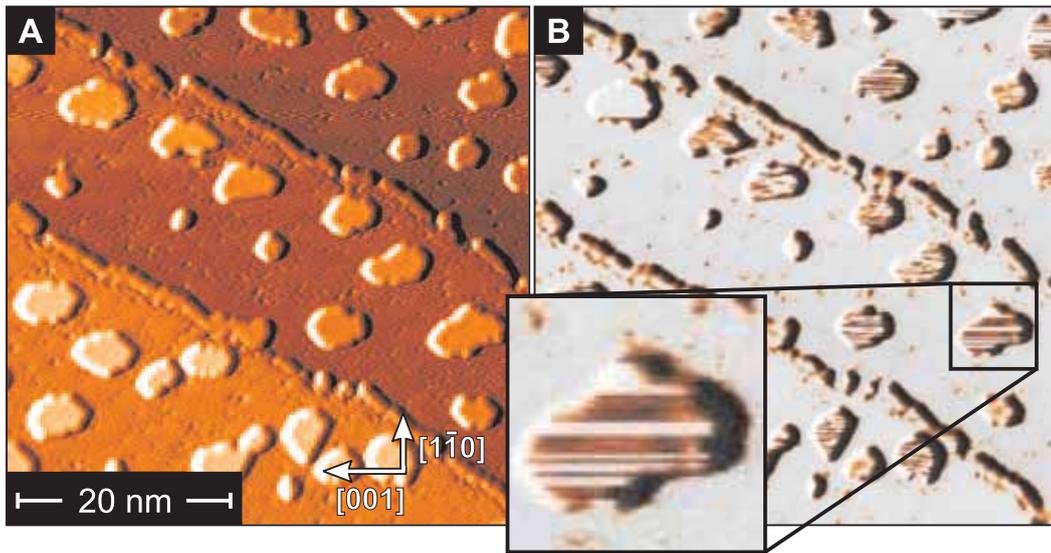
Figure 3.36: (a) Topography and (b) in-plane magnetic dI/dU map of Fe monolayer islands on W(110) measured at $T = 56.0\,\mathrm{K}$ (parameters: $I = 2\,\mathrm{nA}$, $U = -200\,\mathrm{mV}$). A dark or bright signal on the islands represents a magnetization direction parallel or antiparallel to the tip magnetization, respectively. Stripes appear on small islands (for example in the inset) because they switch their magnetization state frequently.

positioned stationary above the central region of small Fe nanoislands with a typical surface area of $7\,\mathrm{nm}^2$, i.e. consisting of about 100 atoms. All measurements have been performed in the constant-current mode obtaining different tunneling currents by adjusting the tip-sample distance. For example, the traces in the panels of Fig. 3.37(a) show the first 5 s of the spin-resolved dI/dU signal measured on one particular island at tunneling currents $I = 2\,\mathrm{nA}$, $800\,\mathrm{nA}$, and $2000\,\mathrm{nA}$. Fig. 3.37(b) shows the histograms of the magnetic dI/dU signal recorded over a much longer period ($700\,\mathrm{s}$) normalized with respect to the state "1" level at the different tunneling currents. At a low tunneling current, the dI/dU signal statistically switches between two discrete levels, states "0" and "1" (top panel of Fig. 3.37(a)). The respective histogram of Fig. 3.37(b) reveals that both states occur with the same probability. This is as expected since the two magnetization states are energetically degenerate and therefore should be populated equally. As I is increased, however, an imbalance between states "0" and "1" builds up until one state clearly dominates as shown for $I = 2000\,\mathrm{nA}$. Obviously, spin-polarized tunneling currents lead to an energy splitting of the two otherwise degenerate states. Corresponding to experiments on planar junctions an opposite spin-polarization was observed for tunneling currents flowing in the opposite direction.

The microscopic processes leading to the asymmetries can be understood by a statistical analysis of the lifetimes of states "0" and "1", τ_0 and τ_1, as defined in the top panel of Fig. 3.37(a). Fig. 3.38(a) shows histograms of τ_0 and τ_1 of one particular Fe
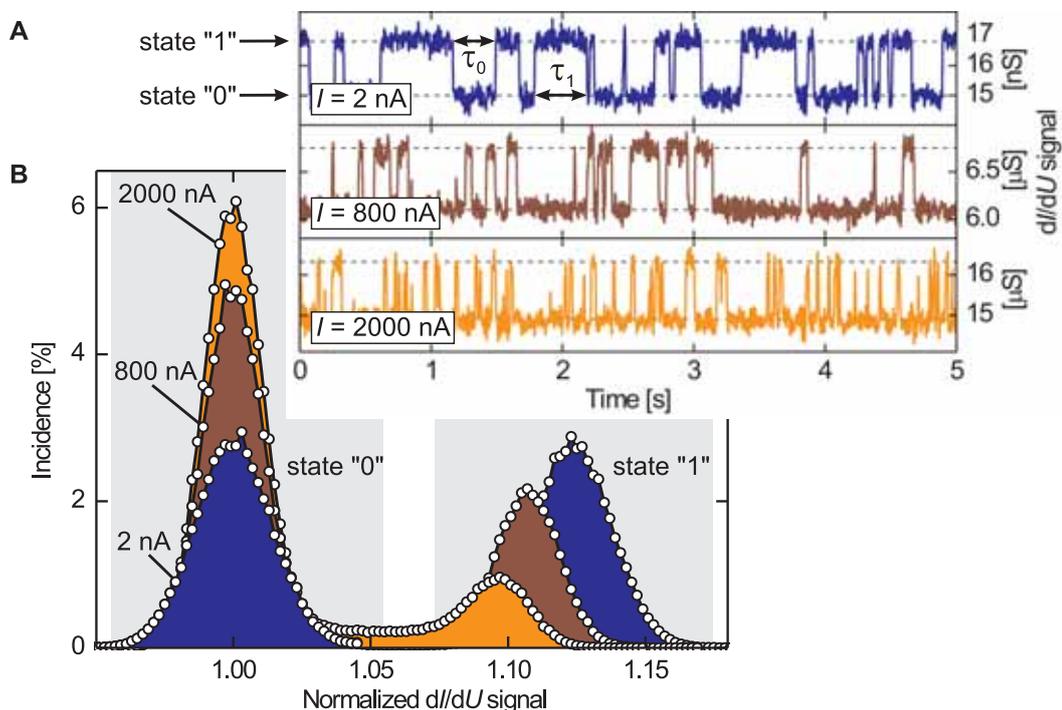
Figure 3.37: (a) Trace section of the time-dependent magnetic dI/dU signal of one particular nanoisland (area: 5.7 ± 0.4 nm^2) recorded with a Cr-coated probe tip at different tunneling currents I ($T = 48.4$ K, $U = -200$ mV). (b) Histogram of the overall magnetic dI/dU signal normalized with respect to the state "0" level at different tunneling currents. While state "1" and state 0 are equally populated at low currents a significant asymmetry towards state "0" can be recognized at high currents.

nanoisland measured at $I = 1$ nA (top panel) and $I = 800$ nA (bottom panel) with the same tip. Fitting with a decay law results in the respective mean lifetimes $\bar{\tau}_0$ and $\bar{\tau}_1$. At low tunneling current, $\bar{\tau}_0$ and $\bar{\tau}_1$ are very similar. A different behavior is observed at high tunneling currents, where the mean lifetime is found to depend strongly on the relative magnetization direction between the tip and sample. In this case, for $I = 800$ nA, one state has a much higher mean lifetime than the other. Fig. 3.38(b) shows a plot of the current dependence of the mean lifetimes $\bar{\tau}_0$ and $\bar{\tau}_1$. The trend from equal lifetimes at low current to an imbalance at high current can clearly be recognized. This lifting of the degeneracy of the effective activation barriers at high tunneling currents is caused by the spin torque of the spin-polarized current. Furthermore, the mean lifetime of both states has decreased, an effect which we attribute to Joule's heating due to the high tunneling current.

Using an SP-STM tip as the source/drain for spin-polarized electrons allows us to perform spatially resolved measurements where the tip is moved to different sites of one particular nanoisland. Thereby, information of site-specific properties can be

gained which cannot be obtained in spatially averaging experiments performed with nanopillars. Fig. 3.39(a) shows the topography of a Fe ML island consisting of about 100 atoms on W(110). While scanning this island we have measured the magnetic dI/dU signal on each of the pixels for a duration of $12\,s$ to calculate the site-specific histogram asymmetry a_H on the basis of the corresponding data-point histograms. The result is shown in a gray-scale-coded representation in Fig. 3.39(b). In spite of the rather large statistical error a gradient along the [001] direction can clearly be recognized. The effect can even be analyzed quantitatively by averaging a_H column- and row-wise, i.e. along the [1$\bar{1}$0] and the [001] direction, respectively. The resulting data are plotted in the panels below and at the right of Fig. 3.39(b). While $\bar{a}_H$ is constant within the error when moving the tip along the [1$\bar{1}$0] direction, it clearly reduces by about $16\,\%$ from the left to the right side of the island.
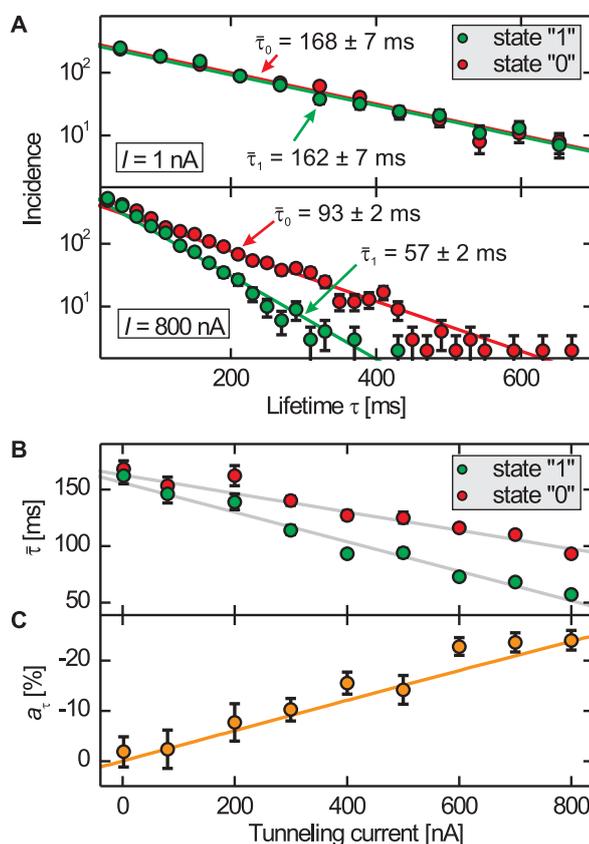
Figure 3.38: (a) Histograms of the lifetimes τ_1 and τ_0 of states "0" and "1" measured at $I = 1\,nA$ (upper panel) and $I = 800\,nA$ (lower panel) ($T = 50.6\,K$, $U = -200\,mV$; island area: $5.5 \pm 0.4\,nm^2$). A decay function was fitted to the experimental data (lines) resulting in the mean lifetime $\bar{\tau}$. Obviously, $\bar{\tau}_0$ and $\bar{\tau}_1$ become different at high tunneling currents. (b) Tunneling current dependence of the mean lifetimes $\bar{\tau}_{0,1}$ (gray lines are guides to the eye) and (c) of the mean lifetime asymmetry $a_{\bar{\tau}}$.
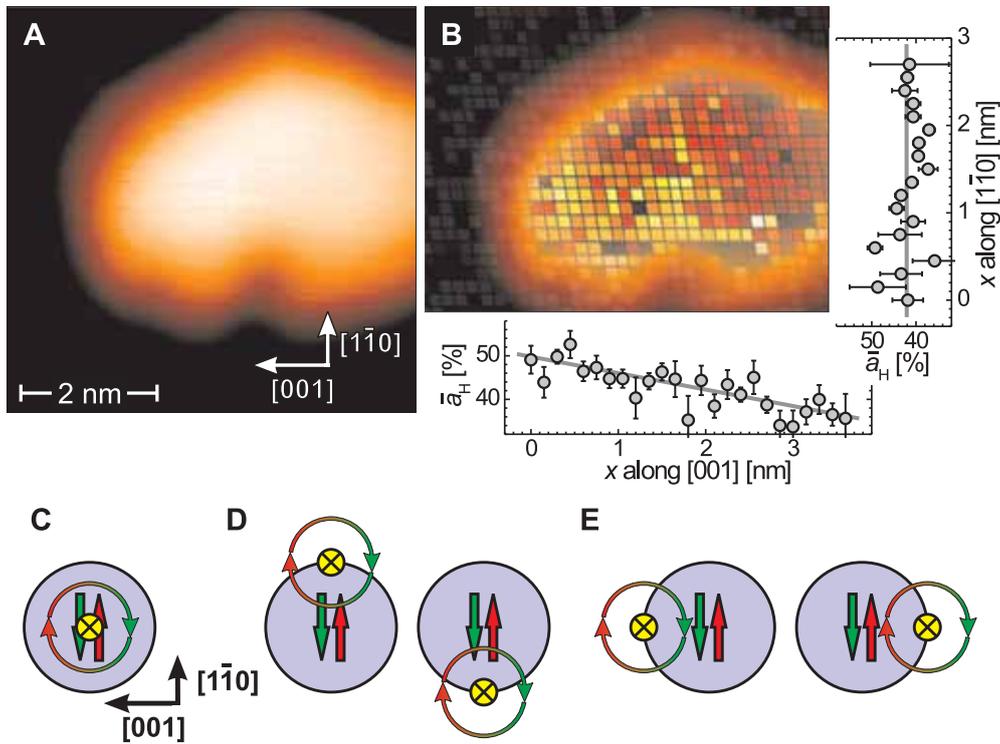
Figure 3.39: (a) Topography and (b) map of the current-induced asymmetry a_H as measured with a Cr-coated probe tip at $I = 600\,\text{nA}$ (island area: $6.7 \pm 0.6\,\text{nm}^2$, $T = 55.0\,\text{K}$). The plots show a_H averaged in rows and columns, i.e. along the $[1\bar{1}0]$ and $[001]$ direction, respectively. While $\bar{a}_H$ is constant within the error bar along the $[1\bar{1}0]$ direction, it clearly reduces by about 16 % from the left to the right side of the island (lines are guide to the eye only). The schematic drawings illustrating the influence of the Oersted field with the tip positioned (c) in the center, (d) at the magnetic poles, or (e) at the charge-free side of the nanoisland.

The influence of the tip position on the switching behavior of a sample with an uniaxial anisotropy is schematically represented in Fig. 3.39(c)-(e). If the tip is positioned above the island center the influence of the Oersted field along the $[1\bar{1}0]$ direction, which is the easy axis of the nanoisland, cancels [Fig. 3.39(c)]. In this case, pure spin-current induced switching occurs. Likewise, no influence by the Oersted field is expected if the tip is moved from the center to either island edge along the $[1\bar{1}0]$ direction [Fig. 3.39(d)] since the effective field acting on the island is oriented perpendicular to the easy axis. Only if the tip is moved from the center along the $[001]$ direction one magnetic state is favored over the other by the Oersted field [Fig. 3.39(e)]. In this case Oersted field effects influence the magnetic switching behavior, dependent on the tip position. A detailed analysis of the data yields that a mean energy splitting of $\Delta E = -2.4 \pm 0.2\,\text{meV}$ at the center of the island is increased or decreased by up to $0.7 \pm 0.2\,\text{meV}$ when moving along the $[001]$ direction to either island edge. This finding

indicates that the magnetization switching is dominated by the spin torque induced by the spin-polarized current, whereas the influence of the Oersted field remains small.

In conclusion, we have shown experimentally that it is possible to switch individual superparamagnetic nanoislands by the injection of a spin-polarized current with a SP-STM. Furthermore, our experiments allow to clearly separate three fundamental contributions involved in magnetization switching, i.e. current-induced spin torque, heating the island by the tunneling current, and Oersted field effects. These results provide new insight into the details of current-induced magnetization switching that has been inaccessible in experiments with lithographically fabricated tunnel junctions. The ultimate lateral resolution of SP-STM combined with CIMS promises new perspectives for future data storage technologies.

References

[1] J. C. Slonczewski, J. Magn. Mater. **159**, L1 (1996).

[2] L. Berger, Phys. Rev. B **54**, 9353 (1996).

[3] M. Tsoi *et al.*, Phys. Rev. Lett **80**, 4281 (1998).

[4] E. B. Myers, D. C. Ralph, J. A. Katine, R. N. Louie, R. A. Buhrmann, Science **285**, 867 (1999).

[5] J. Z. Sun, J. Magn. Magn. Mater. **202**, 157 (1999).

[6] J. A. Katine, F. J. Albert, R. A. Buhrman, E. B. Myers, D. C. Ralph, Phys. Rev. Lett. **84**, 3149 (2000).

[7] F. J. Albert, N. C. Emley, E. B. Myers, D. C. Ralph, R. A. Buhrman, Phys. Rev. Lett. **89**, 226802 (2002).

[8] U. Gradmann, G. Liu, H. J. Elmers, M. Przybylski, Hyperfine Interact. **57**, 1845 (1990).

[9] H. J. Elmers *et al.*, Phys. Rev. Lett. **73**, 898 (1994).

[10] H. J. Elmers *et al.*, Phys. Rev. Lett. **75**, 2031 (1995).

[11] M. Bode, O. Pietzsch, A. Kubetzka, R. Wiesendanger, Phys. Rev. Lett. **92**, 067201 (2004).

[12] M. Bode, A. Kubetzka, K. von Bergmann, O. Pietzsch, R. Wiesendanger, Microsc. Res. Tech. **66**, 117 (2005).

Preparation and electronic properties of clean W(110) surfaces

M. Bode, S. Krause, L. Berbil-Bautista, S. Heinze, and R. Wiesendanger,
[Surface Science **601**, 3308 (2007)]

Among the refractory metals which are very popular substrates for thin film growth because - in contrast to many noble metals - the problem of intermixing between film and substrate is strongly reduced, the densely-packed (110) surface of tungsten is most-widely used. In order to clean the dense-packed W(110) surface from its main impurity, carbon (C), a variety of processes have been proposed. Common to these cleaning procedures are cycles of prolonged annealing in an oxygen atmosphere and subsequent short high-temperature treatments, so-called flashes. During the annealing in oxygen, C is removed from the surface by the formation of CO and CO_2, which are both gaseous substances and can be pumped after thermal desorption. Simultaneously, however, the tungsten surface oxidizes. The resulting tungsten oxides can only be removed by thermal desorption at $T \geq 2300\,\mathrm{K}$.

While keeping the duration of annealing fixed at about $30\,\mathrm{min}$ we have experimentally studied the topography and electronic properties of W(110) surfaces in dependence of the oxygen pressure p_{ox} during annealing by means of scanning tunneling microscopy (STM) and spectroscopy (STS).

Figure 3.40 shows constant-current STM images of the W(110) surface obtained after several dozens of cleaning cycles consisting of oxygen annealing and a subsequent high temperature flash. In each case the initial oxygen partial pressure was $p_{\mathrm{ox}} = 2 \times 10^{-6}\,\mathrm{mbar}$. Between two successive annealing cycles p_{ox} was typically reduced by 30 to 50%. The cleaning process was stopped at different values of p_{ox} in the final cycle. Fig. 3.40(a) shows a W(110) surface which was heated in $p_{\mathrm{ox}} = 1 \times 10^{-6}\,\mathrm{mbar}$ in the final cycle. Numerous point-like depressions with an apparent depth of 0.1–0.3 Å and a typical diameter of 0.5–1 nm can be recognized. Analysis reveals that after annealing at $p_{\mathrm{ox}} = 1 \times 10^{-6}\,\mathrm{mbar}$ about 2% of the surface atoms are impurities, probably C. As the oxygen partial pressure during the final cycle is lowered, the number of depressions in the STM images reduces. For instance, the surfaces shown in Fig. 3.40(b) and (c) were prepared at final pressures of $p_{\mathrm{ox}} = 3 \times 10^{-7}\,\mathrm{mbar}$, and $p_{\mathrm{ox}} = 2 \times 10^{-8}\,\mathrm{mbar}$, respectively. The inset in Fig. 3.40(c) shows the best surface quality obtained at higher magnification. The density of impurity atoms amounts to 2×10^{-3} only. A further reduction of p_{ox} was not considered to be useful since it led to a significantly increase of the relative CO pressure in the residual gas of the UHV system.

The improved surface quality has significant consequences for the surface electronic properties as detected by STS. Fig. 3.41(a) and (b) shows the simultaneously measured topography and constant-current $\mathrm{d}I/\mathrm{d}U$ map of clean W(110), respectively. The $\mathrm{d}I/\mathrm{d}U$ map which was measured at a sample bias voltage $U = +100\,\mathrm{mV}$ reveals a pronounced wave pattern at step edges and around impurities which resemble earlier observations of surface state interference patterns on noble metal (111) surfaces [1]. We would like to emphasize that this pattern could not be observed on less perfect
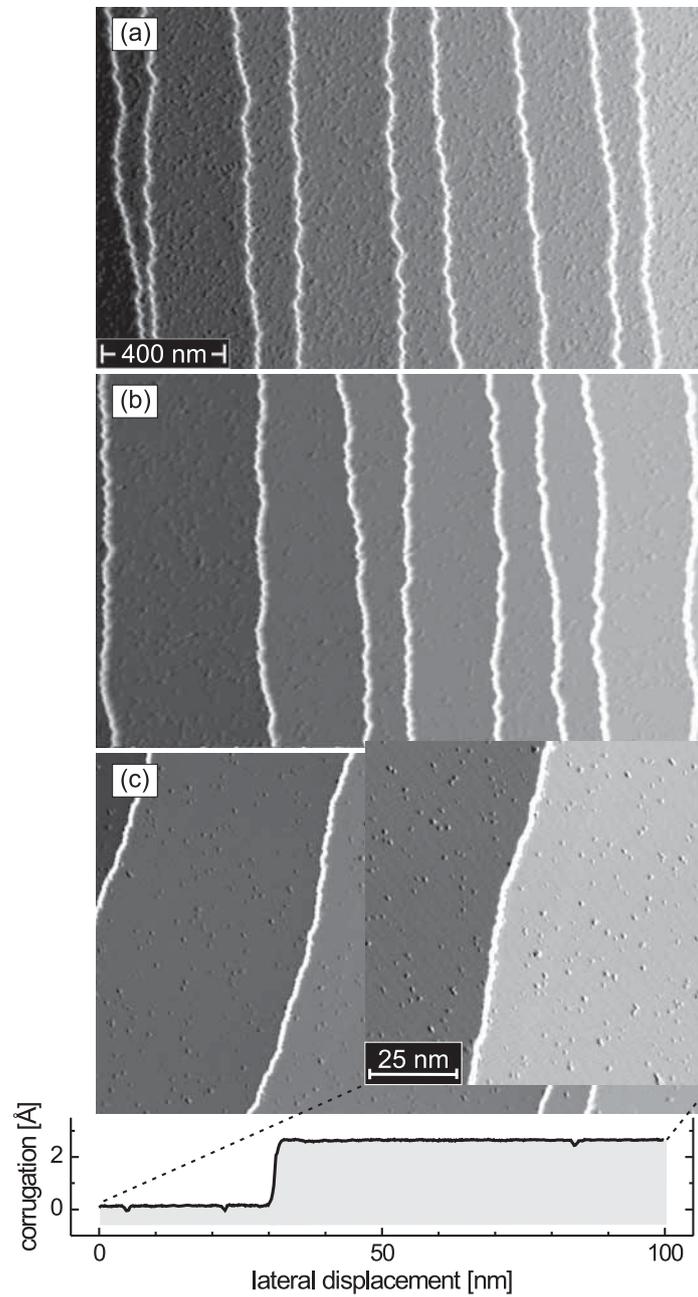
Figure 3.40: Constant-current images of W(110) surfaces after annealing cycles with a final oxygen partial pressure (a) $p_{\mathrm{ox}} = 1 \times 10^{-6}$ mbar, (b) $p_{\mathrm{ox}} = 3 \times 10^{-7}$ mbar, and (c) $p_{\mathrm{ox}} = 2 \times 10^{-8}$ mbar. The density of impurity atoms decreases significantly down to less than 2×10^{-3} in (c).
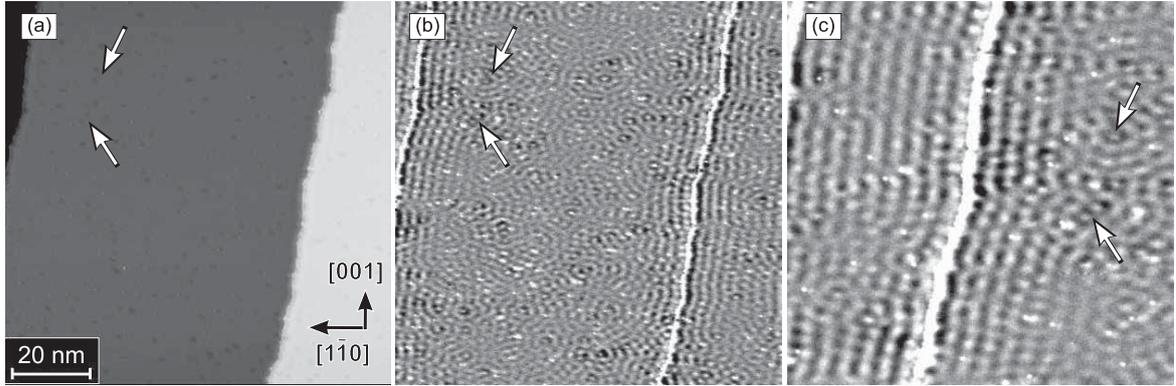
Figure 3.41: (a) Constant-current topographic image and (b) the simultaneously measured I/dU map of a clean W(110) surface ($I = 1\,\text{nA}$, $U = +100\,\text{mV}$). The dI/dU map of the region around the two arrows is shown at higher magnification in (c). While three atomically flat terraces separated by monatomic step edges can be recognized in the topography the dI/dU map reveals striking periodic variations, mainly along step edges and around remaining surface impurities.

surfaces such as those shown in Fig. 3.40(a) and (b). A higher resolution dI/dU map of the region around two impurities which are marked by arrows is shown in Fig. 3.41(c). Note, that the period of the interference pattern is slightly anisotropic with the longer real-space periodicity along the $[1\bar{1}0]$ direction.

In order to analyze the dispersion relation of the electronic states which might be responsible for the standing wave pattern observed in Fig. 3.41 we have performed STS measurements by measuring full dI/dU spectra at every pixel of an image. While both, the topography as well as the dI/dU signal, are featureless within the noise level at the set-point bias voltages of $-400\,\text{mV}$ and $+600\,\text{mV}$, striking oscillations were observed between $-300\,\text{mV}$ and $+250\,\text{mV}$.

The bias-dependent oscillation period was determined quantitatively by fitting dI/dU line sections taken perpendicular to the W step edges, i.e. approximately along the $[1\bar{1}0]$ direction, with an exponentially decaying sine function:

$$dI/dU(x) = dI/dU_0 + e^{-\frac{x}{D}} \cdot A \cdot \sin\left(\pi\frac{x - x_0}{\lambda}\right), \qquad (3.9)$$

where λ is the wavelength of the LDOS oscillations, x is the tip position, and D is the phase coherence length of the involved electronic states [2,3]. The resulting bias-dependence of λ is shown in Fig. 3.42(a). Obviously, the oscillation period becomes smaller with decreasing sample bias. From these data we can calculate the wave number $k = \pi/\lambda$ which is plotted in Fig. 3.42(b). By fitting the band with a parabolic function we obtain a band edge at $E_0 = 314 \pm 12\,\text{meV}$ and an effective electron mass $m_{\text{eff}} = 1.15 \pm 0.05\,m_e$, where m_e is the electron rest mass.

In order to interpret the observed spectroscopic features based on the electronic

structure of the W(110) surface, we start by comparing the calculated local density of states (LDOS) in the vacuum with the measured dI/dU spectra. Within the Tersoff-Hamann model [4] these quantities are directly comparable. Strikingly, there is an enhanced LDOS around the Fermi energy which displays a fine structure with several peaks. While such a structure appears in the experimental spectra as well, the positions of the peaks are slightly shifted. The agreement between experiment and theory is almost perfect if we assume a slight shift of the experimental Fermi energy by 200 meV with respect to the calculation.

We can attempt to relate the peaks in the LDOS to specific electronic states by taking a look at the band structure along the direction $\overline{S\Gamma N}$ in the 2D-BZ. From its high localization in the first few surface layers and in the vacuum we can identify a surface resonance starting at $\overline{\Gamma}$ with a downward band dispersion and an upper band edge at about 600 meV above the (theoretical) Fermi energy. The upper band edge
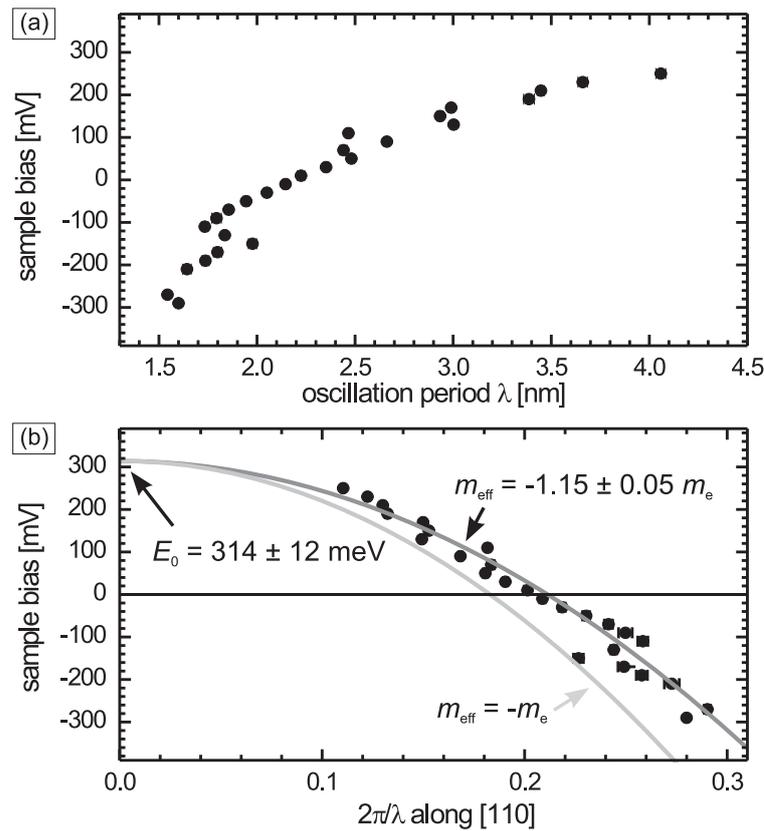
Figure 3.42: (a) Plot of the periodicity of the standing wave patterns and (b) the resulting dispersion ($b = (0.448 \times 10^{-9}\ \mathrm{m})^{-1}$ is the reciprocal periodicity of the crystal lattice along the [1$\bar{1}$0] direction). Fitting with a parabola (dark gray line) results in a band onset energy $E_0 = 314 \pm 12$ meV and an effective electron mass $m_{\mathrm{eff}} = -1.15 \pm 0.05\ m_{\mathrm{e}}$. The light gray line shows a band with $m_{\mathrm{eff}} = -m_{\mathrm{e}}$.

causes a peak in the vacuum LDOS. This surface resonance is of p_z-d_{xz} character. The upper band edge is located about 200-300 meV higher than the band edge determined by fitting the experimental dispersion. However, if we rigidly shift the entire band structure by 200 meV downwards there is a nearly perfect agreement of the surface resonance dispersion and the observed band. Such a shift has been motivated above from a comparison of the LDOS, and we find more evidence by comparing our calculations to the experimental band dispersions of surface states and resonances determined from photo-emission experiments [5]. The shift of 200 meV results in an excellent agreement of the band dispersions along the $\overline{\Gamma S}$-direction and of the Fermi surface. A discrepancy of the theoretical and experimental Fermi surface has been reported before [6]. The reason for these differences is presumably a lack of the LDA exchange-correlation potential to correctly describe the real self-energy [6].

In summary, we have shown that the oxygen partial pressure p_{ox} applied during the annealing cycles has a significant impact on the surface quality of W(110) surfaces. On the clean W(110) surface we find a pronounced wave pattern in differential conductance maps which is linked to a downwards dispersing electron band. Comparison with the W(110) band structure obtained by density functional theory (DFT) calculations reveals that a p_z-d_{xz}-like surface resonance is responsible for these observations.

References

[1] M.F. Crommie, C.P. Lutz, D.M. Eigler, Nature **363**, 524 (1993).

[2] Y. Hasegawa, P. Avouris, Phys. Rev. Lett. **71**, 1071 (1993).

[3] S. Crampin, J. Kröger, H. Jensen, R. Berndt, Phys. Rev. Lett. **95**, 029701 (2005).

[4] J. Tersoff, D.R. Hamann, Phys. Rev. B **31**, 805 (1985).

[5] E. Rotenberg, J.W. Chung, S.D. Kevan, Phys. Rev. Lett. **82**, 4066 (1999).

[6] B. Kohler, P. Ruggerone, M. Scheffler, Phys. Rev. B **56**, 13503 (1997).

3.2.10 Theoretical study of the magnetic ordering in nanostructures

Introduction

The rapid rise of the scientific research on ever-smaller magnets is to a great extent due to the appearance of new experimental techniques like spin resolved scanning tunnelling microscopy (SP-STM), magnetic force microscopy (MFM), atomic force microscopy (AFM) and exchange force microscopy (ExFM). All these extraordinary experimental tools are available in Hamburg and enable the fabrication and manipulation of nanosystems. Exploring the nanoworld has created an urgent need for a quantitative and qualitative understanding of matter at the atomic scale.

Many new problems, that are not characteristic of bulk materials, arise at the nanoscale. These new problems generate many questions. Such as: what is the role of frustrated spin arrangements for the stability and hysteretic properties of two-dimensional magnets and nanoparticles, what are the size- and the temperature-dependent properties of nanomagnets, and which effects may arise due to the discrete nature of matter? Theoretically, these questions can be effectively studied by model Hamiltonian methods or within analytical approaches. One of the best investigative tools based on model Hamiltonians to solve these stochastic optimization problems are Monte-Carlo methods. They are particularly good for realistically evaluating all kinds of transition probabilities and the effects of entropy. Since magnetic ordering at nanoscale is driven by entropy as well as by energy, Monte-Carlo calculations are really essential for describing magnetization configurations on the nanoscale. Modern classical Monte-Carlo schemes are able to describe large systems consisting of many ten thousands of atoms. The method naturally incorporates long-range dipolar interactions, effects of the atomic lattice, the temperature and the entropy. In combination with analytical calculations, and experimental evidence, the Monte-Carlo treatment is a powerful tool for the description of magnetic ordering in magnets of reduced dimensionality.

Multipolar Ordering and Magnetization Reversal in Nanoarrays

E. Y. Vedmedenko, N. Mikuszeit, and R. Wiesendanger,

Among the interactions in many-body atomic, molecular or nanoparticle systems those of electrostatic or magnetostatic nature are very important. Recently, arrays of nanoparticles or adsorbates have been proposed for a number of applications as

storage, high speed non-volatile magnetic memory (MRAM), and logic functions for computations. Different applications require different properties of an array. While in storage applications every particle should be individually addressed; *i.e.* the nanoelements should not interact, for logic schemes strong interactions are necessary. In both cases the control of interactions between nanoparticles is crucial. To derive the theory of these interactions one needs to know the charge distribution of a particle. One of the simplest and most effective ways to do this is to describe a distribution of charges as a series of multipole moments.

Multipole moments: Spherical Coordinates

Any two-dimensional periodic function can be expanded in terms of an infinite sum of sines and cosines with corresponding coefficients. This expansion is known as Fourier series

$$f(x) = \frac{1}{2}a_0 + \sum_{n=1}^{\infty} a_n \cos(nx) + \sum_{n=1}^{\infty} b_n \sin(nx) \ . \tag{3.10}$$

The coefficients a_n and b_n can be described as integrals of the periodic function Eq. 3.10 multiplied with $\cos(nx)$ or $\sin(nx)$

$$
\begin{aligned}
a_n &= \frac{1}{\pi} \int_{-\pi}^{\pi} f(x) \cos(nx) dx \ , \\
b_n &= \frac{1}{\pi} \int_{-\pi}^{\pi} f(x) \sin(nx) dx \ .
\end{aligned}
\tag{3.11}
$$

Similarly, any scalar field on a sphere, which is periodic by definition, can be expressed in spherical coordinates $r = f(r, \theta, \varphi)$ as a series of spherical harmonics with corresponding coefficients,

$$H(\theta, \varphi) = \sum_{l=0}^{\infty} \sum_{m=-l}^{l} Q_{lm} R_{lm}(r) = \sum_{l=0}^{\infty} \sum_{m=-l}^{l} Q_{lm} Y_{lm}(\theta, \varphi) \frac{4\pi}{2l+1} r^l \ . \tag{3.12}$$

The coefficients Q_{lm} are the multipole moments, $R_{lm}(r) = \sqrt{\frac{4\pi}{2l+1}} r^l Y_{lm}(\theta, \varphi)$- normalized spherical harmonics, $Y_{lm}(\theta, \varphi)$- complex spherical harmonics. The spherical harmonic with $-l < m < l$ is a function of the two coordinates θ, φ on the surface of a sphere and can be modeled by a special set of polynomials known as Legendre functions $P_{lm}(\cos \theta)$. Similarly to the Fourier coefficients of the Eq. 3.11, a multipole moment is nothing else as a volume integral of a charge distribution multiplied with the normalized spherical harmonic

$$Q_{lm} = \int_V \rho(r) R_{lm}(r) dV \ . \tag{3.13}$$
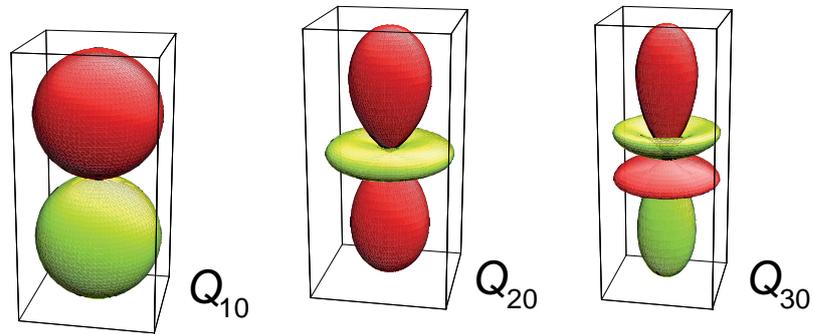
Figure 3.43: Real spherical harmonic representation of multipole moments.

Hence, the multipoles themselves can be visualized as real spherical harmonics, which are a linear superposition of the complex ones. Fig. 3.43 represents then a dipole Q_{10}, a quadrupole Q_{20}, and an octopole Q_{30}.

Multipolar Moments of Nanomagnetic Particles

Particles with lateral size smaller than the characteristic exchange length $d < \chi_{ex}$ have a single domain magnetization configuration with a macroscopic magnetic moment. In
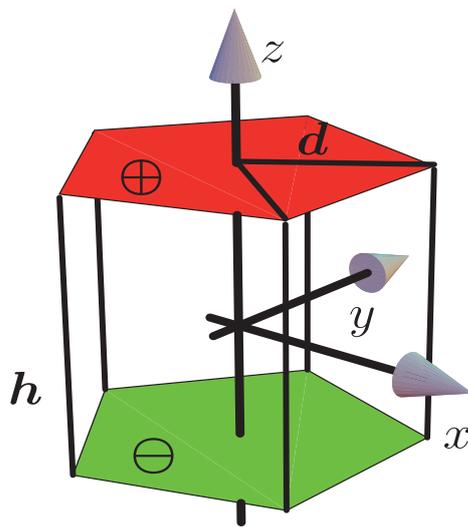
Figure 3.44: Scheme of a nanoparticle with n-fold symmetry. Every surface can be divided into n equivalent isoscele triangles with edge length d. The particle is magnetized in $z-$ direction.
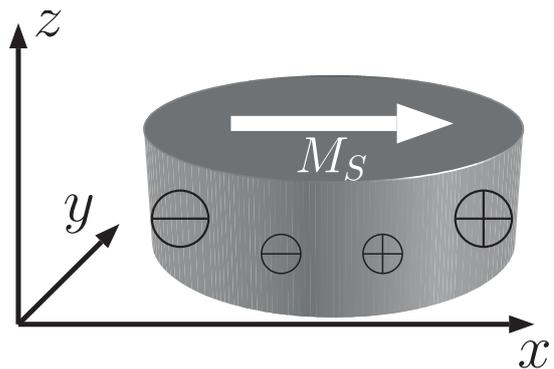
Figure 3.45: Scheme of a disk within the $x-y$-plane (magnetized in x-direction). Due to the magnetization a magnetic surface positive and negative charges emerge. In case of a uniform magnetization the charge is cosine distributed.

case of an ideal single domain all elementary dipoles inside of a particle are compensated and only at the boundary appear uncompensated positive and negative magnetic poles (see Fig. 3.44).

Isolated magnetic poles have never been observed in nature. They occur always in pairs as in the example described. However, it is often convenient to use instead of magnetic poles and the vector field quantity $\mathbf{H}$ the notion of magnetic charges and a scalar potential φ. The quantity φ is defined so that it's negative gradient is the magnetic field $\mathbf{H} = -\nabla\varphi$ with $\nabla = \mathbf{i}\frac{\partial}{\partial x} + \mathbf{j}\frac{\partial}{\partial y} + \mathbf{k}\frac{\partial}{\partial z}$. Here $\mathbf{i}, \mathbf{j}, \mathbf{k}$ are the unit vectors of a Cartesian coordinate system, and (x, y, z) are the coordinates at the point where the field or potential is under consideration. In the framework of this approximation the macroscopic moment of a polarized or magnetized particle can be obtained by means of the multipole expansion of a continuous magnetization distribution within a dot. As can be seen from Eq. 3.13 the strength of a multipole moment depends solely on the charge distribution; *i.e.* on the shape of an object and on the magnetization/polarization configuration. Hence, for typical magnetization distributions corresponding multipolar moments can be calculated on the basis of Eq. 3.13. In [1, 2] the multipole moments of in- and out-of-plane magnetized prisms and cylinders have been calculated analytically. The low order moments of a particle (Fig. 3.44) with four-fold and cylinder symmetry as a function of surface area and height are brought together in the Tab. 3.2.

Table 3.2: The multipole moments Q_{lm} in units of the surface charge density up to the order $(l, m) = (7, 0)$ of particles with four-fold and cylindrical symmetry homogenously magnetized in z-direction

l	m=0 (Four-fold Symmetry)	M=0 (Cylindrical Symmetry)
1	$2hd^2$	$\pi h d^2$
3	$hd^2(\frac{h^2}{2} - d^2)$	$\frac{\pi}{4}hd^2(h^2 - 3d^2)$
5	$\frac{h^5 d^2}{8} - \frac{5h^3 d^4}{6} + \frac{7hd^6}{12}$	$\frac{\pi}{16}hd^2(h^4 - 10h^2 d^2 + 10d^4)$
7	$\frac{h^7 d^2}{32} - \frac{7h^5 d^4}{16} + \frac{49h^3 d^6}{48} - \frac{3hd^8}{8}$	$\frac{\pi}{64}hd^2(h^6 - 21h^4 d^2 + 70h^2 d^4 - 35d^6)$

The dependence of the strength of multipole moments on the effective aspect ratio h/a of a particle with out-of-plane magnetization (Fig. 3.44) is shown in Fig. 3.46a while for an in-plane magnetized disc (Fig. 3.45) the result is presented in Fig. 3.46b.

The most important conclusions of Ref. [1, 2] are the following: First, all homogeneously out-of-plane magnetized prismatic particles with even rotational symmetry (Fig. 3.44) and all in-plane magnetized discs (Fig. 3.45) do not possess multipolar moments with even l; i.e., the quadrupoles (Q_{20}), the hexadecapoles (Q_{40}) etc. are not allowed (see Fig. 3.44). The lowest moment with l even is $(l, m) = (4, 3)$ for an odd, three-fold prism. The first possible multipole moment with even l for a five-fold symmetry is $(l, m) = (6, 5)$. The functions $Q_{lm}(h, a)$ may cross zero. This happens for example for the octopole moments of a cube (see Fig. 3.46a). For vertically mag-
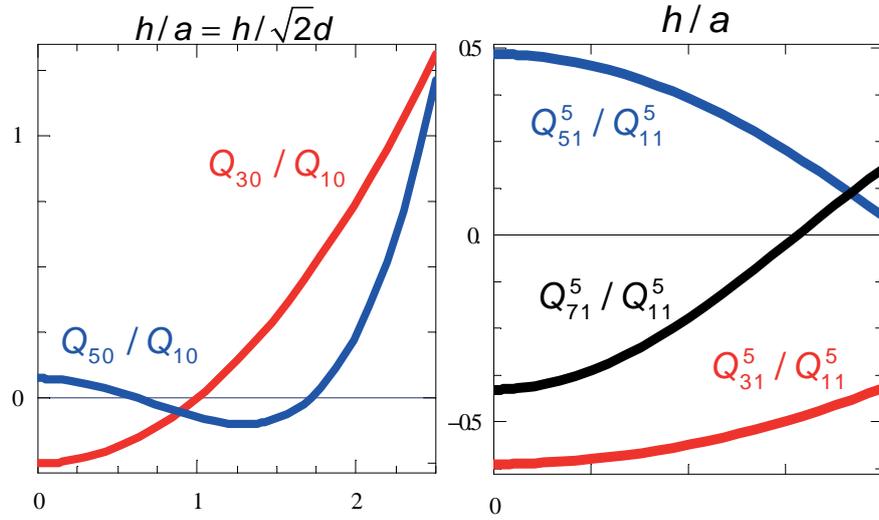
Figure 3.46: a) The low order multipole moments Q_{lm} (normalized to dipolar moment Q_{10}) of particles with fourfold symmetry with height h and edge length a. For $h \rightarrow 0$ $Q_{30} \approx -0.25 Q_{10}$. (b) The multipole moments in units of the dipolar moment of the in-plane magnetized discs with height h and radius a. The magnetization configuration is a non-uniform onion state

netized particles the octopole moment reaches 25% of the dipole moment in the limit of small thicknesses. This geometry corresponds to sizes of particles often used in experimental studies [3–5]. For vertically elongated particles, such as arrays of magnetic nanocolumns or liquid colloidal crystals with rod-like components [6,10] the magnitude of the octopole moments exceeds that of the dipolar one. Similar results have been obtained for in-plane magnetized dots [8,9,11]. For $h \approx a$ the multipolar moments are smaller than the dipolar one. However, in the limit of small thickness ($h << r_0$) the octopole moment Q_{31}^p reaches -61% of the dipole moment Q_{11}^p for all odd p and even the dotriacontapole (Q_{51}^p) is of the order of $0.5 Q_{11}^p$. Hence, the multipole moments of ultrathin, in-plane magnetized discs may also be comparable with their dipolar counterparts. The described geometry is typical for on-going experimental studies on magnetic arrays.

Ground States of Classical, Odd Rank Multipolar Rotors

Several studies of dipolar ground state on a square lattice demonstrated that the ground configuration of an infinite square lattice is highly degenerate and defines a continuous manifold of spin configurations at $T = 0$, although the dipolar coupling itself is not rotationally invariant. A typical configuration obtained by Monte-Carlo simulations for a finite square lattice at finite temperature is given in Fig. 3.47(e). Lines of dipoles are observed at the edges which are formed due to the pole avoidance principle. The microvortex configuration is formed in the center. Hence, the finite size and temperature remove the continuous degeneracy of the dipolar ground state on a

square lattice.

While the dipolar ground states on many periodic lattices are known for several decades [12] ground states of two-dimensional arrays of multipoles or their combinations have been considered only recently [13, 14]. The octopolar moments ($Q_{30} >> Q_{10}$) are unidirectional, i.e. the components of an octopole moment behave themselves like the components of a vector. Therefore, they can be still represented by arrows. It has been found [14] that on a square lattice octopoles form lines being aligned antiparallel (Fig. 3.47(c)) while on a triangular lattice the moments are ferromagnetically ordered. The lines are oriented in principal crystallographic directions. Hence, the octopolar interaction on a triangular and a square lattice introduces an easy-plane and a tri- and a biaxial in-plane anisotropy, respectively. In contrast to finite dipolar systems avoiding uncompensated poles by vortex or domain formation, a finite octopolar system is not sensitive to the formation of free poles in most geometries. To understand the reason for such a behavior one has to bear in mind that in general dipoles only interact with the field, *i.e.* the first derivative of the potential $H_i = -\frac{\partial \Phi}{\partial r_i}$. Higher order moments interact with higher derivatives, *i.e.* quadrupoles with $\frac{\partial^2 \Phi}{\partial r_i \partial r_j}$, octopoles with $\frac{\partial^3 \Phi}{\partial r_i \partial r_j \partial r_k}$ etc. Hence, octopoles do not interact with a demagnetizing field but with the field curvature. Therefore, the gain in the internal energy due to the compensation of free magnetic poles at the sample boundary is not so strong as for pure dipolar systems and low-temperature configurations in finite samples are still parallel lines for a triangular and antiparallel lines for a square lattice.

As shown in [2], the in-plane magnetized nanodiscs with height-to-diameter ratio $h/a = 0.5$, that are often used in modern experimental studies on nanoarrays, possess dipolar and octopolar moments with $Q_{30}/Q_{10} \approx 0.5$. Hence, for a real nanomagnetic array neither pure dipolar, nor pure octopolar configurations are relevant. Instead, ground states of an ensemble of combined multipoles should be calculated. Our recent results [14] demonstrate that the ground state of a system of particles possessing both of multipolar contributions $Q_{10} + Q_{30}$ the pattern changes with respect to the pure dipolar or pure octopolar pattern. Whereas the ground state on an infinite square lattice still consists of antiparallel lines as for pure octopoles, in finite systems alternating regions of parallel and antiparallel chains have been found at finite temperatures [14]. A typical Monte-Carlo configuration for $Q_{30}/Q_{10} = 0.5$ on a square lattice is shown in Fig. 3.47 (f). The width of regions with parallel lines for this Q_{30}/Q_{10} ratio is usually 2-3 lattice parameters. In $\approx 10\%$ of calculations superdomains (Fig. 3.47 (f)) appear despite a very long relaxation procedure. On an infinite triangular lattice the ground state is a ferromagnetic single domain as in the pure dipolar system. However, in finite systems the vortex configuration is never formed for $Q_{30}/Q_{10} \geq 0.5$. Instead, large domains appear. Hence, the interaction of dipoles with the demagnetizing field is still too weak in comparison to the anisotropy induced due to the octopole-octopole coupling.
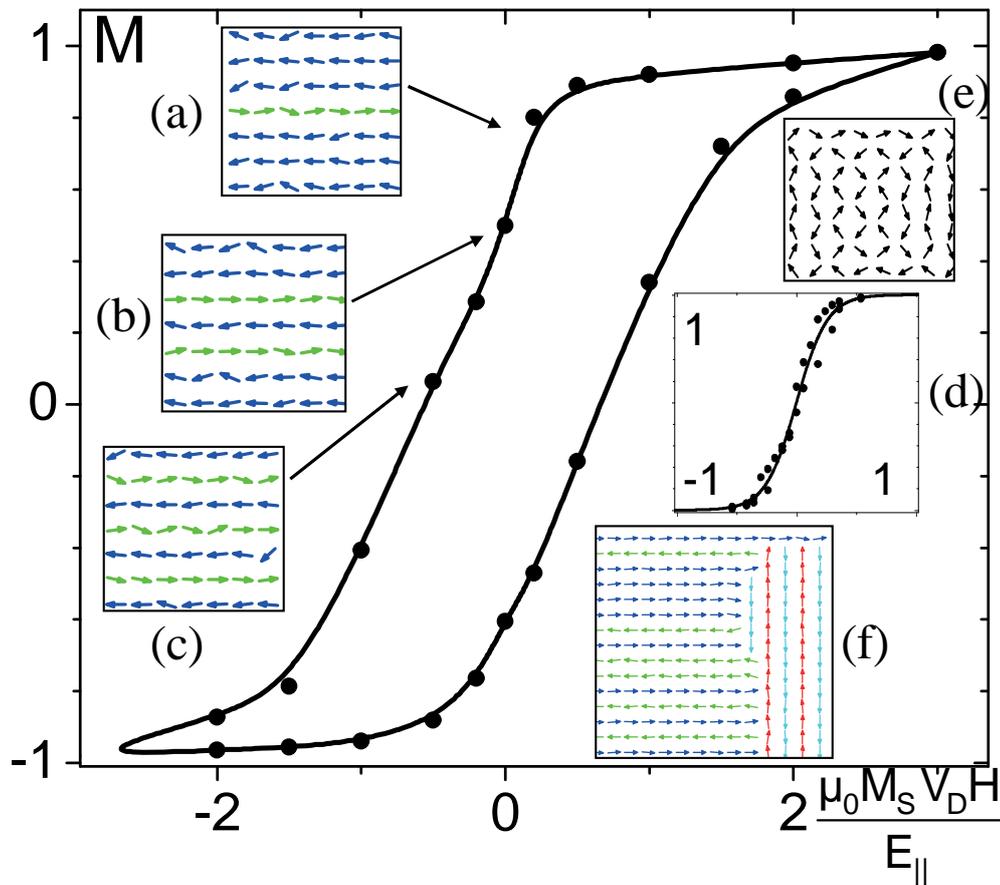
Figure 3.47: Monte-Carlo hysteresis loops for a 20×20 square nanoarray with $Q_{30} = 0.5Q_{10}$ and a pure dipolar system (inset (d)). The magnetic field is applied in x-direction. Insets (a-c) give the central part of intermediate magnetic configurations; (f) and (e) show stable zero-field configurations for combined multipoles and the pure dipolar case, respectively. Thermal energy is $kT = 0.6E_{\parallel}$. The field is expressed in $\frac{\mu_0 M_S V_D}{E_{\parallel}}$ with μ_0 - the permeability of free space and V_D - the volume of a dot.

Magnetization Reversal in densely packed Nanomagnetic Arrays

Experimental investigations have shown that, in comparison to an infinite film, the interparticle interactions usually lead to a decrease in the switching field in patterned media with out-of-plane magnetization [3, 4], and to an increase of the coercivity for in-plane magnetized particles [5, 7]. Although in some cases an agreement of switching behavior with theoretical predictions has been obtained, it is often found that measured switching fields deviate significantly (by 10–15%) from those expected with pure dipolar interactions. In the following the field dependence of magnetization in square array of dots with in-plane magnetization will be analyzed and compared with hysteretic properties of a pure dipolar system. An array with higher-order interactions corresponds to an ensemble of ultrathin particles with height to diameter ratio

$h/a \leq 0.5$ and interparticle distance $d \leq 1.5a$ as a particle of such geometry possesses an octopolar moment of $Q_{30} = 0.5Q_{10}$. A pure dipolar system corresponds to another dimensional aspect ratio $h/2a \approx 1$ or to $h/a \leq 0.5$ but $d > 1.5a$. Each particle is expected to be in a single domain state and remagnetizes by means of the Néel-Brown mechanism; i.e., a coherent rotation of magnetization. This model is reasonable for particles of size comparable with the exchange length. The multipole moments of such a particle do not change during the magnetization reversal. Therefore, such a system can be simulated by means of MC simulations, where each particle is represented by its macroscopic multipole moment. Figure 3.47 shows the magnetization reversal of a square lattice with $Q_{30} = 0.5Q_{10}$ obtained from MC calculations (main view of Fig.3.47) and $Q_{30} << Q_{10}$ (inset Fig.3.47(d)).

A pure dipolar system (Fig.3.47(d)) does not show any easy-axis hysteresis. In a pure dipolar case all macroscopic magnetic moments rotate coherently, and therefore the total magnetization decreases continuously from unity at saturation field H_s to zero for $H = 0$. In a multipolar array, on the contrary, the hysteresis loop is quite open. The squareness s depends on the composition, the strength of the multipoles, and on the temperature. The field is scaled with $E_\parallel$, as described in the previous paragraph. Therefore, contributions from moments of different order in combined multipoles scale differently with R_{AB}. All values are given for $Q_{30} = 1$, $Q_{10} = 2$, and $R_{AB} = 1$. This gives $s \approx 0.5$ and $H_c \mu_0 M_S V_d \approx 0.7E_\parallel$ with M_s the saturation magnetization and V_d the particle volume. By calculating $E_\parallel$ this result can be scaled to a square array of any material with any interdot distance. For example, for an array of permalloy particles at room temperature $M_S = 8 \cdot 10^5 \text{A m}^{-1}$, and vanishing anisotropy $K_1 < 1000 \text{ J m}^{-3}$ with $h = 20$ nm, $d = 2a = 70$ nm and $R = 100$ nm, a coercive field $Hc \approx 20$ mT has been found [14]. Magnetic moments do not rotate continuously, as in a pure dipolar system, but are reoriented line-by-line (Fig. 3.47 (a)-(c) as non-collinear configurations are energetically unfavorable.

As follows from simulations the total energy of the configuration in Fig. 3.47 (b) is close to or even lower than that of Fig. 3.47 (c), where all chains are antiparallel. Hence, to go from the configuration of Fig. 3.47 (b) to that of Fig. 3.47 (c), an external magnetic field must be applied and the hysteresis appears. H_c increases with decreasing temperature; this effect is similar to superparamagnetic temperature-assisted switching, and thus the hysteretic behavior is predefined by competition between the octopole-dipole contribution of the magnetostatic energy and its dipole-dipole and octopole-octopole counterparts. Pure dipolar systems do not show any significant hysteresis. Hence, the ground states and magnetization reversal in densely packed nanomagnetic arrays is strongly influenced as much by the order of magnetostatic interactions as by the underlaying lattice symmetry.

References

[1] N. Mikuszeit, E.Y. Vedmedenko, and H. Oepen, J. Phys. Condens. Matter **16**, 9037 (2004).

[2] N. Mikuszeit, E.Y. Vedmedenko, R. Wiesendanger, and H. P. Oepen, J. Appl. Phys. **97**, 10J502 (2005).

[3] T. Aign et al., Phys. Rev. Lett. **81**, 5656 (1998).

[4] C. A. Ross et al., Phys. Rev. B **65**, 144417 (2002).

[5] J.Y. Cheng, W. Jung, and C. A. Ross, Phys. Rev. B **70**, 064417 (2004).

[6] K. Nielsch et al., J. Magn. Magn. Mater. **249**, 234 (2002).

[7] R. P. Cowburn J. Phys. D: Appl. Phys. **33**, R1 (2000).

[8] W. Kleemann, O. Petracic, C. Binek, G. N. Kakazei, Y. G. Pogorelov, J. Sousa, S. Cardoso, and P. P. Freitas, Phys. Rev. B **63**, 134423 (2001).

[9] M. R. Scheinfein, K. E. Schmidt, K. R. Heim, and G. Hembree, Phys. Rev. Lett. **76**, 1541 (1996).

[10] P. Warin, R. Hyndman, J. Glerak, J. N. Chapman, J. Ferre, J. P. Jamet, V. Mathet, and C. Chappert, J. Appl. Phys. **90**, 3850 (2001).

[11] R. F. Wang et al., Nature **439**, 4447 (2006).

[12] E. Y. Vedmedenko, Competing Interactions and Pattern Formation in Nanoworld, Wiley, Weinheim (2007).

[13] E. Y. Vedmedenko, Phys. Stat. Sol. (b) **244**, 1133 (2007).

[14] E. Y. Vedmedenko, N. Mikuszeit, H. P. Oepen, and R. Wiesendanger, Phys. Rev. Lett. **95**, 207202 (2005).

3.2.11   Magnetic exchange force microscopy with atomic resolution

U. Kaiser, A. Schwarz, and R. Wiesendanger,
[Nature **446**, 522 (2007)].

Introduction

The understanding of magnetic phenoma on the nanoscale is closely related to the experimental techniques that are at hand to study these systems. A valuable tool for such investigations is spin-polarized scanning tunneling microscopy [1]. It allows the real space mapping of spin configurations with atomic resolution. However, this technique is limited to conducting samples because it relies on the detection of a tunneling current between tip and sample. In contrast to this, scanning force microscopy can be performed on all kinds of samples, independent of their conductivity. Magnetic force microscopy [2] is one prominent representative for a force detection based method and it can be used to study ferromagnetic domain patterns. Since this method senses the long-ranged magnetostatic interactions between a magnetically coated tip and a sample, its resolution is limited to the nanometre scale, but atomic resolution cannot be achieved. An approach to overcome this limitation is magnetic exchange force microscopy, which was proposed in [3]. It also bases on atomic force microscopy (AFM) [4] and like for MFM a magnetically coated tip is used. However, it is approached much closer to the sample in order to detect the short-ranged magnetic exchange forces between the foremost tip atom and the underlying sample atoms. In the following, we present our experimental data obtained on the (001) surface of the antiferromagnetic insulator nickel oxide. We demonstrate for the first time that it is possible to simultaneously visualize the arrangement of surface atoms and their spins [5]. In contrast to earlier attempts [6–9], we used an external magnetic field to align the magnetic polarization of the tip apex in a desirable orientation.

Experimental Approach

Figure 3.48 sketches the general concept of MExFM on NiO(001). The main feature of this force microscopy approach is that the atomic resolution capabilities of AFM are combined with spin sensitivity by using as force sensor a magnetic tip mounted on the free end of a cantilever. The cantilever self-oscillates with constant amplitude A_0 while the actual cantilever frequency f is shifted due to tip-sample interactions by an amount of $\Delta f = f - f_0$ from the resonance frequency f_0 of the free cantilever ($\Delta f < 0$ and $\Delta f > 0$ for attractive and repulsive forces, respectively) [10]. During scanning in the xy-plane, Δf is kept constant by adjusting the z-position of the tip relative to the surface so that the recorded $z(x, y)$ map, i.e. the topography, provides contour lines of constant tip-sample interaction force. Selecting a more negative Δf set-point increases
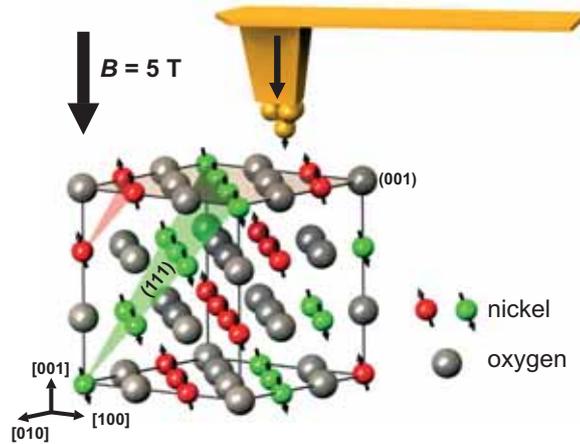
Figure 3.48: Concept of magnetic exchange force microscopy (MExFM) on the insulating antiferromagnet nickel oxide. Nickel magnetic moments (spins) within {111} planes are ordered ferromagnetically and point in ⟨211⟩ directions. Since neighbouring {111} planes are aligned antiferromagnetically, nickel spins of opposite orientation alternate along ⟨110⟩ directions on the (001) surface. To perform MExFM, a cantilever with an iron coated tip is scanned above the (001) surface. An external magnetic field with a flux density of $B = 5$ T maximizes the sensitivity of the tip apex to the out-of-plane component of the canted spins at the nickel atoms (see Fig. 3.49 b)). A purely chemical and structural contrast would only reflect the arrangement of nickel and oxygen atoms. If the magnetic exchange interaction between the spins of the foremost iron atom at the tip apex and the nickel atom directly below is detected, an additional contrast modulation between neighbouring rows of nickel atoms should appear in an image of the (001) surface.
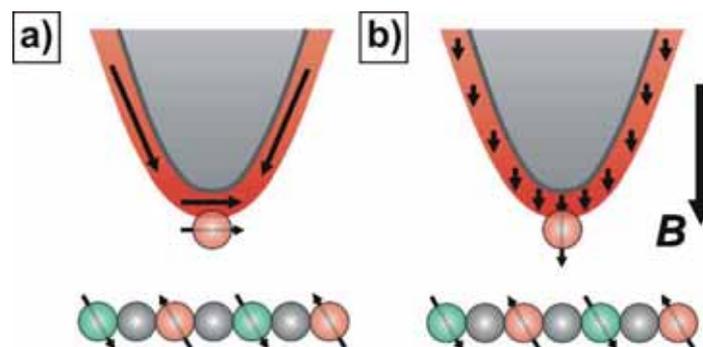
Figure 3.49: Influence of an external magnetic field on the magnetic polarization of the tip. a) Due to the shape anisotropy the preferred orientation of the foremost tip atom follows the curvature of the tip and is therefore in-plane. b) In a strong external magnetic field the magnetic polarization is everywhere aligned along the field direction leading to a foremost tip atom which is also oriented in the out-of-plane direction.

the attractive interaction, because the z-regulator reduces the tip-sample distance. This method enables atomic resolution on conducting and non-conducting surfaces in the non-contact regime [11,12], with height differences in topography images reflecting variations of the short-range forces between the foremost tip atom and different atomic species of a surface.

The sample material, nickel oxide, crystallizes in the rock salt structure with a lattice constant of $a = 417$ pm and exhibits a nearly perfectly bulk terminated (001) surface [13]. Below its Néel temperature of 525 K, it is a collinear antiferromagnet with ferromagnetic {111} sheets stacked in an antiferromagnetic order as indicated in Fig. 3.48. According to the superexchange model the magnetic exchange interaction between the localised Ni d-states is mediated via bridging oxygen atoms [14]. Within each sheet the magnetic moments of the nickel atoms point in one of the twelve possible $\langle 211 \rangle$ orientations. X-ray linear magnetic dichroism data of single crystals indicate that the surface magnetic structure is bulk terminated [15]. Therefore, the spin orientation alternates on neighbouring rows along $\langle 110 \rangle$-directions on the (001) surface and only the short-range magnetic exchange interaction varies between the chemically and structurally equivalent neighbouring nickel rows. For this reason, the exchange interaction can be distinguished unambiguously from all other long and short-range tip-sample interactions.

To prepare a clean (001) surface, the crystal is cleaved in ultrahigh vacuum and heated to 483-493 K for about 15 min to remove residual charges. All measurements are then performed with a silicon cantilever coated in situ with a 22 nm thick ferromagnetic iron film using our home-built low-temperature force microscope (Hamburg-design) [16]. Due to its shape anisotropy, the preferred magnetic polarization at the tip apex is in-plane with respect to the (001) surface (see Fig. 3.49 b)). However, application of an external magnetic flux density of $B = 5$ T perpendicular to the sample surface aligns the magnetization of the iron film along the field direction. In this configuration, the tip apex becomes mainly sensitive to the out-of-plane component of the spins at the sample surface [17] (see Fig. 3.49 a)). Note that since the exchange coupling between the spins of the nickel atoms is much stronger than the Zeeman energy, the antiferromagnetic order in the nickel oxide crystal is not affected.

According to the Heisenberg model the magnitude of the interaction between two spins $\vec{S_1}$ and $\vec{S_2}$ is given by their scalar product $H = J_{12}\vec{S_1}\cdot\vec{S_2}$, where J_{12} is the exchange integral. Thus, the interaction between tip spins and sample spins is strongest for either parallel or antiparallel spin orientations. In the sample, all twelve possible $\langle 211 \rangle$ spin orientations of the nickel atoms possess a significant in-plane as well as out-of-plane component with respect to the (001) surface. In the absence of a magnetic field, coated tips have an in-plane magnetic polarization with no preferred spin orientation within the plane (see Fig. 3.49 a)). Spins at the apex of such tips can thus exhibit any angle with respect to the in-plane component of the spins at the nickel atoms, including unfavourable relative orientations characterized by a vanishing magnetic exchange interaction. Application of an external magnetic field (cf., Fig. 3.49) and

probing the interaction between tip spins and the out-of plane component of the sample spins overcomes this problem, because the respective spins are always either parallel or antiparallel. We note that such controlled manipulation of the tip apex spins into the favourable out-of-plane direction is the main difference between this study and all previous MExFM measurements on NiO(001) with magnetically coated tips in zero field [6–9]. An external magnetic field is not a prerequisite for MExFM, but alignment of the spins at the tip apex in a favourable direction with respect to the spins at the sample surface significantly improves the overall measurement performance. Such alignment can be induced by an external magnetic field as in this study, or by choosing different magnetic materials and appropriate growth modes to control the easy axis of magnetization.

Experimental Results

Figure 3.50 displays two atomically resolved unfiltered data sets for NiO(001). Both sets were acquired on the same sample area using the same iron coated tip, and with a bias voltage $U_{\mathrm{bias}} = $ -1.2 V applied between tip and sample to minimize electrostatic forces. No evidence for changes in tip characteristics was observed during data acquisition. The topographic image in a) recorded at $\Delta f = $ -22.0 Hz exhibits maxima and minima that reflect the (1×1) symmetry of the chemical surface unit cell. In the Fourier transform of the data (cf., Fig. 3.50 c)), the chemical unit cell is represented by four spots, which appear as peaks in the two line sections along the diagonals of the Fourier transform (cf., Fig. 3.50 e)). The apparent height difference between minima and maxima along the [100] direction is about 4.5 pm. Since the total valence charge density is largest above the oxygen atoms [18] and the chemical affinity between oxygen and iron is larger than between nickel and iron [19], the protrusions correspond to the oxygen sites [20].

The image in Fig. 3.50 b) was acquired at $\Delta f = $ -23.4 Hz; compared to the data in Fig. 3.50 a), this corresponds to the sample having been moved by about 30 pm towards the cantilever. However, the stronger attractive interactions at shorter distances pull the tip-apex atoms towards the surface atoms and vice versa, so the true distance between the foremost tip atom and the surface atom underneath can be reduced significantly further [20]. When comparing the raw data sets, an additional modulation is apparent in Fig. 3.50 b): every second row of nickel atoms along the [110] direction appears more depressed, as indicated by the black arrows. In the Fourier transform (Fig. 3.50 d)), this is reflected by the appearance of one additional pair of peaks located halfway between the centre and two (opposing) peaks corresponding to the chemical unit cell. The line sections through the Fourier transform (Fig. 3.50 f)) confirm that the additional peaks are only present along one diagonal, as expected. When rotating the scan direction by $30°$, the chemical contrast and the additional modulation on neighbouring nickel rows rotated accordingly (see Fig. 3.51); this excludes the possibility of an oscillatory noise source in phase with the lattice periodicity causing the additional peaks seen in Figs. 3.50 b), d), f). Note that a multiatom tip apex
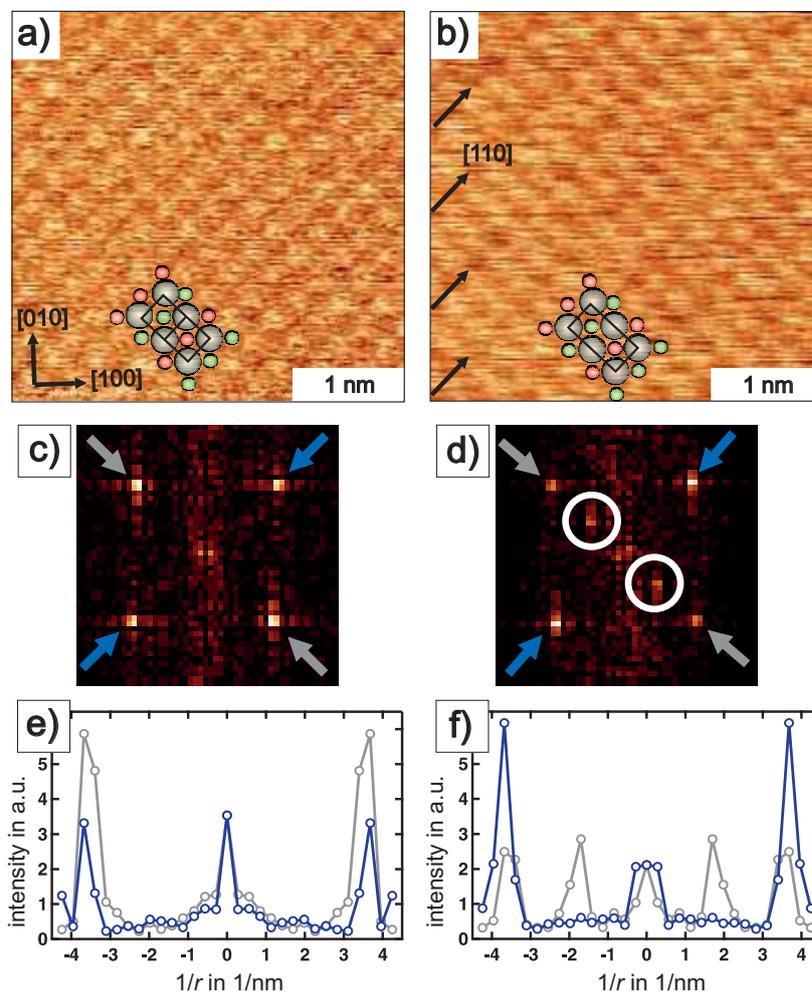
Figure 3.50: Chemical and magnetic exchange contrast with atomic resolution on NiO(001). Both images are unfiltered raw data, which have been obtained with the same tip at 7.9 K in 5 T on the same 3.5 nm × 3.5 nm area. Image a) has been recorded at a constant frequency shift of -22.0 Hz. Protrusions and depressions reflect the arrangement of oxygen and nickel atoms, respectively. The four spots in the Fourier transform c) correspond to the chemical surface unit cell. Image b) has been recorded at a smaller tip-sample distance realized by setting a larger negative frequency shift of -23.4 Hz. It exhibits an additional contrast modulation along neighbouring rows of nickel atoms (see arrows) that results from the arrangement of spins at the NiO(001) surface (cf., Fig. 3.48). The additional modulation is visible in the Fourier transform d) as additional pair of peaks, which represent the size of the magnetic surface unit cell. Line sections across the Fourier transforms e) and f) clearly show that the additional pair of peaks is only visible at smaller tip sample separations and only along one diagonal. Cantilever parameters: spring constant: 34 N/m, $f_0 = 159$ kHz, mechanical Q-factor at 5 T: 27.720, $A_0 = 6.65$ nm, $U_{\text{bias}} = $ -1.2 V.

interacting in a purely non-magnetic fashion with the sample also cannot generate the observed modulation as all Ni atoms of the surface are structurally and chemically identical. Besides that we observed the modulation between neighbouring Ni rows with several different iron coated tips on different nickel oxide crystals. We therefore conclude that the observed additional contrast modulation on neighbouring nickel rows and the corresponding pair of peaks in the Fourier transform reflect the (2×1) antiferromagnetic surface unit cell of NiO(001), which demonstrates the feasibility of MExFM.

To quantify the chemical and magnetic atomic scale contrast, we averaged over all chemical unit cells in Fig. 3.50 a) and over all magnetic unit cells in Fig. 3.50 b). The left-hand panels in Fig. 3.52 display zooms of the raw data in Fig. 3.50, together with insets that have been constructed by tiling together the respective single unit cell image obtained through averaging. The right-hand panels give the Fourier transform line sections, from which all relevant apparent height differences h between chemically and magnetically different atoms can be determined. The data in Fig. 3.52 a) are consistent with detection of only purely chemical interactions between nickel or oxygen atoms and the iron tip: the apparent height differences are constant, with $h_{\mathrm{Ni\downarrow-O}} = h_{\mathrm{Ni\uparrow-O}} = h_{\mathrm{Ni-O}} \approx 4.5$ pm. This contrasts with the data in Fig. 3.52 b), where apparent height differences between oxygen and nickel atoms are seen to depend on the spin orientation of the latter: $h_{\mathrm{Ni\downarrow-O}} \approx 3.7$ pm and $h_{\mathrm{Ni\uparrow-O}} \approx 5.2$ pm, respectively, for nickel atoms with opposite spin orientations (Ni↑ and Ni↓). Thus, the resulting apparent height difference due to the magnetic exchange interactions is $h_{\mathrm{Ni\downarrow-Ni\uparrow}} = |h_{\mathrm{Ni\downarrow-O}} - h_{\mathrm{Ni\uparrow-O}}| \approx 1.5$ pm. Note that in Fig. 3.52 b) the chemical contrast between nickel and oxygen atoms, which can be estimated as $h_{\mathrm{Ni-O}} = \frac{1}{2}|h_{\mathrm{Ni\downarrow-O}} + h_{\mathrm{Ni\uparrow-O}}| \approx 4.5$ pm, is the same as in Fig. 3.52 a). Furthermore, no significant difference in contrast is observed for
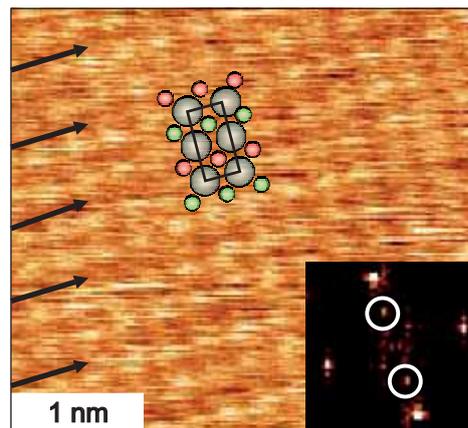
Figure 3.51: Raw data topography image showing the MExFM contrast on neighbouring rows of nickel atoms by changing the scan angle by 30° relative to Fig. 3.50 (b). Nickel rows that appear lower are marked by arrows. The inset displays the Fourier transform with the two additional peaks stemming from the 2 × 1 magnetic surface unit cell.

oxygen atoms in neighbouring rows.
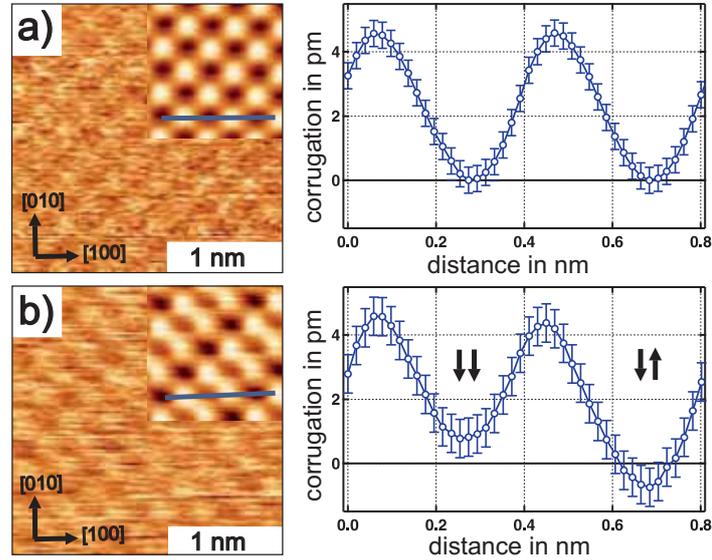
Figure 3.52: Quantification of the chemical contrast and the MExFM contrast after unit cell averaging. The raw data are displayed together with an inset tiled from the single chemical a) and magnetic b) unit cell, respectively, obtained after averaging over all imaged unit cells of the raw data in Fig. 3.50. From the line section along the [001]-direction the purely chemical apparent height difference between nickel and oxygen in a) obtained at a relatively large tip-sample distance can be measured to about 4.5 pm. At smaller separation the additional apparent height difference between nickel atoms of opposite spin orientations due to the magnetic exchange interaction with the spin of the iron tip is 1.5 pm. The error bars (± 0.2 pm in a), ± 0.3 pm in b)) represent the root-mean-square noise after unit cell averaging. Note that the indicated relative spin orientation between iron tip and nickel, which is indicated in b) by arrows corresponds to a ferromagnetic exchange coupling as predicted in [21].

The contrast dependence on the tip-sample distance apparent in the data of Fig. 3.50 agrees with density functional calculations for the Fe/NiO(001) system, which found that chemical interactions are detectable at relatively large separations while magnetic exchange forces give rise to detectable contrast only for distances below 340 pm [21]. At larger tip-sample distances, such as used in Fig. 3.50 a), the foremost iron atom at the tip apex mainly interacts with the $O(2p)$ electrons that dominate the total valence charge density and are expected to reach further into the vacuum region above the surface than the localised $Ni(3d)$ electrons [22]. The latter electrons, which carry the magnetic spin in this system, can be probed by the tip only at relatively small separations as in Fig. 2 d). Assuming the magnetic exchange interaction involves ferromagnetic coupling between tip and sample spins [21], it will add to the chemical interaction such that the total attractive interaction becomes stronger (weaker) if the z-component of the magnetic moment of the Ni atoms is parallel (antiparallel) to that

of the Fe atom at the tip apex. Considering that the topography (i.e., constant Δf) images represent contour lines of constant interaction strength, such a spin-dependent variation of the tip-sample interaction readily explains the observed apparent height differences between neighbouring nickel rows.

We note that successful detection of a MExFM contrast is accompanied by the observation of a much fainter chemical contrast than typically seen in earlier studies that only observed chemical contrast (cf., 4.5 pm in Fig. 3.50 a) compared to corrugation amplitudes of 20 - 40 pm reported [6–9] for earlier force measurements over NiO(001).). This behaviour agrees with theoretical predictions that strong chemical interactions prevent a close approach due to spontaneous modifications of the tip apex [20], which precludes reaching the small separations that are necessary to attain a significant overlap between the itinerant d-electrons of the iron tip and the localized d-electrons at the nickel atoms. We found that the magnitude of the observed MExFM contrast varies from tip to tip, ranging between 0.5 pm and 1.5 pm. Such variations are expected because the magnitude of the magnetic exchange interaction depends on the relative orientation between tip and sample spins.

Conclusions

This study is a first step to establish MExFM as a versatile technique to probe magnetic moments of surfaces on the atomic scale and independent of the samples' conductivity. We anticipate that this approach can be used to study systems such as the antiferromagnetic insulating pinning layers in exchange-bias systems [23] that are widely used in the development of future magnetic storage and sensor devices, or magnetically active single atoms and molecules that are adsorbed on insulators to avoid hybridization. By carrying out measurements as a function of tip-sample distance, it should be possible to quantify the magnitude of the interaction force and to distinguish between different spin coupling mechanisms underlying the exchange interaction. Even dynamic processes like spin precession or spin wave (magnon) excitation might be accessible, through evaluation of the dissipated energy during scanning.

References

[1] S. Heinze et al., Science **288**, 1805-1808 (2000).

[2] Y. Martin et al., Appl. Phys. Lett. **50**, 1455-1457 (1987).

[3] R. Wiesendanger et al., J. Vac. Sci. Technol **B 9**, 519-524 (1990).

[4] G. Binnig et al., Phys. Rev. Lett. **56**, 930-933 (1986).

[5] U. Kaiser et al., Nature **446**, 522 (2007).

[6] H. Hölscher et al., Appl. Phys. Lett. **81**, 4428-4430 (2002).

[7] S. Langkat et al., Surf. Sci. **527**, 12-20 (2003).

[8] R. Hoffmann et al., Phys. Rev. **B 67**, 085402 (2003).

[9] H. Hosoi et al., Nanotechnology **15**, 506-509 (2004).

[10] T. R. Albrecht et al.,J. Appl. Phys. **69**, 669-673 (1991).

[11] F. J. Giessibl, Science **267**, 68-71 (1995).

[12] S. Morita, R. Wiesendanger, and E. Meyer (Eds.) Noncontact Atomic Force Microscopy, Springer (2002).

[13] T. Okazawa et al., Phys. Rev. B **67**, 195406 (2003).

[14] P. W. Anderson et al., Phys. Rev. B **79**, 350-356 (1950).

[15] F. U. Hillebrecht et al., Phys. Rev. Lett. **B 86**, 3419-3422 (2001).

[16] M. Liebmann et al., Rev. Sci. Instrum. **73**, 3508-3514 (2002).

[17] A. Kubetzka et al., Phys. Rev. Lett. **94**, 087204 (2005).

[18] M. R. Castell et al., Phys. Rev. B **59**, 7342-7345 (1999).

[19] T. J. Regan et al., Phys. Rev. B **64**, 214422 (2001).

[20] A. S. Foster et al., Surf. Sci. **490**, 211-219 (2001).

[21] H. Momida et al. Surf. Sci. **590**, 42-50 (2005).

[22] M. R. Castell et al., Phys. Rev. B **55**, 7859-7863 (1997).

[23] J. Nogues et al., J Magn. Mag. Mat. **192**, 203-232 (1999).

3.2.12 Magnetization reversal of $Bi_2Sr_2CaCu_2O_{8+\delta}$ with single flux line resolution

A. Schwarz, U. H. Pi, and R. Wiesendanger,
[Appl. Phys. Lett **88**, 012507 (2006) and Phys. Rev. B **73**, 144505 (2006)].

Introduction

The magnetic behavior in the mixed state of high temperature superconductors has been of considerable scientific and technological interest. For example, the dynamics of flux lines affect the transport properties of superconductors. A direct observation of the magnetic flux distribution is expected to contribute to a better understanding of the properties of superconductors. Magnetic force microscopy (MFM) has achieved single vortex resolution [1–3]. In the low flux density regime (distance between flux lines $r > \lambda$, where λ is the London penetration depth), individual flux lines can be easily distinguished as objects with radii on the order of λ. However, MFM can also be operated in high external fields and we have demonstrated that the resulting higher flux densities ($r < \lambda$) can be studied as well [4]. The contrast formation of MFM in this high flux density regime is very similar to that obtained by magnetooptical means utilizing indication layers [5].

Here, we report our MFM studies on visualizing flux distributions in transversal geometry of a $Bi_2Sr_2CaCu_2O_{8+\delta}$ (BSCCO) single crystal in the low as well as high flux density regime. In the former case we investigated the magnetization reversal process with single flux line resolution. Flux lines of opposite polarity annihilate each other forming a zone of zero flux density between flux and antiflux regions [6]. In the large flux density regime the general behavior follows predictions of the Bean model [7]. However, locally the distribution is altered due to the presence of defects.

Sample and Experimental Set-Up

The sample studied here, i.e., BSCCO, is an extreme anisotropic type-II high T_c superconductor. A magnetic field can penetrate this type of superconductors by creating vortices, which are confined to the CuO-planes of the crystal. The normal conducting core of such a vortex is screened from the superconducting phase by circular super currents, which decay on the length scale of the London penetration depth λ. Due to Josephson coupling and magnetostatic attraction, vortices align each other along the c-axis forming flux lines. Each flux line contains one quantum flux Φ_0, which can be detected by MFM. Since vortices of the same polarity in the same CuO-plane repel each other, flux lines also repel each other and thus tend to arrange each other in a triangular Abrikosov lattice. On the other hand, vortices of opposite polarity attract and annihilate each other. Hence, whole flux lines of opposite polarity attract and annihilate each other as well.

Our BSCCO single crystal (about $a \times b \times c = 2.2\,\text{mm} \times 0.72\,\text{mm} \times 0.048\,\text{mm}$ in size) was grown by a floating zone method. After growth the crystal was irradiated with 1.3 GeV uranium ions to form artificial columnar defects [10] parallel to the *c*-axis. They act as strong pinning centers and the flux lines are attached to them [4]. Therefore, the arrangement of flux lines reflects the random distribution of columnar defects rather than a regular triangular lattice. The ion dose corresponded to a matching flux density of $B_\text{m} = 2$ mT. Furthermore, antiphase boundaries induced by stacking fault dislocations, an intrinsic crystal defect that exhibit an anisotropic pinning behavior [11], are present in the investigated crystal.

All experiments have been performed with our home built force microscope (*Hamburg design*) [8], which is operated in ultrahigh vacuum at a base temperature of 5.2 K. An externally magnetic flux density B_a of up to 5 T can be applied perpendicular to the sample surface, i.e., parallel to the *c*-axis of BSCCO. To detect the tip-sample interaction, the frequency modulation technique was utilized [9]. In this mode of operation a cantilever with eigenfrequency f_0 and force constant c_z is oscillated at a constant amplitude A by a self-excitation resonance loop. Due to tip-sample interactions its actual resonance frequency f is shifted by Δf, i.e., $\Delta f = f - f_0$. During scanning in the *xy*-plane across the surface, Δf, and therefore the tip-sample interaction, is kept constant by a *z*-feedback loop that adjusts the tip-sample distance in *z*-direction accordingly. The resulting $z(x, y)$ image recorded with constant Δf reflects the surface topography revealing surface features like terraces, steps and defects. To achieve magnetic sensitivity, silicon cantilevers are coated with *in situ* deposited iron.

For MFM measurements we apply the plane-subtraction mode. In the topographic mode (*z*-feedback on) the slope between tip and sample is compensated by adding an appropriate *xy*-position dependent voltage to the *z*-electrode of the scan unit. Thereafter, the *z*-feedback is switched off and the tip is retracted from the sample surface to a scanning height h of typically 20 nm. An MFM image is obtained by recording $\Delta f(x, y)$ while scanning in this plane, which is parallel to the surface (constant height mode). At this separation the image contrast is dominated by long range magnetostatic force and Δf is related to the derivative of the vertical interaction force F_z' by $\Delta f = -(F_z'/2c_z)f_0$. In all MFM images, brighter contrast represents more negative frequency shifts, i.e., a larger attractive interaction.

Magnetization Reversal

To investigate details of the magnetization reversal process with single flux line resolution we polarized the tip perpendicular to the surface in $B_\text{a} = +100$ mT. Thereafter, the sample was field cooled from above T_c down to $T = 5.2\,\text{K}$ in $B_\text{a} = B_\text{FC} = -3\,\text{mT}$. Then, B_a was ramped stepwise from -3 mT to +50 mT. To study the magnetization reversal and in particular the mechanisms of the boundary displacement, snapshots of the vortex configuration were recorded for each B_a on the same $7 \times 7 \mu\text{m}^2$ sample area. Four of them are displayed in Fig. 3.53, i.e., (a)-(d). For comparison, the flux density $B_z(x)$ and its evolution with increasing B_a according to the 1-dimensional Bean model

is sketched in (e).

The glass-like random flux line configuration after field cooling is imaged in (a). Since MFM detects the magnetic field associated with the quantum flux $\Phi_0 = 2 \cdot 10^{-15}$ T m^{-2}, each flux line appears as object with a radius on the order of the London penetration depth $\lambda \approx 200$ nm. The dark contrast indicates a repulsive tip-vortex interaction, i.e., tip magnetization and flux line polarity are antiparallel. The total number of $N = a_{\mathrm{scan}}/\Phi_0 \cdot B_{\mathrm{FC}} = 62$ vortices corresponds reasonably well to $B_{\mathrm{FC}} = -3$ mT and the scan area $a_{\mathrm{scan}} = 49$ μm^2. Four strong pinning sites are marked by crosses, to evaluate their role during magnetization reversal. For the same reason, the barely visible faint line is marked by two arrows. In the topographic mode a step with a height of about (0.36 ± 0.05) nm was found at exactly that position. Previously, we identified such straight steps with heights less than the surface cleavage step height of $c/2 = 1.55$ nm as an antiphase boundary and reported a strong anisotropic pinning behavior [11].

After applying a field opposite to the direction during field cooling, flux lines of opposite polarity (antiflux) enter the sample from the edges, where the magnetization reversal due to flux-antiflux annihilation starts. At 30 mT the first antiflux lines enter the scan area. In (b) the situation at 32.5 mT is shown. The incoming antiflux lines (bright contrast due to the attractive interaction between tip and antiflux) already penetrated the scan area from the right. The four crosses mark the same strong pinning sites as identified in (a). The two on the left are still occupied by flux lines, the one between the two parallel white lines is empty and the right one is already occupied by a flux line of opposite polarity - named antiflux line in the folowing. Flux and antiflux regions are well separated from each other by an approximately 1 μm wide *zone of zero flux density* marked by two parallel white lines. The following propagation mechanism can be inferred: In the boundary region flux closure is achieved by the formation of flux-antiflux loops. Their radii shrink while the antiflux region is moved forward by increasing B_{a}. Finally, the loop collapses below a certain radius if its elastic energy becomes larger than its pinning energy. Thereby, a flux line and an antiflux line are annihilated. The remaining empty columnar defect is reoccupied by another mobile incoming antiflux line.

In (c) the antiflux front has reached the antiphase boundary (see arrows). It now appears as a bright strip. In a previous investigation [11] we found that along such defects flux lines are very mobile, while they are strongly pinned in the perpendicular direction. For an attractive interaction flux lines are attracted towards the tip if scanned across the line defect, whereby the whole crystal defect appears bright, even if only a few flux lines are attached to it. If the interaction is repulsive, like in (a) and (b), flux lines are pushed to the side along the line defect and are therefore not imaged. Note further, that on the left side of the line defect only a few individual antiflux lines are visible, while their density is much larger on the right side. This inhomogeneous distribution occurs, because the antiphase boundary can accommodate a large amount of flux lines, which then repel other flux lines of the same polarity. Clearly, the advance
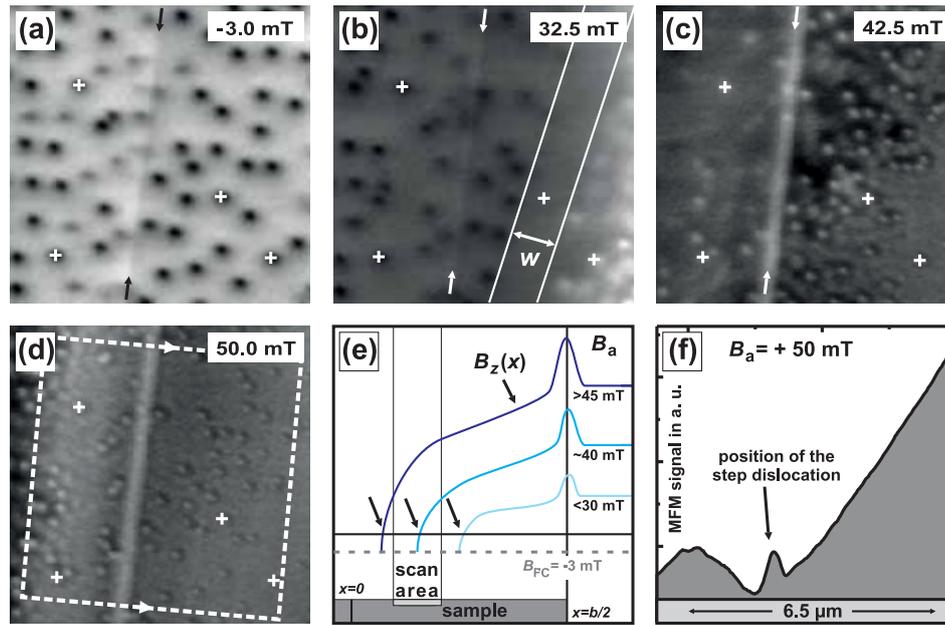
Figure 3.53: (a) MFM image of the flux glass state after field cooling in $B_{\mathrm{FC}} = -3$ mT (scan area: $a_{\mathrm{scan}} = 7\ \mu$m $\times\ 7\ \mu$m). (b) After increasing B_{a} to 32.5 mT, the flux-antiflux boundary is visible as *zone of zero vortex density* between the parallel lines separated by $w \approx 1\ \mu$m. (c) At 42.5 mT the antiflux region have reached the antiphase boundary (marked by arrows), which now appears as bright strip. (d) The situation after complete magnetization reversal of the scan area. (e) Sketch of the experimental situation according to the 1-dimensional transversal Bean model [12,13]. Flux penetration $B_z(x)$ (mirror symmetric with respect to the sample center at $x = 0$) with increasing field and propagation of the boundary (see arrows) with respect to the scan area is shown. The dashed line corresponds to the homogeneous flux density after field cooling. (f) Averaged cross section taken perpendicular to the line defect in the boxed area from (d). Due to the stacking fault dislocations, the flux density changes not monotonically.

of the flux-antiflux boundary is much stronger inhibited by the presence of such an extended planar crystal defect perpendicular to the propagation direction than by a porous random distribution of point-like defects.

Further increasing of B_a results in a complete magnetization reversal of the imaged area, as visible in (d). The flux line density is so large that only the strongly pinned vortices can be identified, because they repel the more mobile flux lines, leaving a dark ring around them. According to the transversal Bean model sketched in (e), the flux line density between the flux-antiflux boundary and the sample edges should decrease monotonically towards the sample center. Since the magnitude of the MFM signal is proportional to the magnetic field generated by the flux lines, density variations can still be detected [4]. In (f) the average cross section taken perpendicular to the incoming antiflux front from the boxed area in (d) is displayed. Right to the antiphase boundary a steady decrease of the flux density towards the sample center is observed. Where the antiphase boundary intersects the surface the flux density is enhanced, but reduced in the vicinity, due to the repulsion between flux lines of the same polarity. Thereby, a non-monotonic flux distribution is induced near such a defect. It can be concluded that randomly distributed point defects result in a flux line distribution as predicted by the Bean model, while strong deviations are induced by extended planar defects perpendicular to the propagation direction, which can accommodate a large number of flux lines. At even larger flux densities we observed unexpected shifts of the MFM signal, which are related to very long-range interaction between the magnetic tip and the current and flux distribution at the flux front [14]. This effect has to be considered, when interpreting MFM data with respect to the Bean model in the high flux density regime.

References

[1] A. Moser et al., Phys. Rev. Lett. **74**, 1847 (1995).

[2] A. Volodin et al., Appl. Phys. Lett.**73**, 1134 (1998).

[3] M. Roseman and P. Grütter, New J. Phys. **3**, 24 (2001).

[4] U. H. Pi et al., J. Low Temp. Phys. **131**, 993 (2003).

[5] C. Jooss, Rep. Prog. Phys. **65**, 651 (2002).

[6] A. Schwarz et al., Appl. Phys. Lett. **88**, 012507 (2006).

[7] C. P. Bean, Phys. Rev. Lett. **8**, 250 (1962).

[8] M. Liebmann et al., Rev. Sci. Instr. **73**, 3508 (2002).

[9] T. Albrecht et al., Appl. Phys. Lett. **69**, 668 (1991).

[10] T. W. Lee et al., Progress in Superconductivity **3**, 36 (2001).

[11] U. H. Pi et al., Phys. Rev. B **69**, 094518 (2004).

[12] E. H. Brandt and M. Indenbom, Phys. Rev. B **48**, 12893 (1993);

[13] E. Zeldov et al., Phys. Rev. B **49**, 9802 (1994).

[14] U. H. Pi et al., Phys. Rev. B **73**, 144505 (2006).

3.3 Semiconductor nanostructures

3.3.1 Two- and three-dimensional electron systems in III/V semiconductors

Introduction

Two-dimensional (2D) and three-dimensional (3D) phase transitions have been of considerable interest as they may be the paradigms of a quantum phase transition [1]. Three prominent examples, metal-insulator (MI) [2], quantum Hall (QH) [3], and superconductor-insulator [4] transitions can be described by microscopic percolation like models [5–7], which may be even unified [8, 9]. The macroscopic aspect of the percolative behavior has been verified by the transport measurements [5, 10, 11], leading to the universal values of the critical exponents (describing the divergence of the correlation length at the transition). However, no experiment so far has clarified the most fundamental and microscopic aspect, i.e. how the electron wave functions behave at the transition in real space. Here we study the microscopic percolative nature of the QH transition in the integer QH (IQH) regime. By scanning tunnel spectroscopy (STS), we directly probe, at high spatial and energy resolution, the local density of states (LDOS) of a 2D electron system (2DES) in high magnetic fields (B) up to 12 T. The observed LDOS spectra reveal that the spin- and Landau levels (LL) energetically fluctuate with position. This is reproduced by single-particle calculations including the known electrostatic potential disorder, demonstrating our ability to probe the intrinsic states in the IQH regime. We find that the localized electron states observed on the LL tail coalesce and finally fully percolate to the whole area as the energy is varied toward to the LL centre. This indeed proves the theoretically proposed picture of the QH transition from the localized to extended states [12]. The strongly corrugated charge density of the percolating states suggests the occurrence of the quantum tunneling which plays a key role in the quantum phase transition [13, 14].

References

[1] Sondhi, S. L., Girvin, S. M., Carini, J. P. and Shahar, D. Continuous quantum phase transitions. Rev. Mod. Phys. **69**, 315–333 (1997).

[2] Abrahams, E., Kravchenko, S. V. and Sarachik, M. P. Colloquium: Metallic behavior and related phenomena in two dimensions. Rev. Mod. Phys. **73**, 251–266 (2001).

[3] Huckestein, B. Rev. Mod. Phys. **67**, 357 (1995).

[4] Jaeger. H. M., Haviland, D. B., Goldman, A. M. and Orr, B. G. Threshold for superconductivity in ultrathin amorphous gallium films. Phys. Rev. B **34**, 4920–4923 (1986).

[5] Meir, Y. Prcolation-type Description of the metal-insulator transition in two dimensions. Phys. Rev. Lett. **83**, 3506–3509 (1999).

[6] Huckestein, B. &Kramer, B. One-parameter scaling in the lowest Landau band: precise determination of the critical behavior of the localization length. Phys. Rev. Lett. **64**, 1437–1440 (1990).

[7] Fisher, M. P. A. Quantum phase transitions in disordered two-dimensional superconductor. Phys. Rev. Lett. **65**, 923–926(1990).

[8] Shimshoni, E., Auerbach, A. & Kapitulnik, A. Transport through quantum melts. Phys. Rev. Lett. **80**, 3352–3355 (1998).

[9] Dubi, Y., Meir, Y. & Avishai, Y. Unifying model for several classes of two-dimensional phase transition. Phys. Rev. Lett. **94**, 156406 (2005).

[10] Wei, H.P., Tsui, D. C., Paalanen, M. A. & Pruisken, A. M. M. Experiments on delocalization and universality in the integral quantum Hall effect. Phys. Rev. Lett. **61**, 1294–1296 (1988).

[11] Haviland, D. B., Lie, Y. & Goldman, A. M. Onset of superconductivity in the two-dimensional limit. Phys. Rev. Lett. **62**, 2180–2183 (1989).

[12] Joynt, R. & Prange, R. E. Conditions for the quantum Hall effect. Phys. Rev. B **29**, 3303–3317 (1984).

[13] Ando, T. Electron localization in a two-dimensional system in strong magnetic fields. II. Long-range scatterers and response functions. J. Phys. Soc. Jpn. **53**, 3101–3111 (1984).

[14] Kramer, B., Ohtsuki, T. & Kettemann, S. Random network models and quantum phase transitions in two dimensions. Phys. Rep. **417**, 211–342 (2005).

Evolution of drift states of the 2DES on Fe/InAs(110) in high magnetic fields

K. Hashimoto, F. Meier, J. Wiebe, M. Morgenstern, and R. Wiesendanger

To explore the microscopic nature of the quantum Hall system, we also investigated the Fe (3.9% ML) induced 2DES on n-InAs(110) ($N_\mathrm{D} = 3 * 10^{16}$ cm^{-3}), which was previously studied at $B = 0$ T [5] and below 6 T [6] by our group. Here, we examine the local density of states (LDOS) in detail at higher magnetic fields up to 12 T. According to the previous study [5], the onset of the first and second subbands of the 2DES should appear at sample voltages (V_s) of -108 mV and -43 mV, respectively. In Fig. 3.54, the spatially averaged dI/dV curve taken at 0 T shows a steplike feature, i.e., a signature of the onset of the second subband of the 2DES at V_s= 45mV, while such a feature due to the first subband is hidden by the peak of the tip-induced quantum dot (QD) state [1] appearing near $V_\mathrm{s} = -120$ mV. We applied strong magnetic fields of 8.5 T and 12 T. The corresponding curves show regularly separated peaks with large energy separations. The peak separation corresponds to the Landau level (LL) separation $E_\mathrm{C} = \hbar\omega_\mathrm{C} = \hbar e B / m_\mathrm{InAs}$ (m_InAs: effective mass of InAs); For instance, $E_\mathrm{C} \approx 43$ meV at 8.5 T. Note, that the LL separation slightly decreases with energy since m_InAs increases with energy.

Figures 3.55 (a) and (b) show spatial maps of the LDOS in the tails of the LLs at $B = 8.5$ T and 12 T, respectively [the measuring V_s are marked by arrows in Fig. 3.54]. One can see irregularly distributed, elongated stripe-like structures. Similar structures
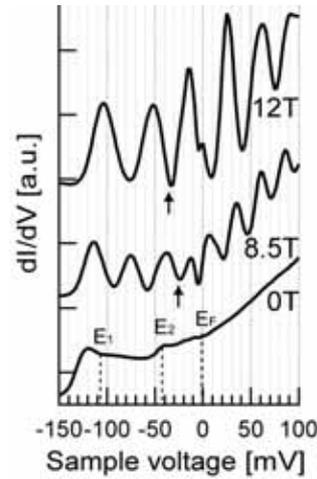
Figure 3.54: dI/dV curves spatially averaged over $350*350$ nm^2 for different B-fields: $I_{\text{stab}} = 0.4$ nA, $V_{\text{stab}} = 0.2$ V, $V_{\text{mod}} = 2$ mV. Subband energies E_1, E_2, and the Fermi level E_{F} are indicated in (b).

were previously observed at $B = 6$ T [6] and interpreted as drift states since their width is close to the magnetic length ($l_{\text{B}} \approx 10$ nm at 6 T). The width of these structures observed in our experiments at higher magnetic fields is about 8 nm which is close to $l_{\text{B}} \sim 9$ nm at 8.5 T and $l_{\text{B}} \sim 7.5$ nm at 12 T, suggesting that the observed structures are indeed drift states. In the tail of the LL, the drift states are localized
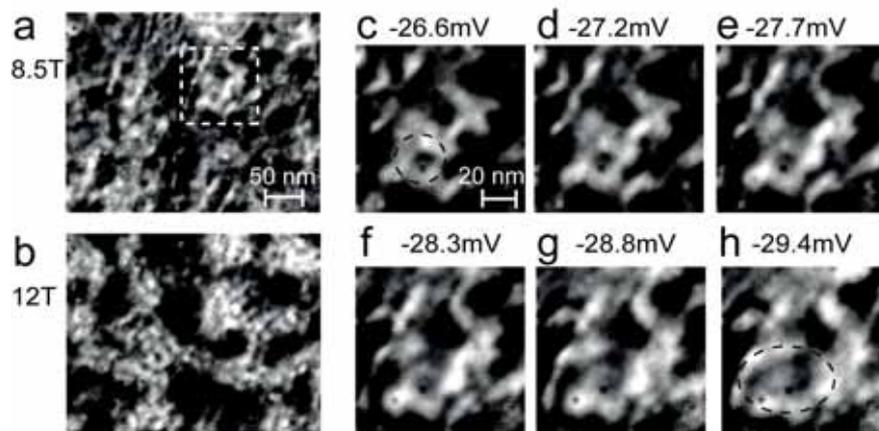
Figure 3.55: Spatial maps of LDOS: $I_{\text{stab}} = 0.4$ nA, $V_{\text{stab}} = 0.2$ V (a) $V_{\text{s}} = -25.0$ mV, $V_{\text{mod}} = 1$ mV and $B = 8.5$ T. (b) $V_{\text{s}} = -37.0$ mV, $V_{\text{mod}} = 1$ mV, $B = 12$ T; the same area as (a). (c) - (h) Evolution of the drift state with energy (V_{s} is indicated in the figure) in the area marked in (a).: $V_{\text{mod}} = 0.4$ mV and $B = 8.5$ T; A loop-like structure guided by the dotted circle in (c) expands to the larger structure guided in (h).

around the maxima or minima of the potential landscape and expected to appear as loop-like structures. In Figs. 3.55 (a) and (b), some drift states indeed show loop-like structures with the diameters of 20–50 nm. An interesting property of such drift states is their energy dependency. Since the energetically adjacent states appear along adjacent equipotential lines, the drift state should jump to adjacent equipotential lines by varying the energy. The change of the area (ΔS) accompanied with the jump is expected to be close to the area occupied by one magnetic flux quantum, $2\pi\hbar/eB$ [2]. Indeed, this can be observed in Figs. 3.55 (c)–(h), which are recorded in the marked area in Fig. 3.55 (a) at $B = 8.5$ T. One can see a looplike structure [marked by a circle in Fig. 3.55 (c)] settling between $V_\mathrm{s} = -26.6$ mV and -27.7 mV. It, however, quickly expands between $V_\mathrm{s} = -28.3$ mV and -28.8 mV and finally becomes a larger loop at $V_\mathrm{s} = -29.4$ mV. The increase of the area ΔS is close to the expected value $2\pi\hbar/eB = 486$ nm^2 as calculated using $B = 8.5$ T. The corresponding areas covering approximately one and two flux quanta are indicated in Figs. 3.55 (c) and (h) by a circle and an ellipse, respectively, for comparison.

Influence of the adsorbates on the 3DES of low doped n-InSb(110)

K. Hashimoto, F. Meier, J. Wiebe, M. Morgenstern, and R. Wiesendanger

We additionally studied the influence of adsorbates on the 3DES using low doped n-InSb ($N_\mathrm{D} = 1.4 * 10^{14}$ cm^{-3}). It is well known that the 3DES of the III-V narrow
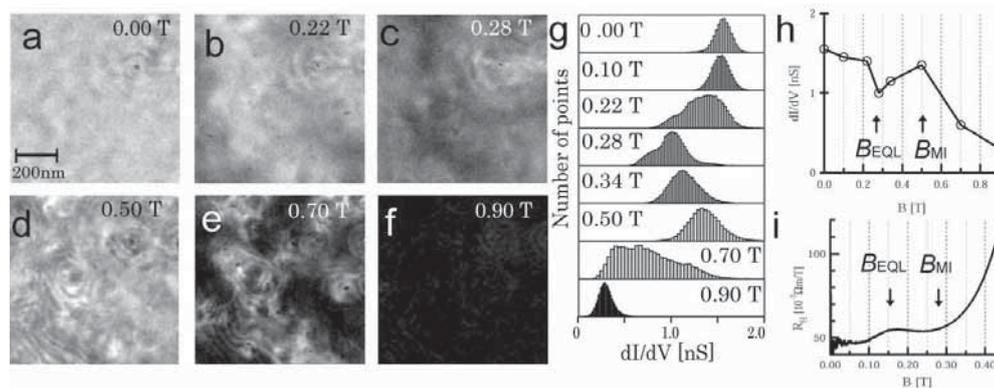
Figure 3.56: (a)-(f) Selected dI/dV maps at $V_\mathrm{s} = 0$ mV and at different B-fields as indicated. The contrast of the images is aligned, i.e., the same gray value represents the same local conductivity in each image. $V_\mathrm{stab} = 200$ mV, $I_\mathrm{stab} = 500$ pA, and $V_\mathrm{mod} = 0.6$ mV. All images show the same area. (g) Histograms of dI/dV values taken from (a)-(f) at different B-fields as indicated. (h) Averaged dI/dV values as a function of B-field. (i) Hall resistance, $R_\mathrm{H} = \rho_\mathrm{xy}/eB$, deduced from transport measurements.

gap semiconductors shows a transition to the extreme quantum limit (EQL) followed by a MI transition at high magnetic fields. The LDOS in the EQL was studied by our group on n-InAs with an electron density of 1–$2*10^{16}$ cm^{-3} [3], but the MI-transition was not accessible in this sample ($B_{\mathrm{MI}} > 9$ T). Using low doped n-InSb, both the EQL and the MI-transition are easily attainable with our experiments ($B_{\mathrm{EQL}} = 0.15$ T, $B_{\mathrm{MI}} = 0.28$ T). Figures 3.56 (a)-(f) show the $d\mathrm{I}/d\mathrm{V}$ images of the same surface area of $800*800$ nm^2 at E_{F} and at different B-fields. The LDOS patterns appear rather uncorrugated at $B = 0$ T and at low magnetic fields (not shown). At $B = 0.22$ T, the image starts corrugating with a long range contrast. At $B = 0.5$ T a serpentine-like structure appears, while an additional long range contrast is rather dominant at $B = 0.7$ T. At $B = 0.9$ T the overall intensity is strongly decreased. Figure 3.56 (g) shows histograms of the $d\mathrm{I}/d\mathrm{V}$-values contributing to the images. This clearly demonstrates that the LDOS distribution shifts alternately up and down above $B = 0.28$ T. To clarify the magnetic field dependency, the averaged $d\mathrm{I}/d\mathrm{V}$-value, $(d\mathrm{I}/d\mathrm{V})_{\mathrm{avera}}$, is plotted as a function of the magnetic field in Fig. 3.56 (h). It turns out that the oscillation with the magnetic field (magneto-oscillation) shows a minimum at $B = 0.28$ T, a maximum at $B = 0.5$ T and then abruptly decreases above $B = 0.50$ T. At 0.90 T, $(d\mathrm{I}/d\mathrm{V})_{\mathrm{avera}}$ finally diminishes to 0.2 nS and the corresponding image [Fig. 3.56 (f)] becomes featureless, suggesting that we reach the insulating phase. The observed magneto-oscillation is consistent with the well-known magneto-oscillation of the Hall resistance which shows an enhancement near B_{EQL}, and an abrupt decrease above B_{MI}. The observed reduction of the averaged LDOS should increase the Hall resistance. We therefore determine B_{EQL} and B_{MI} to be 0.28 T and 0.50 T, respectively. To compare the observed transition points with the bulk transition points, we performed transport measurements, which are shown in Fig. 3.55 (i). The determined bulk transition points are $B_{\mathrm{EQL}} = 0.15$ T $B_{\mathrm{MI}} = 0.28$ T. It turns out that transition points determined by the SPS experiments are higher than the bulk transition points. We speculate that a small amount of adsorbates on the surface gives impact to the electronic property of the 3DES near the surface and therefore shifts the transition points.

To investigate the influence of the adsorbates, we cleave the same low-doped n-InSb at a higher pressure of 10^{-8} mbar. As a result, we observed adsorbates with the density of 30 adsorbates/100nm $*$ 100nm (not shown). Using the $d\mathrm{I}/d\mathrm{V}$-peak of the tip-induced QD state [Fig. 3.57 (a)] [2], we mapped the potential landscape as indicated in Fig. 3.57 (b). The fluctuation of the QD peak shows 9 potential minima which are about 20 meV in depth. Since the expected number of the substrate donors in the probed area is only 0.1, the observed potential minima are mainly induced by the adsorbates. In contrast to the cleaner sample shown in Fig. 3.56, the $d\mathrm{I}/d\mathrm{V}$ images now start corrugating not until $B = 2$ T (not shown). We therefore conclude, that the EQL is shifted to $B_{\mathrm{EQL}} > 2$ T. When the magnetic field is further increased to 4.0 T, we observe an apparent serpentine contrast in the $d\mathrm{I}/d\mathrm{V}$ image as shown in Fig. 3.57 (c). Note, that the magnetic field is now one order of magnitude higher than the magnetic field at which we observed the serpentine contrast on the cleaner sample
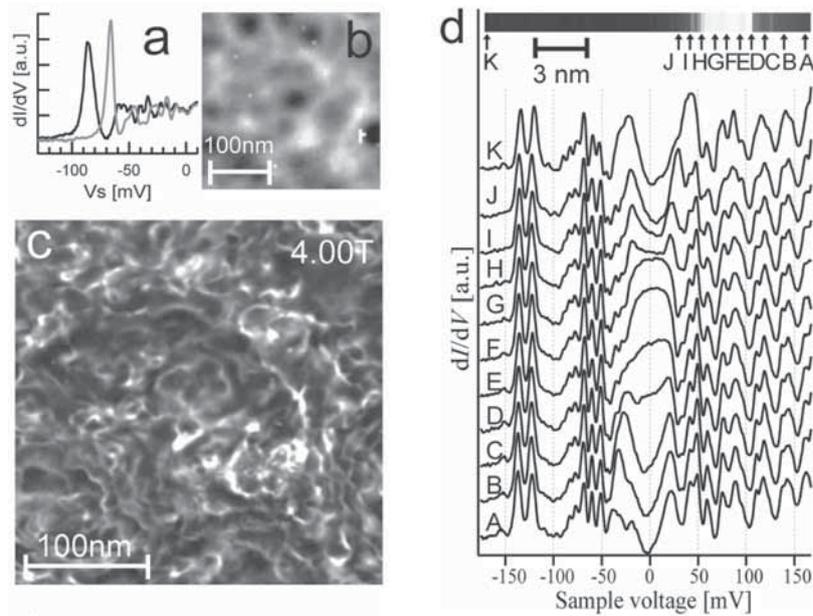
Figure 3.57: (a) $d\mathrm{I}/d\mathrm{V}$ curves taken at $B = 0$ T in the two different areas where the peak associated with the tip-induced quantum dot state shifts to the lowest and highest voltages. (b) Potential landscape as determined from the laterally fluctuating QD peak voltage at $B = 0$ T. (c) $d\mathrm{I}/d\mathrm{V}$ map at $V_\mathrm{s} = 0$ mV and $B = 4$ T in the same area as (b) ; $V_\mathrm{stab} = 300$ mV, $I_\mathrm{stab} = 1.5$ nA, and $V_\mathrm{mod} = 1$ mV. (h) $d\mathrm{I}/d\mathrm{V}$ curves taken at $B = 4.10$ T and different positions indicated in the inset; $V_\mathrm{stab} = 300$ mV, $I_\mathrm{stab} = 1.5$ nA, and $V_\mathrm{mod} = 1$ mV. Inset: $d\mathrm{I}/d\mathrm{V}$ line map at $V_\mathrm{s} = 0$ mV. Measurement positions are labeled by letters which correspond to the letters on each curve.

[Fig. 3.56 (d) and (e)]. Several ring-like structures with diameters of 20–60 nm can be seen. Figure 3.57(d) shows the $d\mathrm{I}/d\mathrm{V}$ curves taken at $B = 4.10$ T and at different positions on a line across a serpentine structure. The positions are labeled by A to K and indicated in the $d\mathrm{I}/d\mathrm{V}$ image in the inset, where one serpentine is visible as a bright stripe. The obtained curves show peaks at $V_\mathrm{s} < -20$ mV and an oscillation at $V_\mathrm{s} > 20$ mV which are caused by the states of the tip induced QD and of the spin-split Landau levels, respectively. At $-20\mathrm{mV} < V_\mathrm{s} < 20\mathrm{mV}$, i.e. near E_F, a distinct feature is observed. On the position A and K, i.e., far away from the serpentine line, the feature shows a gap-like structure. As crossing the serpentine structure, the gap degrades and then changes to a hump-like structure on the position of the serpentine (position F). Since we do not observe any shifts of the QD peaks across the serpentine, we can rule out that the observed serpentines are caused by a local charging of the surface due to the tunneling current. In contrast, we conclude that the gap in the LDOS found in between the serpentines is associated with localization due to electron-electron interaction [4]. The serpentine structures are thus identified with delocalized states of the 3D electron system in the external magnetic field.

References

[1] R. Dombrowski, Chr. Steinebach, Chr. Wittneven, M. Morgenstern, and R. Wiesendangaer, Phys. Rev. B **59**, 8043 (1999).

[2] R. E. Prange and S. M. Girvin, The quantum Hall effects, Springer-Verlag New York (1989).

[3] D. Haude, M. Morgenstern, I. Meinel, and R. Wiesendanger, Phys. Rev. Lett. **86**, 1582 (2001).

[4] M. Morgenstern, D. Haude, J. Klijn, and R. Wiesendanger, Phys. Rev. B **66**, 121102 (2002).

[5] M. Morgenstern, J. Klijn, Chr. Meyer, M. Getzlaff, R. Adelung, K. Rossnagel, L. Kipp, M. Skibowski, and R. Wiesendanger, Phys. Rev. Lett. **89**, 136806 (2002).

[6] M. Morgenstern, J. Klijn, Chr. Meyer, and R. Wiesendanger, Phys. Rev. Lett. **90**, 056804 (2003) (**90**, 179901 (E)(2003)).

3.3.2 Magnetic dopants and adatoms on III/V semiconductors

Introduction

Diluted magnetic semiconductors show promise for seamless integration of magnetic elements in electronic devices [19–22]. However, the ongoing search for room-temperature ferromagnetism in semiconductors, a prerequisite for the realization of many of the proposed devices, calls for a detailed investigation of the local coupling between the magnetic impurities and the host material. An excellent tool for such local investigations is scanning tunneling microscopy (STM), which provides unrivaled spatial resolution [23]. Recent STM measurements revealed that the hole state bound to a Mn acceptor in GaAs [1] and InAs [2] has an anisotropic cross-like shape which persists up to short Mn-Mn distances [3]. This implies a strong influence of the shape anisotropy on the local coupling and, indeed, an anisotropic exchange interaction between neighboring Mn atoms has been observed by STM at the GaAs(110) surface [4]. The STM observations so far are in agreement with theoretical predictions [5,24]. However, the detailed influence of the Mn acceptor on the local density of states (LDOS) in the host bands, and the effect of an interface on the bound states themselves, have not been elucidated so far. The Mn acceptor state in InAs provides an opportunity for all these investigations, with well-characterized surface properties and a Mn binding energy of $E_B = 28$ meV (about one quarter the binding energy in GaAs due to a weaker p-d exchange interaction, but still about twice the hydrogenic binding energy, 17 meV [6–8]). We did a detailed study of the Mn acceptor state near the (110) surface of InAs.

Furthermore we studied the electronic structure of Fe chains *on* the (110) surface. We find that their electronic states are also strongly influenced by the substrate mediated interactions.

Local Electronic Structure near Mn Acceptors in InAs

F. Marczinowski, J. Wiebe, J.-M. Tang, M. E. Flatté, F. Meier, M. Morgenstern,
R. Wiesendanger,
[Phys. Rev. Lett. **99**, 157202 (2007)]

We show that the (110) surface leads to a substantial increase in the asymmetry of the acceptor bound hole state. Detailed spectroscopic data exhibit excited states of the acceptor, an enhancement of the valence band (VB) LDOS and reduction of the conduction band (CB) LDOS in a region of 2 nm around the acceptor, and an anisotropic shape of the scattering states in the CB. Most of the results are in accordance with tight binding model (TBM) calculations, showing the importance of local anisotropies principally caused by the p-d exchange interaction.

The Mn concentration within the InAs samples is $\sim 1 \times 10^{19}$ cm^{-3} and the samples

show paramagnetic behavior down to $T = 2$ K. The clean (110) surface is prepared by *in situ* cleavage [11]. STM topographs showing the position and the shape of the Mn acceptors are taken in constant current mode with the voltage V applied to the sample.

For the TBM calculations, we use the theory of Ref. [5], a Koster-Slater approach with a 16-band sp^3 TBM for InAs [25]. Most of the state's binding energy comes from the p-d exchange interaction, which is modeled as a spin-dependent potential (V_{pd}) present at the four 1st-nearest-neighbor sites. $V_{pd} = 2.19$ eV is set to obtain the experimental binding energy E_B. This value is smaller than the 3.634 eV previously obtained for GaAs [26]. An on-site potential (V_n) accounts for the direct Coulomb contribution to the binding energy, and is chosen to be the same value as for Mn in GaAs (1 eV). Thus,

$$V_{\mathrm{Mn}} = V_n \sum_{\ell,s} c^\dagger_{0,\ell,s} c_{0,\ell,s} + V_{pd} \sum_{\substack{j \in 1^{st}\,\mathrm{NN} \\ \ell \in p_x, p_y, p_z}} c^\dagger_{j,\ell,\uparrow} c_{j,\ell,\uparrow} , \qquad (3.14)$$

where j labels atomic sites (Mn is at $j = 0$), ℓ labels atomic orbitals, and s labels spins. The quantization axis is the spin orientation of the Mn core $3d$ electrons. The LDOS spectra are obtained by calculating the lattice Green's functions with an energy resolution of 10 meV.

Figure 3.58 shows typical $\mathrm{d}I/\mathrm{d}V(V)$ curves taken above an acceptor and on the bare InAs surface far from any Mn. The $\mathrm{d}I/\mathrm{d}V$ signal on Mn shows a sharp peak at $V_{\mathrm{peak}} \approx 0.8$ V, i.e. in the region of the bulk CB and not at the VB edge where the acceptor state is located. This apparent discrepancy is due to the tip-induced band bending (TIBB), which shifts the bound hole state across the Fermi level of the sample [1] as sketched in Fig. 3.58 (left panels). At a certain voltage, the acceptor state crosses the Fermi level resulting in a new tunneling path which appears as a peak in $\mathrm{d}I/\mathrm{d}V$. To estimate the TIBB, we use a 1D-Poisson solver neglecting the 3D potential distribution below the tip [12,27]. We use the following parameters: work function for the W tip ($\Phi_{\mathrm{tip}} = 4.5$ eV), band gap ($E_g = 0.41$ eV), electron affinity ($E_A = 4.9$ eV), Mn density (10^{19} cm^{-3}), Mn ionization energy ($E_B = 28$ meV), and tip-sample distance (6 Å). The resulting band profiles are plotted in Fig. 3.58 for different bias voltages. The flat band condition appears at $e \cdot V_{FB} = E_A + E_g - E_B/2 - \Phi_{\mathrm{tip}} \approx 0.8$ eV in good agreement with the measured V_{peak}. The position of the peak is slightly different for different acceptors due to the lateral potential fluctuations induced by neighboring charged acceptors and, in turn, can be used to estimate V_{FB} as a function of position. Notice that, for $V < V_{FB}$ ($V > V_{FB}$), the bands bend downwards (upwards) and the Mn acceptor is in the charged state A^- (neutral state A^0) [1].

An STM topograph taken at about V_{FB} is shown in Fig. 3.59(a). It mainly exhibits the shape of the acceptor states because the tunneling current through the CB states is still relatively small. The different Mn acceptors appear as anisotropic features superimposed on the As sublattice [11]. The depth of the corresponding Mn atoms below the surface is deduced from the topographic height of the observed feature and
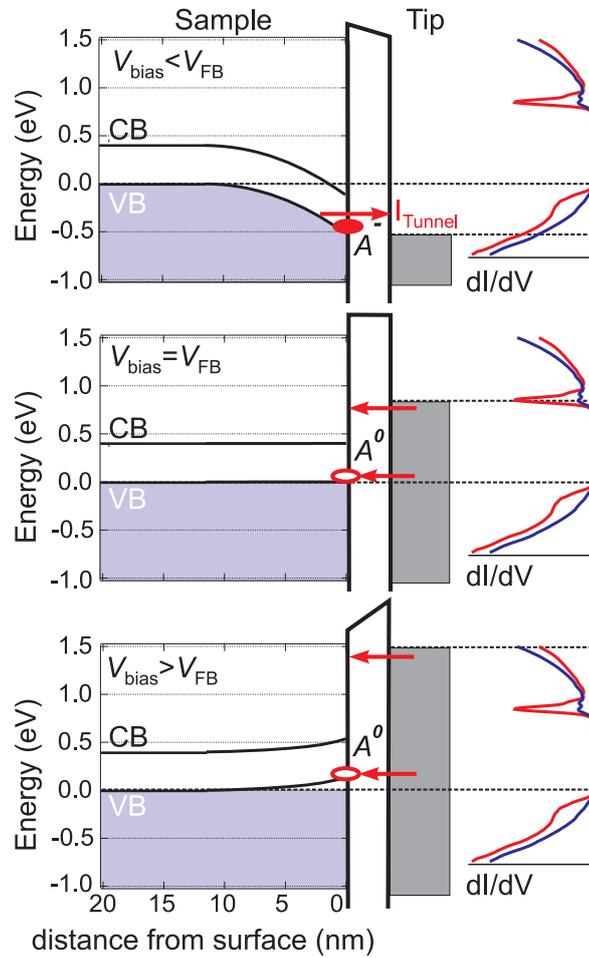
Figure 3.58: Left panels: Poisson model of the TIBB at different bias voltages as marked by the Fermi levels of tip and sample (dashed lines). The resulting tunneling paths through the neutral (A^0) or charged (A^-) acceptor are indicated. The tunneling barrier is sketched schematically. Right panels: dI/dV curves measured above a Mn site (red) and on the bare InAs surface (blue). The acceptor state appears as a peak at V_{FB}. ($V_{\mathrm{stab}} = 1.5$ V, $I_{\mathrm{stab}} = 1$ nA, $V_{\mathrm{mod}} = 20$ mV).

from the symmetry of the feature with respect to the visible surface As sublattice [1]. It is indicated by numbers (surface layer counted as 0) showing Mn atoms down to ten layers below the surface. The relative orientation of In and As rows deduced from voltage dependent topographs of the bare surface [11] is sketched in Fig. 3.59(b). A corresponding side view is sketched in Fig. 3.59(c). Figure 3.59(d) shows the experimentally observed topographs for Mn atoms at different depths together with the calculated LDOS at the Mn acceptor level in bulk InAs at different distances from the Mn. The topographic height is compared directly with the logarithm of the LDOS [1].

The general shapes of the acceptor states are rather similar to the ones observed for Mn in GaAs [1, 4]. However, a systematic depth dependence has not been shown for GaAs. Interestingly, the topographic height for the surface Mn appears to be 40 % lower than for Mn in the 1st subsurface layer. Although the TBM data largely reproduce the extension and the general shape of the acceptor state, obvious discrepancies are found, in particular, with respect to the (001) mirror plane. For example, the states in the 2nd layer appear brighter above the (001) mirror plane within the STM data but brighter below the (001) mirror plane within the TBM data. The agreement between TBM and STM improves with increasing Mn depth and the shapes are nearly identical for the 8th and 9th layer. This depth corresponds to about half the lateral
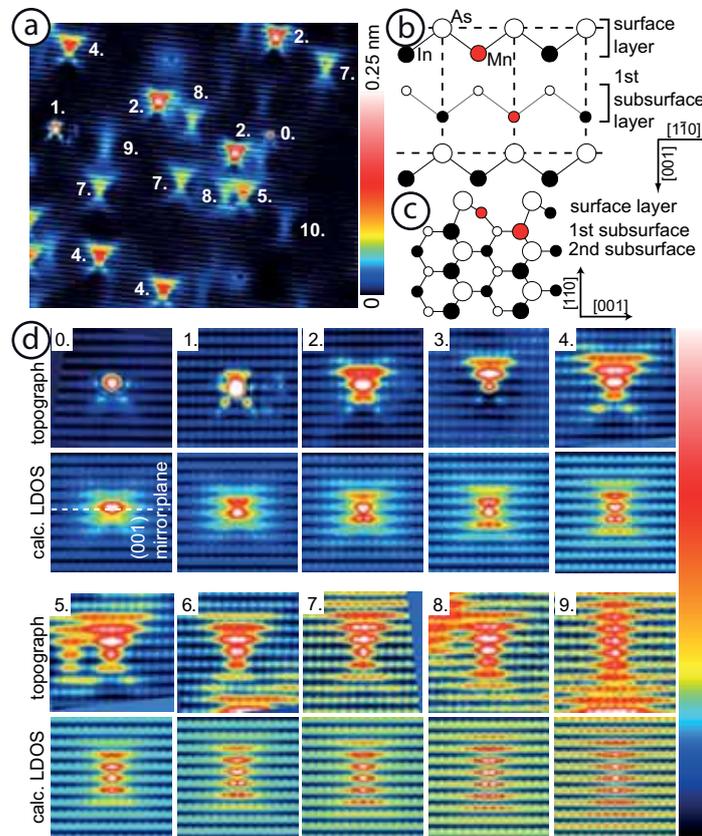
Figure 3.59: (a) Topograph at a voltage close to the acceptor level ($320 \times 365\text{Å}^2$, 1.0 V, 0.5 nA). The layer number below the surface where the Mn is located is marked (surface layer counted as 0). (b) Top view model of the (110) surface aligned with the experimental images (surface orientation determined according to [11]); a Mn in the surface and 1st subsurface layer is added; (c) side view according to (b) [11]. (d) Topographs of Mn atoms at different layer depths compared with calculated LDOS at the acceptor energy at different distances from the Mn as marked. The LDOS is plotted on a logarithmic scale with a spatial broadening factor of 2Å.

extension of the acceptor. Therefore, we conclude that the relaxed InAs(110) surface sketched in Fig. 3.59(c), which is not included in the calculations, has a significant influence on the spatial distribution of the Mn hole state down to about 7 layers. Recently strain (from an embedded quantum dot) was shown to distort the Mn acceptor wave function in GaAs, lowering the spatial symmetry of the acceptor state [26].

Figure 3.60(a) shows $\mathrm{d}I/\mathrm{d}V$ curves on Mn acceptors in different layers. The characteristic peak voltage (A) depends on the spatial position of the Mn, with $V_{\mathrm{peak}} = 0.4 - 0.9$ V (cf. peaks of the two 2$^{\mathrm{nd}}$-layer acceptors (1), (2)). The differences are caused by potential fluctuations due to the random distribution of charged dopants [17]. Close inspection of the upper $\mathrm{d}I/\mathrm{d}V$ curves reveals at least two additional peaks (B) and (C) above peak (A), with an energetic separation of about 200 mV. These peaks, which appear exclusively around acceptors, but never on the bare InAs, thus must be attributed to the Mn. Due to TIBB the undisturbed level spacings to the ground state (A) are a factor of five smaller as can be calculated using the Poisson solver with the corresponding V_{FB}. They are, therefore, 40 mV (B) and 80 mV (C). These splittings are too large to be splittings of the $J = 1$ acceptor ground state by reasonable strains or local electric fields [28]. Similar to the case for Mn in GaAs, our TBM calculations predict that the spin-orbit interaction leads to higher-energy spin states of the bound hole at ~ 25 meV and ~ 75 meV above the $J = 1$ ground state. They are shown in Fig. 3.60(d) and are in good agreement with the experimental data. The excited spin states of neutral Mn acceptors have previously been measured optically [29], but here are seen for the first time for an individual Mn on the local scale.

The influence of the Mn acceptor on the CB and VB can be revealed after subtraction of the $\mathrm{d}I/\mathrm{d}V$ curve obtained on bare InAs. Corresponding curves above different Mn atoms are shown in Fig. 3.60(b). Besides the peaks (A), (B), (C), an increase in VB LDOS by up to 400 % and a 10 % reduction in CB LDOS is observed [1]. The same trend is found in the TBM calculations shown in Fig. 3.60(d), and is due to the stronger influence of the *p-d* exchange interaction on the valence band than on the conduction band. Normalized $\mathrm{d}I/\mathrm{d}V$ curves as shown in Fig. 3.60(b) are grey scaled in Fig. 3.60(c) up to 4.5 nm away from the Mn. They reveal that the CB suppression and VB enhancement have about the same extension as the acceptor state of 2 nm, and depend only slightly on energy. A more detailed analysis shows anisotropies which are visible in the calculated LDOS in Fig. 3.61(a)-(e) as deviations from the circular shape of the dark area around the Mn. More importantly, the extension of the dark area indicating CB suppression is also about 2 nm in the TBM.

Around the depression region of the neutral acceptor, also visible in the $\mathrm{d}I/\mathrm{d}V$ maps of Fig. 3.61(g) and (h), a ring-like structure appears, which shrinks in diameter with increasing V as expected for the CB scattering states of InAs [18]. The signal for the scattering states is weak in the calculated LDOS, but visible as a slight en-

---

[1]At about 1.75 eV the differential tunneling conductance starts to rise due to the onset of surface states.
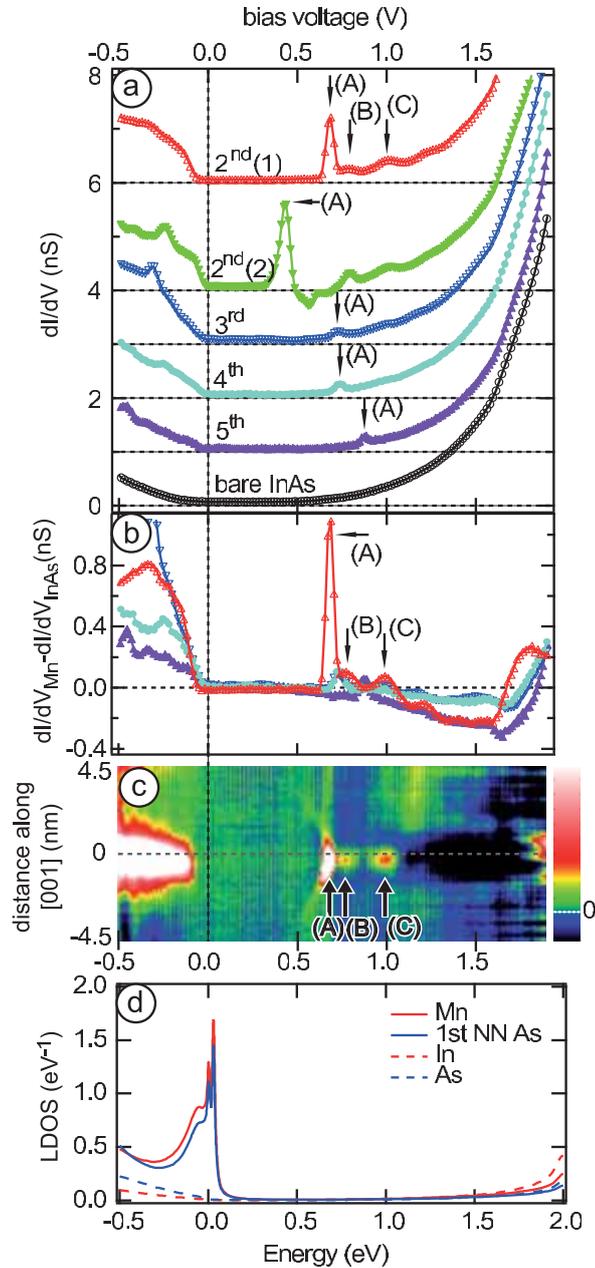
Figure 3.60: (a) Spatially resolved dI/dV curves from the bare InAs and on Mn in different subsurface layers as marked ($2^{nd}(1)$ and $2^{nd}(2)$ denote two different 2nd layer Mn acceptors). Curves are offset for clarity with dotted zero lines. (b) dI/dV curves on Mn from (a) after subtraction of the InAs curve. (c) Voltage dependent section of the relative differential conductance across a Mn in the 2nd layer. Acceptor-related peaks (A,B,C) are marked ($V_{stab} = 2$ V, $I_{stab} = 2$ nA, $V_{mod} = 20$ mV). (d) Calculated LDOS at the Mn site, the 1st-nearest-neighbor sites, and at the bare In and As sites.
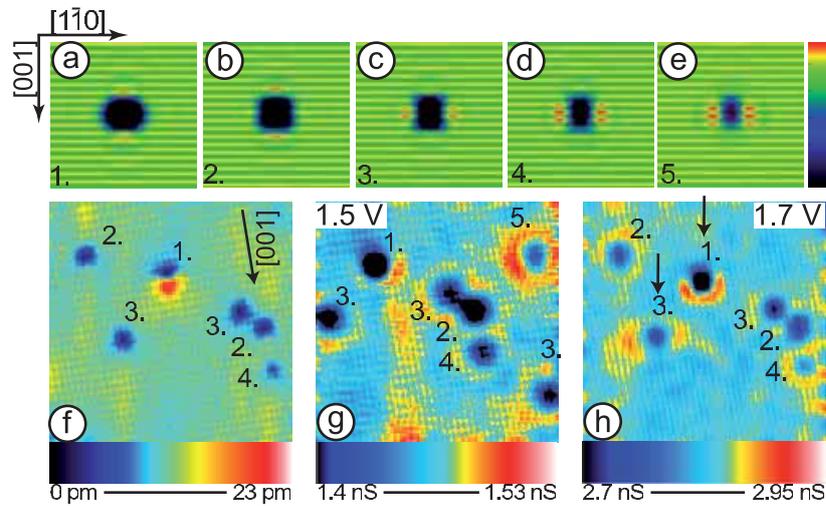
Figure 3.61: (a)-(e) $108 \times 108 \text{Å}^2$ cross-sectional views of the calculated LDOS at 1.4 eV; spatial broadening factor: 5 Å. The distance from the Mn is indicated. (f) $180 \times 180 \text{Å}^2$ topograph taken at $V_{\text{stab}} = 2$ V. (g),(h) dI/dV maps of an area with the same Mn acceptors as in (f) taken at the indicated voltages.

hancement of row intensity above and below the dark region in Fig. 3.61(a) and (b) and as a slight enhancement right and left of the dark region in Fig. 3.61(c)-(e). The calculated anisotropy of the scattering states depends in detail on the layer as well as on the energy and the strength of the p-d interaction. It is found in a similar fashion in the experimental data, e.g. in Fig. 3.61(h), as a preferential scattering along $[\bar{1}10]$ for the 3$^{\text{rd}}$ layer Mn, but along $[001]$ for the 1$^{\text{st}}$ layer Mn (see arrows). However, a more detailed analysis based on additional data is required to extract further information about the p-d interaction beyond the value of V_{pd} we have reported here.

References

[1] A. M. Yakunin, A. Y. Silov, P. M. Koenraad, J. H. Wolter, W. V. Roy, , J. D. Boeck, J.-M. Tang, M. E. Flatté: Phys. Rev. Lett. **92**, 216801 (2004).

[2] P. I. Arseev, N. S. Maslova, V. I. Panov, S. V. Savinov, C. van Haesendock: JETP Lett. **77**, 172 (2003).

[3] A. M. Yakunin, A. Y. Silov, P. M. Koenraad, J.-M. Tang, M. E. Flatté, W. V. Roy, J. D. Boeck, J. H. Wolter: Phys. Rev. Lett. **95**, 256402 (2005).

[4] D. Kitchen, A. Richardella, J.-M. Tang, M. E. Flatté, A. Yazdani: **442**, 436 (2006).

[5] J.-M. Tang, M. E. Flatté, Phys. Rev. Lett. **92**, 47201 (2004).

[6] E. Georgitse, I. Postolaki, V. Smirnov, P. Untila: Sov. Phys. Semicond. **23**, 469 (1989).

[7] A. Baldereschi, N. O. Lipari: Phys. Rev. B **8**, 2697 (1973).

[8] J. Okabayashi, T. Mizokawa, D. D. Sarma, A. Fujimori, T. Slupinski, A. Oiwa, H. Munekata: Phys. Rev. B **65**, 161203 (2002).

[9] J. Wiebe, A. Wachowiak, F. Meier, D. Haude, T. Foster, M. Morgenstern, R. Wiesendanger, Rev. Sci. Instrum. **75**, 4871 (2004).

[10] C. Wittneven, R. Dombrowski, S. H. Pan, R. Wiesendanger: Rev. Sci. Instrum. **68**, 3806 (1997).

[11] J. Klijn, L. Sacharow, C. Meyer, S. Blügel, M. Morgenstern, R. Wiesendanger, Phys. Rev. B **68**, 205327 (2003).

[12] R. Dombrowski, Chr. Steinebach, Chr. Wittneven, M. Morgenstern, R. Wiesendanger, Phys. Rev. B **59**, 8043 (1999).

[13] R. de Kort, M. C. M. M. van der Wielen, A. J. A. van Roij, W. Kets, H. van Kempen: Phys. Rev. B **63**, 125336 (2001).

[14] G. Mahieu, B. Grandidier, D. Deresmes, J. P. Nys, D. Stiévenard, P. Ebert: Phys. Rev. Lett. **94**, 026407 (2005).

[15] S. Loth, M. Wenderoth, L. Winking, R. G. Ulbrich, S. Malzer, G. H. Döler: Phys. Rev. Lett. **96**, 066403 (2006).

[16] S. Loth, M. Wenderoth, L. Winking, R. G. Ulbrich, S. Malzer, G. H. Döler: Jpn. J. Appl. Phys. **45**, 2193 (2006).

[17] M. Morgenstern, J. Klijn, C. Meyer, M. Getzlaff, R. Adelung, R. Römer, K. Rossnagel, L. Kipp, M. Skibowski, R. Wiesendanger, Phys. Rev. Lett. **89**, 136806 (2002).

[18] C. Wittneven, R. Dombrowski, M. Morgenstern, R. Wiesendanger: *Scattering States of Ionized Dopants Probed by Low Temperature Scanning Tunneling Spectroscopy.* Phys. Rev. Lett. **81**, 5616 (1998).

[19] H. Ohno, Science **281**, 951 (1998)

[20] D. D. Awschalom, N. Samarth, and D. Loss, eds., Semiconductor Spintronics and Quantum Computation (Springer-Verlag, 2002).

[21] A. H. MacDonald, P. Schiffer and N. Samarth, Nature Mater. **4**, 195 (2005)

[22] D. D. Awschalom and M. E. Flatté, Nature Physics **3**, 153 (2007)

[23] R. Wiesendanger, *Scanning Probe Microscopy and Spectroscopy*, Cambridge University Press, 1994

[24] P. Mahadevan, A. Zunger and D. D. Sarma, Phys. Rev. Lett. **93**, 177201 (2004)

[25] D. J. Chadi, Phys. Rev. B **16**, 790 (1977)

[26] A. M. Yakunin *et al.*, Nature Mater. **6**, 512 (2007)

[27] G. J. de Raad, D. M. Bruls, P. M. Koenraad, and J. H. Wolter, Phys. Rev. B **66**, 195306 (2002).

[28] J.-M. Tang, J. Levy and M. E. Flatté, Phys. Rev. Lett. **97**, 106803 (2006)

[29] M. Linnarsson *et al.*, Phys. Rev. B **55**, 6938 (1997)

Effect of charge manipulation on scanning tunneling spectra of single Mn acceptors in InAs

F. Marczinowski, J. Wiebe, F. Meier and R. Wiesendanger

In the following we show, that the STM tip can be used to switch the Mn acceptor from a neutral to a negative charge state using negative bias voltages. In topographic STM measurements we observe voltage dependent ring-like depressions around each individual Mn-acceptor. In STS-measurements, the observation is even more pronounced and shows up as rings of significantly increased differential tunneling conductance, often with diameters as large as 20 nm, which shrink with increasing voltage. Sometimes, we find that this is followed by a combination of a peak and negative differential conductance, which in contrast are strongly localized to the acceptor. We conclude, that the ring feature is the signature of charging/discharging each individual acceptor, and that the second feature is due to direct tunneling through the localized acceptor state. Using the ring feature one can deduce the shape of the tip induced quantum dot and the screening behaviour of the acceptor.

Our samples were commercially produced Mn-doped InAs single crystals with doping concentrations of $1 \times 10^{17}\,\mathrm{cm}^{-3}$ and $1 \times 10^{19}\,\mathrm{cm}^{-3}$. Since these Mn-densities are well below the solubility limit, the samples are virtually free of unwanted defects like interstitial Mn or MnAs clusters, otherwise found in highly doped Mn samples. The crystals were cleaved at room temperature under UHV condition along the (110)-plane, resulting in an almost defect-free surface. We emphasize that the $dI/dU(U)$-spectra shown in this work cannot be interpreted directly as the local density of states (LDOS) at the corresponding energy eU, as done in most STS-studies. The reason is the strong tip-induced band bending, which has to be taken into account.

Figures 3.62 a) and b) show two STM topographs. The positions of the Mn acceptors in different depths, as obtained from topographs at higher voltage, are marked by white crosses. Obviously, the wave function of some of the Mn-acceptors are not imaged at $U_{\mathrm{bias}} = 1\,\mathrm{V}$ in Fig. 3.62. Instead, a faint larger scale depression is observed around or close to those acceptors. This depression becomes smaller at higher bias voltage and the previously invisible wave functions become visible (compare Fig. 3.62b). At even higher bias voltages the depression in STM topographs completely vanishes, leaving behind just the image of the acceptor wave function. Due to this bias dependency of the large scale depression we conclude that the feature is of purely electronic origin. Figures 3.62 c-f show the dI/dU-maps acquired simultaneously to topographs with increasing bias voltage. The images show zones of enhanced differential conductance on a background of lower, InAs-related signal. Corresponding to the depression in topographs, we find around each Mn-acceptor a bow or ring-like feature of increased differential conductance, tracing the sharp borders of the topographic depression. The feature appears as a faint extended arc as marked by the circle in Fig. 3.62 c. With increasing voltage, the feature shrinks towards its central point (see circles in Figs. 3.62 d,e.). Exactly when the ring crosses the position of the corresponding Mn-acceptor,
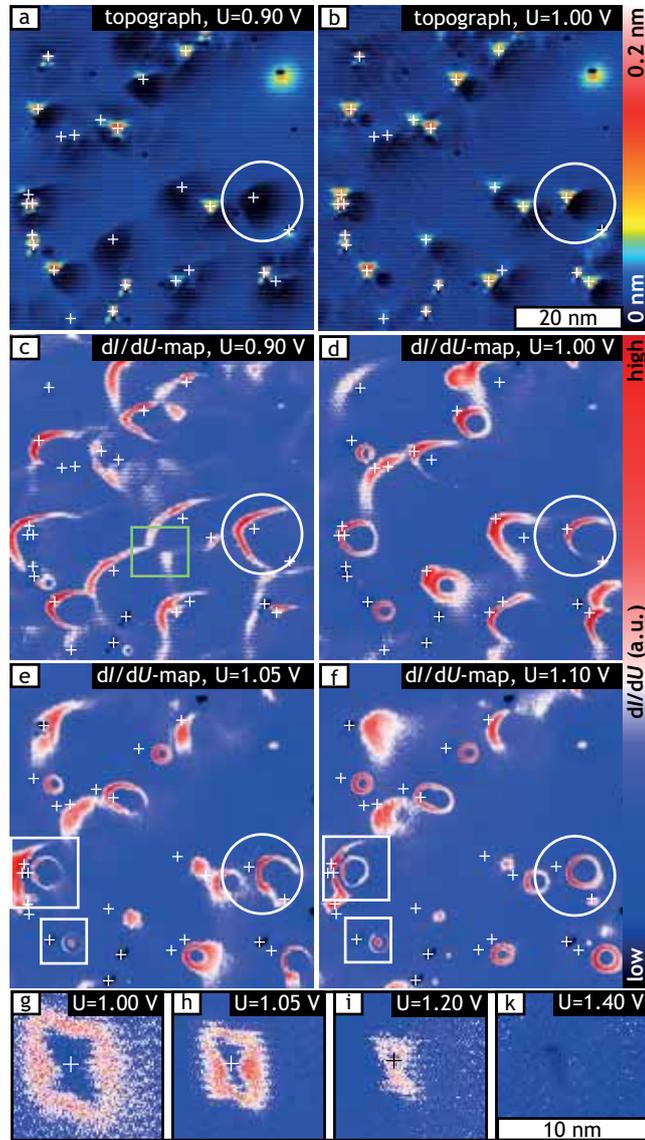
Figure 3.62: Evolution of the ring-like feature in dI/dU-maps over voltage. a),b) STM-topographs obtained at $U_{\mathrm{bias}} = 0.9\,\mathrm{V}/1.0\,\mathrm{V}$, $I_{\mathrm{set}} = 0.5\,\mathrm{nA}$. c)-f) dI/dU-maps of same area with increasing U_{bias} ($U_{\mathrm{mod}} = 10\,\mathrm{mV}$). The center of the evolving feature is sligthly shifted away from the dopants positions which are marked with white crosses. This can for example be seen in the evolution of one dopant, marked by circles in c)-f). In c), note the "'anti-crossing"' marked in the lower half by a square. Double ring features on Mn-dopant pairs are marked by white boxes on the left side in e) and f). g) demonstrates the short range evolution of the feature in a series of dI/dU slices ($U_{\mathrm{stab}} = 1.5\,\mathrm{V}$, $I_{\mathrm{stab}} = 0.6\,\mathrm{nA}$, $U_{\mathrm{mod}} = 10\,\mathrm{mV}$, U_{bias} as indicated) measured with a differently shaped tip on a lower doped sample $n \approx 1 \times 10^{17}\,\mathrm{cm}^{-3}$

the asymmetric LDOS of the Mn acceptor wave function becomes visible both in dI/dU-maps as well as in topographs (see circles in Figs. 3.62 b and d). At even higher voltage, each arc eventually closes and forms a ring as marked by a circle in Fig. 3.62 f. This ring continues to shrink for further increased voltages and finally forms a bright spot slightly aside the location of an acceptor, before it vanishes completely.

Each of the described ring-features develops in a similar fashion, although not exactly identical as they overlap, and seem to interact (see for example the area marked by squares in c and e). Each one is clearly related to a Mn-acceptor close to the feature's center. The bias voltages at which the ring appears depends on the local environment of the acceptor and is spread over a range of about 0.3 V.

In experiments with different STM tips, a strong influence of the tip shape and material on the described topographic depression and dI/dU-rings is observed. As an example, panels g)-i) of Fig. 3.62 show dI/dU-slices from an STS measurement of a single acceptor in a lower doped sample, using a different tip than in a)-f). Due to the low doping, no interaction effects are observed. With this particular tip, the dI/dU-ring appeared to be centered perfectly around the position of the Mn acceptor marked by a cross. The shape of the ring immediately before it collapses as shown in Figs. 3.62 g) and h) has the symmetry of the Mn-acceptor wave function. In Fig. 3.62 i) the ring closes and perfectly resembles the shape of the acceptor wave function as calculated in a tight-binding model. Finally, in Fig. 3.62 j) the ring has disappeared and only a small-scale depression about the size of the acceptor is left.

When performing STS on the center of the (topographic) Mn-feature, a dI/dU-spectrum as shown in Fig. 3.63 (top panel) is obtained. The pronounced peak at ca. 1 V corresponds to the situation of the ring marked by the circle in Fig. 3.62 d), where the dI/dU-ring crosses the Mn position and the anisotropic Mn-feature appears in topography. A spectrum averaged over the area of the ring as it appears at lower voltage (i.e. at larger distance from the Mn-center) is also shown in Fig. 3.63 (top panel), where a relatively smaller peak is observed. This peak is the dI/dU intensity forming the ring feature in dI/dU-maps, and so appears at lower energies for increasing lateral distance from the Mn-center (additional curves). The ranges given for the lateral distance are a result of the feature's non-circular shape of the ring. Furthermore, we observe strong NDC at the center of the Mn-acceptor as shown in the inset of Fig. 3.63 (top panel). This NDC is only found for some ($\approx 30\%$) of our tips. Another feature that is strongly dependent on the tip condition are follow-up peaks which we regularly observe above the main peak, i.e. in Fig. 3.63 (top panel) at 1.1 V and 1.3 V.

Figure 3.63 (middle panel) gives a different view of the same spectroscopic data set. The dI/dU-signal intensity is grey-scale coded, and the y-axis gives the real-space displacement along a line through the center of a Mn-acceptor feature. The dotted line indicates the spectrum measured at the center. The ring feature, which in Fig. 3.63 (top panel) took the form of a series of peaks, shows up now as two "wings" besides the main central peak, extending far out from the acceptor. In strong contrast to this,
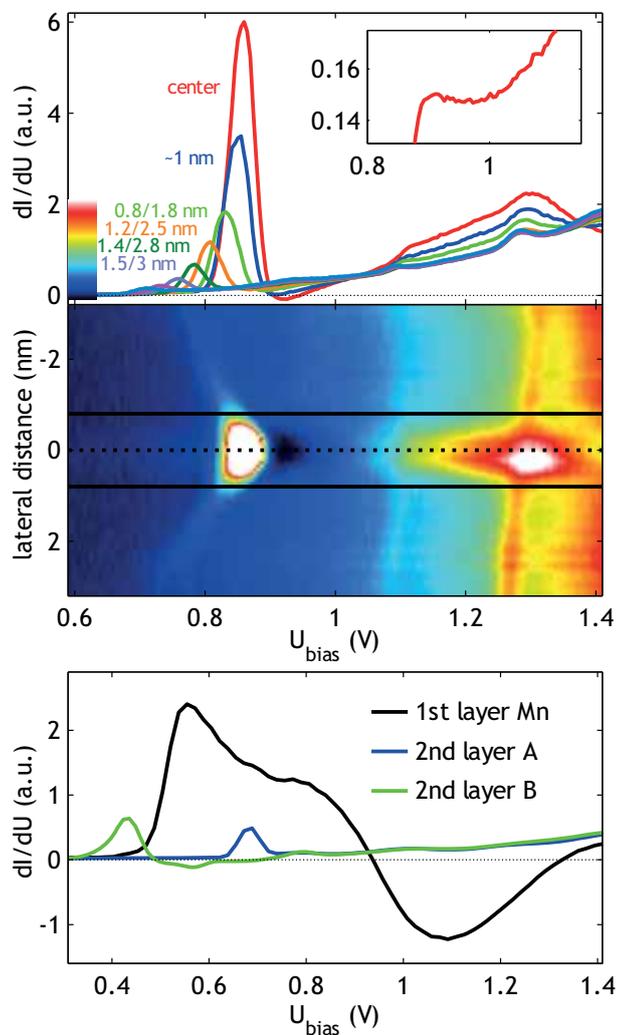
Figure 3.63: Local peak position of the ring feature. Top panel: *dI/dU*-spectra averaged in different distances from a Mn acceptor, as indicated. Right above the main peak, negative differential conductance is observed close to the Mn acceptor. The small inset graph shows an *I(U)* curve taken centrally on the acceptor. Middle panel: *dI/dU* spectra measured in different lateral distances from the Mn-center as indicated by the y-axis. The two horizontal black lines indicate the extension of the acceptor state in the topograph. The bow-like feature is equivalent to the ring feature in *dI/dU*-maps. The localized nature of the observed negative differential conductance (black area), as well as of the follow-up peaks are visible. Bottom panel: *dI/dU*-spectra of a Mn acceptor in the first subsurface layer and two different Mn in the second subsurface layer. ($U_{stab} = 2\,V, I_{stab} = 2\,nA, U_{mod} = 20\,mV$)
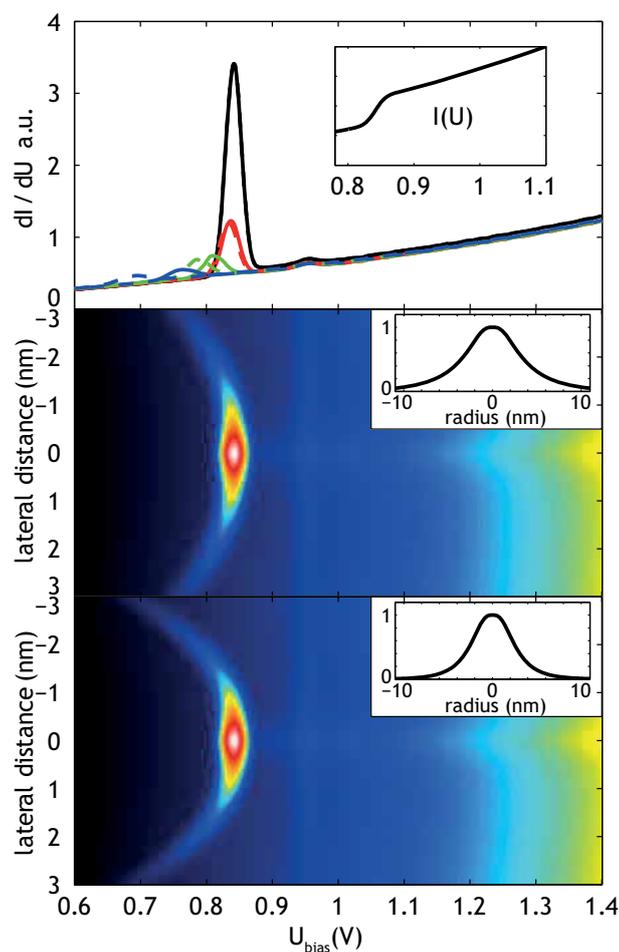
Figure 3.64: Model of the charge-switching effect in *dI/dU*-spectra (see text for details). Top panel: Simulated *dI/dU*-spectra in the presence of a switchable charge, calculated for two different potential radii ($r_{\mathrm{FWHM}} = 3\,\mathrm{nm}$: solid line, $r_{\mathrm{FWHM}} = 5\,\mathrm{nm}$: dashed line) and tip-acceptor distances: $0\,\mathrm{nm}$, $1\,\mathrm{nm}$, $2\,\mathrm{nm}$ and $3\,\mathrm{nm}$. Inset: Simulated current vs. voltage for central spectrum. Center panel: Lateral characteristics of spectral intensity for a blunt tip ($r_{\mathrm{FWHM}} = 5\,\mathrm{nm}$). Bottom panel: Lateral characteristics of spectral intensity for a sharp tip ($r_{\mathrm{FWHM}} = 3\,\mathrm{nm}$). Insets in the two lower panels show the lateral profile of the tip potential within the sample.

the main peak, the NDC, and the follow-up features are strictly confined to a range of less than $1\,\mathrm{nm}$ from the center, approximately one surface unit cell. We attribute the local phenomena to effects of the Mn-acceptor's wave function, as discussed in our earlier publication [7], while the extended ring feature needs another explanation which we deal with in the next section.

When charging the acceptor, the abrupt change in the local potential has an effect on the surrounding of the impurity, fading with distance due to screening effects. In a

low-conductance sample like this one, we estimate the screening length to $\approx 25\,\mathrm{nm}$. In other words, the impurity contributes to its environment an additional offset potential corresponding to its charge state.

It is important to note that in the considered voltage range (about $0.4\,\mathrm{V}$ to $0.9\,\mathrm{V}$), basically only conduction band states are involved in the tunneling process, as long as tip states are not directly overlapping with an impurity state. Going from lower voltages upwards in a spectroscopy measurement with fixed tip, or equivalently, entering the switching radius of an impurity at a fixed bias voltage, the local potential will abruptly jump downwards as the impurity goes from A^- to A^0, i. e. from negative to neutral. In a very straightforward manner, we can consider this changing potential in the form of an offset to the potential argument for the sample LDOS ρ_s, which is not constant but a function of the bias voltage. It can be added to the applied bias and the band bending potential ϕ_{BB}. As a consequence, above the switching point a downshifted sample LDOS is included in the current integral, yielding a higher current than below the switching point. This step up in current, or peak in dI/dU, matches our observations, i.e. in Fig. 3.63. Since this is no separate Mn-related tunneling mechanism, but solely an effect of the interaction between the tip potential, the impurity charge and the LDOS under the tip, the extended range of the effect is plausible.

This very simple model is also able to reproduce the discussed peak/ring-feature numerically, as shown in Fig. 3.64. For this simulation, we used

$$I(U) = \int_{E_{\mathrm{F}}}^{E_{\mathrm{F}}+eU} \rho_{\mathrm{sample}}(\epsilon + \phi_{\mathrm{BB}})T(\epsilon, eU, z)\ d\epsilon$$

$$\rho_{\mathrm{sample}}(E) = \left\{ \begin{array}{rl} \sqrt{E - E_{\mathrm{CB}}} & \text{for } E > E_{\mathrm{CB}} \\ 0 & \text{for } E <= E_{\mathrm{CB}} \end{array} \right.$$

$$T(\epsilon, eU, z) = \exp\left(-2z \cdot \sqrt{\frac{2m_{\mathrm{e}}}{\hbar^2}\left(\bar{\Phi} + eU/2 - \left(\epsilon - \hbar^2 k_\parallel^2/2m_{\mathrm{e}} \right) \right)} \right)$$

$$\bar{\Phi} = (\Phi_{\mathrm{tip}} + \Phi_{\mathrm{sample}})/2$$

The tip-sample distance was assumed to be $z = 0.6\,\mathrm{nm}$, and $\Phi_{\mathrm{tip}} = 4.5\,\mathrm{eV}$. We further assumed that the tip causes a voltage-dependent band-bending $\phi_{\mathrm{BB}}(U_{\mathrm{bias}})$ as simulated by a one dimensional poisson-solver, and which decays laterally analogous to the case of a hyperbolic tip [4]. The used decay functions for two different tip diameters are also shown in the inset graphs in Fig. 3.64 (middle and bottom panel). We then assumed the localized (acceptor) charge at a given lateral distance from the tip to switch at the *local* $\phi_{\mathrm{BB}}(U_{\mathrm{bias}}, r) = -E_{\mathrm{acc}} = 28\,\mathrm{mV}$, i.e., when the local band-bending aligns the acceptor state with the Fermi energy. For numerical stability and as a crude simulation of thermal and other broadening effects, we simulated the switching as a soft transition centered at $\phi_{\mathrm{BB}} = -E_{\mathrm{acc}}$ and broadened by $1\,\mathrm{meV}$. We assumed the potential of the localized charge to decay like

$$\phi_{\mathrm{charge}} = \frac{e}{2\pi\epsilon\epsilon_0 r}e^{-r/r_{\mathrm{screen}}}$$

with a screening length of $r_{\text{screen}} = 10\,\text{nm}$, $\epsilon = 14.6$. While this model includes all dominant terms and thus can be expected to maintain a strong qualitative agreement with the experiment, due to the simplicity of this model it can only produce $I(U)$-curves of arbitrary dimension. Such a curve, as well as derived dI/dU-curves are given in Fig. 3.64 (top panel). Using the sample work-function Φ_{sample} and the extension of the tip potential as the only free parameters we achieved the best agreement with the data shown in Fig. 3.63 for $\Phi_{\text{sample}} = 5.46\,\text{eV}$ (theoretically $5.3\,\text{eV}$) and a tip potential radius of $r = (3\,\text{nm}, 5\,\text{nm})$. The peculiar shifting and lowering of the peak is excellently reproduced by the model. A notable difference between experimental and simulated results are found around $r = 0\,\text{nm}$: the NDC missing in the simulation and a broader central peak in the measured data. We interpret this as strong indication that the ring is indeed purely related to conduction band tunneling and that a different effect, tunneling through the acceptor state, is causing an additional peak/NDC feature with certain tips. It might be noted that this is compatible to earlier conclusions [7] about the structure of dI/dU-spectra at higher energies.

References

[1] G. J. de Raad, D. M. Bruls, P. M. Koenraad, and J. H. Wolter, Phys. Rev. B, **66**, 195306, (2002)

[2] A. Depuydt, C. Van Haesendonck, N. S. Maslova, V. I. Panov, S. V. Savinov, and P. I. Arseev, Phys. Rev. B, **60**, 2619, (1999)

[3] R. Dombrowski, Chr. Steinebach, Chr. Wittneven, M. Morgenstern, and R. Wiesendanger, Phys. Rev. B, **59**, 8043 (1999)

[4] R. M. Feenstra, Journal of Vacuum Science & Technology B: **21**, 2080 (2003)

[5] J. Klijn, L. Sacharow, C. Meyer, S. Blügel, M. Morgenstern, and R. Wiesendanger, Phys. Rev. B, **68**, 205327 (2003)

[6] S. Loth, M. Wenderoth, L. Winking, R. G. Ulbrich, and S. Malzerand G. H. Dohler, Phys. Rev. Lett., **96**, 066403 (2006)

[7] F. Marczinowski, J. Wiebe, J.-M. Tang, M. Flatté, F. Meier, M. Morgenstern, and R. Wiesendanger, Phys. Rev. Lett., **99**, 157202 (2007)

[8] J. Wiebe, A. Wachowiak, F. Meier, D. Haude, T. Foster, M.Morgenstern, and R. Wiesendanger, Rev. Sci. Instrum., **75**, 4871 (2004)

[9] J. W. G. Wildöer, A. J. A. van Roij, C. J. P. M. Harmans, and H. van Kempen, Phys. Rev. B, **53**, 10695 (1996)

[10] Chr. Wittneven, R. Dombrowski, S. H. Pan, and R. Wiesendanger, Rev. Sci. Instrum., **68**, 3806 (1997)

[11] A. M. Yakunin, A. Yu. Silov, P. M. Koenraad, J.-M. Tang, M. E. Flatté, J.-L. Primus, W. Van Roy, J. De Boeck, A. M. Monakhov, K. S. Romanov, I. E. Panaiotti, and N. S. Averkiev, Nature Mater., **6**, 512 (2007)

[12] A. M. Yakunin, A. Yu. Silov, P. M. Koenraad, J. H. Wolter, W.Van Roy, J. De Boeck, J.-M. Tang, and M. E. Flatte, Phys. Rev. Lett., **92**, 216806 (2004)

Electronic States of Fe Atoms and Chains on InAs(110)

T. Matsui, Chr. Meyer, L. Sacharow, J. Wiebe, and R. Wiesendanger,
[Phys. Rev. B **75**, 165405 (2007)].

Chains of metallic atoms on various substrates are of great interest for applications in future electronic devices and for fundamental studies of one dimensional (1D) electron systems [1–8]. By using the scanning tunneling microscope (STM) one can artificially fabricate atomic chains and study their electronic properties on the atomic scale. Similar to the 2D surface state of a bulk (3D) electron system one can expect a singular state for the 1D electron system at the end of such chains called "end state", which shows a zero dimensional (0D) character [5].

Recently, the electronic and magnetic properties of Fe chains on InAs(110) for two different relative orientations, i.e. parallel to the [1$\bar{1}$0] and to the [001] direction of the substrate, were calculated with an *ab-initio* method using density functional theory (DFT) [9,10]. The calculations suggest that the antiferromagnetic (AF) ground state found for the [1$\bar{1}$0] chains and the ferromagnetic (FM) ground state found for the [001] chains are stabilized by superexchange via substrate As and In atoms. This impressively shows the importance of the substrate-mediated interactions for the magnetic as well as for the electronic properties of Fe chains on InAs(110).

Triggered by this study, we investigate the electronic properties of Fe single atoms as well as [1$\bar{1}$0]- and [001]-chains from dimers to pentamers on the n-InAs(110) substrate using scanning tunneling spectroscopy (STS). In this case, the inter-atomic distances of the Fe atoms are more than twice as large as in bulk Fe (2.5 Å), implying a very weak direct interaction between the atoms in the chains. Hence, each Fe atom can be well resolved in STM images as shown in Figs. 3.65(b) and (c). Nevertheless, clear indications for interactions between the Fe atoms within the chains were experimentally found as a uniform state, an end state, and inner states. In contrast to former examples, this end state is proven to exist in both filled and empty DOS.

The Fe chains are self-assembled at room temperature after the evaporation of Fe atoms onto the clean cleaved n-InAs(110) surface ($N_{\mathrm{D}} \simeq 1 \times 10^{16}$ cm^{-3}) in ultra high vacuum [11]. The samples are then transferred *in-situ* into the microscope and cooled down to $T \simeq 6$ K [12].

An Fe atom appears as a bright spot with a pentagonal shaped dark rim on the background of the bright rows of As atoms in constant current images at $V < 400$ mV (Fig. 3.65(a)) [13,14]. From the position of the bright spot with respect to the As-atom rows which are indicated in Fig. 3.65(a), a position of the Fe atom relative to the distant InAs lattice as sketched in Fig. 3.65(d) can be deduced [14]. Because it is known from the calculations of the Fe monolayer [14] as well as of infinite Fe chains [9,10] that the neighboring As atoms are relaxed closer to the Fe atom, while the In atoms are relaxed away, the position of the nearest neighbor In and As atoms around Fe atoms and chains can be expected as shown in Fig. 3.65(d). Since the electronic states are asymmetric with respect to the (001) plane due to the asymmetry
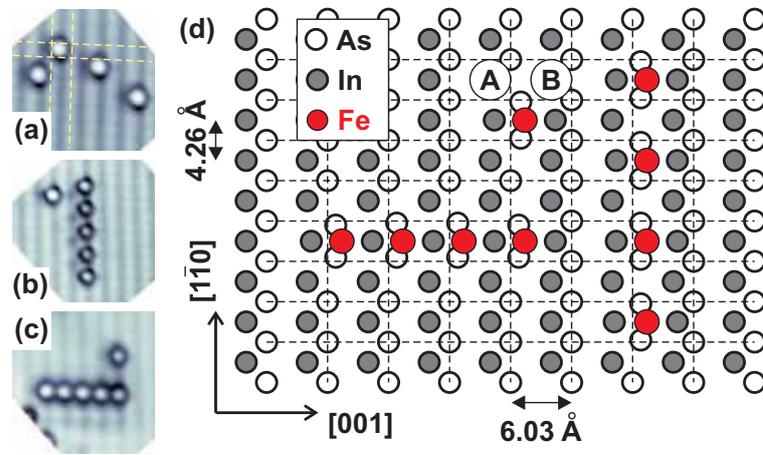
Figure 3.65: Constant current images of (a) Fe single atoms (500 pA, 50 mV), (b) a $[1\bar{1}0]$-pentamer (200 pA, 100 mV), and (c) a $[001]$-pentamer (200 pA, 100 mV). (d) Structural model of the Fe single atom and chains adsorbed on the InAs(110) surface.

in the Fe neighborhood, the position on the left-hand side (right-hand side) of the Fe atoms in [001] direction is referred as A-side (B-side). An example for a $[1\bar{1}0]$- and a [001]-pentamer is shown in Figs. 3.65(b) and (c). In contrast to the [001]-chains, which consist of close packed Fe atoms, it is almost impossible to find close packed $[1\bar{1}0]$-chains longer than three atoms, and moreover, they are easily broken up to chains with a vacant unit cell in-between by applying higher bias voltages ($V > 1$ V). Therefore, $[1\bar{1}0]$-chains in which Fe atoms occupy every second unit cell as shown in Fig. 3.65(b) are studied. Consequently, the inter-atomic distance of the Fe atoms in the $[1\bar{1}0]$- and [001]-chains is 8.5 Å and 6.0 Å, respectively.

First, the LDOS on and around Fe single atoms is discussed. In contrast to other atomic chains [2,4,5], no resonant states in the band gap, which extends from -500 mV to -100 mV, are observed on Fe single atoms and chains. Instead, characteristic peaks are found at higher energies around $V = \pm 1$ V. Figures 3.66(a) and (b) show the normalized dI/dV spectra observed on top of an Fe atom (red dots) and on the InAs substrate far from the Fe atoms (black circles). On the Fe atom, the spectrum shows a sharper peak at $V \simeq 1000$ mV and a broader peak at $V \simeq 1200$ mV, which can be assigned to two characteristic states of the Fe atoms or the neighboring In and As atoms. The energies of the two characteristic states vary slightly from Fe atom to Fe atom presumably because of changes in the background potential which depends on the distance from charged Fe atoms and donors [11, 17]. Note that the peak energies shift downwards by more than 100 mV when the Fe atom is manipulated laterally from the virgin position. It suggests that the binding between the Fe atom and the substrate is changed by the manipulation and that the two states are strongly hybridized with the substrate.

Interestingly, the two characteristic peaks have a strong spatial dependence. The
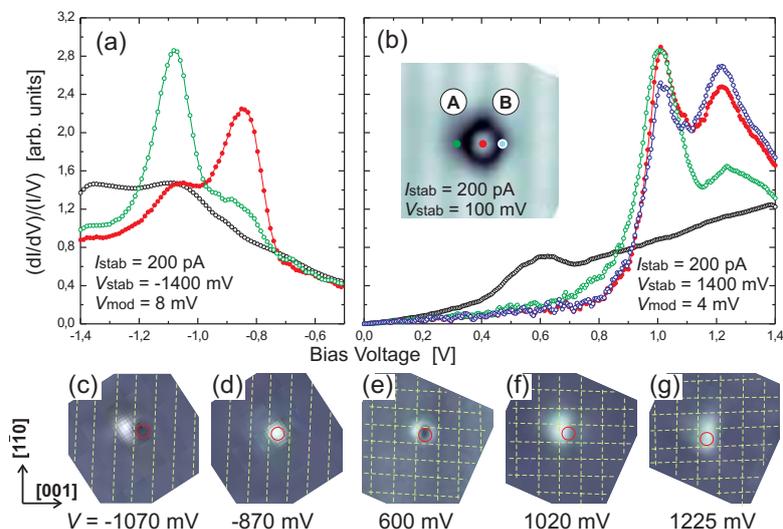
Figure 3.66: Normalized dI/dV spectra at negative (a) and positive (b) sample bias voltages measured on a single Fe atom and on the InAs substrate. The spectra taken on the A-side and the B-side of the Fe atom are also shown. (c), (d) dI/dV slices of filled states taken from (a). (e)-(g) dI/dV maps of empty states (200 pA, $V_{mod} = 4$ mV). The circles and the dotted lines show the positions of the Fe atom and the As rows of the substrate, respectively.

dI/dV spectrum in Fig. 3.66(b) taken on the A-side of the Fe atom shows a strong occurrence of the peak at $V \simeq 1000$ mV, while the peak at $V \simeq 1200$ mV is more pronounced on the B-side. This behavior can also be confirmed with the dI/dV images around an Fe atom in Figs. 3.66(e)-(g). At lower bias voltages below 900 mV (e), the Fe atom appears as a dark spot surrounded by a brighter ring. The first state at $V = 1020$ mV (f) is spatially asymmetric with respect to the (001) plane and shows a lobe that extends to the A-side of the Fe atom. In contrast, the second state at $V = 1225$ mV (g) is located approximately on top of the Fe atom and shifted only slightly to the B-side. Comparison with the structural model in Fig. 3.65(d) suggests that both states are extended over about two unit cells of the InAs. Furthermore, one can conclude that the first state is related to the In atom on the A-side (In-related state), while the second state is most probably related to an Fe state or a hybridization between states of the Fe and of the two neighboring As atoms (Fe-related state).

Subsequently, we have studied the electronic states of Fe chains aligned along the [1$\bar{1}$0] direction. Figures 3.67(a) and (b) show the normalized dI/dV spectra measured on each Fe atom in a [1$\bar{1}$0]-tetramer. The peak structure is significantly different from the single atom suggesting a considerable interaction of the Fe atoms within the tetramer. The In-related peak is shifted to lower voltages at $V \simeq 900$ mV and the Fe-related peak splits up into two peaks at $V \simeq 1100$ mV and 1300 mV with intensities depending on the position in the tetramer. Figure 3.67(e) shows the dI/dV

map corresponding to the lowest empty state at $V = 900$ mV. Here, the LDOS is found to be equally distributed on the whole tetramer to form a "uniform state". This is confirmed by the equal intensity of the lowest peak measured on all four Fe atoms in Fig. 3.67(b). Because the uniform state is shifted to the A-side of the tetramer similar to the In-related state of the single atoms, we conclude that it is formed by the overlapping In-related states of the four Fe atoms. The other two empty states at higher voltages are shifted slightly to the B-side as visible in Figs. 3.67(f) and (g). Since their spatial distribution regarding the [001] direction is similar to the Fe-related state of the single atoms, it may well be concluded that the Fe-related state of the
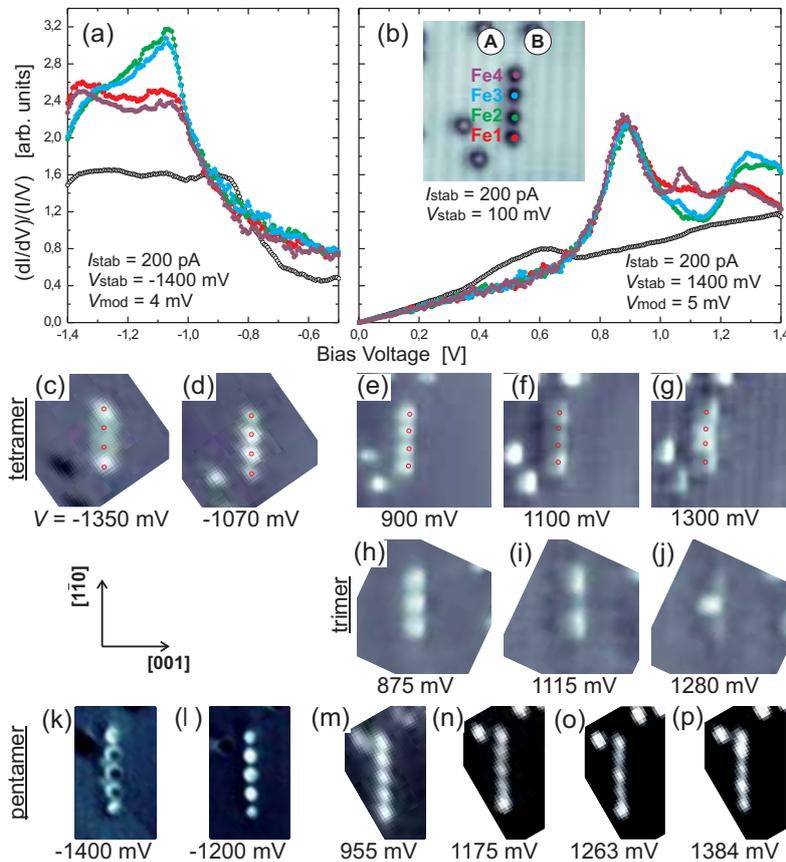
Figure 3.67: Normalized dI/dV spectra measured at negative (a) and positive (b) sample bias voltages on each Fe atom (Fe1 to Fe4) in a $[1\bar{1}0]$-tetramer (see inset constant current image), and on the InAs substrate (black circles). (c), (d) dI/dV slices of the filled states taken from (a). (e)-(g) dI/dV maps of the empty states of the tetramer (200 pA, $V_{\mathrm{mod}} = 10$ mV). (h)-(j) dI/dV maps of the empty states of a trimer (200 pA, $V_{\mathrm{mod}} = 4$ mV). (k), (l) dI/dV maps of the filled states of a pentamer (200 pA, $V_{\mathrm{mod}} = 4$ mV). (m)-(p) dI/dV slices of the empty states of the pentamer (200 pA, 1400 mV, $V_{\mathrm{mod}} = 4$ mV).
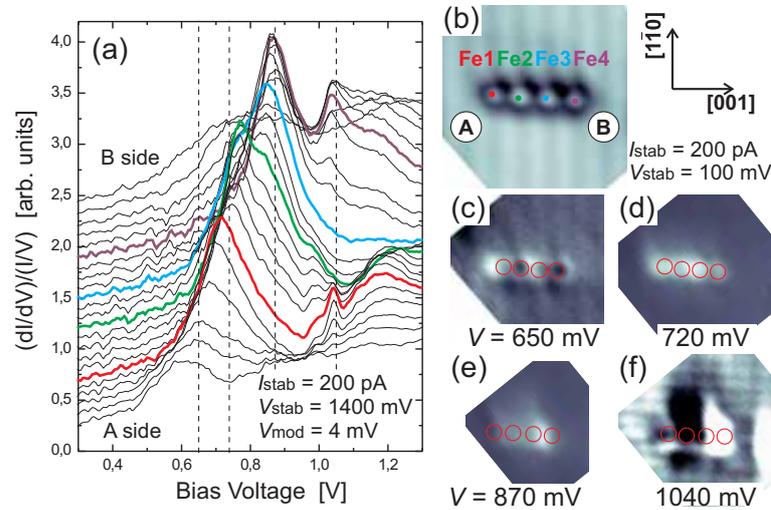
Figure 3.68: (a) Normalized dI/dV spectra measured along a [001]-tetramer shown in the constant current image in (b). The curves from the lower to the upper part of (a) correspond to the points from the A-side to the B-side of the tetramer. Spectra obtained on the Fe atoms (Fe1 to Fe4) are colored corresponding to the dots in (b). (c)-(f) Corresponding dI/dV maps (200 pA, $V_{mod} = 4$ mV). The red circles show the position of each Fe atom.

single atom splits up into these two states after the formation of the tetramer. Most importantly, these two Fe-related states have a different lateral position of the LDOS maxima along the chain axis. While the state at lower energy in Fig. 3.67(f) is localized on the two end atoms of the tetramer (Fe1 and Fe4) and forms an "end state", the higher energy state in Fig. 3.67(g) is localized on the two inner atoms (Fe2 and Fe3) and forms an "inner state". The dI/dV spectra in Fig. 3.67(b) confirm this behavior. Similar *filled* end states and inner states are observed at negative bias voltages as shown in Fig. 3.67(c) and (d). The inner atoms have a sharper peak at $V \simeq -1070$ mV, while the end atoms have a broad peak at $V \simeq -1350$ mV (Fig. 3.67(a)).

We also analyzed the electronic states of trimers and pentamers. The empty uniform state, end state and inner state are clearly observed for a trimer in the dI/dV maps in Figs. 3.67(h), (i) and (j), respectively. For the longer pentamer, the sequence of the empty Fe related states becomes more complex. While the lowest two empty states are still the uniform (In-related) state and the end state visible in Figs. 3.67(m) and (n), two other empty states are distinguishable in dI/dV maps at higher voltages shown in Figs. 3.67(o) and (p). State (o) is localized on the middle Fe atom and on the two end atoms, and state (p) is localized mainly on the two remaining atoms. This suggests that the empty inner state splits up into more complex states for longer chains. At negative voltages down to -1400 mV, on the other hand, the filled end state (Fig. 3.67(k)) and the simple inner state (Fig. 3.67(l)) are observed as for tetramers.

Chains aligned along the [001] direction of the substrate have been studied as well. Different from the [1$\bar{1}$0]-chains, the [001]-chains have no inversion symmetry along the chain axis, which results in a strong asymmetry of the electronic states. Figure 3.68(a) shows the normalized dI/dV spectra obtained along a [001]-tetramer. Colored curves are measured on each Fe atom (Fe1 to Fe4). Here, three peaks can be found along the tetramer. First, a peak appears at $700 < V < 800$ mV on Fe1 and Fe2. This peak is rapidly attenuated along the [001] direction and a second peak appears at $800 < V < 900$ mV on Fe3 and Fe4. Finally, a sharper peak appears at $V \simeq 1040$ mV, which is localized on the end atoms (Fe1, Fe4). The two peaks at lower energies shift continuously to higher energies by moving along the tetramer from Fe1 to Fe2 and from Fe3 to Fe4, i.e. from the A-side to the B-side of the tetramer. This is also visible in the dI/dV maps in Figs. 3.68(c)-(e), where the maximum in intensity shifts from the A-side to the B-side of the tetramer. In contrast, the state at 1040 mV is localized mainly on the two end atoms as can be seen in Fig. 3.68(f). The same tendencies are also found for [001]-trimers and pentamers.

The experimentally observed electronic properties of the short Fe chains were compared with DFT calculations of the vacuum DOS for infinite [1$\bar{1}$0] and [001] Fe-chains on InAs(110) visible in Fig. 3.69. Different from the experiment, the Fe atoms in the chains are close packed to the substrate unit cell in both orientations. The vacuum DOS calculated for the magnetic ground states, i.e. the AF state for [1$\bar{1}$0]-chains and the FM state for [001]-chains, shows two dominant peaks located around 1 eV with an
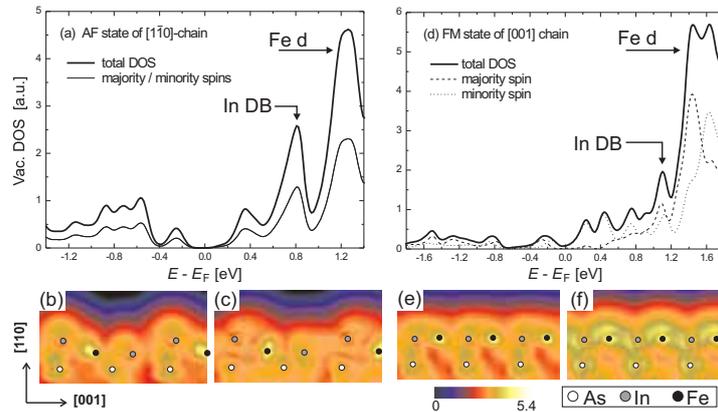
Figure 3.69: Calculated vacuum DOS of the [1$\bar{1}$0]-chain in AF configuration (a) and of the [001]-chain in FM configuration (d). The DOS is averaged at a distance of 5.3 Å from the surface. Corresponding total LDOS calculated for the [1$\bar{1}$0]-chain at the peaks of $V = 800$ mV(b), 1200 mV(c) and for the [001]-chain at the peaks of $V = 1100$ mV (e), 1400 mV (f). The unit of the color scale is 10^{-19} [C/^{3}]. Because of the upwards relaxation of the In atom on the A-side of the Fe atoms in the [1$\bar{1}$0] chains, the vacuum LDOS of the In related state is shifted to the A-side of the chain.

energy separation of about 400 meV (see Fig. 3.69(a) and (d)). These peaks occur at similar energies as the experimentally observed empty states in the single atoms and the chains. Especially for the $[1\bar{1}0]$-chains, the peak separation between the uniform state and the inner state is also comparable. The corresponding spatial distributions of the vacuum LDOS for the chains indicate that the lower energy state can be attributed to the In dangling bond (DB), while the higher energy state is due to an Fe d-like state. Because of the upwards relaxation of the In atom on the A-side of the Fe atoms in the $[1\bar{1}0]$ chains, the vacuum LDOS of the In related state is shifted to the A-side of the chain (see Fig. 3.69 (b)). This behaviour substantiates the experimental evidences for the single atoms and $[1\bar{1}0]$-chains. Since the Fe state consists of majority and minority spin states, it appears broader than the In-DB state, and in case of the FM state of the [001]-chain, the two spin states are splitted by 190 meV.

In the following, we want to discuss the experimentally observed state sequence on the $[1\bar{1}0]$-chains. By forming chains from the single atoms, the Fe related state splits into a series of states localized on the end and on the inner atoms, clearly indicating hybridization of the states from each atom. The separations of these states and their downwards shifts are on the order of only 100 meV and thus much less than for Au chains on NiAl(110) and Cu chains on Cu(111) where splittings and shifts observed for dimer formation are larger than 1 eV [2, 4]. This indicates a very weak direct interaction between the neighboring Fe atoms and the importance of substrate mediated interactions via the neighboring As and In atoms [3]. In fact, as our DFT calculations of infinite Fe chains on InAs(110) show, the indirect exchange via the substrate is also crucial for the magnetic ground state of the chain [9, 10].

As a result, the state sequence cannot be described by a simple particle-in-a-box model. Within this model, standing wave patterns which are not affected by the positions of the constituent atoms are anticipated. Therefore, one maximum in the LDOS in the middle of the chain is expected for the $n = 1$ state, two maxima are expected for the $n = 2$ state, three maxima for the $n = 3$ state,... Instead, as visible in Fig. 3.67, the lowest Fe related state of Fe trimers and tetramers shows two maxima localized at the end atoms and the second lowest state has only one maximum located on the middle atoms. For the pentamer, the state sequence is getting even more complex. Thus, a more elaborate TB model would be necessary to describe our results.

In analogy to the results for Au chains on Si(553), we interpret the lowest Fe related state localized on the end atoms of the chain in terms of a 0D end state of the 1D electron system [5]. For Au/Si(553) this end state was observed exclusively in the filled DOS. It was proposed that an empty end state is not formed because it cannot lower the energy of the electron system. This reduction in energy as driving force for the formation of end states obviously does not apply for the Fe chains on InAs(110), where the end state is found in the filled *and* empty DOS. In both cases, the energy of the end state is $100 \sim 300$ meV lower than that of the first inner state.

Finally, the behavior of the [001]-chains is rather complex. First, we cannot separate the states into an In and Fe related state as done for the $[1\bar{1}0]$-chains. Second, the

continuous shifting of the lower energy states along the chain axis suggests a different hybridization of each Fe atom to the substrate. This prevents the formation of clear inner states for chains up to a length of five atoms. Nevertheless, a remainder of the end state is still visible.

References

[1] T. M. Wallis, N. Nilius, and W. Ho, Phys. Rev. Lett. **89**, 236802 (2002).

[2] N. Nilius, T. M. Wallis, and W. Ho, Science **297**, 1853 (2002).

[3] N. Nilius, T. M. Wallis, M. Persson, and W. Ho, Phys. Rev. Lett. **90**, 196103 (2003).

[4] S. Fölsch, P. Hyldgaard, R. Koch, and K. H. Ploog, Phys. Rev. Lett. **92**, 056803 (2004).

[5] J. N. Crain and D. T. Pierce, Science **307**, 703 (2005).

[6] J. N. Crain, A. Kirakosian, K. N. Altmann, C. Bromberger, S. C. Erwin, J. L. McChesney, J.-L. Lin, and F. J. Himpsel, Phys. Rev. Lett. **90**, 176805-1 (2003).

[7] T. Yamada, C. W. Bauschlicher, Jr., and H. Partridge, Phys. Rev. B **59**, 15430 (1999).

[8] A. Calzolari and M. B. Nardelli, Phys. Rev. B **72**, 45416 (2005).

[9] L. Sacharow, Ph.D. thesis, Institute of Applied Physics, University of Hamburg (2006); http://www.physnet.uni-hamburg.de/services/fachinfo/search.php.

[10] L. Sacharow, R. Wiesendanger, G. Bihlmayer, S. Blügel, and M. Morgenstern, unpublished.

[11] M. Morgenstern, M. Getzlaff, D. Haude, R. Wiesendanger, and R. L. Johnson, Phys. Rev. B **61**, 13805 (2000).

[12] Chr. Wittneven, R. Dombrowski, S. H. Pan, and R. Wiesendanger, Rev. Sci. Instrum. **68**, 3806 (1997).

[13] J. Klijn, L. Sacharow, Chr. Meyer, S. Blügel, M. Morgenstern, and R. Wiesendanger, Phys. Rev. B **68**, 205327 (2003).

[14] L. Sacharow, M. Morgenstern, G. Bihlmayer, and S. Blügel, Phys. Rev. B **69**, 85317 (2004).

[15] M. Bode, Rep. Prog. Phys. **66**, 206523 (2003).

[16] J. W. G. Wildöer, A. J. A. van Roij, C. J. P. M. Harmans, and H. van Kempen, Phys. Rev. B **53**, 10695 (1996).

[17] M. Morgenstern, J. Klijn, Chr. Meyer, M. Getzlaff, R. Adelung, R. A. Römer, K. Rossnagel, L. Kipp, M. Skibowski, and R. Wiesendanger, Phys. Rev. Lett. **89**, 136806 (2002).

3.3.3 Semiconductor quantum dots

Introduction

Quantum dots (QDs) have attracted great attention in the last years as ideal materials where three-dimensional (3D) electronic confinement leads to novel phenomena and applications, from optoelectronics to implementation of quantum computation. In particular, strain-induced InAs QDs have been largely investigated and used in optoelectronics due to the possibility of achieving emission at wavelengths of interest for telecommunications. The wave functions (WFs) of electrons and holes confined in the QDs are the most basic features ultimately determining all QD properties. We previously demonstrated that it is possible to map the dot WFs in the one-electron regime by means of spatially resolved tunneling spectroscopy images [1]. The presence of more electrons in a QD leads to a Coulomb interaction between carriers. As a consequence the injection of an additional electron into the QD affects its energy spectrum and ultimately changes the WFs, leading to novel ground and excited states. Understanding this basic but fundamental issue would be a key step forward for the comprehension of few-particle interactions in strongly correlated systems as well as for applications in the fields of single-electron devices, spintronics, and quantum information encoding. Additionally we have successfully extended our wave-function-mapping method to colloidal semiconductor nanocrystals.

Correlation Effects in Molecular Beam Epitaxy Grown Quantum Dots

G. Maruccio, M. Janson, A. Schramm, C. Meyer, T. Matsui, C. Heyn, W. Hansen, R. Wiesendanger, M. Rontani, and E. Molinari,
[Nano Lett. **7**, 2701 (2007)]

Despite theoretical predictions that WF mapping of QDs should be sensitive to correlation effects [2, 3], there has been no clear experimental evidence yet. Here, we investigate correlation effects in the regime of a few electrons in uncapped InAs quantum dots by tunneling spectroscopy and wave function (WF) mapping at high tunneling currents where electron-electron interactions become relevant. Four clearly resolved states are found, whose approximate symmetries are roughly s and p, in order of increasing energy. Because the major axes of the p-like states coincide, the WF sequence is inconsistent with the imaging of independent-electron orbitals. The results are explained in terms of many-body tunneling theory, by comparing measured maps with those calculated by taking correlation effects into account.

The strain-induced InAs QDs were grown on n-doped GaAs(001) substrates by molecular beam epitaxy (MBE). First, an n-doped GaAs buffer layer ($N_D \approx 2 \times 10^{18} cm^{-3}$) 200 nm thick was deposited at a temperature of 620°C. Then, an undoped

tunneling barrier 5 nm thick ($N_A < 10^{15} cm^{-3}$) was overgrown (see Figure 3.70a) in order to provide the decoupling necessary to investigate the inherent electronic properties of the QDs and to obtain direct images of the dot WFs disentangled from the electronic structure of the substrate. Finally, the sample was cooled down to 500°C in order to form the QDs by depositing 2.1 ML of InAs at a growth rate of 0.05 ML/s. Reflection high-energy electron diffraction was used to monitor in situ QD formation. A transition from a streaky to a spotty pattern (indicating the onset of three-dimensional islanding) and chevron-like spots generally attributed to QD facets were observed [4].

Since correlation effects are strong, the concept of LDOS is not appropriate and $\mathrm{d}I/\mathrm{d}V(V, x, y)$ is instead expected to be proportional to $-1/\hbar\pi \mathrm{Im} G(x, y; x, y; eV)$, where G is the interacting retarded Green's function (or single-electron propagator) resolved in both energy and space [2–4]. The imaginary part of $-G/\hbar\pi$ (known as spectral density) may be regarded as the modulus squared of a *quasi particle* $WF\varphi_i(E_i, x, y)$, which can considerably deviate from its independent-particle counterpart $\varphi_i(E_i, x, y)$ (refs [2] and [3]).

The sample structure and experimental setup are sketched in Figure 3.70a. Large-scale constant-current STM images (not shown) revealed a QD density of $2.5 \times 10^{10} cm^{-2}$, while the shape of the QDs was determined from STM images acquired within a smaller area, as in Figure 3.70a. Despite some variation in size (with a typical lateral extension of 30 nm along both [110] and [1$\bar{1}$0] directions and an average height of 5-6 nm), all QDs exhibit similar facets. As shown in Figure 3.70a, the QDs have a pyramidal shape with well-defined facets and a fairly sharp summit. We observed a pronounced shape anisotropy as visible from the three-dimensional (3D) view of Figure 3.70a as well as from the height profiles reported in Figure 3.70b. In particular, the height profile is triangular along [110] and rounded along the perpendicular direction [1$\hbar$10]. The inclination angle between the facets and the substrate is approximately 19°, in line with (114) planes. Similar structural features and anisotropic
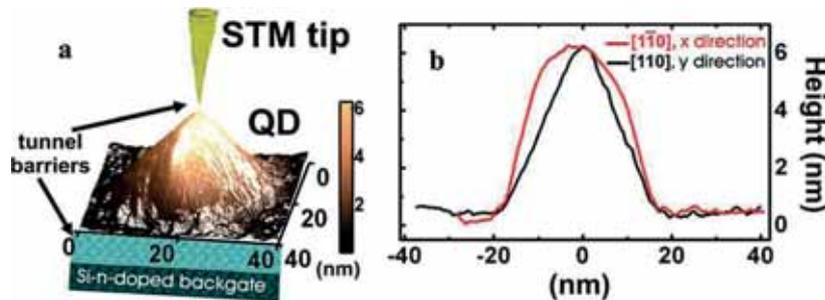

Figure 3.70: **Experimental setup and dot morphology.** (a) Experimental setup and three-dimensional STM image of a representative uncapped QD grown on a n-doped GaAs(001) substrate. (b) Height profiles of the same QD along two perpendicular axes, parallel to the [110] and [1$\bar{1}$0] directions, respectively.
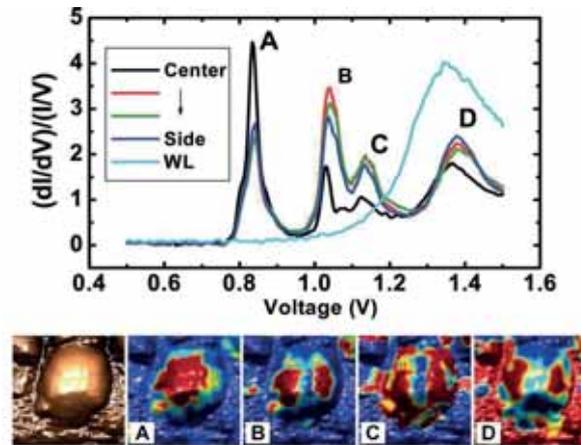
Figure 3.71: **STS spectra and wave function maps.** Top panel: $(\mathrm{d}I/\mathrm{d}V)/(I/V)$ spectra vs V measured at different positions on a single QD, moving from the QD center to its sides. Bottom panel: STS spatial maps of a single representative dot, taken at 840, 1040, 1140, and 1370 mV, for resonances A, B, C, and D, respectively (second–fifth panel). The grey scale represents the STS signal with respect to the topographic STM image on the left-hand side (first panel). The dot height in the first panel varies from 0 to ≈ 6 nm. The lateral extension of all maps is 30×30 nm. $I_{\mathrm{stab}} = 100$ pA, $V_{\mathrm{stab}} = 1.5$ V, $V_{\mathrm{mod}} = 4$ mV.

shapes were reported in recent studies, in particular by Marquez et al [5]. Besides the bright QDs, several steps are visible on the wetting layer (WL), which has a 2×4 reconstructed structure similar to that of the GaAs(001) surface [1]. To examine the electronic structure in our QDs, scanning tunneling spectroscopy was performed on individual dots. Figure 3.71 (top part) shows typical $(\mathrm{d}I/\mathrm{d}V)/(I/V)$ spectra taken on a relatively small QD in different positions.

In Figure 3.72a the calculated STS map for the ground state $\rightarrow$ ground state tunneling transition $N = 1 \rightarrow N = 2$ (being N the number of electrons in the QD before and after the tunneling transition) is shown in the correlated case for increasing values of the dot anisotropy (from left to right). For a perfectly circular QD (left plot) we unambiguously predict an isotropic s symmetry for the WF (in the noninteracting case the STS map is only slightly squeezed with respect to the correlated image on the left-hand side of Figure 3.72a). On the other hand, by increasing the QD eccentricity, we see that progressively the interacting WF forms two peaks along the major axis, while its noninteracting counterpart is simply a Gaussian being elongated along the same direction (not shown). We thus identify the state C in WF mapping with this tunneling transition $N = 1 \rightarrow N = 2$ from ground to ground state. The formation of the two peaks, together with the loss of weight at the dot center, is due to the destructive interference between s and d states of the harmonic oscillator along the major axis (belonging to the same representation A_1 of the C_{2V} group), which is a correlation effect. Such an effect is ultimately connected with the loss of angular
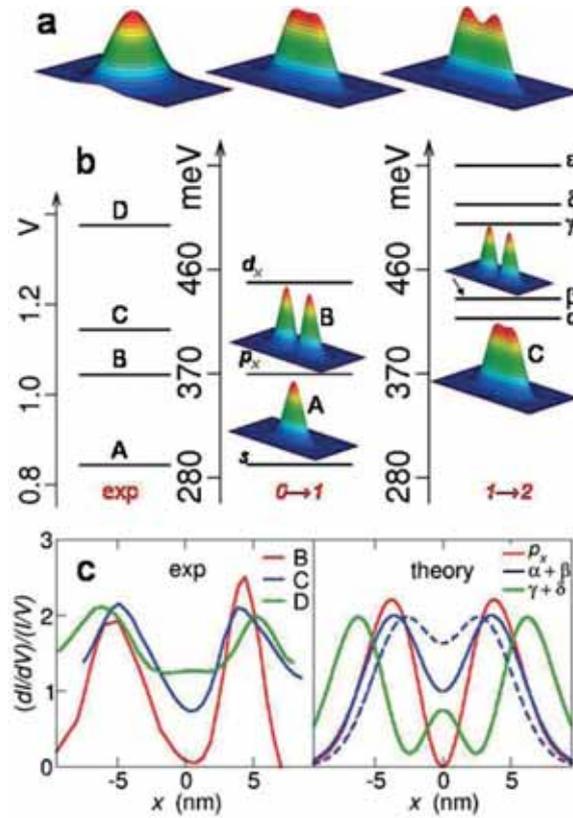
Figure 3.72: **Comparison between measured and predicted wave function maps.**
(a) Calculated STS maps (WF square moduli) for the ground state to ground state tunneling
transition $N = 1 \rightarrow N = 2$, as a function of dot anisotropy (the central image is labeled C in
panel b). From left to right, the ratios of the lateral extension of the major to minor axes are 1,
2.5, and 5, respectively. (b) Experimental STS energy spectrum (left column) and calculated
states for the tunneling processes $N = 0 \rightarrow N = 1$ (center column) and $N = 1 \rightarrow N = 2$
(right column). The predicted images of experimentally relevant states are also shown. The
in-plane size of all 3D plots is 4×2 units of the lateral extension of the noninteracting s orbital
in the elongated direction. (c) Profiles of STS maps (left) and predicted probability densities
(right, in arbitrary units) along a QD volume slice. The measured profiles were extracted
from the data of Figure 3.71 after averaging in the transverse direction. The predicted curves
correspond to the overlaps of α and β (γ and δ) states, mixed with a 1:1 ratio. The dashed
line is the 1:1 overlap of s and p_x non-interacting orbitals.
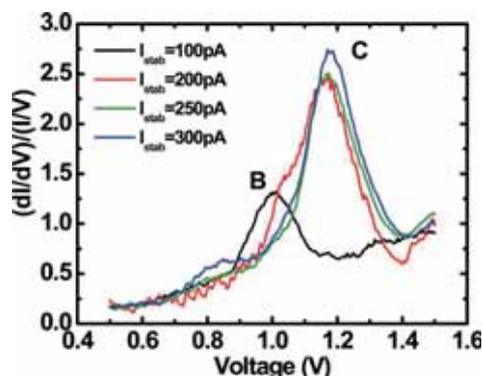
Figure 3.73: Changing the dot occupancy by varying the stabilization current. $(dI/dV)/(I/V)$ tunneling spectra vs V as a function of the stabilization current I_{stab} measured at the QD side, where states B and C are dominant.

correlation induced by the breaking of circular symmetry, which is compensated by radial correlation along the major axis. This can also be seen as a manifestation of the general statement that the importance of correlation increases as the system dimensionality is reduced (in this case, from 2D to 1D).

In Figure 3.72b, we present (from left to right) the experimental STS energy spectrum (first column) and typical predicted maps calculated separately for the charging processes corresponding to the injection of the first (second column) and second (third column) electron into the QD. Different FCI calculations for different sets of input parameters were performed, showing the same qualitative trend as displayed in Figure 3.72. Note that the tip-induced band bending has to be taken into account to transform the voltage scale into the energy scale. Specifically, the comparison of experimental energy spacings (left diagram) with those calculated (center and right) suggests that states A and B can be ascribed to the two lowest-energy states predicted for the tunneling process $N = 0 \rightarrow N = 1$, while states C and D could be associated to the tunneling process $N = 1 \rightarrow N = 2$. Moreover, the tunneling regime appears to switch from $N = 0 \rightarrow N = 1$ to $N = 1 \rightarrow N = 2$ at larger voltages/ energies due to the increased current flowing in the tunneling junction.

Thus, in this case the quasi-particle WFs probed by dI/dV mapping considerably deviate from the noninteracting WFs. As far as the energy scale is concerned, theoretical results are consistent with experimental ones if a voltage/energy conversion factor around 2.6 is assumed, while a factor around 2 is obtained from a lever-arm-rule estimation considering that the applied voltage drop is shared between a 5–6 nm high QD and a 5 nm tunnel barrier while the tip-sample distance is typically around 1 nm. However, a strict quantitative comparison between measured and predicted quantities is presently out of reach because sample details, such as the exact confinement potential, and the degree of anisotropy are unknown. Since the peak's FWHM in the WF mapping is around 50 mV, the energy resolution is not sufficient to distinguish the cal-

culated ground-→(ground-) excited-state transitions (right column of Figure 3.72b) α from β (experimental state C) and γ from δ (D). A comparison of the experimental line profiles (Figure 3.72c left, showing the maps of states B, C, and D along a QD volume slice) and theoretical ones (Figure 3.72c right, for state p_x, and overlaps of α and β, γ and δ, respectively) reinforces this conclusion. Nevertheless, the excellent agreement between the measured and predicted curves of Figure 3.72c demonstrates that the spatial modulation of map C is a genuine effect of Coulomb interaction: In fact, the overlap (dashed line) of the noninteracting counterparts of states α and β–the s and p_x orbitals, mixed together with the same 1:1 ratio as α and β–poorly compares to C.

Our interpretation is further supported by a study of the dependence of the STS spectra on the stabilization current. In the present case, the tunneling rate through the undoped GaAs tunnel barrier is much larger than the typical tunneling rate from the tip to the QD [1]. To systematically investigate charging effects we recorded tunneling spectra at different stabilization currents I_{stab} (i.e., we varied the tip-dot distance) to gradually increase the tunneling rate into the QD and therefore to populate it [6]. In Figure 3.73, we focus on states B and C, which are visible at voltages between 1040 and 1140 mV, dominating the spectra acquired on the QD sides. In the dI/dV spectra collected at increasing I_{stab}, the first (second) peak corresponding to the first (second) p-like orbital gradually disappears (appears). This suggests that at low (high) values of the stabilization current we probe the energy spectrum of an uncharged (charged) quantum dot, while for intermediate values we can see both peaks (as in our WF maps). Thus, the state C must be associated with the tunneling process $N = 1 \rightarrow N = 2$ since it appears at higher I_{stab} (the STS levels measured at increasing values of the current correspond to higher values of QD occupancy). On the other hand, a discussion of state D is more complicated. It could be tentatively ascribed to the tunneling process $N = 1 \rightarrow N = 2$ (states γ and δ in Figure 3.72b) according to theoretical results. However, from Figure 3.71 peak D appears to be located at an energy where the wetting layer significantly contributes to the spectral density (which is high also outside the QD). So, a coupling is possible and this could explain the increased FWHM observed for state D (Figure 3.72).

Wavefunction Mapping of Immobilized Semiconductor Nanoparticles

G. Maruccio, C. Meyer, T. Matsui, D. V. Talapin, S. G. Hickey, H. Weller, and R. Wiesendanger

Semiconductor quantum dots/nanocrystals (QDs/NCs) [7] are commonly called artificial atoms as they share many similar features related to the electronic properties of atoms. This analogy is further reinforced by the theoretical prediction of atomic-like symmetries for the electron wavefunctions (WFs) in semiconductor nanocrystals [8].
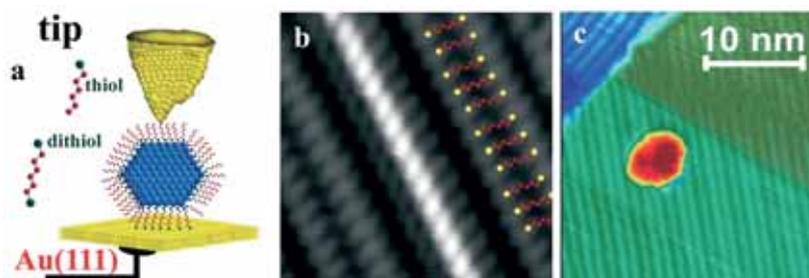
Figure 3.74: **Experimental setup and morphology. a**, Experimental setup. InP nanoparticles are immobilized on a Au(111) surface via hexane dithiol molecules. **b-c**, STM images of the hexane dithiol layer and an immobilized nanoparticle. The measured length of the adsorbed molecules (the distance between adjacent stripes is around 1.2 nm) and nanoparticle size are in good agreement with the expected values. STM parameters: $I_{set\text{-}point} = 150$ pA, $V_{bias} = 0.5$ V, scan rate = 1 Hz (dithiols), $I_{set\text{-}point} = 30$ pA, $V_{bias} = 3.5$ V, scan rate = 1 Hz (NC).

However, there is no direct experimental evidence for s- and p-like symmetries in nanoparticle WFs to date. In fact, in all the reports on STS studies of nanoparticles published so far, s- and p-type states were identified by their two- and six-fold single electron charging multiplets [9–12] as a consequence of the atom-like Aufbau principle of sequential energy level occupation [10]. Here, we use for the first time WF mapping [13–17] to obtain direct information about the spatial distribution of WFs in semiconductor nanoparticles. In particular, we investigate colloidal InP nanocrystals and acquire spatially resolved dI/dV maps on individual nanoparticles to determine the symmetry of the squared WFs corresponding to the different confined states resolved in the spectral density. Thanks to our spatial and energy resolution, we are able to distinguish clear s- and p-like WFs in individual nanoparticles for the first time. We also observe charging peaks in the derivative spectra whose energies are in good agreement with theoretical predictions [18] and found a clear influence of the coupling with the surrounding molecules and the gold substrate on the WF symmetry and energies.

We focused on InP nanoparticles prepared via the dehalosilylation reaction between indium chloride and tris-(trimethylsilyl)phosphine in mixtures of trioctylphosphine and trioctylphosphine oxide [19]. The nanoparticles were deposited onto an atomically-flat Au(111) surface covered by a layer of hexane dithiol molecules. This procedure led to an immobilization and a stable attachment of individual NCs. Both the functionalization of the Au(111) substrate by hexane dithiols (0.2 ml diluted in ~60 ml ethanol) and the subsequent nanocrystal deposition were carried out by Langmuir-Blodgett (LB) withdrawal of the substrate (~10 s for the entire sample to cross the solution surface), which was then rinsed with the respective solvent.

The experimental configuration (sketched in Fig. 3.74a) can be depicted as a dou-

ble barrier tunnel junction (DBTJ) where the stabilizing parameter set determines the tip-sample distance and ultimately the tunneling regime which is dependent on the tunneling rates into and out of the nanoparticle (Γ_{in} and Γ_{out}). A low temperature STM image of the dithiol layer is shown in Fig. 3.74b. Individual molecules are distinguishable on the thiolated Au surface which exhibits small molecularly-ordered domains together with some vacancy islands [20, 21]. After vacuum annealing at moderate temperature (around 100°C for approximately 1 hour), the degree of long-range order increases and the molecules self-assemble in a striped phase with stripes oriented along three equivalent directions, corresponding to the main crystallographic orientations of the Au(111) substrate. The bright features are associated with sulfur-containing endgroup dimers/pairs [22], i.e. two neighbouring adsorbed sulphur atoms belonging to adjacent molecules [20, 21]. The separation between adjacent stripes is around 1.2 nm in good agreement with the molecular length (0.9 nm increased by 0.3 nm of S-S distance), indicating that the molecules usually lie flat on the surface with their hydrocarbon backbones fully extended. However, some molecules are oriented perpendicular to the surface (brighter stripe in Fig. 3.74b) in a "standing up phase", in which the alkyl chains are aligned along the surface normal [21, 23]. The distance between stripe segments (i.e. along stripes) is 0.5 nm, in agreement with $\sqrt{3}a_{\text{Au}}$, where $a_{\text{Au}} = 2.884$ Å is the lattice spacing of Au(111) [20, 21]. A possible molecular structure of the hexanedithiol striped phase was proposed in ref [21].

Dipping the thiolated Au substrate in a toluene solution containing the NCs leads to distinct additional features, having apparent lateral dimensions and heights which are in good agreement with the nanoparticles' size range (4-6 nm) as determined by TEM (the lateral dimension of nanoparticles appears slightly larger in STM than their height due to tip convolution effects). The density of particles on the substrate can be controlled and optimized to obtain isolated NCs in the STM images. The ordered dithiol layer and an immobilized nanoparticle are shown in Fig. 3.74c.

To examine the electronic structure of NCs, scanning tunneling spectroscopy (STS) was performed on individual nanoparticles. As expected, we observed a nonconducting gap around zero bias in the *I-V* curve, followed by a series of steps at both negative and positive bias [10, 12]. In the following, we focus on the positive sample bias voltage regime where we succeeded in mapping the WF symmetries of the corresponding electronic states. Typical normalized derivative $((\text{d}I/\text{d}V)/(I/V))$ spectra, acquired at low temperature on the nanoparticle (size 5 nm) shown in Fig. 3.74c, are shown in Fig. 3.75. Discrete peaks are observed, which can be associated with a number of confined states grouped in different multiplets/families. The tunneling spectra were acquired at different positions on the same nanoparticle in order to investigate the spatial distribution of specific electronic states. Moving from the NC center to its sides, the intensities of the low-energy peaks decrease while the others increase in weight. For comparison, the STS curves on the dithiol layer (outside the NC) are almost featureless and no pronounced peaks in the dI/dV spectra were observed for the same bias voltage range. The peaks in the dI/dV spectra measured above the nanoparticles
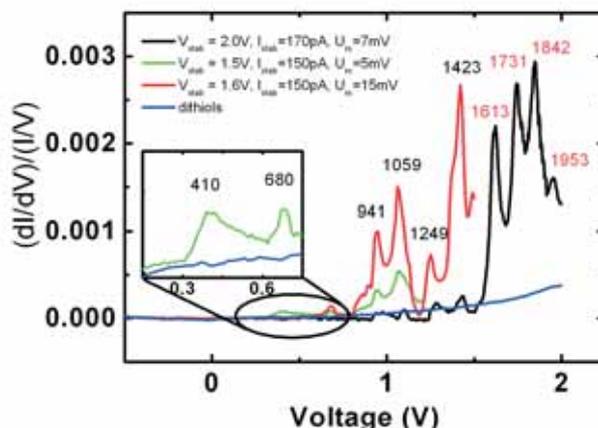
Figure 3.75: **STS spectra.** Individual $(\mathrm{d}I/\mathrm{d}V)/(I/V)$ spectra vs. V measured at different positions on a single InP NC. Moving from the NC center to its sides, the intensities of the low-energy peaks decrease while the others increase in weight. A significant downwards band-bending was typically observed (i.e. Fermi level no longer in the middle of the band gap).

can thus be assigned to the successive charging of s-, p-, and d-states with different electrons.

Concerning the charging energies, it is worth noting that peaks belonging to the same peak family exhibit similar separations which can be ascribed to the different charging energies for the different wavefunction symmetries. The spacing between the peaks within the multiplets is $V_{C-s} = 0.270$ V for the s-doublet, $V_{C-p} = 0.120 - 0.190$ V for the p-peaks and $V_{C-d} = 0.110 - 0.120$ V for the d-peaks. Thus, the peak separation decreases with increasing total angular momentum from s- to p- and d-type states in agreement with the expected decrease of Coulomb interaction when higher orbitals with broader wavefunctions are occupied. According to the constant interaction (CI) model, the addition energy for the dot is: $E_{\mathrm{ADD}}(N) = E_c + \Delta E(N)$, where $Ec = e^2/C$ is the electrostatic charging energy to add an electron to the dot (C is the total capacitance between the dot and the electrodes), while $\Delta E(N)$ is the difference in the single-particle energies for N and $N-1$ electrons on the dot [24]. The charging energies for the lowest orbitals can be calculated from the dimensionless Hamiltonian [18], assuming the interaction between two electrons in the s-state as unit value. Quantitatively, using the value $V_{C-s} = 0.270$ V to calculate the expected separations for p- and d-peaks, we obtain $V_{C-p, \text{ theory}} = 0.185 - 0.200$ V, $V_{C-p, \text{ theory}} = 0.095 - 0.145$ V in quite good agreement with the experimental values [18].

For wave function mapping, we take $\mathrm{d}I/\mathrm{d}V$ images which represent the peak intensity as a function of position. Typical results are shown in Fig. 3.76 for the case of two different NCs with similar sizes. They support the proposed assignment of the

different states in STS spectra since s- and p-symmetry states are visible at the energies corresponding to the first two peaks in the dI/dV spectra. A topographic image was recorded simultaneously with the spatially-resolved dI/dV signal and is shown in Fig. 3.76a for the first NC, while three STS spatial maps taken at resonance voltages are reported on the right (Fig. 3.76b-d). For tunneling conditions corresponding to the energy gap of the NCs (Fig. 3.76b), the LDOS inside the NCs is negligible and the position occupied by the NC appears blue. When we are resonant with the s-state, we observe a roughly circular symmetric intensity distribution (Fig. 3.76c). Then, at higher voltages the tunneling becomes resonant with the p-state and we observe two clear p-like lobes with a pronounced node in between (Fig. 3.76d). No hybridization of p$_x$ and p$_y$ states was observed in our experiments and we ascribe this to the coupling with the substrate which removes their degeneracy and results always in a selection of the p-state oriented along one of the Au(111) main crystallographic directions. To the best of our knowledge, this is the first report of wavefunction mapping of immobilized colloidal nanoparticles and study of the substrate's influence on the confined states. The main difficulties are related to the achievement of a proper and stable immobilization of the NCs on the substrate, their very small size (around 5 nm in contrast to the 40 nm of MBE-grown quantum dots), and the sample preparation from solution. As far as the reproducibility of our data is concerned, in the bottom image of Fig. 3.76, the s- and p-type states of another nanoparticle are shown (Fig. 3.76f-g) along with the corresponding topographic image (Fig. 3.76e). Apart from some differences in the extension of the s-state, WFs of the different NCs look similar. Two lobes with a node between them (the weight in the NC center is considerably less) and located inside the NCs are clearly observable at energies corresponding to the p-states. We can ascribe
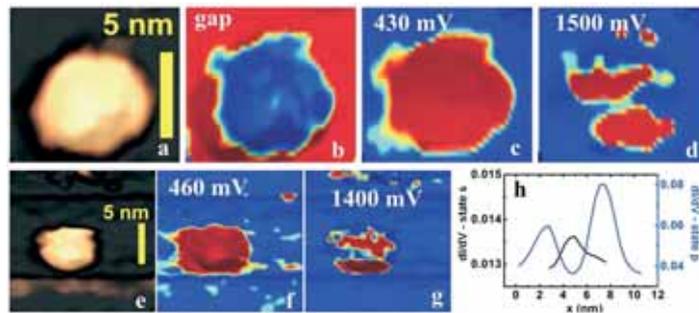
Figure 3.76: **Wave function maps. a**, Topography; **b-d**, Simultaneously acquired STS spatial maps of a single representative NC, taken in the band gap, at 430 and 1500 mV respectively (2nd–4th panel), corresponding to peaks in the $(\mathrm{d}I/\mathrm{d}V)/(I/V)$ spectrum. The grey scale represents the STS signal with respect to the topographic STM image on the left hand side (1st panel). The scale bar is 5 nm. **e-g**, Topography and STS spatial maps showing the s- and p-states for another NC. **h**, Line profiles from a third NC showing how the local density changes along a NP volume slice for s- and p-states. These data were obtained by averaging the differential tunneling conductance in the transverse direction.

the differences in the extension of the s-states (and the selection rule on the low energy p-state) to a partial coupling with the environment (dithiols and gold substrate). This conclusion is supported by the smaller weight and increased full width at half maximum (FWHM) of the s-peak as compared to the other states visible in Fig. 3.75. As a consequence the WF map of the s-state is more perturbed. In Fig. 3.76h, we also report the line profiles extracted from the s-state and the p-state of a third NC, which show how the local electronic density changes along a NC volume slice. We would like to emphasize that the p-state exhibits a clear node between the p-like lobes.

References

[1] Maltezopoulos, T.; Bolz, A.; Meyer, C.; Heyn, C.; Hansen, W.; Morgenstern, M.; Wiesendanger, Phys. Rev. Lett. 2003, **91** (19), 196804.

[2] Rontani, M.; Molinari, E., Phys. Rev. B 2005, **71** (23), 233106.

[3] Rontani, M.; Molinari, E., Jpn. J. Appl. Phys., Part 1 2006, **45** (3B), 1966–1969.

[4] Rontani, M., Phys. Rev. Lett. 2006, **97** (7) 076801.

[5] Marquez, J.; Geelhaar, L.; Jacobi, K., Appl. Phys. Lett. 2001, **78** (16), 2309–2311.

[6] Bakkers, E.; Hens, Z.; Zunger, A.; Franceschetti, A.; Kouwenhoven, L. P.; Gurevich, L.; Vanmaekelbergh, D., Nano Lett. 2001, **1** (10), 551–556.

[7] Alivisatos, A. P., Science **271**, 933–937 (1996).

[8] Brus, L. E., J. Chem. Phys. **80**, 4403-4409 (1984).

[9] Millo, O., Katz, D., Cao, Y. W. and Banin, U., Phys. Rev. Lett. **86**, 5751–5754 (2001).

[10] Banin, U., Cao, Y. W., Katz, D. and Millo, O., Nature **400**, 542–544 (1999).

[11] Liljeroth, P. et al., Phys. Rev. Lett. **97** (2006).

[12] Liljeroth, P. et al., Phys. Rev. Lett. **95** (2005).

[13] Maltezopoulos, T. et al., Phys. Rev. Lett. **91**, 196804 (2003).

[14] Lemay, S. G. et al., Nature **412**, 617–620 (2001).

[15] Repp, J., Meyer, G., Stojkovic, S. M., Gourdon, A. and Joachim, C., Phys. Rev. Lett. **94** (2005).

[16] Folsch, S., Hyldgaard, P., Koch, R. and Ploog, K. H., Phys. Rev. Lett. **92** (2004).

[17] Lu, X. H., Grobis, M., Khoo, K. H., Louie, S. G. and Crommie, M. F., Phys. Rev. Lett. **90** (2003).

[18] Warburton, R. J. et al., Phys. Rev. B **58**, 16221–16231 (1998).

[19] Adam, S. et al., J. Chem. Phys. **123**, 084706 (2005).

[20] Esplandiu, M. J., Hagenstrom, H. and Kolb, D. M., Langmuir **17**, 828–838 (2001).

[21] Leung, T. Y. B. et al., Langmuir **16**, 549–561 (2000).

[22] Claypool, C. L. et al., J. Phys. Chem. B **101**, 5978–5995 (1997).

[23] Prolonged dosing leads to a phase transition from a striped phase to the standing-up phase, while lower thiol coverage (obtained by partial reductive desorption at 0.3V or annealing) results in thiols lying flat on the gold surface [24].

[24] Kouwenhoven, L. P., Austing, D. G. and Tarucha, S., Rep. Prog. Phys. **64**, 701–736 (2001).

3.4 Molecular systems

3.4.1 STM/SPSTM on magnetic molecules

Introduction

The central goal of our activities in this field is the local magnetic characterization of molecules by means of spin-polarized scanning tunneling microscopy. We intend to address the paths of magnetic interaction between magnetic molecules as well as between molecules and magnetic or nonmagnetic surfaces.

Within the last three years period the research was focussed on the following aspects as discussed in greater details below:

1. Setting up and improving a variable-temperature STM for the screening of volatile paramagnetic molecules.

2. Development and construction of a 300 mK/17 Tesla STM for the local magnetic characterization of magnetic molecules.

3. Growth study of suitable paramagnetic molecular systems.

A variable-temperature STM for screening of molecular systems

S. Kuck, J. Wienhausen, G. Hoffmann, and R. Wiesendanger

We developed a new vacuum setup for the preparation and the characterization of volatile magnetic molecules with a variable-temperature STM (VT-STM). For this purpose, new vacuum components were constructed which enable a flexible handling of transportable evaporators. Therefore, without breaking the vacuum conditions, molecules and other evaporation materials, as NaCl, can be introduced into the vacuum system on a short time scale within a few hours. Moreover, the preparation of molecular samples with the substrate held at low temperatures became possible (Fig. 3.77 gives an overview of the setup).

For the local characterization a custom-made VT-STM [1] was installed in the analysis chamber. The VT-STM was mounted on a modified commercially available damping stage platform (Omicron). Modifications included the mounting points to host the STM as well as a side entrance to evaporate molecules directly into the cooled STM (see Fig. 3.78).

For the first design, the lowest possible working temperature was approx. 30 K with the helium flux and therefore the liquid helium consumption at its maximum. To reduce helium consumption and the working temperature we recently designed and
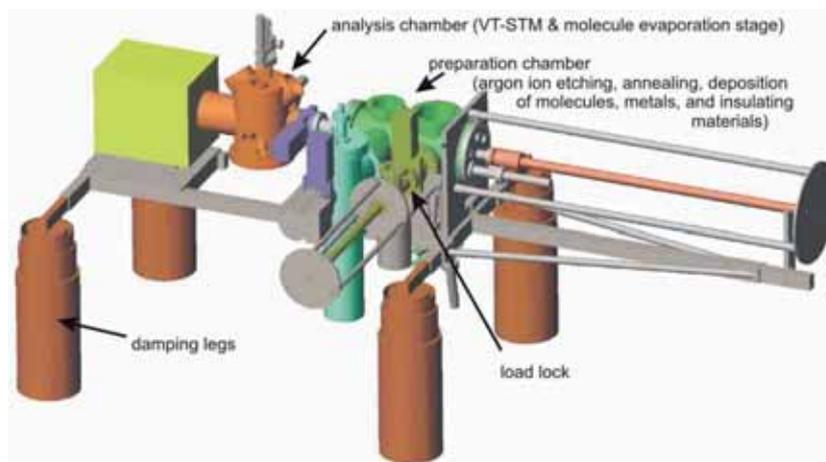
Figure 3.77: 3D-sketch of the ultra-high vacuum system for the preparation and characterization of volatile molecules. The system consists of a load lock to introduce samples, tips, and molecule evaporators, and a preparation chamber to sputter and anneal metallic crystals and to prepare thin layers of molecular, insulating, and magnetic films. The system is completed by the analysis chamber equipped with a VT-STM and a heating stage to deposit molecules with the sample loaded in the cooled STM.

Figure 3.78: Image of the VT-STM head. The STM head is mounted on an eddy current damping stage by Omicron. The gold-plated copper platform is additionally modified to host the self-made STM and enables the integration of a molecule evaporator.
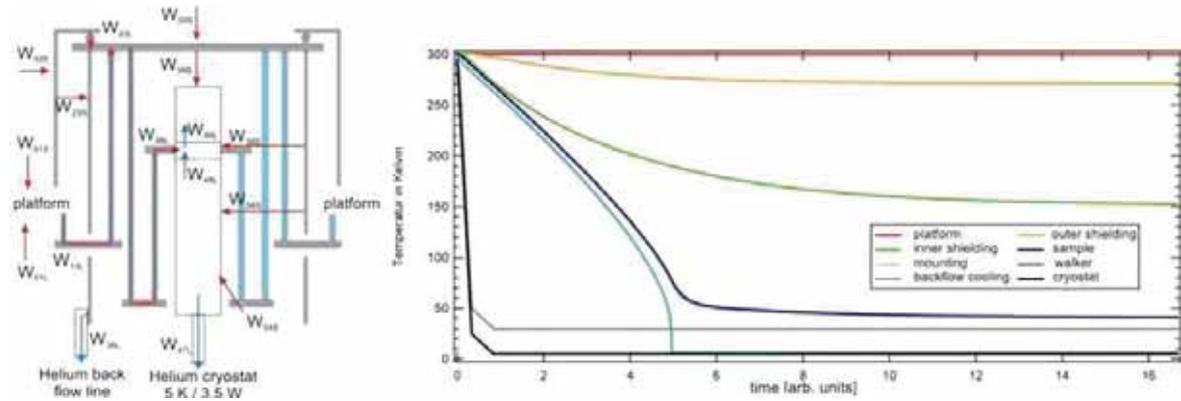
Figure 3.79: Left: schematic representation of the experimental setup and paths of heat dissipation. The numerical modeling covers heat radiation (W_{xyS}) and heat transport (W_{xyL}) between the different parts of the STM setup. The right graph indicates the time-dependent temperature variations for the different parts of the setup after start of the cooling at the time $= 0$.

installed a new VT-STM head with improved thermal shielding. To minimize thermal conductivity, we numerically modeled the heat dissipation paths through the different mechanical parts of the STM and the cooling system (see Figure 3.79).

Here, we used an iterative approach to numerically simulate the cooling of the system with time. In this approach, we accounted also for the temperature dependence of the thermal conductivity (λ) and the thermal capacitance (C) for each material individually [2,3]. At the time $i = 0$ the complete system starts at room temperature. Then, cooling through the cryostat is switched on. The time-dependent response of the system reflects transport of thermal energy between the different parts (W_{xy}) and the temperature-dependent heat capacitance $C_x(T_{(x,i)})$. Then, the new temperature T for each part (x) after a time step i_{step} is derived from :

$$T_{(x,i+i_{step})} = T_{(x,i)} - W_{xy}(T_{(x,i)}, T_{(y,i)}) \cdot \frac{i_{step}}{C_x(T_{(x,i)})}. \tag{3.15}$$

The transport of thermal energy W_{xy} is proportional to the temperature dependent thermal conductivity (λ) and the shape of the different parts (described by the cross section area A and the length L) :

$$W_{xy}(T_{(x,i)}, T_{(y,i)}) = \frac{A_{xy}}{L_{xy}} \cdot \lambda_{xy}(T_{(x,i)}, T_{(y,i)})(T_{(x,i)} - T_{(y,i)}). \tag{3.16}$$

Based on this mathematical description we simulated and optimized the setup. For verification, we applied the same approach to other similar experimental setups already present at the institute (not shown) with good quantitative agreement. The STM head is connected to the liquid helium cryostat through a copper braid and isolated from the environment by a radiation shield which operates at the temperature
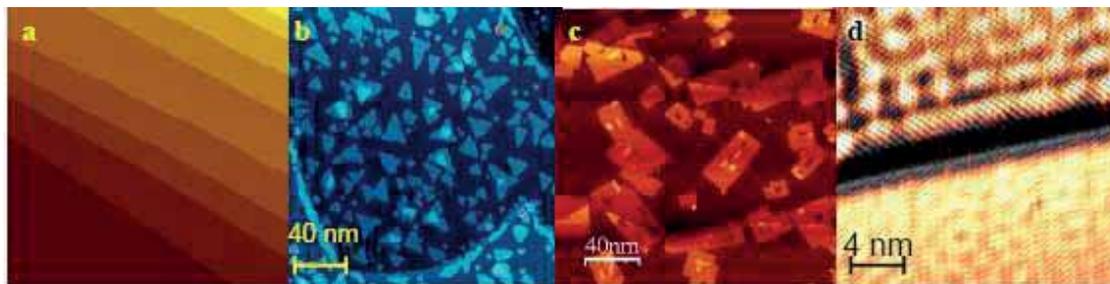
Figure 3.80: STM images of template surfaces for the growth and investigation of molecular systems: (a) a pure noble metal surface, (b) triangular shaped magnetic Co islands on Cu(111), (c) insulating NaCl adlayers on Cu(111). (d) Image zoomed into the region of a NaCl island with spectroscopic information overlayed. Wave patterns reflect constructive and destructive scattering of surface state electrons along the monoatomic NaCl/Cu(111) step edge.

of the Helium back flow line. The STM is fixed to the radiation shield via several stainless steel tubes. These tubes are circularly arranged around the STM resulting in a large effective area to maximize stiffness. The wall size of the tubes is minimal for lowest heat transport. The minimal achievable working temperature is now approx. 18 K at highest Helium flux (2 l/hour). During routine experiments the STM is operated in the range of 22 - 25 K at a consumption of approx. 0.9 l/hour.

For illustration of the capabilities of the final setup in terms of preparation and STM experiments, Fig. 3.80 shows four representative examples of relevant template surfaces: (a) the pure metallic host substrate, (b) magnetic islands on a diamagnetic surface, and (c) insulating NaCl islands on Cu(111) for electronic decoupling. Beyond imaging, spatial mapping of electronic states became possible. In Fig. 3.80d the topographic image of an atomically resolved NaCl island on Cu(111) is overlayed by the electronic information, parallely acquired. The scattering of surface state electrons at the step edges is visible. Moreover, in the current setup the preparation of molecular systems directly onto the cold surface is possible. Low temperature preparation reduces (or even prevents) thermally induced mobility of single molecules. Figure 3.81 depicts two STM images after deposition of CuPc onto a copper substrate. The deposition of CuPc at room temperature leads to the decoration of copper step edges, whereas the deposition at low temperatures reduces thermally induced molecular mobility and step edges stay untouched. Recently, we additionally installed a gas inlet system to introduce molecules with a high vapor pressure at room temperature as metallocenes.
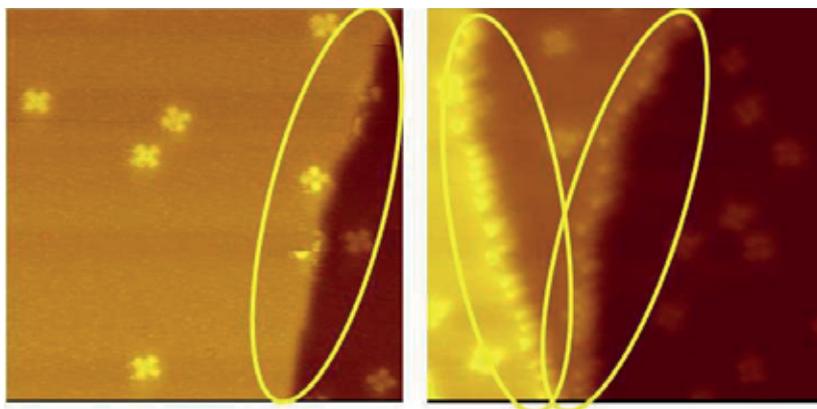
Figure 3.81: Two images of CuPc deposited on a copper substrate at different substrate temperatures. Molecular deposition at room temperature leads to the decoration of copper steps, i.e., the decoration of step edges indicates thermally induced mobility of molecules. After deposition at low temperatures with the sample stored in the STM head (approx. 30 K) only terraces are covered with CuPc molecules.

References

[1] S. Kuck, Diploma Thesis, Universität Hamburg, 2004.

[2] Lakeshore Ltd., 'cryogenic reference table'.

[3] E. P. Roth and A. C. Anderson, J. Appl. Phys. **47**, 3644 (1976).

[4] S. H. Pan, 'Piezo-electric motor, international patent publication No. WO 93/19494', 1993.

[5] A. Wachowiak, Dissertation, Universität Hamburg 2003.

[6] J. Wienhausen, Diploma Thesis, Universität Hamburg, 2006.

Setup of a new 300 mK/17 Tesla STM

J. Wienhausen, J. Schwöbel, R. Ravlić, M. Nohme, K.-P. Gemmer, G. Hoffmann, and R. Wiesendanger

In 2004, the planning for the installation of a 300 mK (^{3}He cryostat) STM system equipped with a 17 Tesla magnet for the investigation of molecular systems started. A working temperature in the range of a few hundreds of mKelvins enables the precise detection of local excitations in molecular systems down to a few ten μeV by inelastic tunneling spectroscopy [1]. At the same time a high external magnetic field will cause an observable Zeman splitting of molecular states.

In such a system the STM head is connected to a liquid ^{3}He reservoir. The working temperature of 300 mK is achieved through pumping on the liquid ^{3}He reservoir by a sorption pump. The ^{3}He system is fully shielded by a ^{4}He cryostat. The ^{4}He cryostat acts as a radiation shield and cools during the STM operation the ^{3}He sorption pump. For recondensation of ^{3}He in the reservoir, the reservoir itself is brought into thermal contact with the ^{4}He cryostat.

After intensive evaluation of different design concepts for such a ^{3}He cryostat system the final selection of the manufacturer was made in 2005. Relevant aspects were an acquisition time beyond 100 hours without the need of recondensation of ^{3}He, the possibility to prepare surfaces at cryogenic temperatures, and two mechanically separate systems for ^{4}He and ^{3}He for vibrational isolation.

The STM head is mechanically fixed to a ^{3}He insert and will be operated at 300 mK. To reach different positions the insert can be vertically displaced but stays during all operations within the ^{4}He cryostat to sustain efficient cooling. During STM experiments the STM head is lowered into the center of a Nb-alloy superconducting magnet with the ^{3}He condensation pump in thermal contact with the ^{4}He cryostat. Sample and tip exchange as well as a ^{3}He condensation and deposition of molecules are taking place in the region above the magnet with the STM kept at 5 K.

Currently, the design, the construction, and the assembling of the STM head is finished. For future developments the design includes the possibility to integrate a xy table for lateral course positioning. Assembling and testing of the preparation system, i.e., for argon ion etching, heating of crystals, metal and molecule evaporation as well as the installation of the transfer system are nearly finished. Figures 3.82 and 3.83 depict images of the current status with most components mounted through the top view port and from the side.

A side chamber explicitly for the preparation of crystals with high melting points, e.g. tungsten crystals has been developed (see Fig. 3.84). This chamber includes a leak valve for oxygen dosage and a heating stage for temperatures up to 2200 degree Celsius. The heating stage is fully covered by a water-cooled shielding to minimize thermal radiation, i.e., the release of undesired adsorbates from the chamber walls during warm up. Still, optical access from the top for temperature measurements is provided. Although further extensions are currently not planned additional ports are
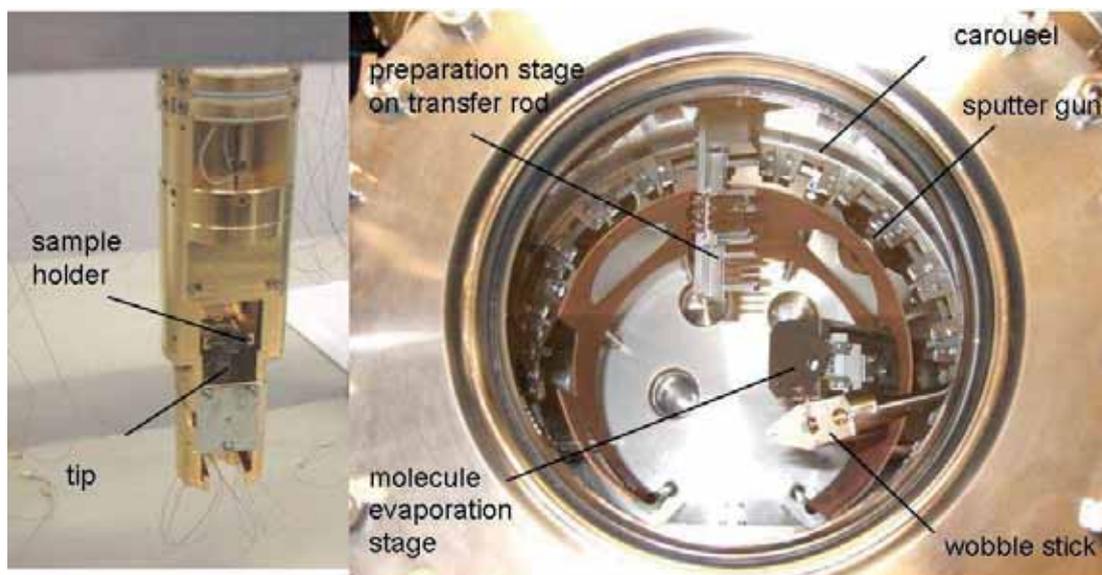
Figure 3.82: (left) Image of the STM head for the new 300 mK system mounted on an ex-situ test stage. A test sample as well as a tip are introduced for first calibration experiments under ambient conditions. (right) Top view into the preparation chamber equipped with most relevant parts. Currently, only the metal evaporators are still missing and testing of the different components is ongoing.
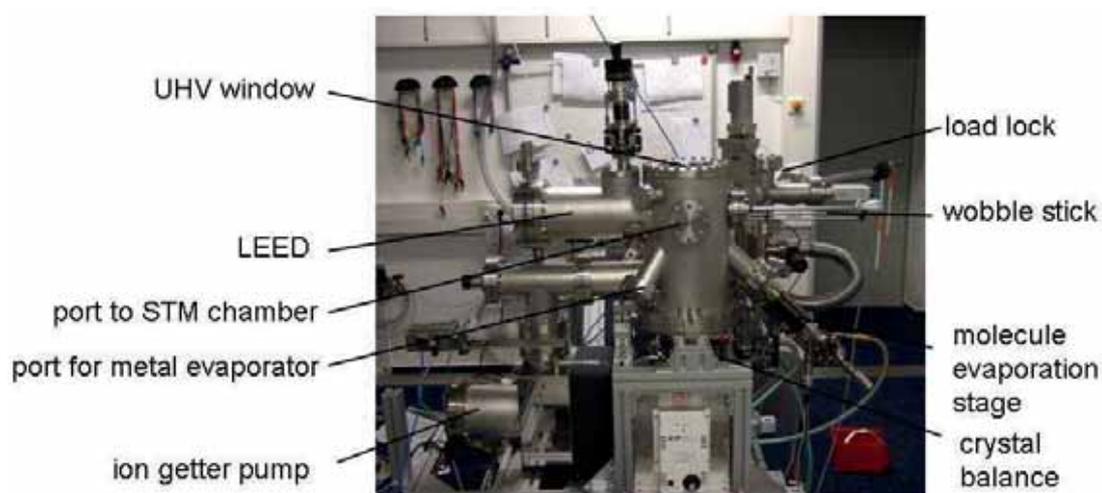
Figure 3.83: Side view of the preparation chamber fixed to a rigid frame which will also host the cryostat system.
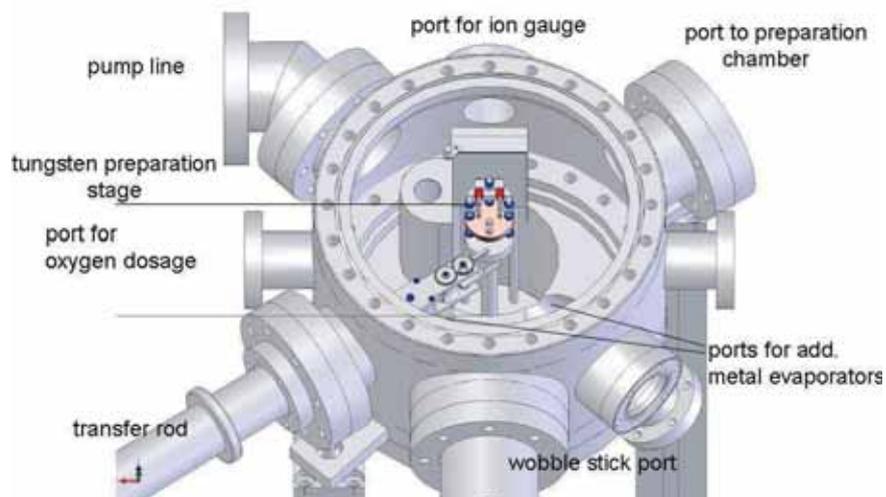
Figure 3.84: An extra side chamber for the high-temperature preparation of tungsten crystals was developed. In this setup other vacuum components are protected against the heat load during the preparation by a water-cooled shield. For temperature measurements optical access for a pyrometer is granted from the top view port.

integrated in the flange system for future developments.

References

[1] X. H. Qiu, G. V. Nazin, and W. Ho, Phys. Rev. Lett. **92**, 206102 (2004).

3.4.2 AFM/MExFM on magnetic molecules

Introduction

In order to study physical properties of magnetic molecules with atomic force microscopy (AFM) as well as with magnetic exchange force microscopy (MExFM) we added an *in-situ* evaporation facility to an existing UHV system. In collaboration with the chemistry department, salenes and metallocenes are being studied. Since their properties can be modified by changing the metallic center atom or by adding functional groups we intend to study different types of molecules. Therefore, an *in-situ* exchangeable evaporator was designed to avoid extended downtimes of the UHV system during bakeout.
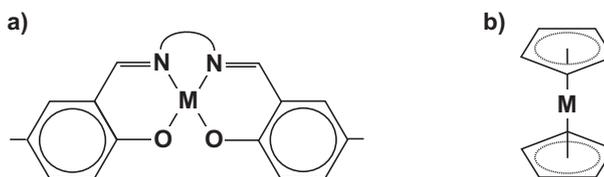
Figure 3.85: **(a)** Salene molecule and **(b)** Metallocene molecule. Their properties can be modified by exchanging the metal center or by adding functional groups.

Exchangeable Molecule Evaporator for UHV studies

K. Lämmle, A. Schwarz, and R. Wiesendanger

The existing UHV system is composed of three chambers and a load lock as shown in figure 3.86. New samples and cantilevers are transfered into the system through the load look connected to the preparation chamber, which is used to prepare substrates and AFM-cantilevers. The analysis chamber contains a LEED/AES unit and a commercial room temperature AFM/STM [Omicron]. In the cryostat chamber AFM and MExFM experiments are performed at liquid helium temperatures with a home-built instrument [1] at an external flux density of up to 5T. To prevent all these parts of the UHV system from contamination during molecule evaporation, we added a separate chamber. The new chamber is equipped with an ion getter pump, a turbopump, a titanium sublimation pump and a gate valve to be able to operate it autonomously. Basic design requirements for the chamber and the molecule evaporator inside were compatibility with the existing transfer system between chambers, *in situ* exchangeability of the evaporator/crucible, a heatable sample station and means for well controlled molecule evaporation.
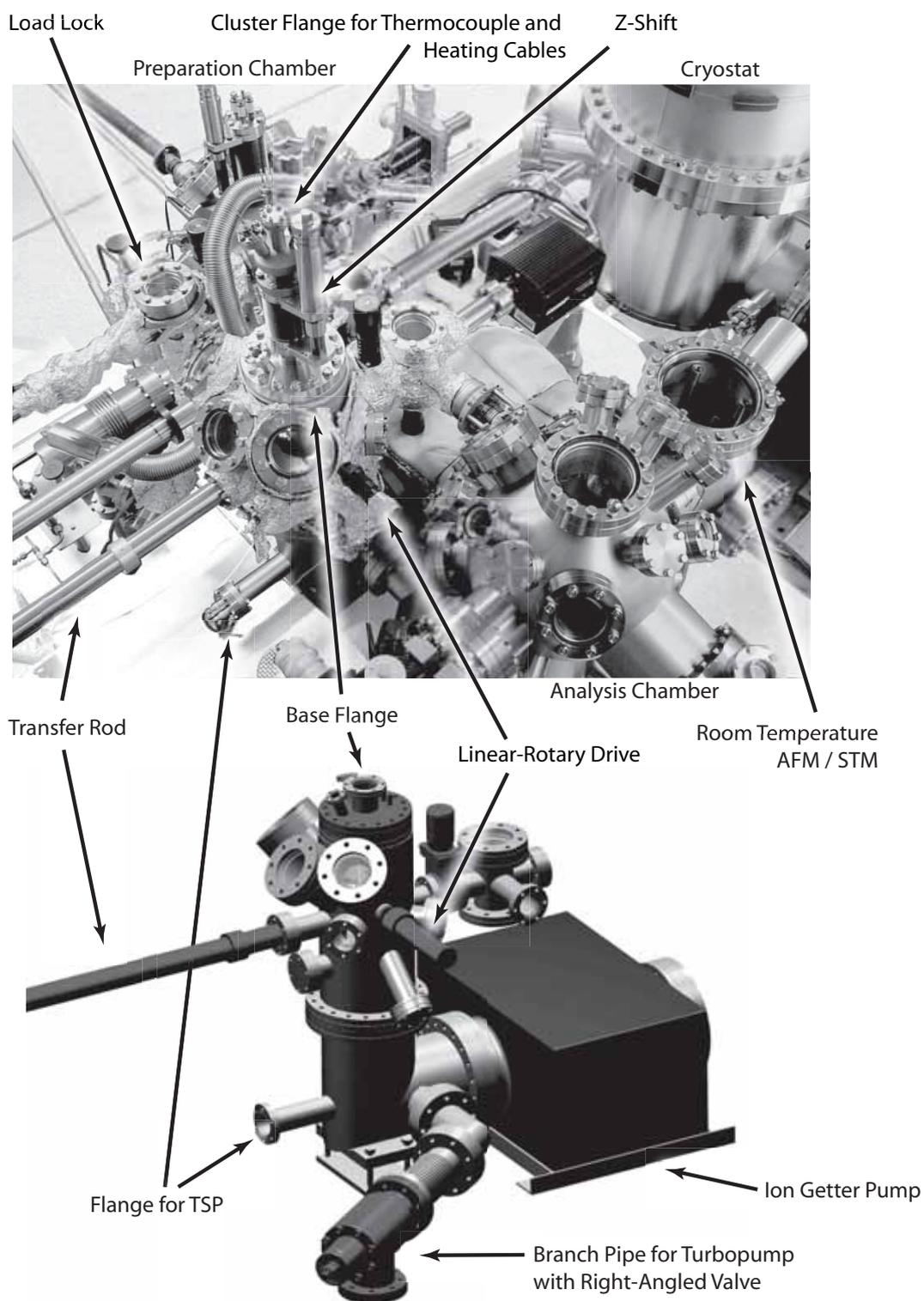
Figure 3.86: Picture of the UHV system with the implemented molecule evaporation chamber. Samples and crucibles can be transfered into the molecule evaporation chamber using the load lock and several transfer rods.

To bring samples and crucibles into the new molecule evaporation chamber we place them into transfer adaptors. These adaptors can be moved with a magnetically coupled transfer rod. The chamber contains a lift mechanism with two stages in a fixed distance of a few centimeters to each other, one for the sample and one for the evaporator (see figure 3.87). Both stages can be moved by a z-shift into the transfer level. The lower stage is occupied by the exchangeable crucible, which is plugged on a special connector, that provides the required mechanical stability and the electrical contacts. The upper one can be loaded with transfer adapters including sample holders upside down. During or after molecule evaporation the sample can be heated by a cartridge heater, which is pressed to the backside of the sample holder. To move the heater up- and downwards, a linear-rotary drive is used, which is approached from the side. The front end of this drive has the shape of an allen wrench which fits into the coupler at the sample stage (see figure 3.87). For thermal decoupling from other parts the sample plus transfer adaptor is placed on four cones made of ZrO_2, a material which has a very small thermal conductivity (2.5 W/mK) and a high mechanical stability. In order to control the temperature a feedback loop with a thermocouple (type E) regulates the heater. To block the molecule beam in the warming-up phase of the evaporator a shutter is included in the sample stage, which can be moved in front of the crucible opening by the same linear-rotary drive used to press the heater onto the sample holder (see figure 3.87). A quartz crystal microbalance (QCMB) is used to control the evaporation rate. It is placed next to the sample, thus the same amount of molecules reaches both, QCMB and sample. To obtain clean samples one has to prevent contamination of the sample surface by additional adsorbates. To minimise the number of unwanted adsorbates the desorption due to friction during transfers and other movements has to be reduced. Therefore, all moving elements described above are guided with Si_3N_4-balls or Dicronite^{TM} coated ball bearings. Furthermore, during thermal evaporation, heating should be confined to the crucible containing the molecules. Otherwise desorption from warm surfaces will increase the contamination level of the sample surface. This is also important for the design of the sample heater. Hence we use the ZrO_2 cones in the sample stage and a special design for the crucible.

Design of the Crucible

To keep the heating of surrounding material during molecule evaporation as small as possible, we developed a crucible that is heated by a tungsten filament directly. The tungsten wire also remains stiff at high temperatures which allows to use the filament as support for the crucible as well. Therefore the connections between the crucible and the environment are limited to the two ends of the filament (W wire, diameter 0.25 mm) and a thermocouple (Type E, diameter 0.2 mm) which minimises the heating of the surrounding by thermal conduction. In addition this reduces in combination with
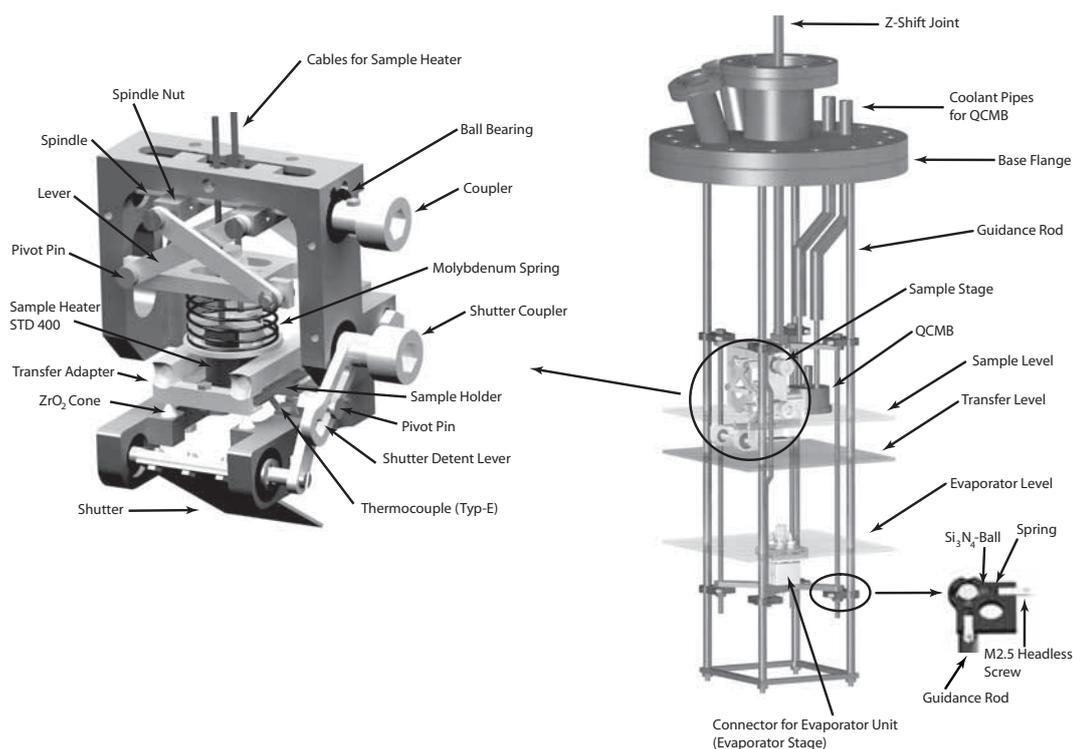
Figure 3.87: Lift mechanism of the evaporator chamber with close-ups of the sample stage and the guidance. The four guidance rods together with the base flange form an inflexible frame for the slide with the two stages. The transfer level is fixed, given by the geometry of the UHV system. The z-shift can be used to move the sample or evaporator level to the transfer level, allowing the exchange of sample or crucible with the transfer rod. In the close-up of the sample stage a sample holder is shown with the heater pressed on his backside. To move the heater up- and downwards one has to rotate the coupler with the linear-rotary drive, which is shown in figure 3.86. The same device can drive the shutter coupler when the sample stage is slightly shifted upwards with the z-shift.

the small-sized crucible (diameter 6 mm / height 9 mm) and the excellent thermal contact between tungsten filament and crucible the required power for evaporation. Hence the heating of the surrounding by radiation is small. The crucible has two parts, a reservoir and a cap, to attain a big volume with a small aperture which maximizes the operation time. Since the tungsten wire is directly wound in an external thread around the crucible, we have to use insulating material for the body. We chose Shapal-M^{TM}, a machinable and inert ceramic. Its thermal conductivity (90 W/mK) is less than that of metals (e.g. tungsten 173 W/mK), but higher than for other suitable materials like Macor^{TM} (1.7 W/mK). The thermocouple is implemented as a sensor for a feedback loop to keep the temperature constant. The design combines four well defined electric contacts (two for the heater and two for the thermocouple) together with a safe support for the evaporator unit plus transfer adaptor.

References

[1] M. Liebmann *et al.*; Rev. Sci. Instr. **73**, 3508 (2002).

3.4.3 Scanning tunneling microscope study of iron(II) phthalocyanine growth on metal and insulating surfaces

A. Scarfato, S.-H. Chang, S. Kuck, J. Brede, G. Hoffmann, and R. Wiesendanger

Introduction

Due to the broad field of applications metal phthalocyanine (MPc) molecules and their derivatives have attracted intense interest of researchers within previous decades. They are important compounds for optical and organic electronic devices such as organic light-emitting diodes, thin film transistors, and solar cells [1–3]. The physical properties of MPc molecular films are strongly affected not only by the molecular structure but also by the molecular orientation in thin films as well as by the interface to the hosting carrier. Therefore, molecule-molecule and molecule-substrate interactions are important issues for the formation of highly ordered MPc molecular films and attracted considerable interest in these planar molecular model systems, in experiments [4–7] and in numerical modeling [8–10].

Thanks to its spatial resolution scanning tunneling microscopy (STM) and spectroscopy (STS) are intensively used to determine both, geometric and electronic structure of MPc molecules deposited on metallic surfaces. The adsorption configurations of several MPc molecules on various metal substrates have been studied with STM under ultrahigh vacuum (UHV) conditions [4–7, 11–22]; Hipps and his colleagues demonstrated the growth of well-ordered molecular monolayers of Cu-, Ni-, Co-, and FePc on Au(111) [11,22]. They attribute the observed variation of contrast in the molecular center between different MPc to the specific occupation of metallic d-orbital states. For larger overages, Cheng et al. [5], J. Åhlund et al. [6] (FePc) and Takada et al. [20] (CoPc) reported on an improved homogeneity and discussed their findings in terms of molecule-molecule and molecule-substrate interaction. Moreover, spin-scattering processes manifest themselves as a 'Kondo-resonance' in STS and were reported for paramagnetic MPc with a 'Kondo-temperature' depending on the molecule-substrate coupling [22, 23].

Common to all above mentioned experiments is the limitation to MPc deposited on metallic carrier substrates. However, in most applications for optical and molecular devices [1, 24–26] molecular layers are combined with insulating substrates, such as glass and silica, to prevent quenching of optical and electronic properties due to hybridization of molecular states with those of the substrates. In consequence, most relevant physical and chemical properties of molecules differ not only quantitatively but qualitatively from those on metal substrates. It is therefore desirable to overcome the limitations of metallic substrates in STM experiments. Pioneering STM/STS work in recent years successfully demonstrated [13, 14, 27] that single molecules adsorbed on a thin layer of an insulating material are indeed efficiently decoupled from the metallic carrier substrates and recover their pristine properties.

Here, we report on the first STM investigation of the growth behavior of complete layers of molecules on an insulating layer. We study FePc molecules deposited on NaCl/Cu(111) and, for comparison, FePc on Cu(111) utilizing our home-built variable-temperature STM (VT-STM). Short-range ordered molecular domains with different molecular orientations are found on the Cu(111) surface. In the second FePc monolayer long-range ordered domains are observed. Adsorption configuration and molecular structure as well as molecule-molecule and molecule-substrate interactions are compared to previous findings for FePc on Au(111) and for FePc on NaCl.

Experimental procedures

The experiments were performed in an ultra-high vacuum system equipped with a variable-temperature STM and a preparation chamber for substrate cleaning, thin film and molecular deposition. Cu(111) samples were prepared at room temperature and then transferred into the STM operated at $\sim$ 30 K. As STM probes we used electro-chemically etched tungsten tips.

Images shown represent raw data after line flattening. Bias voltages refer to the sample potential with respect to the tip. Thermal drift and scanner piezo creep result in an estimated error of $\sim$ 3 per cent in lateral dimensions after recalibration of x and y scales based on the atomically resolved structure of the 2nd ML of NaCl present in most images.

FePc.

The MPc molecule with a central iron atom in a Pc skeleton has a planar structure with a four-fold symmetry in the gas phase. The molecular structure of FePc molecule is shown in Fig. 3.88a. The lateral dimension of an individual FePc molecule is approx. 1.48 nm.

FePc molecules were thermally deposited from a Cu-crucible with the deposition flux controlled via a microbalance. The deposition rate was approx. one ML per 30 s. We used commercially available FePc powder (90 per cent purity, Sigma-Aldrich) which was heated prior to the sample preparation by 70 hours just below deposition temperature for purification.

Cu(111).

The Cu(111) surface has a hexagonal close-packed lattice structure with a three-fold symmetry. The three equivalent close-packed directions are [-110], [-101], and [0-11]. The orientation of the Cu(111) crystal was determined previous to the experiments and the crystallographic axes are indicated in all relevant images. The monolayer step height of Cu(111) is $\sim$ 2.08 Å, and the size of the (111) surface unit cell is $\sim$ 2.56 Å. Cu(111) surfaces were cleaned by repeated cycles of Ar+ ion etching and annealing to $\sim$ 900 K before NaCl and FePc deposition.
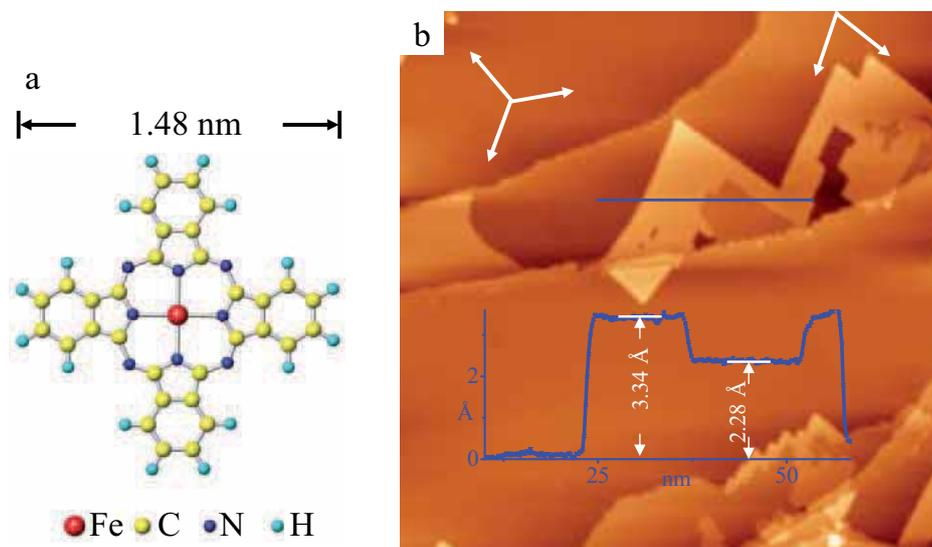
Figure 3.88: (a) Molecular structure of iron(II) phthalocyanine (FePc). (b) STM image of NaCl islands grown on a Cu(111) surface at room temperature. Close-packed directions of Cu(111) and two step edges of NaCl are indicated. Inset: Line-profile over a NaCl island along the blue line. The island is identified as being 2 ML high with an enclosed 1 ML high NaCl terrace ($U_{bias} = 0.97$ V, I = 100 pA, image size: 104×104 nm^2).

NaCl films on Cu(111).

Until now, several insulating layers were grown on metal substrates and were studied by STM [28]. In the present investigation we use NaCl as an insulator to control the interaction of the molecules with the substrate. The growth behavior of NaCl on Cu(111) is reported elsewhere [29–31]: NaCl forms (100) facets with step edges being electrically non-polar and parallel to one of the crystallographic axes [30]. Here, insulating NaCl islands were prepared by deposition of NaCl through a home-made evaporator onto the clean Cu(111) surfaces. Figure 3.88b shows a representative STM image of the substrate after NaCl deposition at room temperature. Rectangular NaCl islands are formed on the Cu(111) surface [30, 31].

The cross section along the blue line indicated in Fig. 3.88b (see inset) reveals that before completion of the first monolayer at an apparent height of ~ 2.28 Å the second monolayer grows on top with a relative height of ~ 1.06 Å. The decrease in experimental height results from the reduced electron conductivity with increasing thickness of a semi-insulating material as discussed in ref. 32. The sample morphology shown is ideally suited to compare growth and molecular appearance of FePc on different adsorption sites, i.e., on top of the bare metallic surface, on the 1st ML NaCl, and on the 2nd ML NaCl, within a single experiment circumventing additional complications due to the unknown properties of the STM probe tips.

Results

1. Growth behavior of FePc at different coverages. Before focusing on the detailed analysis of results for FePc at a coverage of approx. 1 ML, we first provide on overview of experimental results at various coverages of FePc. All these experiments were performed on Cu(111) being partially covered with 1st and 2nd ML NaCl.

At an early stage, the adsorption of FePc molecules starts on the bare Cu(111) surface and no FePc molecules are found on top of NaCl terraces. At a coverage of FePc much below 1 ML we find perfect alignment of one molecular axis (see Fig. 3.89a) relative to one of the equivalent crystallographic axis of Cu(111).

Note: Cu(111) has a threefold symmetry whereas FePc molecule has a fourfold symmetry. This results in an alignment of one molecular axis parallel to one of the surface axes, whereas the second molecular axis is not parallel to any other axes accordingly. Within the experimental resolution we find no indication for substrate induced vertical bending of the molecules nor in-plane deformation,, i.e., the molecular axes enclose an angle of exactly 90°.

At a later stage (Θ <1 ML, see Fig. 3.89b) the orientation of molecules relative to the surface is released; instead short-range ordered domains appear. Few molecules adsorb on the NaCl surface with the step edges fully decorated. FePc molecules are highly mobile on top of the NaCl terraces, whereas they are not visible on the 2nd ML NaCl.

At a coverage of $\Theta \sim 1$ ML, first 2nd ML FePc domains are formed on top of 1st ML FePc. Before completion of the 2nd ML, however, complex molecular clusters of various heights appear which are barely conductive. This prevents the study of
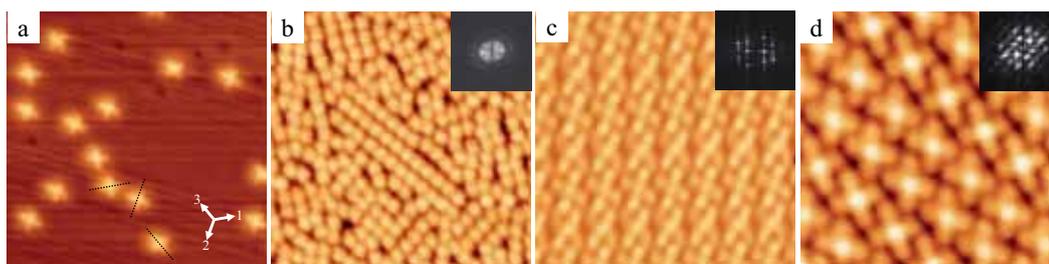
Figure 3.89: STM images of FePc / Cu(111) at different coverages. a) At $\ll$ 1 ML isolated FePc molecules are statistically distributed with one molecular axis aligned to one crystallographic axis. b) At <1 ML, few short range ordered domains appear; however, no preferred domain nor molecular orientation is identified with the FFT data showing a blurred spot (see inset). c, d) At ~1 ML FePc molecules are arranged in well ordered domains. Averaged over a larger surface area no preferred alignment of molecules and domains is found. Within small areas FFT data (insets) show aligned structures but strong variations between different areas. (a) - 200 mV, 100 pA, 23×23 nm^2; (b) 1.6 V, 97 pA, 30×30 nm^2; (c) 0.29 V, I = 39 pA, 10×10 nm^2; (d)- 0.6V, 30 pA, 7.7×7.7 nm^2.

higher coverages. At this stage few, highly mobile FePc molecules start to decorate the 2nd ML NaCl but this system is too unstable for detailed STM investigations and is therefore not further discussed.

2. Growth behavior of FePc at approx. 1 ML coverage: Figure 3.90a shows the result of molecular adsorption on such an inhomogeneous substrate of Cu(111) partially covered with NaCl islands. We identify four distinctively different areas: (A) the bare Cu(111) surface is completely covered with FePc, (B) is partially covered by the second layer of FePc, (C) on NaCl/Cu(111) we find a superstructure of ordered FePc molecules, whereas (D) the 2nd monolayer of NaCl/Cu(111) does not exhibit any adsorbed molecules.

1st ML FePc / Cu(111)

Area A in Fig. 3.90a exhibits a monolayer of FePc molecules on the bare Cu(111) substrate. In higher resolution STM images of FePc monolayers (Figs. 3.89c,d) we find the internal molecular structure of individual FePc molecules nicely resolved. An FePc molecule appears as a crossed four-lobes structure with a protrusion at the center. The observed structure is in reasonable agreement with the chemical structure indicated in Fig. 3.88a and comparable to FePc molecules on other substrates [4,11]. Each lobe represents the delocalized binding orbitals of the phenyl rings whereas the contrast in the center reflects the half-filled d_Z^2 orbital of the Fe ion near the Fermi level [8,11]. However, we already notice that individual molecules are not well aligned to each other.

In Figs. 3.89c and d we identify molecules orientated in different directions. For a closer inspection Fig. 3.91 presents images from different spots of the same surface. With the crystallographic axes indicated we find several orientations of the FePc molecules. As a guide to the eye, for some of the molecules the molecular axes and the most nearby crystallographic axes are indicated. The mismatch angle Θ varies between $+14°$ and $-14°$, i.e., within the statistics of our experiment molecules are arbitrarily aligned. The opening angle γ of the molecular axes is between $80°$ and $90°$ and significantly differs from the unperturbed molecules found isolated at lower coverage. Although an additional electronic contribution due to the incommensurability of surface and molecular symmetry can be assumed the non-systematic variation of opening angles cannot be explained by solely electronic effects but indicates an additional structural effect. We interpret this observation as a deformation of the molecular structure which results from the interaction of molecules in close proximity.

Still, formation of domains is observable (see Figs. 3.89c,d). The typical size of the observed unit cells is 1.35 ± 0.05 nm $\times$ 1.49 ± 0.05 nm. Single domains show well ordered structures with the molecules perfectly aligned within these domains. Therefore, related FFT data (see insets of Fig. 3.89c and d) exhibit pronounced features. However, averaging over larger surface areas, no indication for preferred molecular orientations is given.
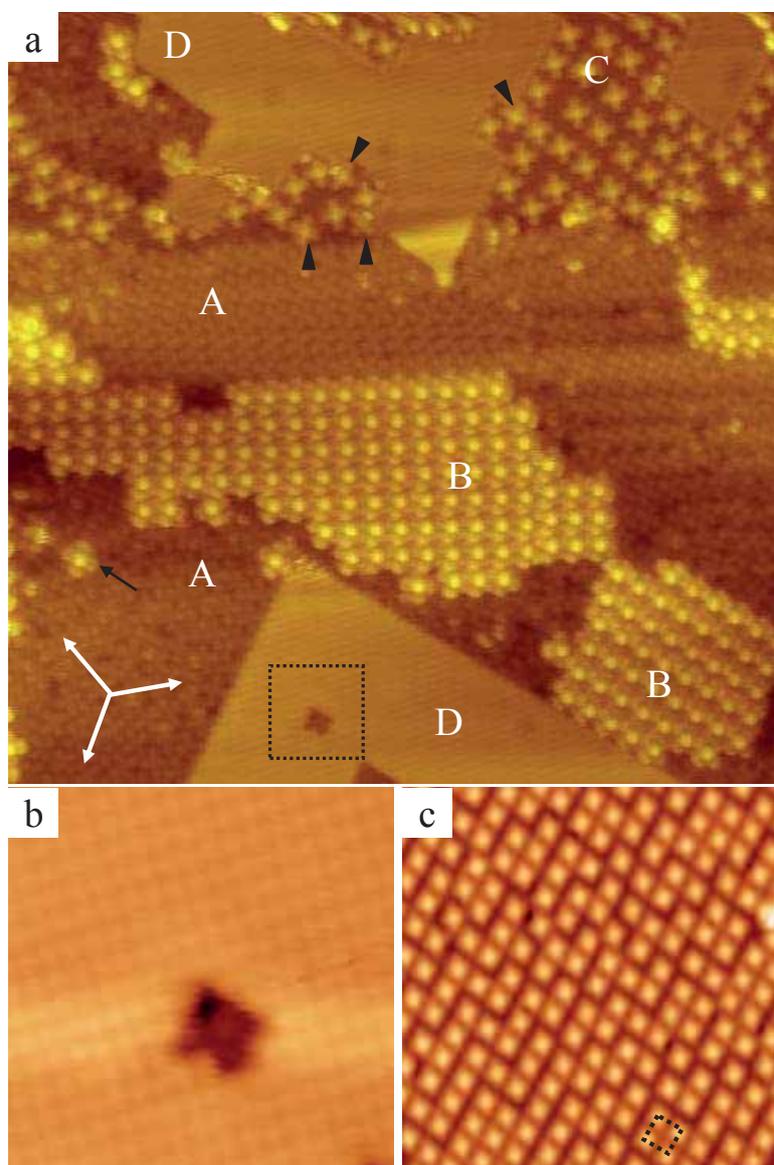
Figure 3.90: (a) STM image of FePc molecules adsorbed on different sites, which are labeled by A, B, C, and D; where A) FePc on Cu(111); B) 2nd ML FePc/Cu(111);C) FePc on 1st ML NaCl; D) bare 2nd ML NaCl. The three crystallographic axes of Cu(111) are indicated by white arrows. The black arrow indicates an isolated FePc molecule on the 1st ML FePc. Black triangles denote FePc molecules on the 1st ML NaCl close to step edges which show different molecular orientation compared to FePc on a free NaCl terrace. (710 mV, 41 pA, 40×40 nm^2). (b) Atomically resolved image of 2 ML NaCl (taken from (a) - black dotted square; 6×6 nm^2). (c) 1 ML FePc molecules on the first NaCl monolayer with a unit cell indicated (710 mV, 41 pA, 24.6×24.6 nm^2).
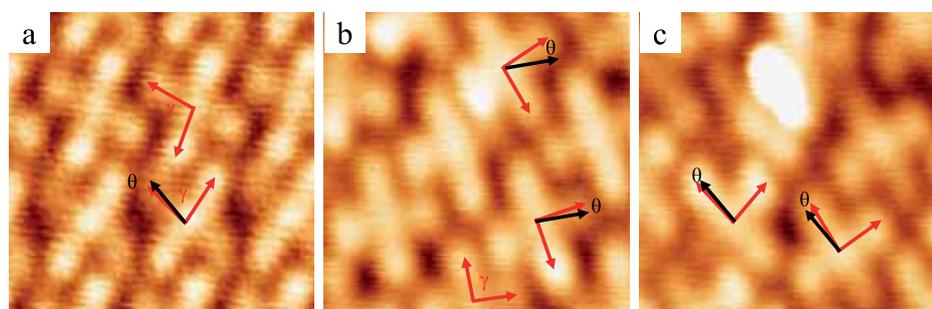
Figure 3.91: High-resolution STM images of the molecular orientation for the first FePc monolayer. All image sizes: 4×4 nm^2. Grey arrows represent the molecular orientations, black arrows the crystallographic directions of Cu(111). γ indicates the opening angle and Θ is the mismatch angle between molecular orientation and crystallographic direction. (a) 0.29 V, 39 pA; (b) 0.51 V, 49 pA; (c) - 0.61 V, 30 pA.

2nd ML FePc / Cu(111)
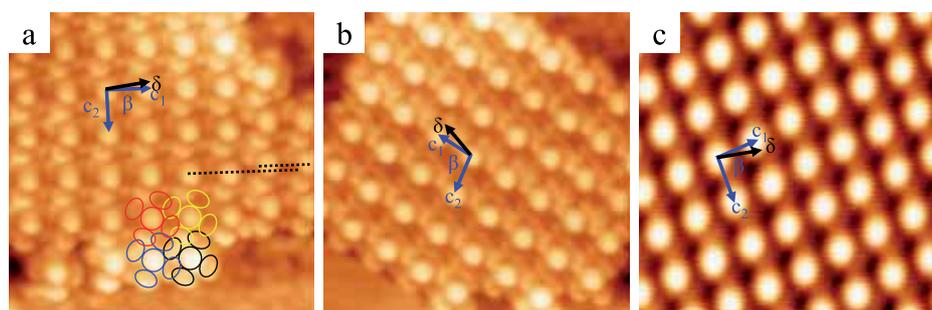
Figure 3.92: High-resolution STM images of second FePc monolayer (0.71 V, 41 A). All image sizes: 10×10 nm^2. c_1 and c_2 represent the unit vectors of the domains. β is the angle between c_1 and c_2, and δ is the angle between unit vectors and crystallographic directions. In (a), simplified sketches of four molecules are introduced.

After completion of the first ML of FePc the growth of the second ML can be observed (area B in Fig. 3.90a). Well ordered domains are formed. Only few isolated FePc molecules are found which appear similar to the ones observed in the first ML but with enhanced structural contrast due to electronic decoupling from the Cu(111) substrate (see FePc molecule in Fig. 3.90a, indicated by a black arrow). Within agglomerated structures identification of individual FePc molecules is not trivial. The center of each molecule appears as a protrusion in the STM images. Between the individual centers a structural variation is clearly recognized but the molecular orientations stay hidden Figures 3.92a, b, and c show three different ordered domains of 2 ML FePc. A quantitative analysis gives the following values for the unit cells: (Do-

main 1) $|c_1| \sim 1.31$ nm, $|c_2|$ is ~ 1.42 nm and $\beta \sim 89^o$, $\delta \sim 8^0$; (Domain 2) $|c_1| \sim 1.32$ nm, $|c_2|$ is ~ 1.37 nm and $\beta \sim 82^o$, $\delta \sim 4^o$; (Domain 3) $|c_1| \sim 1.33$ nm, $|c_2|$ is ~ 1.52 nm and $\beta \sim 86^o$, $\delta \sim 14^o$. We note that the sizes of the units cells are smaller than an individual molecule and smaller than the unit cells in the 1st ML. Therefore, in Fig. 3.92a, the observed domain structure is overlaid with the structure of the molecules as determined in the previous section. We use the clearly resolved molecular lobes visible at the edge of the domain as a marker for the orientation. In agreement with the size of the unit cell, individual molecules are overlapping each other along the phenyl lobes. Cross sections (not shown) through single molecules indicate a tilting angle of approx. 5°. A quantitative interpretation will require numerical simulations whereas the qualitative observation agrees well with bulk molecular properties [33].

Overall, the extension of domains in the 2nd ML FePc is remarkably larger than in the 1st ML FePc with few domain boundaries visible (see black dotted lines in Fig. 3.92a) thus overcoming the inhomogeneity of the 1st ML. The orientation of the domain shown in Fig. 3.92a is quite similar to the model deduced from the LEED pattern [33]. Unfortunately, the structure of the 1st ML underneath is not accessible with STM and remains unknown.

FePc / 1 ML NaCl / Cu(111)

FePc on top of 1 ML NaCl behaves distinctively different. Figure 3.93a gives a detailed insight into the adsorption behavior. All FePc molecules are well aligned with the molecular axes in <01-1> directions; the fourfold molecular symmetry matches with the fourfold symmetry of NaCl. Few exceptions can be observed (see black triangles in Fig. 3.91a) when molecules are close to step edges. FePc are horizontally orientated to the surface - with an intramolecular structure similar to FePc in the 1st ML - whereas a long range ordering is not observed. A precise analysis of the 2nd ML NaCl nearby (with atomic resolution obtained - Fig. 3.91b) reveals the exact atomic positions in the 1st ML NaCl and we find that FePc binds on top of the Cl anions as indicated in Fig. 3.93b [34].

On terraces with a higher density of molecules (see Fig. 3.90c) molecular distances are reduced and short-range domains are formed. Within the experimental resolution the unit cell is square-like (1.67 ± 0.04 nm and 1.68 ± 0.04 nm) and three times the lattice constants of NaCl (0.56 nm). Domain boundaries result from lateral offsets by one NaCl unit cell, i.e. by ~ 0.56 nm.

Discussion and Outlook

STM data of the adsorption of FePc on the bare Cu(111) surface as well as on top of 1 ML NaCl up to an equivalent dosage of 2 ML are presented. At larger coverages formation of molecular clusters prevents STM studies. Variations of molecular arrangements in the first and second ML FePc on Cu(111) are observed. These variations result from the interaction of FePc molecules with the substrate and with neighboring molecules.
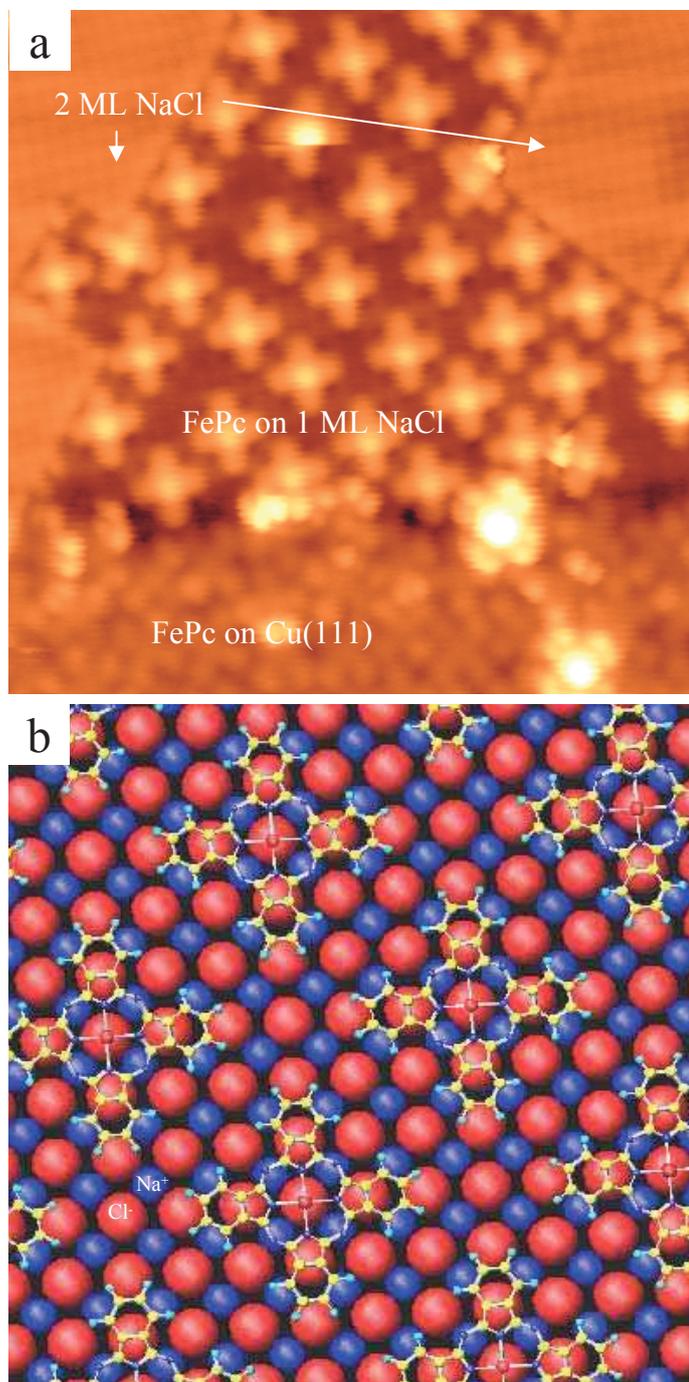
Figure 3.93: (a) Higher magnification image of Fig. 3.90a (14×14 nm^2). (b) Structure of one FePc monolayer on the first NaCl monolayer.

Molecule-substrate interaction governs the orientation of molecules relative to the crystallographic structure of the substrate [35]. Whereas molecule-molecule interaction leads to well aligned domains [5,6]. Both paths of interaction are counteracting each other and can be repulsive or attractive. For single FePc molecules as well as for films of FePc molecules the following results are obtained:

At low coverage, isolated FePc molecules in three equivalent molecular orientations are found on Cu(111) and directly reflect the substrate symmetry. This agrees with previous observations for the growth of FePc on Au(111). Therefore, attractive molecule-molecule interaction can be disregarded whereas a strong molecule-substrate interaction governs the adsorption.

For closed monolayer coverage, short-range ordered domains appear with molecules well aligned to each other. Still, by averaging over larger areas no preferred orientation is identified. Instead molecule-molecule interaction causes an in-plane distortion of molecular structure. We interpret this distortion as a result of repulsive in-plane interaction (attractive interaction can be excluded, see above). In contrast, FePc on a Au(111) surface is reported to be controlled by the directional molecule-molecule interaction resulting in almost perfectly ordered layers with only one adsorption configuration at a saturated monolayer coverage [4,5,11]. It also indicates that the interaction of FePc-Cu(111) is stronger than that of FePc-Au(111).

Attractive out-of-plane molecule-molecule interaction is observed for FePc on top of an FePc monolayer. Regular domains are observed with the size of the unit cell being smaller than a single FePc molecule; molecules are overlapping each other and molecules are tilted out-of-plane. This tilting suggests strong out-of-plane and site-specific interaction. Moreover, the domains are larger than in the (uncovered) 1st ML FePc. Due to the limitation of the used surface sensitive technique we only might speculate about the structure of the 1st ML underneath which might be rearranged due to the layer on top [36].

The adsorption of FePc on 1 ML NaCl is controlled through the interaction of the central iron atom on top of the Cl anions. This interaction is weaker than the interaction between FePc and the metallic substrate but qualitatively stronger than the out-of-plane molecule-molecule interaction which is not observed to occur on top of NaCl. Again, repulsive in-plane molecule-molecule interaction prevents the formation of well ordered domains as long as the coverage is sufficiently low. At nearly full coverage, the molecular orientation is not disturbed by repulsive in-plane molecule-molecule interaction. Instead the distance between two neighboring molecules is larger than on the other surfaces and is determined by the site-specific adsorption of the central iron atom on top of Cl anions. Therefore, the distance between two molecules is about 1.68 nm.

The growth of FePc on the 2nd ML NaCl was not observed although the dosage was sufficient; instead formation of molecular clusters on other sites occurred. We conclude that adsorption of FePc on 2nd ML NaCl is less preferable. Moreover, this indicates that 1st and 2nd ML NaCl are not equivalent. We assume that for the 1st

ML NaCl the Cu substrate influences the electronic properties and therefore the ability of NaCl to capture FePc molecules.

In summary, our study of FePc deposited on different sites reveals (i) repulsive in-plane molecule-molecule interaction, (ii) attractive, site-sensitive out-of-plane molecule-molecule interaction, (iii) site-specific adsorption of the central iron atom on top of the Cl anions, (iv) a strong molecule-Cu(111) interaction with (v) weak directional forces, and (vi) repulsive in-plane molecule-molecule interaction causing deformation of the Pc skeleton. Further investigations to understand this highly relevant molecular model system are required in terms of precise numerical simulations to reveal the different directional repulsive and attractive forces as well as the nature of the adsorption of FePc on NaCl. In the latter case, although interpretation in terms of ionic interaction is tempting, covalent bonding cannot be disregarded as recently discussed by Li et. al. [37].

References

[1] B. Crone, A. Dodabalapur, Y.-Y. Lin, R. W. Filas, Z. Bao, A. LaDuca, R. Sarpeshkar, H. E. Katz, and W. Li, Nature **403**, 521 (2000).

[2] S.R. Forrest, Chem. Rev. **97**, 1793 (1997).

[3] F. Zhao, F. Harnisch, U. Schröder, F. Scholz, P. Bogdanoff, and I. Herrmann, Electrochemistry Communications **7**, 1405 (2005).

[4] Z.H. Cheng, L. Gao, Z.T. Deng, N. Jiang, Q. Liu, D.X. Shi, S.X. Du, H.M. Guo, and H.-J. Gao, J. Phys. Chem. C **111**, 9240 (2007).

[5] Z.H. Cheng, L. Gao, Z.T. Deng, Q. Liu, N. Jiang, X. Lin, X.B. He, S.X. Du, and H.-J. Gao, J. Phys. Chem. **111**, 2656 (2007).

[6] J. Åhlund, J. Schnadt, K. Nilson, E. Göthelid, J. Schiessling, F. Besenbacher, N. Mårtensson, and C. Puglia, Surf. Sci. **601**, 3661 (2007).

[7] E. Barrena, D. de Oteyza, H. Dosch, and Y Wakayama, ChemPhysChem. **8**, 1915 (2007).

[8] Q.-X. Li, J.-L. Yang, L.-F. Yuan, J.-G. Hou, and Q.-S. Zhu, Chin. Phys. Lett. **18**, 1234 (2001).

[9] F. Evangelista, V. Carravetta, G. Stefani, B. Jansik, M. Alagia, S. Stranges, and A. Euocco, J. Chem. Phys. **126**, 124709 (2007).

[10] F. Song, H. Huang, W. Dou, H. Zhang, Y. Hu, H. Qian, H. Li, P. He, S. Bao, and W. Zhou, J. Phys.: Condens. Matter **19**, 136002 (2007).

[11] X. Lu and K.W. Hipps, J. Phys. Chem. **101**, 5391 (1997).

[12] K.W. Hipps, D.E. Barlow, and U. Mazur, J. Phys. Chem. B **104** 2444 (2000).

[13] G.V. Nazin, X.H. Qiu, and W. Ho, Science **302**, 77 (2003).

[14] S.W. Wu, G..V. Nazin, X. Chen, X.H. Qiu, and W. Ho, Phys. Rev. Lett. **93**, 236802 (2004).

[15] D.E. Barlow, L. Scudiero, and K.W. Hipps, Langmuir **20**, 4413 (2004).

[16] X. Lu, K.W. Hipps, X.D. Wang, and U. Mazur, J. Am. Chem. Soc. **118**, 7197 (1996).

[17] J.K. Gimzewski, E. Stoll, and R.R. Schlittler, Surf. Sci. **181**, 267 (1987).

[18] P. Lippel, R. Wilson, M. Miller, C. Wöll, and S. Chiang, Phys. Rev. Lett. **62**, 171 (1989).

[19] T. G. Gopakumar, M. Lackinger, M. Hackert, F. M?ller, and M. Hietschold, J. Phys. Chem. B **108**, 7839 (2004).

[20] M. Takada and H. Tada, Chem. Phys. Lett. **392**, 265 (2004).

[21] I. Chizhov, G. Scoles, and A. Kahn, Langmuir **16**, 4358 (2000).

[22] M. Takada and H. Tada, Jpn. J. Appl. Phys. **44**, 5332 (2005).

[23] L. Gao, W. Ji, Y. B. Hu, Z. H. Cheng, Z. T. Deng, Q. Liu, N. Jiang, X. Lin, W. Guo, S. X. Du, W. A. Hofer, X. C. Xie, and H.-J. Gao, Phys. Rev. Lett. **99**, 106402 (2007).

[24] V. Balzani, A. Credia, and M. Venturi, Nano Today **2**, 18 (2007).

[25] J. Puigdollers, C. Voz, M. Fonrodona, S. Cheylan, M. Stella, J. Andreu, M. Vetter, R. Alcubilla, J. Non-Crystalline Solid **352**, 1778 (2006).

[26] C. Li, W. Fan, B. Lei, S. Zhang, S. Han, T. Tang, X. Liu, Z. Liu, S. Asano, M. Meyyappan, J. Han, and C. Zhou, Apply. Phys. Lett. **84**, 1949 (2004).

[27] J. Repp, G. Meyer, S. Stojkovic, A. Gourdon, and Ch. Joachim, Phys. Rev. Lett. **94**, 02683 (2005).

[28] S. Schintke and W.-D. Schneider, J. Phys. Condens. Matter **16**, R49 (2004), and references herein.

[29] R. Bennewitz, A.S. Foster, L.N. Kantorovich, M. Bammerlin, Ch. Loppacher, S. Schär, M. Guggisberg, E. Meyer, and A.L. Shluger, Phys. Rev. B **62**, 2074 (2000), and references herein.

[30] R. Bennewitz, V. Barwich, M. Bammerlin, Ch. Loppacher, M. Guggisberg, A. Baratoff, E. Meyer, and H.-J. Güntherodt, Surf. Sci. **438**, 289 (1999).

[31] G. Repp, G. Meyer, and K.-H. Rieder, Phys. Rev. Lett. **92**, 036803 (2004).

[32] W. Hebenstreit, J. Redinger, Z. Horozova, M. Schmin, R. Podloucky, and P. Varga, Surf. Sci. **424**, L321 (1999).

[33] J.C. Buchholz and G.A. Somorjai, J. Chem. Phys. **66**, 573 (1977).

[34] First, we extrapolate the lattice periodicity of NaCl from the second NaCl monolayer in our STM images with atomic resolution. From previous work the protrusions in STM images of the NaCl surface are determined to be Cl- anions [32]. The second NaCl monolayer is shifted by one half of lattice constant with respect to the first monolayer. With the atomic structure identified, we determine FePc molecules on the first NaCl monolayer to be located on the Cl- anion sites.

[35] M. Oehzelt, L. Grill, S. Berkebile, G. Koller, F. P. Netzer, M. G. Ramsey, ChemPhysChem **8**, 1707 (2007).

[36] M. Schunack, L. Petersen, A. Kühnle, E. Lægsgaard, I. Stensgaard, I. Johannsen, and F. Besenbacher, Phys. Rev. Lett. **86**, 456 (2001).

[37] B. Li, A. Michaelides, and M. Scheffler, Phys. Rev. Lett. **97**, 046802 (2006).

Chapter 4

Collaborations

4.1   Research Partners

- Institute of Applied Physics and MARCH, University of Hamburg:
  Prof. Dr. W. Hansen, Jr.-Prof. Dr. S. Heinze, Prof. Dr. D. Heitmann,
  Prof. Dr. J. Kötzler, Prof. Dr. U. Merkt, Prof. Dr. K. Nielsch,
  Prof. Dr. H.P. Oepen

- I. Institute of Theoretical Physics, University of Hamburg:
  Prof. Dr. A. Lichtenstein, Prof. Dr. K. Scharnberg

- Institute of Experimental Physics, University of Hamburg:
  Prof. Dr. R. L. Johnson

- Institute for Laser Physics, University of Hamburg:
  Prof. Dr. K. Sengstock

- Institute for Physical Chemistry, University of Hamburg:
  Prof. H. Weller

- Institute for Inorganic and Applied Chemestry, University of Hamburg:
  Prof. Dr. J. Heck, Jun.-Prof. Dr. M. H. Prosenc

- Department of Computer Science, University of Hamburg:
  Prof. Dr. H. S. Stiehl, Prof. Dr. J. Zhang

- HGF-Forschungszentrum GKSS:
  Prof. Dr. A. Schreyer

- University of Münster:
  Dr. H. Hölscher

- HGF-Forschungszentrum Jülich:
  Prof. Dr. S. Blügel

- CMS Vienna, Austria:
  Prof. Dr. P. Weinberger

- Radboud University Nijmegen, The Netherlands:
  Prof. Dr. S. Speller

- IEMN / ISEN, Lille, France:
  Prof. Dr. Ch. Delerue

- National Nanotechnology Laboratory, Lecce, Italy:
  Dr. G. Maruccio

- University of Modena, Italy:
  Prof. Dr. E. Molinari

- University of Iowa, USA:
  Prof. Dr. M. E. Flatté

- University of Ohio, Athens, USA:
  Prof. Dr. A. R. Smith

- Los Alamos National Laboratory, USA:
  Dr. A. V. Balatsky

- Seoul National University, South Korea:
  Prof. Dr. Z. G. Khim, Prof. Dr. D. H. Kim, Prof. Dr. T. W. Noh, Dr. U. H. Pi

- National Institute for Materials Science (NIMS), Tsukuba, Japan:
  Dr. M. Aono

4.2   Industrial Partners

- Beiersdorf, Hamburg

- Merck, Darmstadt

- Wella, Darmstadt

Chapter 5

Theses

5.1 Diploma Theses

1. René Schmidt (2005):
   Rasterkraftspektroskopie auf Ag(111) und Gd/W(110)

2. Niklas Stein (2006):
   Computergestützte Auswertung der Vortexstrukturen im Typ-II Supraleiter $Bi_2Sr_2CaCu_2O_8$ in Magnetkraftmikroskopie-Bildfolgen

3. Jan Wienhausen (2006):
   Aufbau eines temperaturvariablen Rastertunnelmikroskops und erste Messungen an Kupferphthalocyanin

4. Knud Lämmle (2006):
   Aufbau einer Verdampferapparatur zur Präparation von Molekülen im Ultrahochvakuum

5. Matthias Menzel (2006):
   Wachstum und elektronische Eigenschaften von atomaren Eisen-Ketten auf Iridium(001)

6. Mike Gyamfi (2006):
   Construction of a New Scanning Tunneling Microscope for Spin-Sensitive Measurements in Ultrahigh Vacuum, at Low Temperature, and in High Magnetic Fields

7. Matthias Schult (2007):
   Theoretische Untersuchung multipolarer Systeme für den Einsatz als Speichermedium

8. Gabriela Herzog (2007):
   Strominduziertes Schalten magnetischer Nanoinseln auf W(110) mittels spinpolarisierter Rastertunnelmikroskopie

9. Jens Brede (2007):
   A Scanning Tunneling Microscopy Study of Porphyrin Derivatives

5.2   Ph. D. Theses

1. Torben Hänke (2005):
   A new variable-temperature scanning tunneling microscope and temperature-dependent spin-polarized scanning tunneling spectroscopy on the Cr(001) surface

2. Luis Berbil-Bautista (2006):
   Ferromagnetic thin-films and nanostructures studied by spin-polarized scanning tunneling microscopy

3. Lilli Sacharow (2006):
   Calculation of electronic and magnetic properties of hybrid low dimensional structures

4. Focko Karl Meier (2006):
   Co on Pt(111) studied by spin-polarized scanning tunneling microscopy and spectroscopy

5. Uwe Kaiser (2007):
   Magnetische Austauschkraftmikroskopie

5.3   Habilitation Theses

1. Olena (E. Y.) Vedmedenko (2006): *Magnetic Ordering at the Nanoscale*

Chapter 6
Scientific Publications

6.1 Books

1. E. Y. Vedmedenko (ed.), Wiley, Berlin (2007) [ISBN: 3-527-40484-8]: *Competing Interactions and Pattern Formation in Nanoworld.*

6.2 Patents

1. J. Chen, O. Pietzsch, D. Haude, [23.11.06] (University of Hamburg): *Piezoelektrischer Motor*, DE 10 2005 023 988.

2. J. Chen, O. Pietzsch, D. Haude, [03.05.07] (University of Hamburg): *Piezoelektrische Bewegungseinrichtung*, DE 10 2005 052 132.

6.3 Book Contributions and Review Articles

1. E. Y. Vedmedenko, Modern Physics Letters B **19**, 1367 (2005): *Non-collinear Magnetism in Quasicrystals*

2. E. Y. Vedmedenko, Physik Journal **8/2005**, 81 (2005): *Oberfläche zwingt zur Ordnung*

3. M. Bode and R. Wiesendanger, Magnetic Microscopy of Nanostructures, eds. H. Hopster and H. P. Oepen, Springer Berlin, Heidelberg (2005), p. 203: *Spin-polarized scanning tunneling spectroscopy*

4. M. Bode, A. Kubetzka, O. Pietzsch, and R. Wiesendanger, Modern Techniques for Characterizing Magnetic Materials, ed. Y. Zhu, Kluwer Academic Publisher (2005), p. 383: *Spin-polarized scanning tunneling microscopy*

5. E. Y. Vedmedenko and R. Wiesendanger, New Topics in Condens. Matter Res., ed. J. V. Chang, Nova Publishers, New York (2006), p. 147: *Anisotropic domain walls in magnetic nanostructures*

6. A. Schwarz, M. Bode, and R. Wiesendanger, Handbook of Magnetism and Advanced Magnetic Materials, eds. H. Kronmüller and S. S. Parkin, J. Wiley and Sons Ltd., Vol. 3 (Vol. eds. R. Wiesendanger and G. Güntherodt), p. 1687 (2007): *Scanning Probe Techniques: MFM and SP-STM*

7. E. Y. Vedmedenko, Phys. Stat. Sol. (b) (in press): *Influence of the Lattice Discreteness on Magnetic Ordering in Nanostructures and Nanoarrays*

6.4 Original Articles

1. J. Wiebe, F. Meier, K. Hashimoto, G. Bihlmayer, S. Blügel, P. Ferriani, S. Heinze, and R. Wiesendanger, Phys. Rev. B **72**, 193406 (2005): *Unoccupied surface state on Pt(111) revealed by scanning tunneling spectroscopy*

2. E. Y. Vedmedenko, N. Mikuszeit, H. P. Oepen, and R. Wiesendanger, Phys. Rev. Lett. **95**, 207202 (2005): *Multipolar Ordering and Magnetization Reversal in Two-Dimensional Nanomagnet Arrays*

3. T. Hänke, M. Bode, S. Krause, L. Berbil-Bautista, and R. Wiesendanger, Phys. Rev. B **72**, 085453 (2005): *Temperature-dependent scanning tunneling spectroscopy of Cr(001): Orbital Kondo resonance versus surface state*

4. T. Hänke, S. Krause, L. Berbil-Bautista, M. Bode, R. Wiesendanger, V. Wagner, D. Lott, and A. Schreyer, Phys. Rev. B **71**, 184407 (2005): *Absence of spin-flip transition at the Cr(001) surface: A combined spin-polarized scanning tunneling microscopy and neutron scattering study*

5. N. Mikuszeit, E.Y. Vedmedenko, R. Wiesendanger, and H.P. Oepen, J. Appl. Phys. **97**, 10J502 (2005): *Multipole moments of the in-plane magnetized nanodiscs*

6. K. von Bergmann, M. Bode, A. Kubetzka, O. Pietzsch, and R. Wiesendanger, J. Microsc. Res. and Techn. **66**, 61 (2005): *Spin-polarized scanning tunneling microscopy: Insight into magnetism from nanostructures to atomic scale spin structures*

7. M. Bode, A. Kubetzka, K. von Bergmann, O. Pietzsch, and R. Wiesendanger, J. Microsc. Res. and Techn. **66**, 117 (2005): *Imaging the Switching Behavior of Superparamagnetic Nanoislands by Spin-Polarized Scanning Tunneling Microscopy*

8. R. Wiesendanger, J. Microsc. Res. and Techn. **66**, 59 (2005): *Fifteen Years of Spin-Polarized Scanning Tunneling Microscopy*

9. E. Y. Vedmedenko, K. von Bergmann, H. P. Oepen, and R. Wiesendanger, J. Magn. Magn. Mater. **290-291**, 746 (2005): *Lattice-dependent anisotropy in the orientation of magnetic domain walls*

10. M. Liebmann, A. Schwarz, U. Kaiser, R. Wiesendanger, D.-W. Kim, and T. W. Noh, Phys. Rev. B **71**, 104431 (2005): *Magnetization reversal of a structurally disordered manganite thin film with perpendicular anisotropy*

11. A. Kubetzka, P. Ferriani, M. Bode, S. Heinze, G. Bihlmayer, K. von Bergmann, O. Pietzsch, S. Blügel, and R. Wiesendanger, Phys. Rev. Lett. **94**, 87204 (2005): *Revealing Antiferromagnetic Order of the Fe Monolayer on W(001): Spin-Polarized Scanning Tunneling Microscopy and First-Principles Calculations*

12. M. Bode, R. Ravlić, M. Kleiber, and R. Wiesendanger, Appl. Phys. A **80**, 907 (2005): *Growth and Magnetism of Fe on Cr(001): A Spin-Polarized Scanning Tunneling Spectroscopy and Magnetic Force Microscopy Study*

13. C. J. Chen, Nanotechnology **16**, S27 (2005): *A universal relation in NC-AFM, STM, and atom manipulation*

14. M. Ashino, A. Schwarz, H. Hölscher, U.D. Schwarz, and R. Wiesendanger, Nanotechnology **16**, 134 (2005): *Interpretation of the atomic scale contrast obtained on graphite and single-walled carbon nanotubes in the dynamic mode of atomic force microscopy*

15. A. Schwarz and M. Liebmann, Proceedings of SPIE **5843**, 52 (2005): *Barkhausen noise visualized in real space*

16. M. Bode, R. Ravlić, M. Kleiber, and R. Wiesendanger, Nova Acta Leopoldina **340**, 61 (2005): *Spin-polarized scanning tunneling microscopy of antiferromagnetic surfaces*

17. H. Fuchs and R. Wiesendanger, Industrie Management **21 (6)**, 17 (2005): *Die Festplatte von Übermorgen*

18. R. Wiesendanger, Leopoldina Reihe 3, Jahrgang 50, Jahrbuch 2004, Halle/Saale (2005), p. 369: *Nanotechnologie - Aufbruch in neue Welten*

19. M. Ashino and R. Wiesendanger, J. Investig. Dermatology **125**, A30 (2005): *Cryogenic dynamic force microscopy/spectroscopy of molecular systems: Introduction and application to biological macromolecules*

20. F. Meier, K. von Bergmann, P. Ferriani, J. Wiebe, M. Bode, K. Hashimoto, S. Heinze, and R. Wiesendanger, Phys. Rev. B **74**, 195411 (2006): *Spin-dependent electronic and magnetic properties of Co nanostructures on Pt(111) studied by spin-resolved scanning tunneling spectroscopy*

21. S. Krause, L. Berbil-Bautista, T. Hänke, F. Vonau, M. Bode, and R. Wiesendanger , Europhys. Lett. **76**, 637 (2006): *Consequences of line defects on the magnetic structure of high anisotropy films: Pinning centers on Dy/W(110)*

22. C. J. Chen and R. Wiesendanger, Phys. Rev. B **74**, 113102 (2006): *A perturbation theory of exchange interaction*

23. J. Kötzler, D. Görlitz, M. Kurfiß, L. von Sawilski, and E. Y. Vedmedenko, Phys. Rev. B **73**, 224425 (2006): *Vortex fluctuations and ordering of dipolar-coupled granular moments in thin ferromagnetic films*

24. O. Pietzsch, S. Okatov, A. Kubetzka, M. Bode, S. Heinze, A. Lichtenstein, and R. Wiesendanger, Phys. Rev. Lett. **96**, 237203 (2006): *Spin-Resolved Electronic Structure of Nanoscale Cobalt Islands on Cu(111)*

25. M. Bode, E. Y. Vedmedenko, K. von Bergmann, A. Kubetzka, P. Ferriani, S. Heinze, and R. Wiesendanger, Nature Materials **5**, 477 (2006): *Atomic spin structure of antiferromagnetic domain walls*

26. K. von Bergmann, S. Heinze, M. Bode, E. Y. Vedmedenko, G. Bihlmayer, S. Blügel, and R. Wiesendanger, Phys. Rev. Lett. **96**, 167203 (2006): *Observation of a complex nanoscale magnetic structure in a hexagonal Fe monolayer*

27. U. H. Pi, Z. G. Khim, D. H. Kim, A. Schwarz, M. Liebmann, and R. Wiesendanger, Phys. Rev. B **73**, 144505 (2006): *Visualizing the flux distribution of superconductors in external magnetic fields by magnetic force microscopy*

28. M. Ashino and R. Wiesendanger, Jpn. J. Appl. Phys. **45 (3B)**, 2286 (2006): *Atomic-Resolution Dynamic Force Microscopy and Spectroscopy of an Individual Single-Walled Carbon Nanotube*

29. C. J. Chen, Nanotechnology **17**, S195 (2006): *Possibility of imaging lateral profiles of individual tetrahedral hybrid orbitals in real space*

30. M. Bode, K. von Bergmann, A. Kubetzka, O. Pietzsch, and R. Wiesendanger, J. Magn. Magn. Mater. **304**, 1 (2006): *Spin-polarized scanning tunneling spectroscopy of dislocation lines in Fe films on W(110)*

31. C. J. Chen, Phys. Rev. Lett. **96**, 069701 (2006): *Comment on "Signature of a Chemical Bond in the Conductance between Two Metal Surfaces"*

32. K. von Bergmann, M. Bode, and R. Wiesendanger, J. Magn. Magn. Mater. **305**, 279 (2006): *Coverage-dependent spin reorientation transition temperature of the Fe double-layer on W(110) observed by scanning tunneling microscopy*

33. L. Berbil-Bautista, S. Krause, T. Hänke, M. Bode, and R. Wiesendanger, Surf. Sci. Lett. **600**, L20 (2006): *Spin-polarized scanning tunneling microscopy through an adsorbate layer: Sulfur-covered Fe/W(110)*

34. F. Marczinowski, K. von Bergmann, M. Bode, and R. Wiesendanger, Surf. Sci. **600**, 1034 (2006): *Growth of Cr on Ir(111) studied by scanning tunneling microscopy*

35. A. Schwarz, M. Liebmann, R. Wiesendanger, U. H. Pi, Z. G. Khim, and D. H. Kim, Appl. Phys. Lett. **88**, 012507 (2006): *Observation of the flux-antiflux boundary propagation during magnetization reversal in $Bi_2Sr_2CaCu_2O_{8+\delta}$ crystal with single vortex resolution*

36. E. Y. Vedmedenko, U. Grimm, and R. Wiesendanger, Philosophical Magazine **86**, 733-739 (2006): *Interplay between magnetic and spatial order in Quasicrystals*

37. E.Y. Vedmedenko, L. Udvardi, P. Weinberger, and R. Wiesendanger , Phys. Rev. B **75**, 104431 (2007): *Chiral magnetic ordering in two-dimensional ferromagnets with competing Dzyaloshinsky-Moriya interactions*

38. K. von Bergmann, S. Heinze, M. Bode, G. Bihlmayer, S. Blügel, and R. Wiesendanger, New Journ. Phys. **9**, 396 (2007): *Complex magnetism of the Fe monolayer on Ir(111)*

39. M. Schult, N. Mikuszeit, E. Y. Vedmedenko and R. Wiesendanger, J. Phys. A **40**, 14791 (2007): *Multipole moments of general ellipsoids with two polarized domains*

40. F. Marczinowski, J. Wiebe, J.-M. Tang, M. E. Flatte, F. Meier, M. Morgenstern, and R. Wiesendanger, Phys. Rev. Lett. **99**, 157202 (2007): *Local Electronic Structure near Mn Acceptors in InAs: Surface-Induced Symmetry Breaking and Coupling to Host States*

41. S. Krause, L. Berbil-Bautista, G. Herzog, M. Bode, and R. Wiesendanger, Science **317**, 1537 (2007): *Current-Induced Magnetization Switching with a Spin-Polarized Scanning Tunneling Microscope*

42. L. Berbil-Bautista, S. Krause, M. Bode, and R. Wiesendanger, Phys. Rev. B **76**, 064411 (2007): *Spin-polarized scanning tunneling microscopy and spectroscopy of ferromagnetic Dy(0001)/W(110) films*

43. G. Maruccio, M. Janson, A. Schramm, C. Meyer, T. Matsui, C. Heyn, W. Hansen, R. Wiesendanger, M. Rontani, E. Molinari, Nano Letters **7**, A (2007): *Correlation Effects in Wave Function Mapping of Molecular Beam Epitaxy Grown Quantum Dots*

44. A. Kubetzka, M. Bode, and R. Wiesendanger, Appl. Phys. Lett. **91**, 012508 (2007): *Spin-polarized scanning tunneling microscopy in field emission mode*

45. M. Bode, S. Krause, L. Berbil-Bautista, S. Heinze and R. Wiesendanger, Surf. Sci. **601**, 3308 (2007): *On the preparation and electronic properties of clean W(110) surfaces*

46. M. Bode, M. Heide, K. von Bergmann, P. Ferriani, S. Heinze, G. Bihlmayer, A. Kubetzka, O. Pietzsch, S. Blügel, and R. Wiesendanger, Nature **447**, 190 (2007): *Chiral magnetic order at surfaces driven by inversion asymmetry*

47. M. Rontani, E. Molinari, G. Maruccio, M. Janson, A. Schramm, Chr. Meyer, T. Matsui, Chr. Heyn, W. Hansen, and R. Wiesendanger, J. Appl. Phys. **101**, 081714 (2007): *Imaging correlated wave functions of few-electron quantum dots: Theory and scanning tunneling spectroscopy experiments*

48. T. Matsui, Chr. Meyer, L. Sacharow, J. Wiebe, and R. Wiesendanger, Phys. Rev. B **75**, 165405 (2007): *Electronic states of Fe atoms and chains on InAs(110) from scanning tunneling spectroscopy*

49. U. Kaiser, A. Schwarz, and R. Wiesendanger, Nature **446**, 522 (2007): *Magnetic exchange force microscopy with atomic resolution*

50. T. Wehling, A. V. Balatsky, M. I. Katsnelson, A. I. Lichtenstein, K. Scharnberg, and R. Wiesendanger, Phys. Rev. B **75**, 125425 (2007): *Local electronic signatures of impurity states in graphene*

51. R. Wiesendanger, Europhysics News **38**, 16 (2007): *Mapping spin structures on the atomic scale*

52. T. Richter, S. S. Biel, M. Sattler, H. Wenck, K.-P. Wittern, R. Wiesendanger, and R. Wepf, J. Microsc. **225**, 201 (2007): *Pros and cons: cryo-electron microscopic evaluation of block faces versus cryo-sections from frozen-hydrated skin specimens prepared by different techniques*

53. F. Meier, K. von Bergmann, J. Wiebe, M. Bode, and R. Wiesendanger, J. Phys. D **40**, 1306 (2007): *Co double-layer nanostructures on Pt(111) studied by spin-polarized scanning tunnelling microscopy*

54. A. Schwarz, Conference Proceedings EAST 2007 **1**, 32 (2007): *MExFM - A New Force Microscopy Based Technique to Study Atomic Scale Magnetism*

55. R. Wiesendanger, Imaging and Microscopy Vol. **02**, 21 (2007): *Imaging atomic-scale spin structures*

56. R. Wiesendanger, GIT Laborfachzeitschrift **51**, 647 (2007): *Abbildung von Spin-strukturen auf atomarar Ebene*

57. B. Santos, J. M. Puerta, J. I. Cerda, R. Stumpf, K. von Bergmann, R. Wiesendanger, M. Bode, K. F. McCarty, and J. de la Figuera, New J. Phys. (in press): *Structure and magnetism of ultra-thin chromium layers on W(110)*

58. A. Scarfato, S.-H. Chang, S. Kuck, J. Brede, G. Hoffmann, and R. Wiesendanger, Surf. Sci. (in press): *Scanning tunneling microscope study of iron(II) phthalocyanine growth on metal and insulating surfaces*

59. R. Wieser, E. Y. Vedmedenko, and R. Wiesendanger, Phys. Rev. B (in press): *Entropy driven phase transition in itinerant antiferromagnetic monolayers*

60. A. Schwarz, and R. Wiesendanger, Nano Today (in press): *Magnetic sensitive force microscopy: MFM and MExFM*

Chapter 7

Talks and Posters

7.1 Invited Talks

4.3.2005: R. Wiesendanger, 69th Spring Conference, Deutsche Physikalische Gesellschaft, Berlin (Germany): *Spin Mapping on the Atomic Scale: From 2D Antiferromagnets to Single Impurities*

9.3.2005: E. Y. Vedmedenko, 69th Spring Conference, Deutsche Physikalische Gesellschaft, Berlin (Germany): *Theorie der magnetischen Strukturbildung in Nanoteilchen und Nanoarrays*

2.5.2005: R. Wiesendanger, IMM Symposium, Nijmegen (The Netherlands): *New Horizons in Magnetism by Atomic-Scale Magnetic Probing*

9.5.2005: A. Schwarz, The 5th Heinrich-Hertz MINERVA Workshop on High Temperature Superconductivity, Tel Aviv (Israel): *Vortex states in high T_c superconductors studied by low temperature magnetic force microscopy*

25.5.2005: A. Schwarz and M. Liebmann, Fluctuation and Noise in Materials II, Austin (USA): *Barkhausen Noise Visualized in Real Space*

4.6.2005: M. Ashino and R. Wiesendanger, Joint Meeting of SCUR (Society for Cutaneous Ultrastructure Research) and ISP (International Society of Skin Pharmacology and Physiology), Hamburg (Germany): *Cryogenic Dynamic Force Microscopy/Spectroscopy of Molecular Systems: Introduction and Application to Biological Macromolecules*

10.6.2005: R. Wiesendanger, IUVSTA Intern. Summer School "Science and Technology at Nanoscale", Tri Studne (Czech Republic): *Scanning tunneling spectroscopy - Part I: Semiconductor nanostructures*

10.6.2005: R. Wiesendanger, IUVSTA Intern. Summer School "Science and Technology at Nanoscale", Tri Studne (Czech Republic): *Scanning tunneling spectroscopy - Part II: Magnetic nanostructures*

21.6.2005: R. Wiesendanger, 25th GIF Meeting: Nanotubes and Nanowires, Dresden (Germany): *Low temperature scanning tunnelling spectroscopy of carbon nanotubes and magnetic nanowires*

25.6.2005: R. Wiesendanger, Physics of Magnetism 05, Poznan (Poland): *Physics of nanomagnetism revealed by spin-polarized scanning tunneling spectroscopy*

25.6.2005: E. Y. Vedmedenko, Moscow International Conference on Magnetism, Moskow (Russia): *Lattice Efeects in magnetic Nanostructures and Nanoarrays*

4.7.2005: R. Wiesendanger, 13th International Conference on STM, Sapporo (Japan): *Recent progress in spin-polarized scanning tunneling spectroscopy*

4.7.2005: R. Wiesendanger, 13th International Conference on STM, Sapporo (Japan): *Teaching Nanotechnology and SPM*

5.7.2005: M. Bode, International Conference on Materials for Advanced Technologies (ICMAT2005), Singapore (Singapore): *Exploring the Frontiers of Nanomagnetism by Spin-Polarized STM*

14.7.2005: A. Kubetzka, International Conference on Nanomaterials (NANO-2005), Sivakasi (India): *New Horizons in Nanomagnetism by Atomic Scale Magnetic Probing*

18.7.2005: A. Kubetzka, International Workshop on Nanotechnology, Perth (Australia): *Frontiers of nanomagnetism studied by spin-polarized scanning tunneling spectroscopy*

25.8.2005: M. Bode, International Symposium on Magnetic Materials and Applications (ISAMT), Taipei (Taiwan): *Recent Progress in Spin-Polarized Scanning Tunneling Microscopy*

8.9.2005: A. Schwarz, R. Wiesendanger, 4th International Conference on Vortex Matter and Nanostructured Superconductors (Vortex IV), Crete (Greece): *Beyond the Bean Model: Magnetization Reversal Observed With Single Vortex Resolution*

9.9.2005: M. Bode, 23rd European Conference on Surface Science (ECOSS-23), Berlin (Germany): *Imaging Magnetic Nanostructures by Spin-Polarized STM*

26.9.2005: R. Wiesendanger, DPG-School on Physics: The Physics of Imaging, Bad Honnef (Germany): *Scanning probe imaging and spectroscopy of the solid state*

29.9.2005: R. Wiesendanger, Spintronics ´05, Poznan (Poland): *Recent progress in spin-polarized scanning tunneling spectroscopy*

21.10.2005: R. Wiesendanger, ERA-Nanoscience Meeting, Berlin (Germany): *Nanoscience research in Hamburg*

28.10.2005: R. Wiesendanger, Joint Meeting of German and Polish Vacuum Societies, Krakow (Poland): *New horizons in nanomagnetism by atomic-scale magnetic probing*

27.10.2005: E. Y. Vedmedenko, Physikerinnentagung, Darmstadt (Germany): *Magnetische Strukturbildung in Nanoteilchen*

30.10.2005: M. Bode, 50th Magnetism and Magnetic Materials Conference (MMM), San Jose (USA): *Spin-Polarized Scanning Tunneling Microscopy: Magnetic Imaging with Atomic Resolution*

2.11.2005: O. Pietzsch, 52nd International Symposium and Exhibition, The American Vacuum Society (AVS), Boston (USA): *Spin-Polarized Scanning Tunneling Spectroscopy of Nano-Scale Co Islands on Cu(111)*

15.11.2005: M. Bode, 4th International Symposium on Surface Science and Nanotechnology (ISSS-4), Omiya (Japan): *Spin-polarized Scanning Tunneling Microscopy: Magnetic Imaging with Atomic Resolution*

5.5.2006: R. Wiesendanger, 2nd Annual Nanoprobes Workshop, Stanford University, Stanford, CA (USA): *Mapping Spin Structures on the Atomic Scale*

26.5.2006: A. Kubetzka, M. Bode, O. Pietzsch, K. von Bergmann, E.Y. Vedmedenko, P. Ferriani, S. Heinze, S. Blügel, and R. Wiesendanger, Advanced Workshop: Organizing and Addressing Molecules on Surfaces (OAMS06), Barcelona (Spain): *Spin-Polarized STM: Investigating Magnetism at the Atomic Scale*

31.5.2006: R. Wiesendanger, E-MRS Spring Meeting, Nice (France): *Atomic- and nano-scale magnetic imaging by spin-polarized scanning tunneling spectroscopy*

7.6.2006: K. von Bergmann, 11th International Conferences on Modern Materials and Technologies (CIMTEC 2006), Acireale (Italy): *SPSTM on Magnetic Nanostructures: Resolving Spin Structures at the Atomic Level*

27.6.2006: M. Bode, 3rd Joint European Magnetic Symposia, San Sebastian (Spain): *Recent Progress in Spin-Polarized STM: Imaging of Non-Collinear Spin Structures in Monolayer Films*

6.7.2006: R. Wiesendanger, Internat. Conf. on Nanoscale Superconductivity and Magnetism, Leuven (Belgium): *Frontiers of nanomagnetism revealed by spin-polarized scanning tunneling spectroscopy*

10.7.2006: M. Bode, Summer School of the ULTRASMOOTH EU-project, Durham (United Kingdom): *Scanning Tunneling Microscopy and Spectroscopy*

17.7.2006: A. Schwarz, U. Kaiser, and R. Wiesendanger, 9[th]International Conference on Noncontact Atomic Force Microscopy (NCAFM´06), Kobe (Japan): *Magnetic Exchange Force Microscopy*

24.7.2006: M. Bode, 4th International Conference on Scanning Probe Spectroscopy (SPS´06) and 1st International Workshop on Spin-Polarized Scanning Tunneling Microscopy (SPSTM-1), Hamburg (Germany): *On the spin structure of antiferromagnetic domain walls*

25.7.2006: K. von Bergmann, 4th International Conference on Scanning Probe Spectroscopy (SPS´06) and 1st International Workshop on Spin-Polarized Scanning Tunneling Microscopy (SPSTM-1), Hamburg (Germany): *Novel magnetic structure in the Fe monolayer on Ir(111)*

26.7.2006: A. Schwarz, U. Kaiser, and R. Wiesendanger, 4th International Conference on Scanning Probe Spectroscopy (SPS´06) and 1st International Workshop on Spin-Polarized Scanning Tunneling Microscopy (SPSTM-1), Hamburg (Germany): *Magnetic Exchange Force Microscopy*

2.8.2006: R. Wiesendanger, International Conference on Nanoscience and Technology, Basel (Switzerland): *Nanoscience education: a multi-level approach*

2.8.2006: R. Wiesendanger, International Conference on Nanoscience and Technology, Basel (Switzerland): *Mapping spin structures on the atomic scale: from antiferromagnetic metals and insulators to novel nanomagnetic states*

3.8.2006: M. Bode, Microscopy and Microanalysis 2006, Chicago (USA): *Spin-Polarized STM: Imaging Magnetic Nanostructures with Atomic Resolution*

15.8.2006: M. Bode, 19th International Colloquium on Magnetic Films and Surfaces (ICMFS2006), Sendai (Japan): *Imaging Non-Collinear Spin-Structures with Spin-Polarized STM*

1.9.2006: R. Wiesendanger, 7th NIMS Symposium on Advanced Nano-Characterization, Tsukuba (Japan): *New horizons in nanomagnetism by atomic-scale magnetic SPM probing*

3.9.2006: R. Wiesendanger, IFSM IMC16 Pre-School, Sapporo (Japan): *Scanning probe microscopy and spectroscopy: methods and applications*

4.9.2006: R. Wiesendanger, IMC16, Sapporo (Japan): *Magnetic microscopy with atomic resolution*

7.9.2006: M. Bode, Gordon Research Conference on Magnetic Nanostructures, Oxford (United Kingdom): *Imaging non-collinear spin structures on the atomic scale*

7.9.2006: R. Wiesendanger, E-MRS 2006 Fall Meeting, Warsaw (Poland): *Current status and future perspectives of spin-polarized STM in spintronics*

8.9.2006: R. Wiesendanger, TNT 2006, Grenoble (France): *New horizons in nano-magnetism by atomic-scale magnetic SPM probing*

12.9.2006: R. Wiesendanger, Nanoscience Symposium at Diamond Light Source, Oxfordshire (U.K.): *Mapping spin structures on the atomic scale: from antiferromagnetic metals and insulators to novel nanomagnetic states*

14.9.2006: H. Fuchs, MNU-Tag 2006, Hamburg (Germany): *Die Ausstellung "Nanotechnologie - Aufbruch in neue Welten" - ein Lernort für Neugierige*

25.9.2006: R. Wiesendanger, WE-Heraeus Summer School on Nanomagnetism, Schloß Rauischholzhausen (Germany): *Nanomagnetism: Characterization by Spin-Polarized Scanning Tunneling Spectroscopy*

25.9.2006: R. Wiesendanger, WE-Heraeus Summer School on Nanomagnetism, Schloß Rauischholzhausen (Germany): *Nanomagnetism: Characterization by Magnetic Force Microscopy*

27.9.2006: M. Bode, Scanning Probe Microscopies and Organic Materials XV, 2006, Dresden (Germany): *Recent progress in spin-polarized scanning tunneling microscopy*

27.9.2006: R. Wiesendanger, nanoTX'06 Meeting, Dallas (USA): *New trends in ultra-high density magnetic data storage*

30.9.2006: R. Wiesendanger, Internat. Workshop on "Surface Spin Correlations", Hamburg (Germany): *Real-space studies of surface spin structures at the atomic level by spin-polarized scanning tunneling spectroscopy and magnetic exchange force microscopy*

8.10.2006: E. Y. Vedmedenko, International Workshop Nanomagnets by Selforganization, Eisenerz (Austria): *Multipolar ordering and magnetization reversal in two-dimensional nanomagnet arrays*

12.10.2006: R. Wiesendanger, European Conference on Molecular Magnetism, Tomar (Portugal): *Spin-polarized scanning tunneling spectroscopy: principles, applications, and perspectives in molecular magnetism*

26.10.2006: R. Wiesendanger, 24th CADFEM Users' Meeting 2006, Stuttgart (Germany): *Simulation in nanoscience and nanotechnology: from multiscale modelling to predictive material design*

6.11.2006: R. Wiesendanger, nanoDE 2006, Berlin (Germany): *Regionale Vernetzung als Strategietrend in der Nanotechnologie*

8.11.2006: M. Bode and R. Wiesendanger, International Conference on Solid Films and Surfaces, Bariloche (Argentina): *Imaging Non-Collinear Spin Structures on the Atomic Scale with Spin-Polarized STM*

5.1.2007: M. Bode, M. Heide, K. von Bergmann, P. Ferriani, S. Heinze, G. Bihlmayer, A. Kubetzka, O. Pietzsch, S. Blügel, and R. Wiesendanger, 381th WE-Heraeus-Seminar "Spin-Polarized Currents in Magnetic Nanostructures", Bad Honnef (Germany): *Static and Dynamic Properties of Complex Magnetic Structures*

24.01.07: R. Wiesendanger, nanoPHYS '07, Tokyo (Japan) *New horizons in nano-magnetism by atomic-scale magnetic SPM probing*

8.2.2007: O. Pietzsch, A. Kubetzka, M. Bode, and R. Wiesendanger, Workshop Nanoscale Materials: Growth, Dynamics, Magnetism. 17th User meeting of the European Synchroton Radiation Facility, Grenoble (France): *Real Space Imaging of Nanoscale Co Islands on Cu(111) by Spin Polarized Scanning Tunneling Spectroscopy*

14.02.07: R. Wiesendanger, 22nd Workshop on Novel Materials and Superconductivity, Donnersbach, (Austria): *Spin-resolved scanning probe microscopy with atomic resolution: principles and applications to novel materials*

7.3.2007: A. Schwarz, APS Spring Meeting 2007, Denver, CO (USA): *Magnetic Exchange Force Microscopy*

29.3.2007: K. von Bergmann, 71st Spring Conference, Deutsche Physikalische Gesellschaft, Regensburg (Germany): *Complex magnetic structures on the atomic scale revealed by spin-polarized STM*

05.06.07: R. Wiesendanger, Leuven Nano-Conference 2007, Leuven (Belgium): *Mapping spin structures on the atomic scale*

02.07.07: R. Wiesendanger, ICMAT 2007, Singapore (China): *Mapping spin structures on the atomic scale*

04.07.07: R. Wiesendanger, ICN + T 2007 and IVC-17, Stockholm (Sweden): *Mapping spin structures on the atomic scale*

05.07.07: R. Wiesendanger, Laserion 2007, Schloß Ringberg (Germany): *Novel nano-magnetic states of matter revealed by magnetic tunneling and exchange force measurements*

2.8.2007: K. von Bergmann, Workshop on atomic/molecular manipulation and spectroscopy using scanning probe techniques, Osaka (Japan): *Complex magnetic structures on the atomic scale revealed by spin-polarized STM*

14.09.07: R. Wiesendanger, 3rd Int. Workshop Nanostructures on Surfaces, Polanica Zdrój (Poland): *Spin mapping on the atomic scale*

16.9.2007: A. Schwarz, 10th International Conference on Non-Contact Atomic Force Microscopy, NC-AFM 2007, Antalya (Turkey): *Lecture: Magnetic Sensitive Force Microscopy*

27.09.07: R. Wiesendanger, Journées Nanosciences & Nanotechnologies, Paris (France): *Les nanosciences dans l'Europe de la Recherche: la demande en infrastructures, les challenges pour la formation interdisciplinaire et pour la popularisation de la science*

14.10.2007: E. Y. Vedmedenko, Quasicrystals: The Silver Jubilee, Tel-Aviv (Israel): *Modulated Multipolar Structures on Two-Dimensional Tilings*

24.10.2007: A. Schwarz, EAST 2007, Nice (India): *MExFM - A New Force Microscopy Based Technique to Study Atomic Scale Magnetism*

26.10.2007: O. Pietzsch, Workshop on Scanning Probe Microscopy and Spectroscopy, Bilateral Scientific Collaboration Flanders - Russia, Leuven (Belgium): *Of antiferromagnetic iron, spiraling spins, and switching magnetic islands: New frontiers in spin-polarized scanning tunneling microscopy.*

6.11.2007: U. Kaiser, 52nd Magnetism and Magnetic Materials Conference, Tampa (Florida) (USA): *Magnetic Exchange Force Microscopy with Atomic Resolution*

13.11.07: R. Wiesendanger, ACSIN-9, Tokyo (Japan): *Spin mapping on the atomic scale*

7.2 Conference Contributions and Talks at Other Institutes

7.2.1 Talks

18.1.2005: M. Bode, Physikalisches Kolloquium des SFB569, Universität Ulm (Germany): *Exploring the Frontiers of Nanomagnetism by Spin-Polarized STM*

4.3.2005: O. Pietzsch, A. Kubetzka, S. Heinze, M. Bode, and R. Wiesendanger, 69th Spring Conference, Deutsche Physikalische Gesellschaft, Berlin (Germany): *Spin-Polarization and Electron Confinement in Nanoscale Co Islands on Cu(111)*

4.3.2005: A. Kubetzka, P. Ferriani, M. Bode, S. Heinze, G. Bihlmayer, K. von Bergmann, O. Pietzsch, S. Blügel, and R. Wiesendanger, 69th Spring Conference, Deutsche Physikalische Gesellschaft, Berlin (Germany): *Revealing Antiferromagnetic Order of the Fe Monolayer on W(001)*

4.3.2005: A. Schliwa, T. Maltezopoulus, M. Morgenstern, R. Wiesendanger, and D. Bimberg, 69th Spring Conference, Deutsche Physikalische Gesellschaft, Berlin (Germany): *Shape and Order of Wavefunctions in Uncapped InAs/GaAs Quantum Dots*

4.3.2005: E. Y. Vedmedenko, U. Grimm, and Roland Wiesendanger, 69th Spring Conference, Deutsche Physikalische Gesellschaft, Berlin (Germany): *Nichtkollineare magnetische Ordnung in Quasikristallen*

5.3.2005: L. Berbil-Bautista, S. Krause, T. Hänke, M. Bode, and R. Wiesendanger, 69th Spring Conference, Deutsche Physikalische Gesellschaft, Berlin (Germany): *Growth and electronic properties of thick films and pyramidal islands of Dy/W(110) studied by SP-STM*

6.3.2005: A. Schwarz, M. Liebmann, U. H. Pi, and R. Wiesendanger, 69th Spring Conference, Deutsche Physikalische Gesellschaft, Berlin (Germany): *Vortex Pinning and Magnetization Reversal Observed in Real Space by Magnetic Force Microscopy*

8.3.2005: M. Ashino, T. Behnke, and R. Wiesendanger, 69th Spring Conference, Deutsche Physikalische Gesellschaft, Berlin (Germany): *Quantitative investigation of tip-sample interaction on single-walled carbon nanotubes in the attractive force regimes*

9.3.2005: S. Krause, L. Berbil-Bautista, T. Hänke, M. Bode, and R. Wiesendanger, 69th Spring Conference, Deutsche Physikalische Gesellschaft, Berlin (Germany): *Spinpolarisierte Rastertunnelmikroskopie auf S-bedeckten Fe-Inseln*

9.3.2005: F. Marczinowski, K. von Bergmann, and R. Wiesendanger, 69th Spring Conference, Deutsche Physikalische Gesellschaft, Berlin (Germany): *Growth and electronic structure of ultrathin chromium films on iridium(111) investigated by scanning tunneling microscopy and spectroscopy*

7.4.2005: J. Wiebe, T. Matsui, Chr. Meyer, L. Sacharow, F. Meier, K. Hashimoto, M. Morgenstern, and R. Wiesendanger, SFB-508-Statusseminar, Haus Rissen, Hamburg (Germany): *Scanning Tunneling Spectroscopy on Hybrid Systems*

14.4.2005: E. Y. Vedmedenko, Gemeinsames Physikalisches Kolloquium des Fachbereichs Physik, Universität Duisburg, Duisburg (Germany): *Multipolare Momente und Wechselwirkungen in magnetischen Nanoarrays*

2.5.2005: M. Bode, Physikalische Kolloquium, Ruhr-Universität Bochum (Germany): *Spinpolarisierte Rastertunnelmikroskopie: Abbildung magnetischer Nanostrukturen mit atomarer Auflösung*

3.5.2005: G. Hoffmann, CERC III - Young Chemists Workshop, Baden Baden (Germany): *Molecules and Magnetism - a local approach*

27.5.2005: A. Schwarz, Seminar Talk, Houston University (USA): *The Mixed State of BSCCO Visualized in Real Space with Single Vortex Resolution: Solid-Liquid Phase Transition and Magnetization Reversal*

30.5.2005: R. Wiesendanger, Colloquium, University of Marburg (Germany): *Neue Einblicke in die Nano-Welt mittels Rastersondenspektroskopie*

2.6.2005: A. Kubetzka, Seminar Talk, RWTH Aachen (Germany): *Spin-Polarized STM: Investigating Magnetism at the Atomic Scale*

2.6.2005: T. Richter, C. Peuckert, M. Sattler, K. Koenig, I. Riemann, U. Hintze, K.-P. Wittern, R. Wiesendanger, and R. Wepf, Joint Meeting SCUR and ISP 2005, Hamburg (Germany): *Dead but highly dynamic - The Stratum Corneum is divided into three hydration zones*

8.6.2005: M. Ashino, Seminar at Dr. H. Hölscher group in CeNTech (University of Muenster), Muenster (Germany): *Quantitative Investigation of Tip-Sample Interaction on Single-Walled Carbon Nanotubes in Attractive Force Regime*

21.6.2005: E. Y. Vedmedenko, Seminar zur Physik der Kondensierten Materie, ITAP, MPI, Stuttgart (Germany): *Nichtkollineare Magnetische Ordnung in Quasikristallen*

4.7.2005: S. Krause, L. Berbil-Bautista, M. Bode, and R. Wiesendanger, 13th International Conference on STM, Sapporo (Japan): *Spin-Polarized STM Through an Adsorbate Layer: Sulfur-Covered Fe/W(110)*

4.7.2005: L. Berbil-Bautista, S. Krause, M. Bode, and R. Wiesendanger, 13th International Conference on STM, Sapporo (Japan): *Ferromagnetic Domains in Dy(0001) Films on W(110) Studied by Means of Spin-Polarized STM*

4.7.2005: K. von Bergmann, M. Bode, A. Kubetzka, O. Pietzsch, and R. Wiesendanger, 13th International Conference on STM, Sapporo (Japan): *Magnetism of Fe on W(001) studied by spin-polarized STM*

4.7.2005: O. Pietzsch, S. Heinze, A. Kubetzka, M. Bode, and R. Wiesendanger, 13th International Conference on STM, Sapporo (Japan): *Spin-Polarized Scanning Tunneling Spectroscopy of Co Islands on Cu(111)*

4.7.2005: C. J. Chen and R. Wiesendanger, 13th International Conference on STM, Sapporo (Japan): *Reciprocal STM and AFM: Probing Tip States with Known Samples*

4.7.2005: A. Schwarz, M. Liebmann, U. Kaiser, T. W. Noh, D. W. Kin, and R. Wiesendanger, 13th International Conference on STM, Sapporo (Japan): *Visualization of the Barkhausen Effect*

4.7.2005: P. Ferriani, A. Kubetzka, S. Heinze, M. Bode, G. Bihlmayer, S. Blügel, K. von Bergmann, O. Pietzsch, and R. Wiesendanger, 13th International Conference on STM, Sapporo (Japan): *Two-Dimensional Antiferromagnetism of Fe and Co Monolayers on W(001) Studied by Spin-Polarized STM*

5.7.2005: J. Wiebe, L. Sacharow, A. Wachowiak, S. Heinze, M. Morgenstern, G. Bihlmayer, S. Blügel, and R. Wiesendanger, 13th International Conference on STM, Sapporo (Japan): *The Spectroscopic Signature of Stacking Faults and Dislocation Lines on Co(0001)*

7.7.2005: M. Ashino and R. Wiesendanger, 13th International Conference on STM, Sapporo (Japan): *Atomic-Resolution Dynamic Force Microscopy and Three-Dimensional Force Field Spectroscopy of Single-Walled Carbon Nanotubes*

8.7.2005: F.Meier, K. Hashimoto, G. Bihlmayer, S. Blügel, P. Ferriani, S. Heinze, J. Wiebe, and R. Wiesendanger, 13th International Conference on STM, Sapporo (Japan): *Oberservation of a Surface State on the Pt(111) Surface*

14.7.2005: M. Ashino, Seminar at Prof. Dr. Kunio Takayanagi group (Department of Physics, Tokyo Institute of Technology), Tokyo (Japan): *Dynamic Force Microscopy and Spectroscopy of Single-Walled Carbon Nanotubes with Atomic Resolution*

15.7.2005: M. Ashino, Seminar at Prof. Dr. Yukio Hasegawa group (Institute for Solid State Physics, University of Tokyo), Chiba (Japan): *Atomic-Resolution Dynamic Force Microscopy and Three-Dimensional Force Field Spectroscopy of Single-Walled Carbon Nanotubes*

16.8.2005: C. J. Chen, 8th International Conference on Noncontact Atomic Force Microscopy (NCAFM ´05) , Bad Essen (Germany): *Possibility of imaging lateral profiles of tetrahedral hybrid orbitals in real space*

17.8.2005: M. Ashino and R. Wiesendanger, 8th International Conference on Noncontact Atomic Force Microscopy (NCAFM ´05), Bad Essen (Germany): *Direct observation of individual defects on carbon nanotubes by dynamic force microscopy*

18.10.2005: R. Wiesendanger, Lecture to the Science and Technology Committee of the NATO Parliamentary Assembly, Hamburg (Germany): *Nanotechnology - Takeoff to a new world*

19.10.2005: M. Ashino, VEECO user meeting, Hamburg (Germany): *Atomic-Resolution Three-Dimensional Force Field Spectroscopy of Single-Walled Carbon Nanotubes*

2.11.2005: M. Bode, Advanced Light Source, Berkeley (USA): *Imaging complex spin structures of magnetic nanostructures by spin-polarized STM*

2.11.2005: C. J. Chen, O. Pietzsch, D. Haude, and R. Wiesendanger, 52nd International Symposium of the American Vacuum Society, Boston (USA): *STM and AFM imaging with in-situ tip characterization*

7.11.2005: O. Pietzsch, National Institute of Standards and Technology (NIST), Gaithersburg, MD (USA): *Spin-Polarized Scanning Tunneling Spectroscopy of Magnetic Nanostructures: Co on Cu(111)*

21.11.2005: R. Wiesendanger, CMS-Seminar, Wien (Austria): *Physics of Nanomagnetism revealed by spin-polarized scanning tunneling spectroscopy*

25.11.2005: M. Ashino, Joint Workshop on Molecules, Nanostructures, and Scanning Probe Microscopy, the 21st COE Program for Material Science and Nano Engineering, Osaka University, Osaka (Japan): *Atomic-resolution dynamic force microscopy and spectroscopy of single-walled carbon nanotubes at low temperature*

7.12.2005: R. Wiesendanger, 2. NINa Schwerpunkttreffen: Nanoanalytik für Forschung und Industrie, Kiel (Germany): *Nanoanalytik mittels Rastersensormethoden: Von der Grundlagenforschung zur industriellen Anwendung*

14.12.2005: R. Wiesendanger, HiTec-Seminar: Neue Materialien durch chemische Funktionalisierung und Nanostrukturierung, Hamburg (Germany): *Nanotechnologie - Aufbruch in neue Welten*

18.1.2006: A. Schwarz, Seminar Yale University, New Haven (USA): *Atomic Resolution Force Microscopy and Spectroscopy*

20.1.2006: J. Wiebe, F. Meier, K. Hashimoto, A. Wachowiak, D. Haude, T. Foster, M. Morgenstern, J.-M. Tang, M. E. Flatte, and R. Wiesendanger, Leibniz Institute for Solid State and Materials Research Dresden, Dresden (Germany): *Towards Spin-Resolved Imaging of Single Magnetic Defects Using a 300mK-Scanning Tunneling Microscope*

26.1.2006: A. Schwarz, Seminar Yale University, New Haven (USA): *Local Magnetic Properties of Complex Oxides Studied by Magnetic Force Microscopy*

13.2.2006: J. Wiebe, F. Meier, K. Hashimoto, M. Morgenstern, J.-M. Tang, M. E. Flatte, and R. Wiesendanger, II Physikalisches Institut B, Rheinisch-Westfälische Technische Hochschule Aachen, Aachen (Germany): *Scanning Tunneling Spectroscopy of Individual Mn Acceptors in InAs*

15.2.2006: K. von Bergmann, M. Bode, A. Kubetzka, O. Pietzsch, E.Y. Vedmedenko, P. Ferriani, S. Heinze, and R. Wiesendanger, 215. PTB-Seminar: Herstellung und Charakterisierung von magnetischen Nano-Strukturen und Teilchen, Braunschweig (Germany): *Spinpolarisierte Rastertunnelmikroskopie von magnetischen Nano-Strukturen*

16.2.2006: K. von Bergmann, M. Bode, A. Kubetzka, O. Pietzsch, S. Heinze, P. Ferriani, E.Y. Vedmedenko, G. Bihlmayer, S. Blügel, and R. Wiesendanger, Institute of physical and theoretical chemistry, University of Bonn, Bonn (Germany): *Spin-polarized scanning tunneling microscopy of magnetic iron nanostructures and monolayers*

27.3.2006: M. Bode, E. Vedmedenko, K. von Bergmann, A. Kubetzka, P. Ferriani, S. Heinze, and R. Wiesendanger, 70th Spring Conference, Deutsche Physikalische Gesellschaft, Dresden (Germany): *Atomic Spin Structure of Antiferromagnetic Domain Walls*

27.3.2006: O. Pietzsch, M. Bode, K. von Bergmann, A. Kubetzka, and R. Wiesendanger, 70th Spring Conference, Deutsche Physikalische Gesellschaft, Dresden (Germany): *Spin-Polarized Scanning Tunneling Spectroscopy of Dislocation Lines in Fe Films on W(110)*

27.3.2006: F. Marczinowski, J. Wiebe, F. Meier, K. Hashimoto, M. Morgenstern, R. Wiesendanger, JM. Tang, and M. E. Flatte, 70th Spring Conference, Deutsche Physikalische Gesellschaft, Dresden (Germany): *Scanning Tunneling Spectroscopy on single Mn-acceptors in InAs*

27.3.2006: A. Schliwa, T. Maltezopoulos, M. Morgenstern, R. Wiesendanger, and D. Bimberg, 70th Spring Conference, Deutsche Physikalische Gesellschaft, Dresden (Germany): *Impact of Piezoeletricity on Shape and Order of Wavefunctions in Uncapped InAs/GaAs Quantum Dots*

27.3.2006: M. Ashino and R. Wiesendanger, 70th Spring Conference, Deutsche Physikalische Gesellschaft, Dresden (Germany): *Direct Observation of Individual Defects on Carbon Nanotubes by Dynamic Force Microscopy*

28.3.2006: J. Wiebe, F. Meier, K. Hashimoto, G. Bihlmayer, S. Blügel, P. Ferriani, S. Heinze, and R. Wiesendanger, 70th Spring Conference, Deutsche Physikalische Gesellschaft, Dresden (Germany): *Unoccupied Surface State on Pt(111) Revealed By Scanning Tunneling Spectroscopy*

28.3.2006: R. Schmidt, A. Schwarz, and R. Wiesendanger, 70th Spring Conference, Deutsche Physikalische Gesellschaft, Dresden (Germany): *Hydrogen-altered Gd(0001) surfaces investigated by dynamic force microscopy*

28.3.2006: A. Kubetzka, M. Bode, and R. Wiesendanger, 70th Spring Conference, Deutsche Physikalische Gesellschaft, Dresden (Germany): *Image states on ferromagnetic surfaces explored by tunneling spectroscopy*

28.3.2006: T. Matsui, C. Meyer, L. Sacharow, and R. Wiesendanger, 70th Spring Conference, Deutsche Physikalische Gesellschaft, Dresden (Germany): *STS study of Fe monomers and multimers on InAs(110) surfaces*

30.3.2006: S. Krause, L. Berbil-Bautista, M. Bode, and R. Wiesendanger, 70th Spring Conference, Deutsche Physikalische Gesellschaft, Dresden (Germany): *Thermal Switching Behaviour of Superparamagnetic Nanoislands: SP-STM on Fe/W(110)*

30.3.2006: F. Meier, K. von Bergmann, J. Wiebe, M. Bode, and R. Wiesendanger, 70th Spring Conference, Deutsche Physikalische Gesellschaft, Dresden (Germany): *Spin-resolved STM measurements of Co nanostructures on Pt(111)*

31.3.2006: L. Berbil-Bautista, S. Krause, M. Bode, and R. Wiesendanger, 70th Spring Conference, Deutsche Physikalische Gesellschaft, Dresden (Germany): *Thickness-dependent domain structure of ferromagnetic Dy(0001)/W(110) studied by spin-polarized STM*

31.3.2006: K. von Bergmann, S. Heinze, M. Bode, E. Y. Vedmedenko, G. Bihlmayer, S. Blügel, and R. Wiesendanger, 70th Spring Conference, Deutsche Physikalische Gesellschaft, Dresden (Germany): *Novel magnetic structure in the Fe monolayer on Ir(111)*

31.3.2006: K. Hashimoto, F. Meier, J.Wiebe, D. Haude, M. Morgenstern, and R. Wiesendanger, 70th Spring Conference, Deutsche Physikalische Gesellschaft, Dresden (Germany): *Scanning Tunneling Spectroscopy of magnetic-field-induced localization in InSb*

31.3.2006: A. Schwarz, U. H. Pi, M. Liebmann, Z. G. Khim, D. H. Kim, and R. Wiesendanger, 70th Spring Conference, Deutsche Physikalische Gesellschaft, Dresden (Germany), 2006-3-29:, Dresden (Germany): *Quantitative Dynamic Mode Force Spectroscopy on a Type-II Superconductor Using a Magnetic Tip: Meissner Force, Magnetostatic Tip-Vortex Interaction and Lateral Dragging Force*

31.3.2006: A. Schwarz, M. Liebmann, U. H. Pi, and R. Wiesendanger, 70th Spring Conference, Deutsche Physikalische Gesellschaft, Dresden (Germany): *How the Flux Line Lattice in the Hight-Tc Superconductor $Bi_2Sr_2CaCu_2O_{8+\delta}$ Melts: A Magnetic Force Microscopy Study*

5.4.2006: R. Wiesendanger, Lions Club Hamburg-Harburg, Hamburg (Germany): *Nanotechnologie - Aufbruch in neue Welten*

19.4.2006: K. von Bergmann, Vortragsreihe: Materialcharakterisierung mit modernen Methoden der physikalischen und chemischen Analytik, Fachbereich Chemie, Universität Hamburg, Hamburg (Germany): *Untersuchung von Materialien im Nanobereich mit Hilfe von Rastersensormethoden*

24.4.2006: E. Y. Vedmedenko, Seminaire Magnetisme, University Paris-Sud, Paris (France): *Non-collinear magnetic Structures at the Nanoscale*

4.5.2006: R. Wiesendanger, Condensed Matter Seminar, Stanford University, Stanford, CA (USA): *Frontiers of Nanomagnetism revealed by Spin-Polarized Scanning Tunneling Microscopy*

18.5.2006: T. Matsui, C. Meyer, L. Sacharow, and R. Wiesendanger, Advanced Scanning Probes Workshop, Castelldefels, Barcelona (Spain): *STS Studies of Fe monomers and multimers on n-InAs(110) Surfaces*

23.5.2006: R. Wiesendanger, Nanoscience/Nanotechnology Colloquium, University of Trondheim, Trondheim (Norway): *New Trends in ultra-high density magnetic data storage*

18.7.2006: R. Schmidt, A. Schwarz, and R. Wiesendanger, 9th International Conference on Noncontact Atomic Force Microscopy (NCAFM´06), Kobe (Japan): *Hydrogen-altered Gd(0001) surfaces investigated by dynamic force microscopy*

26.7.2006: M. Rontani, G. Maruccio, M. Janson, C. Meyer, T. Matsui, W. Hansen, A. Schramm, E. Molinari, and R. Wiesendanger, 28th International Conference on the Physics of Semiconductors, Vienna (Austria): *Imaging correlated wave functions of few-electron quantum dots: Theory and STS experiments*

30.7.2006: C. J. Chen, International Conference on Teaching Nanoscience and Technology, Basel (Switzerland): *Teaching Heisenberg´s concept of resonance*

31.7.2006: T. Matsui, C. Meyer, L. Sacharow, and R. Wiesendanger, International Conference on Nanoscience and Technology, Basel (Switzerland): *STS studies of Fe monomer and multimers on InAs(110) surfaces*

31.7.2006: G. Maruccio, M. Janson, A. Schramm, C. Meyer, T. Matsui, W. Hansen, R. Wiesendanger, M. Rontani, and E. Molinari, International Conference on Nanoscience and Technology, Basel (Switzerland): *Correlation Effects in Wave Function Mapping of MBE-Grown Quantum Dots*

2.8.2006: S. Krause, L. Berbil-Bautista, M. Bode, R. Wiesendanger, International Conference on Nanoscience and Technology, Basel (Switzerland): *Thermal Switching Behavior of Superparamagnetic Nanoislands: SP-STM on Fe/W(110)*

2.8.2006: K. von Bergmann, S. Heinze, M. Bode, E. Y. Vedmedenko, G. Bihlmayer, S. Blügel, and R. Wiesendanger, International Conference on Nanoscience and Technology, Basel (Switzerland): *Observation of a Novel Magnetic Structure in the Fe Monolayer on Ir(111) by SP-STM*

2.8.2006: C. J. Chen, International Conference on Nanoscience and Technology, Basel (Switzerland): *Response functions in dynamic-mode atomic force microscopy: analytic treatments for the intermediate case*

4.8.2006: U. Kaiser, A. Schwarz, and R. Wiesendanger, International Conference on Nanoscience and Technology, Basel (Switzerland): *Magnetic Exchange Force Microscopy*

4.8.2006: L. Berbil-Bautista, S. Krause, F. Vonau, M. Bode, and R. Wiesendanger, International Conference on Nanoscience and Technology, Basel (Switzerland): *Thickness-Dependent Domain Structure of Ferromagnetic Dy(0001)/W(110) Films Studied by Spin-Polarized Scanning Tuneling Microscopy*

4.8.2006: J. Wiebe, F. Meier, K. Hashimoto, F. Marczinowski, R. Wiesendanger, M. Morgenstern, J.M. Tang, and M. E. Flatté, International Conference on Nanoscience and Technology, Basel (Switzerland): *Scanning Tunneling Spectroscopy Study on Individual Mn-Acceptors in InAs*

4.8.2006: A. Schwarz, M. Liebmann, U. H. Pi, and R. Wiesendanger, International Conference on Nanoscience and Technology, Basel (Switzerland): *Real Space Flux Line Lattice Melting in $Bi_2Sr_2CaCu_2O_{8+\delta}$ Observed by Magnetic Force Microscopy*

4.8.2006: U. H. Pi, A. Schwarz, M. Liebmann, Z. G. Khim, D. H. Kim, and R. Wiesendanger, International Conference on Nanoscience and Technology, Basel (Switzerland): *Influence of Antiphase Boundaries in $Bi_2Sr_2CaCu_2O_8$ on Flux Lines studied by Low Temperature Magnetic Force Microscopy*

25.8.2006: K. von Bergmann, S. Heinze, M. Bode, E. Y. Vedmedenko, G. Bihlmayer, S. Blügel, and R. Wiesendanger, International Conference on Magnetism (ICM 2006), Kyoto (Japan): *Novel Magnetic Structure in the Fe Monolayer on Ir(111)*

12.10.2006: T. Matsui, C. Meyer, L. Sacharow, and R. Wiesendanger , The University of Tokyo International Symposium and the 10th ISSP International Symposium on Nanoscience at Surfaces, Kashiwa, Chiba (Japan): *STS Studies of Fe Monomers and Multimers on InAs(110) Surfaces*

14.10.2006: R. Schmidt, K. Lämmle, U. H. Pi, A. Schwarz, R. Wiesendanger, GrK Workshop "Design and Characterisation of Functional Materials", Weissenhäuser Strand (Germany): *Towards Magnetic Exchange Force Microscopy*

26.10.2006: A. Schwarz, Seminar NIST (Pierce), Gaithersburg (USA): *Advances in High Resolution Atomic Force Microscopy*

30.10.2006: F. Marczinowski, J. Wiebe, F. Meier, and R. Wiesendanger, Seminar über Methoden der Festkörper- und Halbleiterphysik, Göttingen (Germany): *STM Study on Individual Mn-Acceptors in InAs*

30.10.2006: A. Schwarz, Seminar Yale University (Schwarz), New Haven (USA): *Magnetic Exchange Force Microscopy*

9.11.2006: G. Hoffmann, SPiDMe meeting (EU), Roma (Italy): *Advanced Scanning Probe Microscopy*

27.11.2006: G. Hoffmann, ASPRINT meeting (EU), Dublin (Ireland): *Spin-Polarized Scanning Probe Microscopy*

28.11.2006: G. Hoffmann, Seminar Trinity College Dublin, Dublin (Ireland): *Salens on Surfaces*

30.11.2006: E. Y. Vedmedenko, Colloquium of the SFB 491, Bochum (Germany): *Magnetic Ordering at the Nanoscale*

11.12.2006: A. Schwarz, Seminar Prof. Löhneysen, Karlsruhe (Germany): *Advances in High Resolution Atomic Force Microscopy*

12.1.2007: K. von Bergmann, Colloquium at IBM Almaden Research Center, San Jose (USA): *Complex magnetic structures on the atomic scale revealed by spin-polarized STM*

06.02.07: R. Wiesendanger, Rotary Club Schenefeld, Hamburg (Germany): *Nanotechnologie - ein Blick in eine neue Welt*

21.02.07: R. Wiesendanger, ICTP, Seminar Trieste (Italy): *Mapping spin structures on the atomic scale*

26.3.2007: M. Menzel, A. Kubetzka, K. von Bergmann, M. Bode, and R. Wiesendanger, 71st Spring Conference, Deutsche Physikalische Gesellschaft, Regensburg (Germany): *Electronic properties of self-organized bi-atomic Fe chains on Ir(001)*

26.3.2007: A. Schwarz, U. Kaiser, and R. Wiesendanger, 71st Spring Conference, Deutsche Physikalische Gesellschaft, Regensburg (Germany): *Advances in High Resolution 3-Dimensional Force Field Spectroscopy*

26.3.2007: U. H. Pi, R. Schmidt, A. Schwarz, and R. Wiesendanger, 71st Spring Conference, Deutsche Physikalische Gesellschaft, Regensburg (Germany): *Kelvin Probe Force Microscopy on Electrically Inhomogeneous Fe/W(001) Films*

27.3.2007: F. Meier, K. von Bergmann, P. Ferriani, J. Wiebe, M. Bode, K. Hashimoto, S. Heinze, and R. Wiesendanger, 71st Spring Conference, Deutsche Physikalische Gesellschaft, Regensburg (Germany): *Co on Pt(111): from monolayer islands to single atoms*

27.3.2007: F. Marczinowski, J. Wiebe, J.-M. Tang, M. E. Flatté, M. Morgenstern, and R. Wiesendanger, 71st Spring Conference, Deutsche Physikalische Gesellschaft, Regensburg (Germany): *The Mn Acceptor in InAs: Depth-Dependent Shape and Supression of the Conduction Band*

27.3.2007: F. Marczinowski, J. Wiebe, R. Wiesendanger, M. Morgenstern, J.-M. Tang, and M. Flatté, 71st Spring Conference, Deutsche Physikalische Gesellschaft, Regensburg (Germany): *The Mn acceptor in InAs: Depth-dependent shape and suppression of the conduction band*

27.3.2007: M. Bode, M. Heide, K. von Bergmann, P. Ferriani, S. Heinze, G. Bihlmayer, A. Kubetzka, O. Pietzsch, S. Blügel, and R. Wiesendanger, 71st Spring Conference, Deutsche Physikalische Gesellschaft, Regensburg (Germany): *Discovery of a Cycloidal Spin Spiral in a Two-Dimensional Antiferromagnet*

28.3.2007: R. Wieser, E. Y. Vedmedenko, and R. Wiesendanger, 71st Spring Conference, Deutsche Physikalische Gesellschaft, Regensburg (Germany): *Non-collinear magnetism of magnetic 3d-monolayers on Cu and Ag (111) surfaces*

29.3.2007: S. Krause, L. Berbil-Bautista, G. Herzog, M. Bode, and R. Wiesendanger, 71st Spring Conference, Deutsche Physikalische Gesellschaft, Regensburg (Germany): *Current induced magnetization switching - a possible application für SP-STM?*

29.3.2007: U. Kaiser, A. Schwarz, and R. Wiesendanger, 71st Spring Conference, Deutsche Physikalische Gesellschaft, Regensburg (Germany): *Magnetic Exchange Force Microscopy*

27.3.2007: P. Ferriani, A. Kubetzka, S. Heinze, M. Bode, G. Bihlmayer, S. Blügel, K. von Bergamnn, O. Pietzsch, and R. Wiesendanger, 71st Spring Conference, Deutsche Physikalische Gesellschaft, Regensburg (Germany): *Two-Dimensional antiferromagnetism of the Co monolayer on W(001)*

14.5.2007: G. Hoffmann and R. Wiesendanger, ASPRINT meeting (EU), Nijmegen (Netherlands): *Advanced Scanning Probes for Innovative Nanoscience and Technology*

15.5.2007: R. Wiesendanger, Seminar MPI für Mikrostrukturphysik, Halle/Saale (Germany): *Spin mapping on the atomic scale*

24.5.2007: G. Hoffmann, SPiDMe Meeting (EU), Nijmegen (Netherlands): *Advanced Scanning Probe Microscopy*

2.7.2007: M. Rontani, G. Maruccio, M. Jason, A. Schramm and R. Wiesendanger, International Conference on Nanoscience and Technology, Stockholm (Sweden): *Imaging correlated wave functions of few-electron quantum dots: Theory and STS experiments*

3.7.2007: S. Krause, L. Berbil-Bautista, G. Herzog, M. Bode, and R. Wiesendanger, International Conference on Nanoscience and Technology, Stockholm (Sweden): *Current induced magnetization switching - is it possible with SP-STM?*

3.7.2007: E. Y. Vedmedenko, L. Udvari, P. Weinberger, and R. Wiesendanger, International Conference on Nanoscience and Technology, Stockholm (Sweden): *Dzyaloshinskii-Moriya interactions in nanoparticles*

4.7.2007: K. von Bergmann, A. Kubetzka, M. Bode, and R. Wiesendanger, International Conference on Nanoscience and Technology, Stockholm (Sweden): *Observation of a spin spiral state in the Mn monolayer on W(001) by spin-polarized scanning tunneling microscopy*

4.7.2007: M. Menzel, A. Kubetzka, K. von Bergmann, M. Bode, and R. Wiesendanger, International Conference on Nanoscience and Technology, Stockholm (Sweden): *Growth and electronic properties of atomic Fe chains on Ir(001)*

5.7.2007: H. Weller, G. Maruccio, C. Meyer, T. Matsui, R. Wiesendanger, D. Talapin, and S. Hickey, International Conference on Nanoscience and Technology, Stockholm (Sweden): *Wavefunction mapping of semiconductor nanocrystals*

6.8.2007: K. von Bergmann, Seminar of Prof. H. Fukuyama, Department of Physics, University of Tokyo, Tokyo (Japan): *Complex magnetic structures on the atomic scale revealed by spin-polarized STM*

16.9.2007: A. Schwarz, U. Kaiser, and R. Wiesendanger, 10th International Conference on Non-Contact Atomic Force Microscopy, NC-AFM 2007, Antalya (Turkey): *The Inverse Approach- 3D-Force-Field-Spectroscopy as a Tool to Investigate Properties of the Tip Apex Atoms*

17.9.2007: R. Schmidt, U. H. Pi, A. Schwarz, and R. Wiesendanger, 10th International Conference on Non-Contact Atomic Force Microscopy, NC-AFM 2007, Antalya (Turkey): *Fe/W(001) - a structurally, electronically and magnetically inhomogeneous system studied by force microscopy*

17.9.2007: U. Kaiser, A. Schwarz, and R. Wiesendanger, 10th International Conference on Non-Contact Atomic Force Microscopy, Antalya (Turkey): *Tip Effects in Magnetic Exchange Force Microscopy*

20.09.07: R. Wiesendanger, Int. Summer School "Physics of Functional Micro- and Nanostructures", Hamburg (Germany): *Scanning Tunneling Microscopy and Spectroscopy*

21.09.07: R. Wiesendanger, Int. Summer School "Physics of Functional Micro- and Nanostructures", Hamburg (Germany): *Scanning Force Microscopy and Spectroscopy*

24.09.07: R. Wiesendanger, Int. Summer School "Physics of Functional Micro- and Nanostructures", Hamburg, (Germany): *Recent research highlights based on scanning probe methods*

6.10.2007: J. Schwöbel, GrK 611 Workshop, Weißenhäuser Strand (Germany): *Installation of a new 300 mK STM for the investigation of molecular systems and planned experiments*

23.10.2007: G. Hoffmann, 2nd stage evaluation of ERC Starting Grant , Brussels (Belgium): *Local Probing of Molecular Spintronic Devices (LoPMoS)*

2.11.2007: J. Wiebe, Materials Science Seminar at the University of New Hampshire, Durham, New Hampshire (USA): *Imaging the magnetization of individual atoms*

6.11.2007: J. Wiebe, F. Meier, L. Zhou, and R. Wiesendanger, 52nd Magnetism and Magnetic Materials Conference, Tampa, Florida (USA): *Magnetization Curves from Individual Magnetic Adatoms*

9.11.2007: G. Hoffmann, Seminar AG M. Bröring / University of Marburg, Marburg (Germany): *Local Probing of Magnetic Molecules*

9.11.2007: S. Kuck, Seminar AG M. Bröring / University of Marburg, Marburg (Germany): *Iron-Tri-Phenyl-Corrole (FeTPC) on the Cu(111) and Cu(100) surface probed with STM*

19.11.07: R. Wiesendanger, Seminar Kavli Nanoscience Institute, Caltech, (USA): *Spin mapping on the atomic scale*

20.11.07: R. Wiesendanger, Seminar Kavli Nanoscience Institute, Caltech (USA): *Contributions of low-temperature scanning probe spectroscopy to modern condensed matter research*

3.12.2007: K. von Bergmann, Seminar of Group of Prof. J.I. Pascual, Inst. of Exp. Physics, Free Univ. Berlin , Berlin (Germany): *Complex magnetic structures on the atomic scale revealed by spin-polarized STM*

10.12.2007: G. Hoffmann, SPiDMe Meeting (EU), Dublin (Ireland): *Advanced Scanning Probe Microscopy*

12.12.2007: G. Hoffmann, Seminar University of Mons, Mons (Belgien): *Twisting of Phenyl Groups in Corrole and Porphyrin molecules*

7.2.2 Posters

4.3.2005: T. Behnke, M. Ashino, and R. Wiesendanger, 69th Spring Conference, Deutsche Physikalische Gesellschaft, Berlin (Germany): *Evaluation of the Elasticity on Single-walled Carbon Nanotubes on Graphite(0001) with Dynamic Force Spectroscopy*

4.3.2005: M. Zeyer-Düsterer, R. Schmidt, A. Schwarz, and R. Wiesendanger, 69th Spring Conference, Deutsche Physikalische Gesellschaft, Berlin (Germany): *Formation of Ag islands on Ag(111) using atomic force microscopy in the dynamic mode*

9.3.2005: M. von Sprekelsen and R. Wiesendanger, 69th Spring Conference, Deutsche Physikalische Gesellschaft, Berlin (Germany): *Applications of High Speed Scanning Capacitance Spectroscopy for the analysis of semiconductor microdevices*

9.3.2005: U. Kaiser, N. Plock, A. Schwarz, and R. Wiesendanger, 69th Spring Conference, Deutsche Physikalische Gesellschaft, Berlin (Germany): *Charged and non-charged surface defects on NiO(001) investigated by AFM*

20.6.2005: M. Ashino and R. Wiesendanger, 25th GIF meeting: Nanotubes and Nanowires, Dresden (Germany): *Atomic-Resolution Dynamic Force Microscopy and Three-Dimensional Force Field Spectroscopy of Single-Walled Carbon Nanotubes*

6.7.2005: T. Matsui, C. Meyer, L. Sacharow, and R. Wiesendanger, 13th International Conference on STM, Sapporo (Japan): *STM/STS Observation of Fe multimers on Semiconductor Surface*

17.8.2005: R. Schmidt, M. Zeyer-Düsterer, A. Schwarz, and R. Wiesendanger, 8th International Conference on Noncontact Atomic Force Microscopy (NCAFM ´05), Bad Essen (Germany): *Formation of Ag islands on Ag(111) using AFM in the dynamic mode*

4.1.2006: A. Kubetzka, P. Ferriani, M. Bode, S. Heinze, E.Y. Vedmedenko, O. Pietzsch, K. von Bergmann, G. Bihlmayer, S. Blügel, and R. Wiesendanger, 364th WE-Heraeus Seminar Nanoscale Magnets - Top down meets Bottom up, Bad Honnef (Germany): *The Influence of the W Substrate and its Symmetry onto the Exchange Interaction in ultrathin Fe Nanostructures*

4.1.2006: E.Y. Vedmedenko, N. Mikuszeit, H. P. Oepen, and R. Wiesendanger, 364th WE-Heraeus Seminar Nanoscale Magnets - Top down meets Bottom up, Bad Honnef (Germany): *Multipolar ordering and magnetization Reversal in Two-Dimensional Nanomagnet Arrays*

27.3.2006: U. H. Pi, A. Schwarz, M. Liebmann, Z. G. Khim, D. H. Kim, and R. Wiesendanger, 70th Spring Conference, Deutsche Physikalische Gesellschaft, Dresden (Germany): *Evidences for Flux Line Termination Inside of a Highly Anisotropic Superconductor: A Magnetic Force Microscopy Study*

29.3.2006: M. Gyamfi, O. Pietzsch, J. C. Chen, and R. Wiesendanger, 70th Spring Conference, Deutsche Physikalische Gesellschaft, Dresden (Germany): *Design of an UHV-STM with a Split Coil Magnet for Low Temperature Applications*

29.3.2006: M. v. Sprekelsen and R. Wiesendanger, 70th Spring Conference, Deutsche Physikalische Gesellschaft, Dresden (Germany): *Two dimensional dopant profiling of semiconductor microdevices with high spatial resolution using High Speed Scanning Capacitance Spectroscopy*

29.3.2006: K. Lämmle, A. Schwarz, R. Wiesendanger, 70th Spring Conference, Deutsche Physikalische Gesellschaft, Dresden (Germany): *Development of an in-situ exchangeable inert Shapal-M-based molecule evaporator*

29.3.2006: S. Kuck, A. Wachowiak, G. Hoffmann, and R. Wiesendanger, 70th Spring Conference, Deutsche Physikalische Gesellschaft, Dresden (Germany): *STM study of CuPC molecules on Cu(111) and Au(111)*

29.3.2006: J. Wienhausen, G. Hoffmann, and R. Wiesendanger, 70th Spring Conference, Deutsche Physikalische Gesellschaft, Dresden (Germany): *Improved design for a variable temperature scanning tunneling microscope*

25.7.2006: S. Krause, L. Berbil-Bautista, M. Bode, and R. Wiesendanger, 4th International Conference on Scanning Probe Spectroscopy (SPS´06) and 1st International Workshop on Spin-Polarized Scanning Tunneling Microscopy (SPSTM-1), Hamburg (Germany): *Thermal Switching Behavior of Superparamagnetic Nanoislands: Spin-Polarized STM on Fe/W(110)*

25.7.2006: A. Kubetzka, M. Bode, and R. Wiesendanger, 4th International Conference on Scanning Probe Spectroscopy (SPS´06) and 1st International Workshop on Spin-Polarized Scanning Tunneling Microscopy (SPSTM-1), Hamburg (Germany): *Image-Potential States on Fe(110)*

25.7.2006: M. Gyamfi, S. Meckler, O. Pietzsch, and R. Wiesendanger, 4th International Conference on Scanning Probe Spectroscopy (SPS´06) and 1st International Workshop on Spin-Polarized Scanning Tunneling Microscopy (SPSTM-1), Hamburg (Germany): *Design of an ultra high vacuum scanning tunneling microscope for low temperature applications*

25.7.2006: L. Berbil-Bautista, S. Krause, F. Vonau, M. Bode, and R. Wiesendanger, 4th International Conference on Scanning Probe Spectroscopy (SPS´06) and 1st International Workshop on Spin-Polarized Scanning Tunneling Microscopy (SPSTM-1), Hamburg (Germany): *Thickness-dependent domain structure of ferromagnetic Dy(0001)/W(110) films studied by SP-STM*

25.7.2006: F. Meier, K. von Bergmann, J. Wiebe, P. Ferriani, M. Bode, K. Hashimoto, S. Heinze, and R. Wiesendanger, 4th International Conference on Scanning Probe Spectroscopy (SPS´06) and 1st International Workshop on Spin-Polarized Scanning Tunneling Microscopy (SPSTM-1), Hamburg (Germany): *Spin-resolved scanning tunneling spectroscopy of Co nanostructures on Pt(111)*

25.7.2006: T.Matsui, C.Meyer, L.Sacharow, and R.Wiesendanger, 28th International Conference on Physics of Semiconductors, Vienna (Austria): *STS study of Fe monomers and multimers on InAs(110) surfaces*

25.7.2006: T. Hänke, S. Krause, L. Berbil-Bautista, V. Wagner, M. Bode, D. Lott, A. Schreyer, and R. Wiesendanger, 4th International Conference on Scanning Probe Spectroscopy (SPS´06) and 1st International Workshop on Spin-Polarized Scanning Tunneling Microscopy (SPSTM-1), Hamburg (Germany): *Temperature-Dependent Spin-Polarized Scanning Tunneling Microscopy and Spectroscopy on the Cr(001) Surface*

25.7.2006: O. Pietzsch, S. Heinze, A. Kubetzka, M. Bode, S. Okatov, A. Lichtenstein, and R. Wiesendanger, 4th International Conference on Scanning Probe Spectroscopy (SPS´06) and 1st International Workshop on Spin-Polarized Scanning Tunneling Microscopy (SPSTM-1), Hamburg (Germany): *Spin-Polarized Rim State in Co Islands on Cu(111)*

26.7.2006: J. Wiebe, F. Marczinowski, F. Meier, K. Hashimoto, R. Wiesendanger, M. Morgenstern, J.-M. Tang, and M. E. Flatté, 4th International Conference on Scanning Probe Spectroscopy (SPS´06) and 1st International Workshop on Spin-Polarized Scanning Tunneling Microscopy (SPSTM-1), Hamburg (Germany): *Scanning Tunneling Spectroscopy on Individual Mn-Acceptors in InAs*

26.7.2006: K. Hashimoto, F. Meier, J. Wiebe, D. Haude, M. Morgenstern, and R. Wiesendanger, , 4th International Conference on Scanning Probe Spectroscopy (SPS´06) and 1st International Workshop on Spin-Polarized Scanning Tunneling Microscopy (SPSTM-1), Hamburg (Germany): *Oscillation of the density of states due to magnetic-field-induced localization in a three-dimensional semiconductor system*

26.7.2006: F. Marczinowski, K. von Bergmann, M. Bode, and R. Wiesendanger, 4th International Conference on Scanning Probe Spectroscopy (SPS´06) and 1st International Workshop on Spin-Polarized Scanning Tunneling Microscopy (SPSTM-1), Hamburg (Germany): *Growth and electronic structure of ultrathin Chromium films on Iridium(111) Investigated by scanning tunneling microscopy and spectroscopy*

26.7.2006: U. Kaiser, A. Schwarz, and R. Wiesendanger, 4th International Conference on Scanning Probe Spectroscopy (SPS´06) and 1st International Workshop on Spin-Polarized Scanning Tunneling Microscopy (SPSTM-1), Hamburg (Germany): *Advances in 3D-Force-Field-Spectroscopy*

31.7.2006: T. Hänke, S. Krause, L. Berbil-Bautista, V. Wagner, D. Lott, A. Schreyer, M. Bode, and R. Wiesendanger, International Conference on Nanoscience and Technology, Basel (Switzerland): *Temperature-Dependent Spin-Polarized Scanning Tunneling Microscopy and Spectroscopy on the Cr(001) Surface*

31.7.2006: C. J. Chen, A. Schwarz, R. Wiesendanger, O. Horn, and J. Müller, International Conference on Nanoscience and Technology, Basel (Switzerland): *Self-Actuating Self-Sensing Quartz Cantilever for Dynamic Atomic Force Microscopy*

1.8.2006: S. Kuck, J. Wienhausen, A. Wachowiak, F. Vonau, G. Hoffmann, and R. Wiesendanger, International Conference on Nanoscience and Technology, Basel (Switzerland): *Single Cu-PC molecules on Cu(111) and Au(111)*

1.8.2006: J. Wochnowski, T. Göllnitz, G. Hoffmann, J. Heck, and R. Wiesendanger, International Conference on Nanoscience and Technology, Basel (Switzerland): *Atomic Force Microscopy Studies on Catalytic Surfaces*

2.8.2006: K. Hashimoto, F. Meier, J. Wiebe, D. Haude, M. Morgenstern, and R. Wiesendanger, International Conference on Nanoscience and Technology, Basel (Switzerland): *Oscillation of the density of states due to magnetic-field-induced localization in a three-dimensional semiconductor system*

2.8.2006: S. Heinze, K. von Bergmann, G. Bihlmayer, M. Bode, E. Vedmedenko, S. Blügel, and R. Wiesendanger, International Conference on Nanoscience and Technology, Basel (Switzerland): *Insight into the Surprising Magnetism of a Monolayer Fe on Ir(111) by First-Principles Calculations*

6.9.2006: A. Schwarz, Gordon Research Conference on Magnetic Nanostructures, Oxford (UK): *Magnetic Exchange Force Microscopy*

4.1.2007: G. Herzog, S. Krause, L. Berbil-Bautista, E. Y. Vedmedenko, M. Bode, and R. Wiesendanger, 381th WE-Heraeus-Seminar "Spin-Polarized Currents in Magnetic Nanostructures", Bad Honnef (Germany): *Thermal Switching Behavior of Superparamagnetic Nanoislands: SP-STM on Fe/W(110)*

4.1.2007: S. Krause, L. Berbil-Bautista, M. Bode, R. Wiesendanger, 381th WE-Heraeus-Seminar "Spin-Polarized Currents in Magnetic Nanostructures", Bad Honnef (Germany): *Thickness-dependent domain structure of ferromagnetic Dy(0001)/W(110) studied by spin-polarized STM*

17.1.2007: K. von Bergmann, S. Heinze, M. Bode, E.Y. Vedmedenko, G. Bihlmayer, S. Blügel, and R. Wiesendanger, Winter Conference on Condensed Matter 2007, Aspen (USA): *Novel Nano-Scale Magnetic Structure in the Pseudomorphic Fe Monolayer on Ir(111)*

22.2.2007: K. Hashimoto, J. Wiebe, M. Morgenstern, and R. Wiesendanger, International Conference of Nanoelectronics, Nanostructures and Carrier Interactions (NNCI2007), Atsugi, Kanagawa (Japan): *Landau and Zeeman quantization in the absorbate-induced two-dimensional electron system on n-type InSb(110)*

26.3.2007: S. Kuck, J. Brede, F. Vonau, A. Scarfato, G. Hoffmann, and R. Wiesendanger, 71st Spring Conference, Deutsche Physikalische Gesellschaft, Regensburg (Germany): *Phthalocyanines on Surfaces*

26.3.2007: R. Schmidt, A. Schwarz, and R. Wiesendanger, 71st Spring Conference, Deutsche Physikalische Gesellschaft, Regensburg (Germany): *Dynamic Force Spectroscopy on Gadolinium Islands epitaxially grown on W(110)*

27.3.2007: G. Herzog, S. Krause, L. Berbil-Bautista, E. Y. Vedmedenko, M. Bode, and R. Wiesendanger, 71st Spring Conference, Deutsche Physikalische Gesellschaft, Regensburg (Germany): *Thermal Switching Behavior of Superparamagnetic Nanoislands: SP-STM on Fe/W(110)*

28.3.2007: J. Wochnowski, T. Göllnitz, G. Hoffmann, J. Heck, and R. Wiesendanger, 71st Spring Conference, Deutsche Physikalische Gesellschaft, Regensburg (Germany): *Atomic Force Microscopy studies on surfaces prepared by organometallic chemical vapour deposition*

7.5.2007: G. Hoffmann, S. Kuck, J. Brede, A. Scarfato, and R. Wiesendanger, Colloquium of SPP 1137 "Molekularer Magnetismus", Bad Dürkheim (Germany): *Magnetic Molecules in the Scanning Tunneling Microscope*

2.7.2007: R. Schmidt, U. H. Pi, A. Schwarz, and R. Wiesendanger, International Conference on Nanoscience and Technology, Stockholm (Sweden): *Structural and magnetic properties of Fe/W(001) studied by force microscopy*

3.7.2007: J. Wiebe, F. Meier, L. Zhou, K. von Bergmnann, P. Ferriani, K. Hashimoto, M. Bode, S. Heinze, and R. Wiesendanger, International Conference on Nanoscience and Technology, Stockholm (Sweden): *Spin-Resolved Scanning Tunneling Spectroscopy on Individual Adatoms: Cobalt on Platinum(111)*

3.7.2007: J. Wochnowski, G. Hoffmann, J. Heck, R. Wiesendanger, International Conference on Nanoscience and Technology, Stockholm (Sweden): *AFM-Investigations on nanosized metallic surfaces prepared by organometallic chemical vapour deposition*

3.7.2007: S. Kuck, J. Brede, A. Scarfato, G. Hoffmann, R. Wiesendanger, S. May, J.-P. Kloeckner, M. Prosenc, International Conference on Nanoscience and Technology, Stockholm (Sweden): *STM investigation of Salen-complexes*

10.7.2007: M. Gyamfi, S. Meckler, O. Pietzsch, and R. Wiesendanger, SFB491 Summer School 2007 - Magnetic Heterostructures and Nanomagnetism, Schwerte (Germany): *A New Scanning Tunneling Microscope for Spin-Sensitive Measurements in Ultrahigh Vacuum, at Low Temperatures, and in High Magnetic Fields*

18.9.2007: K. Lämmle, A. Schwarz, and R. Wiesendanger, 10th International Conference on Non-Contact Atomic Force Microscopy, Antalya (Turkey): *Growth Study of Salene Molecules on NaCl(001)*

Chapter 8
Talks Given by Guests

10.01.2005: Dr. A. V. Postnikov (FZ Jülich):
"Magnetic interactions in molecular magnets from first principles"

17.01.2005: Prof. Dr. F. Komori (ISSP, Tokyo, Japan):
"Tunneling-electron induced dynamics of a topological defect on the clean Ge(001)surface"

11.04.2005: Dr. J. Repp (IBM Rüschlikon, Switzerland):
"Low-temperature scanning tunneling microscopy and atomic manipulation of adsorbates on ultrathin insulating films"

27.04.2005: Dr. R. Perez (Univ. Madrid, Spain):
"Short-range chemical forces in Scanning Probe Microscopies: STM and Frequency Modulation AFM"

20.05.2005: Dipl.-Phys. A. Yakunin (TU Eindhoven, The Netherlands):
"Mn in GaAs studied by X-STM: From a single impurity to ferromagnetic layers"

23.05.2005: Dr. S. Fölsch (PDI Berlin):
"Construction and spectroscopy of monatomic quantum wire structures by means of low-temperature scanning tunneling microscopy"

26.05.2005: Dr. J. I. Arnaudas (University of Zaragoza, Spain):
"Magnetoelastic Coupling and Magnetic Anisotropy in Rare-Earth superlattices"

06.06.2005: Dr. O. Fruchart (Lab. Louis Néel, Grenoble, France):
"Self-assembled Fe(110) nanostructures: a wealth of growth and model systems for micromagnetism"

27.06.2005: Dr. Ch. Loppacher (IAPP, TU Dresden):
"Molecules adsorbed on insulating surfaces"

01.08.2005: Prof. Dr. A. Smith (Ohio University Athens, USA):
"Scanning Tunneling Microscopy Investigations of Transition Metal Nitride Surfaces"

15.08.2005: Prof. Dr. Xiofeng Jin (Fudan University, Shanghai, China):
"Magnetism of metastable ultrathin films of 3d transition metals and alloys"

22.08.2005: Dr. T. Eguchi (Tokio/Augsburg):
"High Resolution Imaging of Surface Structure and Potential Profile by Atomic Force Microscopy"

24.08.2005: Dipl.-Phys. F. Vonau (Université de Haute Alsace, Mulhouse, France):
"LT-STM investigations of the structures and electronic properties of mesoscopic systems: - 2D Erbium silicide - Self assembly of supramolecular layers on Au(111)"

07.09.2005: Dr. N. Atodiresei (Inst. f. Festkörperforschung, FZ Jülich):
"Density Functional Theory Studies of Organic Molecules on Metal Surfaces"

13.09.2005: Dr. K. Kanisawa (NTT Basic Research Laboratories, Atsugi, Japan):
"Nanometer-scale characterization of low-dimensional semiconductor structures"

16.09.2005: Dr. A. V. Balatsky (Los Alamos National Laboratory, USA):
"Inelastic tunneling spectroscopy in d-wave superconductors and collective mode spectroscopy"

31.10.2005: Dipl.-Phys. O. Mieth (TU Dresden):
"Ferroelectric polarization influenced by mechanical stress"

12.12.2005: Dipl.-Phys. S. Meckler (Univ. Düsseldorf):
"Transportuntersuchungen an zweidimensionalen Elektronengasen in hexagonalen Antidotübergittern"

19.12.2005: Prof. Dr. H. Fukuyama (Univ. of Tokyo, Japan):
"Recent STS studies of the edge state and the possible QHE in 2DES at graphite surfaces"

20.12.2005: Dr. Jian-Ming Tang (Univ. Iowa, USA):
"Electrical control and detection of single spins in a semiconductor"

09.01.2006: Dr. H. Ott (Universität zu Köln):
"Magnetic properties of thin lanthanide-metal films investigated by resonant soft-x-ray scattering"

16.01.2006: Dr. R. Wieser (Universität Duisburg):
"Thermodynamik der Domänenwände/Domänenwandstrukturen"

08.05.2006: Dr. M. Wenderoth (Univ. Göttingen):
"Probing solid state bulk properties with the STM"

15.05.2006: Dr. E. H. Brandt (MPI Stuttgart):
"The Vortex Lattice in High Temperature Superconductors: Thermal Depinning, Melting, and Nonlocal Elasticity"

12.06.2006: Dipl.-Phys. M. Bieletzki (Univ. Dortmund):
"Scanning Tunneling Microscopy and Photoemission of Clusters at Surfaces"

03.07.2006: Prof. Dr. D. K. Morr (University of Illinois at Chicago):
"Nanoscale Structures and Novel Quantum Phenomena in Correlated Electron Systems"

03.07.2006: Dr. A. Balatsky (Los Alamos, USA):
"Inelastic Tunneling Spectroscopy in Cuprates and the Collective Mode Scattering"

21.09.2006: Dr. Abel Robin (University of Groningen, The Netherlands):
"Surface Spin Polarization - Locally investigated by slow Hollow Atoms"

20.10.2006: Dr. J. Crain (NIST Gaithersburg, USA):
"Size Dependent Electronic Effects in Atomic Chains"

11.12.2006: Dr. S. Stepanow (University of Barcelona, Spain):
"Synthesis and properties of metallosupramolecular architectures at metal surfaces"

15.01.2007: M. Heide (FZ Jülich):
"Spin orbit induced spin spirals at magnetic surfaces"

05.02.2007: Dipl.-Phys. D. Obergfell (MPI, Stuttgart):
"Electrical transport measurements on novel, low-dimensional carbon nanomaterials"

07.03.2007: Dipl.-Phys. J. Schwöbel (Universität Freiburg):
"Angle-Resolved Photoelectron Spectroscopy of Sodium Clusters"

17.04.2007: Prof. Dr. P. Koenraad (TU Eindhoven, The Netherlands):
"Acceptor wavefunctions in III/V semiconductors studied by X-STM"

20.04.2007: Prof. Dr. S. Modesti (Trieste, Italy):
"Instabilities and Mott-Hubbard states in two-dimensional systems: the alpha phases on the (111) Si and Ge surfaces"

30.04.2007: Dr. U. Dürig (IBM Zürich):
"Exploiting shape-memory functionality of nano-scale thermo-mechanical indents in polymers for data storage applications"

07.05.2007: Dr. G. Bihlmayer (FZ Jülich):
"Spin-orbit splitting at surfaces"

25.06.2007: Dr. R. Klemm (University of Orlando, Florida, USA):
"Single-ion and exchange anisotropy in high-symmetry tetramer single molecule magnets"

13.07.2007: Dr. M. Ternes (IBM Almaden, San José, USA):
"Using an AFM/STM with sub-Angstrom Modulation to Measure Forces during Atomic Manipulations"

05.09.2007: Dr. Thilo Reusch (Centre for Quantum Computer Technology, University of New South Wales, Australia):
"Nano-scale dopant devices in Si patterned by STM lithography"

11.10.2007: Dr. Jianhua Gao (University of Paris):
"Low dimensional magnetism-magnetic nanowire arrays and ultrathin films"

12.11.2007: Dr. D. Frettlöch (Universität Bielefeld):
"Introduction to the mathematics of quasiperiodic structures"

21.11.2007: Dr. J. Ledieu (Ecole des Mines,Nancy, France):
"Quasicrystal surfaces: structure and potential as templates (STM Study)"

28.11.2007: Prof. Jose Ignacio Pascual (Freie Universität Berlin):
"Charge transfer on a metal surface: scanning tunneling spectroscopy of molecular donor-acceptor assemblies"

10.12.2007: Dr. Y. Yoshida (University of Florida, USA):
"Field-induced phenomena in low-dimensional quantum spin systems"

Chapter 9

Lectures and Courses at the University of Hamburg

- Nanostrukturphysik I und II

- Magnetismus und Oberflächenphysik I und II

- Einführung in die Rastersondenmikroskopie und -spektroskopie

- Ringvorlesung Physik der Mikro- und Nanostrukturen

- Seminar über Nahfeldgrenzflächenphysik und Nanotechnologie

- Seminar über aktuelle Probleme der Rastersensorphysik

- Proseminar über Theorie und Praxis der Rastersensormethoden

- Proseminar über Magnetismus und Oberflächenphysik

- Übungen zur Nanostrukturphysik I und II

- Übungen zu Magnetismus und Oberflächenphysik

- Übungen zur Einführung in die Rastersondenmikroskopie und -spektroskopie

- Physikalisches Praktikum für Fortgeschrittene

- TU - Praktikum

- Studienarbeiten zur Rastersondenmikroskopie

- Schwerpunktpraktikum Grenzflächen- und Tieftemperaturphysik

- Diplompraktikum Grenzflächen- und Tieftemperaturphysik

Chapter 10

Contributions to International Organizations

- Member of the International Advisory Board of the "n-ABLE 2005: Nanotechnology in Manufacturing" Conference (Saarbrücken, 2005)

- Member of the Program Committee of the "13th International Conference on Scanning Tunneling Microscopy STM'05" (Sapporo, Japan 2005)

- Member of the International Organizing Committee of the "Nano-2005" Conference (India 2005)

- Member of the Program Committee of the International Workshop on "Self-Organized Nanostructures" (Cargèse, France 2005)

- Member of the International Advisory Committee of the "International Symposium on Surface Science and Nanotechnology ISSS-4" (Saitama, Japan 2005)

- Member of the International Advisory Board of the "11th International Ceramics Congress" - Special Symposium: Disclosing Materials at Nanoscale (Sicily, Italy 2006)

- Member of the International Advisory and Program Committee of the "Nanoscale Superconductivity and Magnetism NSM 2006" Conference (Leuven, Belgium 2006)

- Co-Chairman of the "4th International Conference on Scanning Probe Spectroscopy SPS'06" (Hamburg 2006)

- Chairman of the "1st International Workshop on Spin-Polarized Scanning Tunneling Spectroscopy" (Hamburg 2006)

- Member of the International Advisory and Program Committee of the "International Conference on Nanoscience and Technology ICN+T 2006" (Basel, Switzerland 2006)

- Member of the International Scientific Advisory Committee of the "16th International Microscopy Congress IMC16" (Sapporo, Japan 2006)

- Member of the Scientific Committee of the DVG 2006 Conference (Darmstadt 2006)

- Member of the International Advisory Committee of the "ISSP-10 Symposium on Nanoscience at Surfaces" (Kashiwa, Japan 2006)

- Organizer of the "International Nanoscience Symposium" (Hamburg 2007)

- Member of the International Advisory and Program Committee of the "International Conference on Nanoscience and Technology ICN+T 2007" (Stockholm, Sweden 2007)

- Member of the International Advisory Committee of the "Second International Conference on Emerging Adaptive Systems and Technologies EAST 2007" (Kumaracoil, Tamil Nadu, India 2007)

Chapter 11

How to reach us

... by mail	write to
	University of Hamburg,
	Microstructure Advanced Research Center and
	Institute of Applied Physics,
	Jungiusstraße 11,
	D-20355 Hamburg, Germany.
... by phone	call (++49) 40 42838 5244.
... by fax	send to (++49) 40 42838 6188.
... by e-mail	send to `wiesendanger@physnet.uni-hamburg.de`
... within the WWW	`www.nanoscience.de`
... personally	